RED-EMITTING ORGANIC FLUOROPHORES

Joshua Karl Gunnar Karlsson

Molecular Photonics Laboratory

School of Natural and Environmental Sciences (Chemistry)

Newcastle University

This dissertation is submitted in fulfilment of the degree:

Doctor of Philosophy

March 2018

Abstract

Our understanding of molecular photophysics has developed over the course of the twentieth and early twenty-first century. Mastering the underlying mechanisms of fluorescence from organic dyes necessitates development of many spectroscopic techniques. For a time the field was driven by studying increasingly elaborate molecular structures, but now attention has returned to smaller systems, even single chromophore entities. This has in part been influenced by cost, and many small chromophores for commercial use are being designed with very specific properties based on classic photophysics concepts. Even relatively small organic fluorophores display subtleties which can be influenced by minor changes in structure or local environment. As is observed in this work, there are cases where manipulation of a single atom can afford a major change in optical properties.

Having understood the nature of absorption and emission, our attention turns to how this knowledge could be applied to understand intricate processes such as energy and electron transfer. Consequently it becomes possible to rationally design dyes with desirable properties, and new technologies emerge as a result. A prime example lies in recent efforts to enhance the efficiency of organic solar cells, where investigators have turned to exploiting E-type delayed fluorescence (a concept introduced decades earlier). Now the field is awash with applications where old principles have been utilized to the advantage of new technologies.

This thesis is concerned with the particular problems of analyzing organic dyes which absorb and emit in the red region. The introductory chapter outlines how the molecular photophysics has evolved over decades and defines key concepts in optical spectroscopy. We also examine two state-of-the-art techniques which rely on an understanding of fluorescence and electron transfer: namely super-resolution fluorescence microscopy and singlet-exciton fission. Finally, some consideration is given to how the field will likely manifest itself in the near future.

An investigation into the origin of the red absorption/fluorescence characteristic to aza-BODIPY dyes, a variant on the popular boron dipyrromethene (BODIPY) dye family, is the

basis of Chapter 3. Aza-BODPIY dyes have a carbon atom replaced by nitrogen at the *meso* site, causing a 100 nm red-shift relative to regular BODIPY. Careful analysis of the photophysics of aza-BODIPY, alongside a non-aza analogue, builds a picture of how this relatively large change in the excited state energy landscape is achieved with such a minor modification to the core structure.

Chapter 4 explores the triplet-exited state properties of a popular red-emitting organic semiconductor chromophore, TIPS-pentacene. We discuss various mechanisms leading to quenching of fluorescence at the expense of enhancing intersystem crossing into the triplet manifold for TIPS-pentacene, which sees high triplet or fluorescence yields depending on the environment. TIPS-pentacene is widely used as the basis for singlet-exciton splitting dyes, where two triplets are formed from the singlet-excited state. This is therefore a pertinent example for explaining just how one can access the triplet state.

In Chapters 5 and 6, we examine a new bridged pentacene bichromophore, which undergoes exciton multiplication by intramolecular singlet fission. Transient absorption spectroscopy suggests there is strong communication between pentacene moieties in the bichromophore, showing an unusually delocalized triplet state. This is contrary to many other singlet fission chromophores based on pentacene.

The problem of how to accurately measure fluorescence quantum yields in the red spectral region is tackled in Chapter 7. The difficulties with measuring fluorescence in this region are highlighted and an alternative method for recording fluorescence yields, thermal blooming spectroscopy, reintroduced. A series of red-emitting cyanine dyes is proposed as new ratiometric fluorescence yield standards. This work has involved construction of a bespoke instrument for the task.

In the final chapter, the mechanism of fluorescence “blinking” in the context of super-resolution fluorescence microscopy is studied. Using a combination of steady-state and time-resolved spectroscopic measurements in conjunction with advanced analysis of super-resolution microscope data allows for an interpretation of how such regular and reliable on/off fluorescence blinking is achieved with a popular commercial cyanine dye. Previously proposed mechanisms are tested extensively by optical characterization of the system. It is inferred that isomerization plays a role in switching between states.

Acknowledgements

Firstly, I would like to thank my family for the years of support making it possible for me to reach this level of education. Getting to this point is the product of many years perseverance, which would not have been possible without a strong support network.

Secondly, I gratefully acknowledge collaborators who have enabled many projects to come to fruition. At the University of Newcastle I thank Dr. Alex Laude (Medical School Bio-Imaging Unit) for his endless patience on matters related to fluorescence microscopy, for donating valuable chemicals, and always accommodating further experiments on his highly specialized instrumentation. Prof. William McFarlane and Dr. Corinne Wills were essential in contributing NMR analysis for key samples and were always willing to help. Dr. Michael Hall very kindly donated samples of aza-BODIPY used in many projects. For data analysis related matters I thank Dr. Jerry Hagon and Dr. Ata Amini. To the school's mechanical and electrical workshops I owe a debt of gratitude for the several projects they have gladly taken up over three years. This was particularly important for construction of the thermal blooming apparatus used in Chapter 5. I am equally grateful to Dr. Alparslan Atahan for his determined work as visiting postdoctoral research associate, who synthesized the compounds used for studying singlet fission.

My work also extended to external collaborations, which provided vital resources. Prof. Nikolai Tkachenko (Tampere University of Technology, Finland) kindly hosted me for a week to conduct ultrafast transient absorption spectroscopy measurements. Prof. Tetsuro Majima has my thanks for conducting pulse radiolysis experiments and being a wonderful host during a visit to Osaka University, Japan. Thanks also to Dr. Heinz Mustroph of FEW Chemicals GmbH (Germany) for donating a series of cyanine dyes.

To the members of our research group and the wider cast of the Molecular Photonics Laboratory, I thank everyone for the friendly and co-operative research environment. Particular thanks go to Owen Woodford and Dr. Patrycja Stachelek, who I have had the pleasure to get to know and work with.

Finally, and most importantly, I am deeply indebted to Prof. Anthony Harriman for his tireless patience, support and enthusiasm throughout my studies. I have benefitted enormously from the introduction and insight into the expansive and fascinating field which is molecular photophysics. As an academic supervisor I could not imagine anyone more able. Thank you!

Publications Associated with this Thesis

Some results chapters are associated with a publication in a scientific journal. Full papers are attached in the appendix.

Chapter 3: Karlsson, J. K. and Harriman, A. 2016. Origin of the Red-Shifted Optical Spectra Recorded for aza-BODIPY Dyes. *The Journal of Physical Chemistry A*, 120 (16), pp. 2537-2546.

Chapter 4/5: Pulse Radiolysis of TIPS-Pentacene and a Fluorene-bridged Bis-Pentacene: Proof of Intramolecular Singlet-Exciton Fission (Submitted).

Chapter 7: Karlsson, J.K., Woodford, O.J., Mustroph, H. and Harriman, A., 2018. Cyanine dyes as ratiometric fluorescence standards for the far-red spectral region. *Photochemical & Photobiological Sciences*, 17 (1), pp. 99-106.

Other papers associated with work in this thesis:

Karlsson, J. K., Woodford, O. J., Al-Aqar, R. A. and Harriman, A., 2017. Effects of Temperature and Concentration on the Rate of Photo-bleaching of Erythrosine in Water. *The Journal of Physical Chemistry A*. 121 (45), pp. 8569-8576.

Table of Contents

Abstract……i

Acknowledgements……iii

Publications Associated with this Thesis……v

Chapter 1: Introduction

1.1 The Versatility of Light-Induced Molecular Processes.....1

1.2 A Mechanistic Understanding of Excited State Dynamics.....4

1.2.1 Timeline of Discovery.....4

1.2.2 The Triplet State.....8

1.3 Quantitative Fluorescence Measurements.....10

1.3.1 The Problem of Measuring Fluorescence in the Red Region.....10

1.3.2 The Englman-Jortner Energy Gap Law.....12

1.3.3 Barrier Crossing Dynamics.....14

1.4 Rational Design of Fluorescence Properties.....15

1.4.1 Case Study 1: Cyanine Dyes.....15

1.4.2 Case Study 2: BODIPY Dyes.....18

1.5 Taking Advantage of Molecular Photophysics in New Technologies.....21

1.5.1 Singlet-Exciton Fission.....21

1.5.2 Super-Resolution Fluorescence Microscopy.....25

1.6 Future Trends.....28

1.7 References.....30

Chapter 2: Experimental Methods

2.1 Materials.....39

2.2 Experimental Error and Reproducibility.....40

2.3 Steady-State Absorption and Emission Spectroscopy.....40

2.4 Time-Resolved Absorption and Emission Spectroscopy.....43

2.4.1 Fluorescence Lifetime Measurements.....43

2.4.2 Laser Flash Photolysis and Pulse Radiolysis.....46

2.4.3 Ultra-Fast Transient Absorption Spectroscopy.....48

2.5 Temperature-Dependent Spectroscopic Measurements.....50

2.6 Thermal Blooming Spectroscopy for Measurement of Fluorescence Quantum Yields.....50

2.7 Variable Path Length Cell for Absorption and Emission Spectroscopy.....55

2.8 Steady-State Photobleaching Studies.....56

2.9 Fluorescence Recovery after Photobleaching: FRAP.....56

2.10 Super-Resolution Fluorescence Microscopy: STORM.....58

2.11 Cyclic Voltammetry.....58

2.12 Data Analysis.....59

2.12.1 Relative Fluorescence Yield, Radiative Rate Constant and Strickler-Berg Relationship.....59

2.12.2 Spectral Deconstruction of Absorption and Emission Spectra – Rational and Relationship with Molecular Dynamics.....60

2.12.3 Analysis of Transient Absorption Spectra.....62

2.12.4 Computational Methods.....63

2.13 References.....64

Chapter 3: On the Origin of the Red-Shifted Optical Spectra Recorded for aza-BODIPY Dyes

3.1 Introduction.....70

3.2 Results and Discussion.....72

3.2.1 Steady-State Spectroscopic Measurements.....72

3.2.2 Stability Against Photobleaching.....77

3.2.3 Characterization of the aza-BODIPY Triplet.....79

3.2.4 Anisotropy Data and Fluorescence Recovery after Photobleaching.....81

3.2.5 Quantum Chemical Calculations.....84

3.3 Conclusions.....90

3.4 References.....92

Chapter 4: On the Triplet-Excited State of TIPS-Pentacene

4.1 Introduction.....96

4.2 Results and Discussion.....100

4.2.1 Steady-State Spectroscopic Measurements.....101

4.2.2 Transient Absorption Spectroscopy.....105

4.2.3 Energy Levels.....114

4.2.4 Redox Chemistry.....120

4.3 Conclusions.....126

4.4 References.....128

Chapter 5: Photophysics of a Bis-Pentacene Derivative in Fluid Solution – Qualitative Results

5.1 Introduction.....134

5.2 Results and Discussion.....139

5.2.1 Steady-State Spectroscopic Measurements.....140

5.2.2 Nanosecond Time-Resolved Optical Measurements.....144

5.2.3 Electrochemistry.....150

5.2.4 Ultrafast Transient Absorption Spectroscopy.....154

5.2.5 Delayed Fluorescence.....160

5.3 Conclusions.....162

5.4 References.....164

Chapter 6: Photophysics of a Bis-Pentacene Derivative in Fluid Solution – Further Considerations

6.1 Introduction.....170

6.2 Pulse Radiolysis in De-aerated Benzene (or Toluene).....172

6.3 Analysis of the Ultrafast Transient Absorption Spectral Data.....177

6.3.1 The Effect of Solvent Polarity on the Ultrafast Photophysics.....181

6.4 Conclusions.....188

6.5 References.....189

Chapter 7: Cyanine Dyes as Ratiometric Fluorescence Standards for the Far-Red Spectral Window

7.1 Introduction.....192

7.2 Results and Discussion.....193

7.2.1 Experimental Protocol.....194

7.2.2 Calibration with Control Compounds.....196

7.2.3 Errors and Reproducibility.....201

7.2.4 Cyanine Dyes.....202

7.2.5 The Interplay of Radiative Decay and Isomerization.....208

7.3 Conclusions.....211

7.4 References.....213

Chapter 8: Photoisomerization-Induced Fluorescence Blinking in a Far-Red Emitting Cyanine Dye under dSTORM Imaging Conditions

8.1 Introduction.....218

8.2 Results and Discussion.....222

8.2.1 Steady-State Spectroscopic Measurements.....222

8.2.2 Characterizing the Triplet-Excited State.....230

8.2.3 Photo-induced Isomerization.....233

8.2.4 STORM Microscope Data Analysis.....241

8.2.5 Computational Modeling.....242

8.3 Conclusions.....246

8.4 References.....249

Appendix: Publications to Accompany Chapters.....253

Chapter 1: Introduction

1.1 The Versatility of Light-Induced Molecular Processes

Humans only perceive a small fraction of the electromagnetic spectrum, notably as visible light (400-700 nm) and heat to the touch (infrared region). Nonetheless, within that small window vast arrays of organic and inorganic compounds display photophysical properties, giving rise to colour in the visible spectrum. Our modern way of life is based on the ready availability of dyestuffs and we need a constant supply of new and unusual colourful materials, many of which are taken for granted. Most of us spend considerable time staring at a coloured computer display. Life itself is sustained by the green pigment central to photosynthesis, chlorophyll.[1] Suffice to say there has been for some time an imperative to understand the processes dictating absorption and emission of light in dyes. Such an understanding underpins much of industrialized society.

Since the nineteenth century, pioneers in the field now known as molecular photophysics have defined the physical basis of light interacting with chromophores (early notable investigators including Stokes, Becquerel, Vavilov, Gaviola, Lewis, Kasha, and Förster).[2,3] In doing so, it has been possible to understand the mechanisms behind plant photosynthesis[4], to make technological breakthroughs with lasers[5,6], solar cells[9,10], and to advance medical sciences with fluorescence microscopy[7,8] and photodynamic therapy as a cancer treatment.[11,12] This is in addition to the myriad of applications that utilize fluorescence as a probe in sensing environmental changes[13,14], a way of lighting up the world with light emitting diodes[15,16] and developments in solar fuels.[17-19]

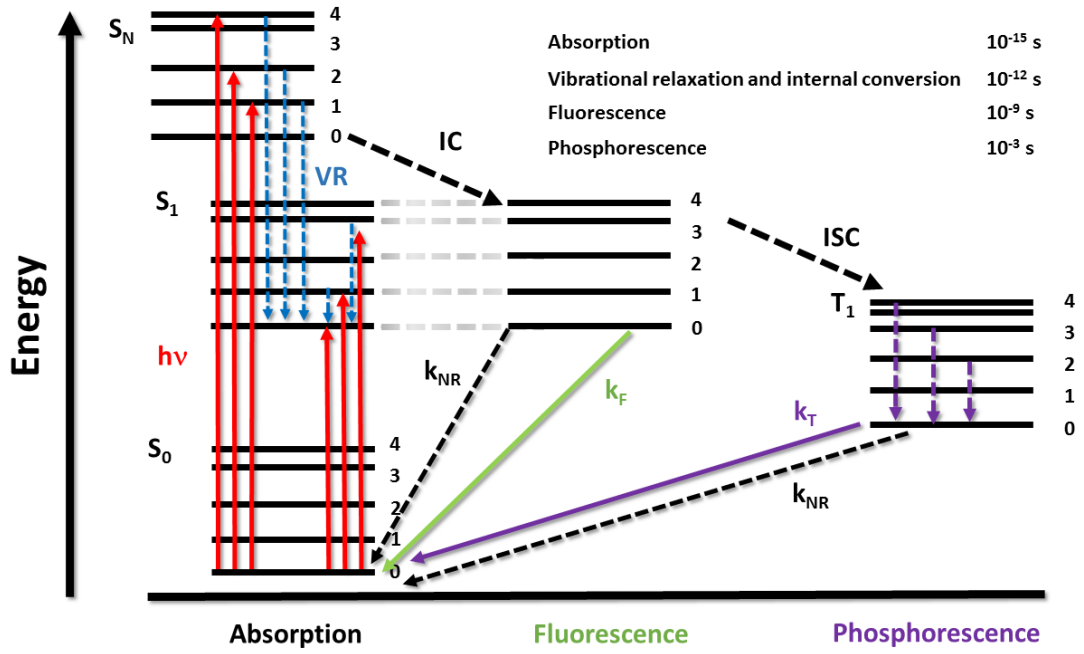

Figure 1.1. Simplified Jablonski diagram illustrating some of the photophysical processes observed in chromophores. The various rate constants for transitions to each state are governed by the structure of the molecule and the local environment. Key: VR (vibrational relaxation), IC (internal conversion), ISC (intersystem crossing). Nonradiative processes are drawn with dashed lines.

The number of processes a molecular dye can undergo upon absorbing a photon and being promoted to the excited state are numerous, leading to many practical applications. Molecular photophysics is primarily concerned with manipulating the excited state. Furthermore, a change in the local environment often affects a change in a dye's optical properties, providing a means of measuring various physical parameters such a pH, temperature, viscosity, pressure, voltage and detecting analytes.[20-23] In cases where the dye fluoresces, the above parameters often have an effect on the fluorescence characteristics, hence fluorescent probes have successfully been utilized in measuring these properties in the field. Practical examples of utilizing such dyes include "lab on a chip" applications, where physiological processes can be monitored quickly with a single device.[24,25]

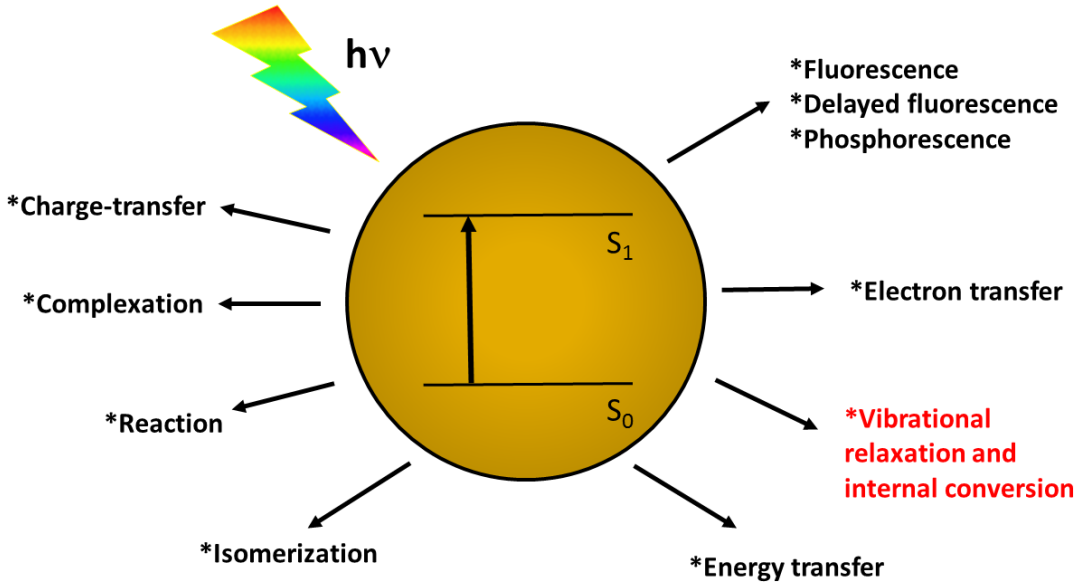

Figure 1.2. Examples of processes that may occur subsequent to a molecular dye absorbing a photon.

Broadly speaking, the array of molecular photophysical processes are encompassed in Figure 1.2. These all compete with vibrational relaxation of the S_1 or higher-energy states by internal conversion to S_0, emitting heat. Engineering other processes, such as electron transfer or energy transfer to compete with alternative decay pathways, can be accomplished with design of new dyes or in some cases by altering the surrounding environment. Knowing what to change, however, in order to achieve the desired effect is easier when one understands the origins of the underlying photophysical processes.

1.2 A Mechanistic Understanding of Excited State Dynamics

1.2.1 Timeline of Discovery

During the early to mid-twentieth century many of the light-emitting properties seen in organic materials were defined and understood from a mechanistic point of view. Early discoveries, such as fluorescence quenching (explained by the Stern-Volmer relationship),[26,27] provided sound, quantitative grounds for characterizing physical interactions related to fluorescence. Later discoveries explained the polarized nature of fluorescence (Weigert, Vavilov, Levschin and Francis Perrin)[28,29] and made the distinction between the electronic transitions related to fluorescence (the singlet-excited state) and phosphorescence (triplet state, Lewis and Jablonski).[30,31] Invoking the triplet state was extremely important as it formally introduced the idea of metastable excited states.

Resonance energy transfer (RET)[32], the nonradiative process by which excited state energy is transferred from one molecule (donor, D) to another (acceptor, A) underpins processes in plant photosynthesis and other donor-acceptor systems. Resonance energy transfer mechanisms fall under two main categories, Förster-type (through space communication, known as FRET)[33] and Dexter[34] (through bond communication). Theodor Förster developed a theory of energy transfer between chromophores by dipole-dipole interactions. This is equally valid for singlet-singlet, singlet-triplet and triplet-triplet processes without direct orbital overlap between donor and acceptor. FRET has become a vital means of measuring distances between donor and acceptor chromophores in biological media.

In the case of two coupled fluorophores, each would have its own distinct radiative rate constant (k_{RAD}) in the absence of any interaction, which is then quenched by competition from FRET. For FRET, the rate of energy transfer has been quantified using Equation 1.1 where all the necessary observables can be obtained from the absorption and fluorescence spectra.[33] Here N is Avogadro's number, n the refractive index, R the distance between donor and acceptor, and τ_s the mean radiative lifetime of the donor. The term on the right describes the overlap integral of donor fluorescence and acceptor absorbance while κ describes the orientation between the D-A, explained in terms of transition dipole moments (Equation 1.2). The term θ_{D-A} refers to the angle between

the transition dipole moment vectors, and the remaining angles are between the individual vectors and the displacement vector of D-A combined (in a randomized system $\kappa^2 = \frac{2}{3}$). The equations simplify to (3) where the well-known sixth power dependence on the D-A separation is emphasized. τ_s being the mean fluorescence lifetime of the sensitizer is related to the fluorescence quantum yield η_s^0 and intrinsic fluorescence lifetime τ_s^0 of the sensitizer in the absence of energy transfer by (4). The efficiency of FRET can experimentally be obtained by recording the relative fluorescence of sensitizer with and without acceptor or from the fluorescence lifetimes (5).

$$k_{FRET} = \frac{9000 \ln 10 \, \kappa^2}{128 \, \pi^6 \, n^4 \, N \, \tau_s R^6} \int_0^\infty f_s(v) \varepsilon_A(v) \frac{dv}{v^4} \qquad (1.1)$$

$$\kappa = cos\theta_{D-A} - 3cos\theta_D * cos\theta_A \qquad (1.2)$$

$$k_{FRET} = \frac{1}{\tau_s}\left(\frac{R_0}{R}\right)^6 \qquad (1.3)$$

$$\tau_s = \tau_s^0 \, \eta_s^0 \qquad (1.4)$$

$$E = 1 - \frac{I_s}{I_s^0} = 1 - \frac{\tau_s}{\tau_s^0} \qquad (1.5)$$

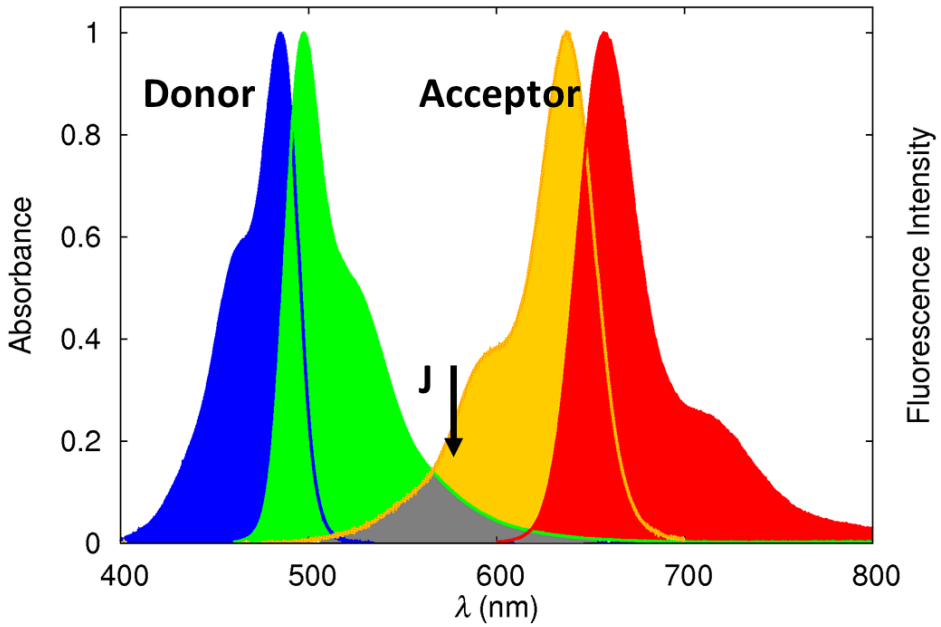

Figure 1.3. Example of a donor-acceptor system which undergoes efficient Förster energy transfer. Here energy transfer is between two cyanine dyes where the donor is Cy3 and acceptor Cy5. The spectral overlap, J, corresponds to the integral in Equation 1.1.

FRET, popularly referred to as a “spectroscopic ruler”, is a fundamental tool for analysis of donor-acceptor systems in liquids, gases and solids. It has been particularly useful in biology. FRET tends to be the dominant mechanism discussed in the context of dyes because Dexter RET operates only over short distances (5-20 Å) where there is orbital overlap between donor and acceptor, whereas FRET propagates by Coulombic coupling between moieties across distances between 10 and 100 Å. In covalently coupled D-A systems, the two processes can work together and it is important to note that singlet-triplet energy exchange most likely occurs with the Dexter mechanism.[35]

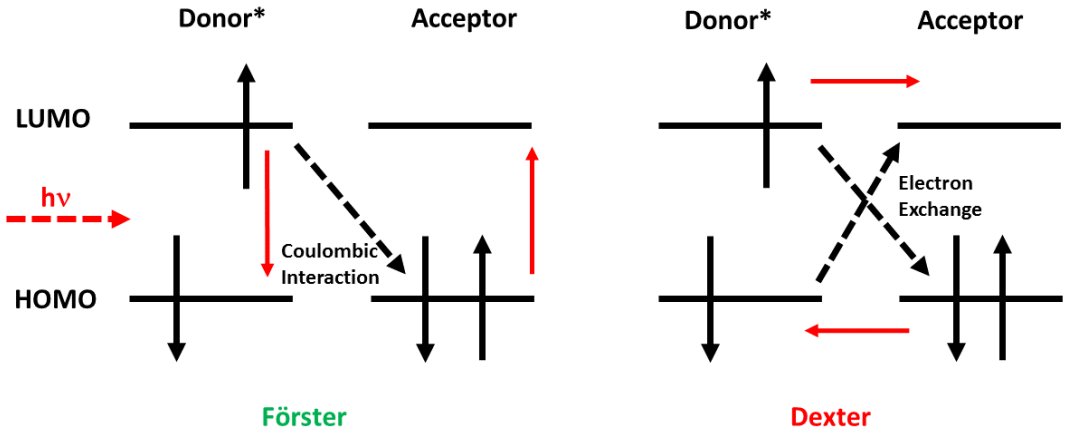

Figure 1.4. Schematic of the main RET mechanisms.

By the 1960s advances in understanding photophysical processes had been applied to new experimental techniques and technologies. A major experimental advance was the development of a means to monitor fast (sub-millisecond) photophysical processes, which was accomplished with flash photolysis.[36,37] Introduced by Porter and Norrish in the 1950s, this pump-probe experiment allowed one to first convert a significant portion of chromopohres to the excited state (with a high intensity flash) and observe the decay kinetics of transient species (with a probe light). Flash photolysis revolutionized photophysical research (the Nobel Prize 1967 in chemistry being awarded to Porter, Norrish and Eigen for developing the technique) and remains highly relevant today. With the advent of lasers in the 1970s it became possible to observe the decay of nanosecond transient species. Later, femtosecond lasers allowed one to probe the nature of the singlet-excited state itself, not just the states reached subsequent to decay of the singlet.

Equally important was the emergence of molecular dyads, i.e. covalently-linked dyes. Where previously processes such as energy and electron transfer were examined as a bimolecular process, one largely relied on diffusion for interaction to occur. This did not allow for fine control of the system, nor did it allow for simple kinetic models. Weak interactions such as hydrogen bonding and electrostatics are useful strategies for bringing donor and acceptor together, but this is rarely a substitute for a covalent bond. A redox-active molecule must be held in very close proximity to a sensitizer if electron transfer is to occur. Covalently linking the two gives one the most control. This, after all is the approach Nature takes in the photosynthetic reaction centre, where cofactors are held rigidly in proteins to ensure good communication between chlorophylls and the redox-active components.

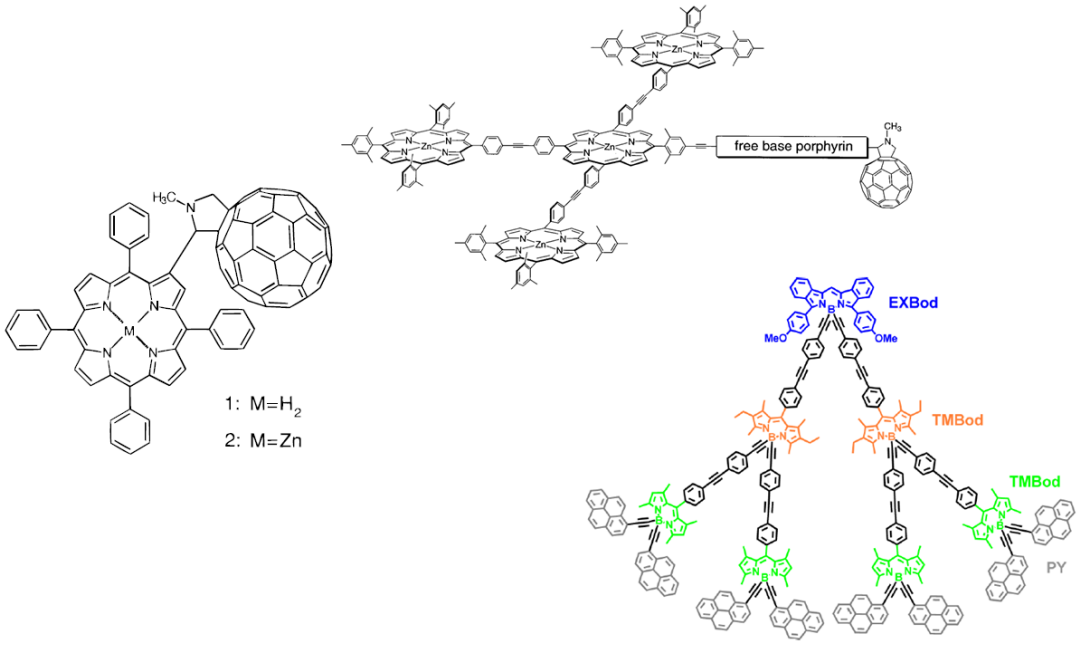

Figure 1.5. Some examples of synthetic donor-acceptor systems from the literature.[43,44,45]

The emergence of molecular dyads was a big boost to the field due to the rational control of through-bond electronic and or through-space communication achieved by adjusting the geometry.[38] Unsurprisingly, early molecular dyads were based on porphyrins, thereby mimicking the chlorophylls in plant photosynthetic systems.[39] Porphyrins being a common donor, C_{60} is perhaps the best known electron acceptor due to its excellent chemical reactivity and low reorganization energy.[40] Having the redox active donor-acceptor linked covalently does present the problem of rapid recombination of charges, this has been overcome by devising dyads with multiple redox active steps, so that electron transfer occurs in a cascade sequence with ever increasing barriers to charge recombination. This bio-inspired approach has been prominently featured in the important work from Wasielewski, Gust, Osuka and their co-workers, a strategy which has led to very complex and elegant chromophore arrays.[41,42]

1.2.2 The Triplet State

It took some considerable time to make the physical distinction between fluorescence and phosphorescence. Although it was recognised that phosphorescence was a relatively slow decay of luminescence, the distinction between fluorescence and phosphorescence simply on the basis of radiative decay rates was a gross oversimplification. Many organic fluorescent dyes do indeed have a lifetime between 1-10 ns,[46] and their phosphorescence lifetimes can be up to seconds, but there are numerous exceptions. Radiative decay longer than 10 ns is quenched by molecular oxygen and low energy emission has a higher decay rate due to the Englman-Jortner energy gap law.[47] In the case of delayed fluorescence, the fluorescence lifetime is similar to that of phosphorescence.[48] By the 1920s instrumentation existed for measuring nanosecond fluorescence lifetimes where previously only the measurement of millisecond phosphorescence lifetimes was possible with the first time-resolved spectrometer, the phosphoroscope by Becquerel.[3]

The quantum mechanical distinction between fluorescence and phosphorescence was gradually recognized by invoking a meta-stable intermediate state. This was postulated by Francis Perrin[49], but his model involved an intermediate state which always returned to the ground state via the singlet, essentially describing delayed fluorescence. The role

of spin multiplicity was introduced by Lewis and Kasha[30], which allowed for radiative decay directly from the intermediate state. The long lifetime was explained by the spin-forbidden change in going from triplet to singlet.

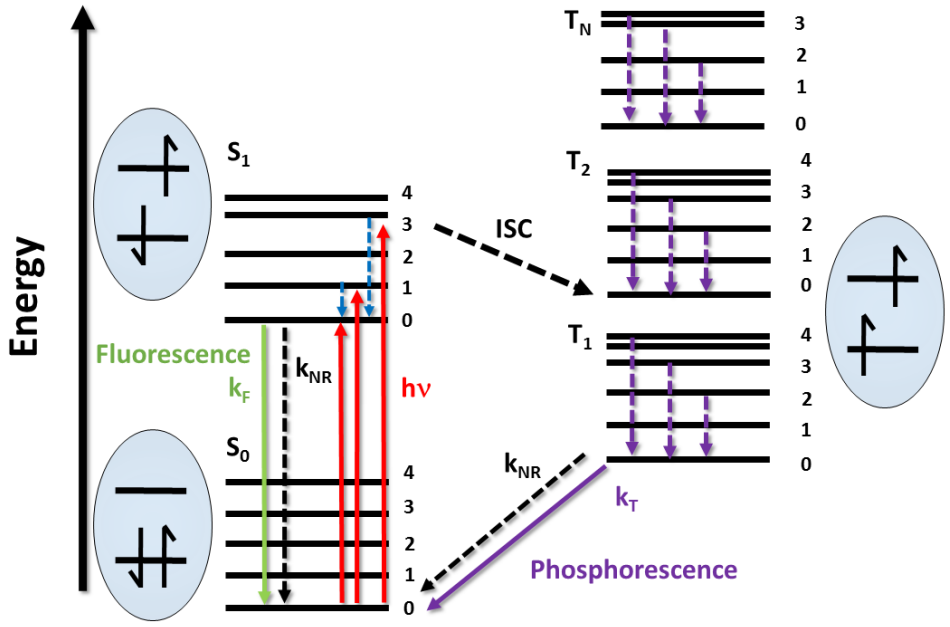

Figure 1.6. Schematic Jablonski diagram illustrating transitions to the triplet manifold with frontier molecular orbitals describing the spin multiplicity.

The quantum mechanical justification outlined by Lewis and Kasha underpins our current understanding of the triplet state. Not only is phosphorescence emission the result of radiative decay from a spin-forbidden transition to the triplet state, but there are multiple transitions in the triplet manifold resulting in a distinct absorption spectrum for the triplet. Knowing that there is a meta-stable excited state, it is possible to explain many organic photochemical reaction mechanisms such as hydrogen abstraction by aromatic ketones. Indeed, electron-transfer reactions take place when the triplet state is populated due to it being sufficiently long-lived to make bimolecular contact with reactants via diffusion under suitable conditions. Delayed fluorescence falls perfectly within the same model, the difference being that the rate of reverse intersystem crossing or triplet-triplet annihilation competes with radiative decay or vibrational relaxation of the triplet. With the aid of flash photolysis, it became possible to record triplet absorption spectra.

1.3 Quantitative Fluorescence Measurements

After early discoveries, it quickly became necessary to quantify the properties of fluorescence that were now becoming better understood. This manifested itself in commercial spectrophotometers for measuring UV-visible absorption and fluorescence. Flash photolysis instrumentation became commonplace once lasers were widely available. Developments in laser technology naturally led on to advances in photophysical experiments. Femtosecond lasers took flash photolysis from monitoring nanosecond processes to the femto- to picosecond domain for pump-probe experiments. Traditionally, fluorophores are studied for absorption and emission from 300 to 750 nm. Such a limitation on detection is mostly a technical one, detectors and optics in spectrophotometers are usually optimized for this wavelength range, which covers much of the visible spectrum with reasonable efficiency. Many commercial fluorimeters only detect fluorescence with a quantum efficiency above 10% from 300 to 600 nm. Such technical restrictions have left the far-red to near-IR region (750-1000 nm for the sake of argument) somewhat underexplored.

1.3.1 The Problem of Measuring Fluorescence in the Red Region

The importance of red-emitting organic fluorophores has increased recently due to interest in their use for biomedical and solar applications.[50,51] Particularly in the cases of fluorescence microscopy[52] and photodynamic therapy,[12] red emitting dyes are useful due to soft tissues and cells being less susceptible to damage and more permeable to light in that region (the so-called biological window).

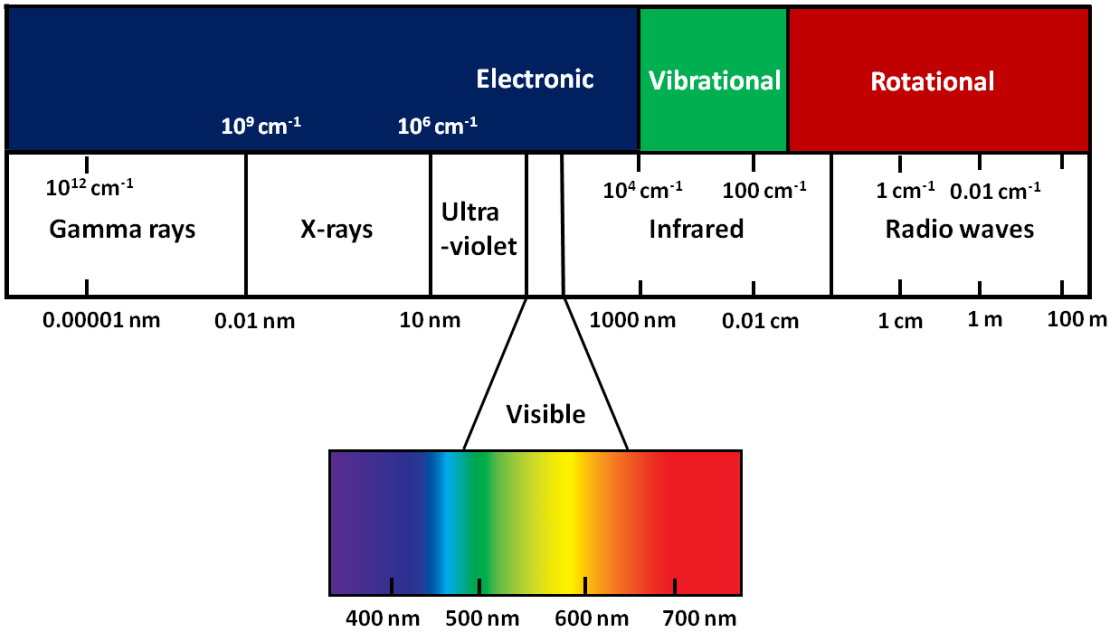

Figure 1.7. Schematic illustration of wavelength ranges across the electromagnetic spectrum and the type of transition associated with each portion of the spectrum (top).

One of the problems of red emission is in obtaining quantitative fluorescence measurements at wavelengths longer than 650 nm. There are few well established fluorescence quantum yield standards for use in this range. Coupled with detectors that are often inefficient in this region, the scope for error becomes large. These problems are compounded by a decline in fluorophore emission efficacy with decreasing energy gap between the ground and excited states. It is inevitable that one will need to contend with lower fluorescence quantum yields for emission past 650 nm, which in turn makes measuring the fluorescence more difficult.

These problems can be partially resolved by introducing new standard fluorophores for the 650-1000 nm region, although specialist detectors and expensive integrating spheres are required for the purpose of determining absolute fluorescence quantum yields. The problem of insensitive detectors has been somewhat alleviated by the replacement of photomultiplier tube detectors with charge-coupled devices (although these can be expensive). Alternative methods for quantitative fluorescence measurements exist, but are not commercialized. These include photoacoustic spectroscopy[53] and thermal lensing[54] (aka. thermal blooming) spectroscopy. The imperative to address the lack of fluorescence standards for the red region though has become more topical since red-emitting fluorophores are now commonplace in fluorescence microscopy.

1.3.2 Englman-Jortner Energy-Gap Law

The Englman-Jortner energy-gap law[47] is a fundamental design consideration for luminescent molecules. In a simple interpretation of the energy-gap law, the non-radiative rate constant k_{NR} will increase as the S_0 to S_1 energy gap, or gap to other electronic states, decreases. From the view of the UV-visible spectrum in Figure 1.7 one must remember that the nanometre wavelength scale commonly used to report absorption and fluorescence is non-linear. When energy is instead expressed in wavenumber, one is presented with a linear energy scale, and the energy gap becomes more obvious. Therefore, a Stokes' shift of 15 nm at the blue end of the spectrum corresponds to a far larger energy gap than a 15 nm shift from 750 nm. This leads to the general conclusion that fluorophores in the red region will tend to have lower quantum yields than those with absorption and emission at higher energy (although this is an oversimplification since there are many competing non-radiative processes). Awareness of this trend allows manipulation of non-radiative decay.

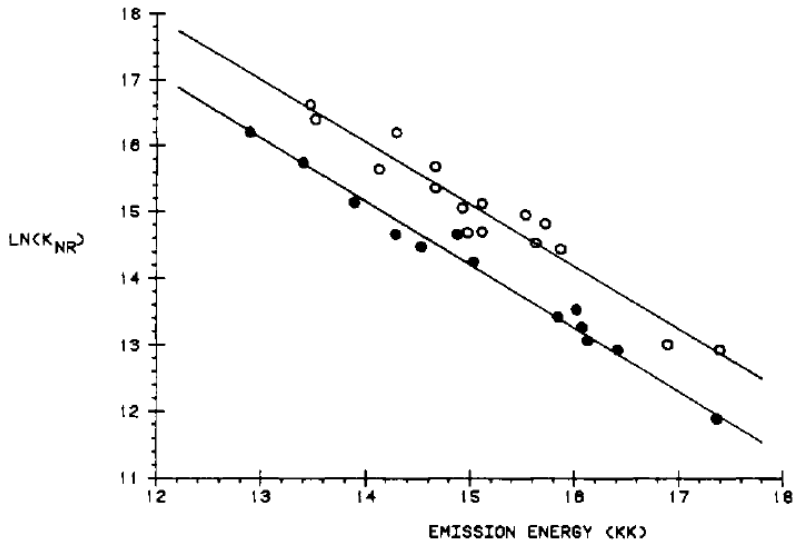

Figure 1.8. Typical example of a series of analogous compounds showing an increase in nonradiative decay rate with decreasing emission energy (in wavenumber). This trend is exactly as predicted by the engery gap law. Figure adapted from ref. 55.

More formally, a simplified expression the energy-gap law is shown in Equation 1.6.1. Here ΔE is the energy gap of the transitions involved and ω_M the dominant vibrational frequency. The coefficient γ can be expressed in terms of equations 1.6.2 and 1.6.3, which result from observables in spectroscopic measurements. The term S refers to the Huang-Rhys factor (aka. S-factor). It describes the nuclear displacement when going from the ground to the excited state. In Equation 1.6.3, λ refers to the extent of nuclear distortion.

$$k_{NR} \propto \exp\left(-\frac{\gamma \Delta E}{\hbar \omega_M}\right) \qquad (1.6.1)$$

$$\gamma = \ln\left(-\frac{|\Delta E|}{Sh\omega}\right) - 1 \quad (1.6.2)$$

$$S = \frac{\lambda}{h\omega} \qquad (1.6.3)$$

The energy-gap law works with a two-state model and without anharmonicities in the potential energy surface, but it has proven very successful in predicting trends in nonradiative rates for many excited state transitions, including charge transfer[56] and triplet states.[57]

An analysis of the energy-gap law also extends to the radiative rate constant, k_{RAD}. Some investigators had shown that in certain donor-acceptor systems the radiative decay rates from charge-separated states (i.e., charge-transfer fluorescence) depends on solvent polarity, showing a greater k_{RAD} in less polar solvent.[58] Jortner *et al*. later demonstrated that in such donor-acceptor systems intensity can be "borrowed" from a locally excited state which comes about from efficient mixing of the states due to stabilization of an exciplex.[59] In a less polar environment, D^+A^- is not stabilized, leading to a decrease in k_{RAD}. This finding accounts for the intense charge-transfer absorption bands found in some donor-acceptor systems (i.e. high oscillator strength) and adds yet another level of control to the photophysics of such systems. If one can understand the coupling between the locally excited and charge separated states, it becomes possible to engineer the radiative rate constant.

1.3.3 Barrier Crossing Dynamics

The photophysical processes discussed above are usually subjected to some level of activation energy. Nonradiative decay can be both activated and activationless, but vibrational relaxation is fundamentally activationless. Other activated processes, such as isomerization and electron transfer, can be introduced, these being sensitive to the environment. In the case of isomerization, the magnitude of the activation energy will depend on solvent viscosity, which is related to the temperature. Electron transfer will be sensitive to solvent polarity as charged species will be stabilized in polar environments, changing the energy of charge-separated state and thus also the activation barrier. Of course, one of the disadvantages from the perspective of molecular photophysics is that one operates from the excited state. Therefore, any activated process will be in competition with radiative decay.

Activated barrier crossing in liquids has, of course, been modelled, most famously by Kramers[60] which allows for a better understanding of how one gets to a transition state and justifies the activation energy obtained from the Arrhenius equation. If one were to go further and manipulate the energies of the HOMO and LUMO in a chromophore, the activation barrier to such processes might be engineered further. Therefore, when introducing an activated photochemical process, it is important to consider whether the process is viable in the selected environment. A classic example illustrating this model is the isomerization of cis-stilbene.[61] Considering the same for electron transfer, the activation barrier is obviously of vital importance in order to assess whether the process is viable at all. This highlights the importance of characterizing the potential energy landscape of a chromophore.

1.4 Rational Design of Fluorescence Properties

For much of the twentieth century, chemists studied the photophysical properties of relatively simple organic dyes. Once an understanding of the underlying photophysical properties had been obtained, a wave of increasingly complex chromophoric systems emerged. Here, two popular families of fluorescent dye are described as case studies to better illustrate how various photophysical parameters are understood and how structural modification with rational design can bring about the desired optical properties.

1.4.1 Case Study 1: Cyanine Dyes

Cyanine dyes have a long history, first emerging as sensitizers for silver halide photographic plates in the late nineteenth century. Indeed, the early development of these dyes is closely related to photography.[62,63] Cyanine dyes constitute a very diverse class of compounds due to relatively simple synthesis and broad scope for modification of their core structure.[64] They remain widely used in industry today and have seen somewhat of a renaissance in research for use as a fluorescent probes in biology[65] due to high molar absorption coefficients and fluorescence quantum efficiencies . Industrial applications for cyanine dyes range from coatings in optical storage media, laser dyes, pigments for photocopying and light-harvesting materials.

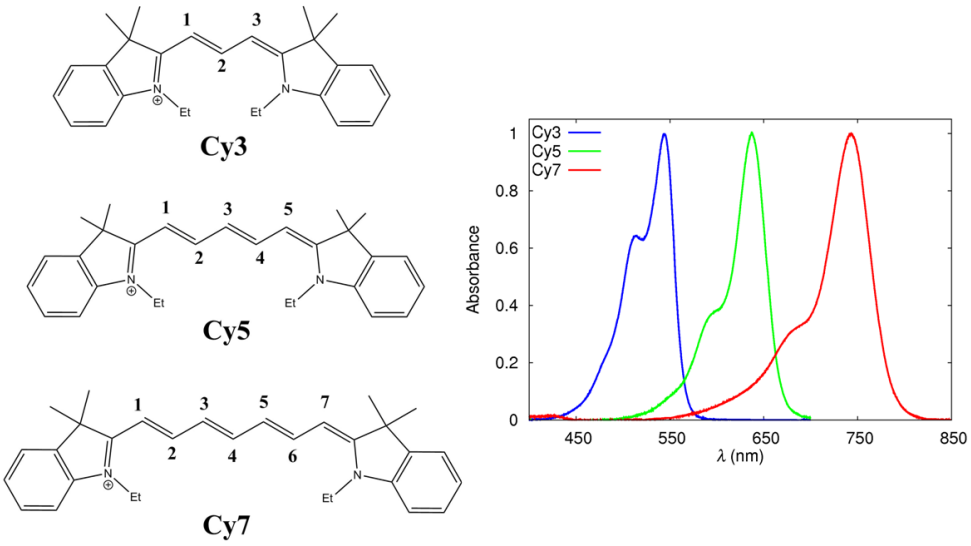

Figure 1.9. Example of three common indocarbocyanine dye derivatives and their absorption spectra.

Changing the length of the polymethine backbone of the cyanine dye (Figure 1.9) is a prime example of how increasing the amount of π-conjugation causes a red-shift (bathochromic shift) for the absorption maximum. This shift in absorption maximum forms the basis of Kuhn's well-know "particle in a box" model[66], which qualitatively predicts the absorption maximum of highly conjugated organic chromophores. The general trend of fluorescence quantum yield across the series falls from 0.5 (for Cy3) to 0.1 (Cy7) for similar cyanine dyes in this range, again in line with the energy-gap law.[67]

A number of fundamental photophysical properties discovered in cyanine dyes are pertinent to other systems. At an early stage, it was observed that cyanines would undergo aggregation in solution, again relating back to their use in colour photography.[68] Aggregation in organic chromophores can lead to drastic alteration in the photophysical properties, depending on the orientation of the interacting chromophores. There are two types of aggregates: J-aggregates (named after E. E. Jelly, the researcher responsible for their discovery) and H-aggregates.[69] The J-type aggregates associate in a tail-to-tail orientation, leading to extension of the conjugated system and a lowering of the total energy. This can be seen as an emergence of a in a red-shifted peak in the absorption spectrum. H-aggregates stack parallel to each other, resulting in a blue-shifted absorption spectrum. Further, the monomers may associate at a slip-stacked angle, where the resulting spectrum would be a combination of two peaks. These models work equally for dimers.

Michael Kasha provided an elegant semi-classical description of these spectroscopic changes with the introduction of the exciton splitting model.[70] Often, dimerization or aggregation can be controlled by altering the solvent. Organic dyes in polar solvents remain monomeric over concentration ranges spanning orders of magnitude, but aggregation is common in aqueous solution due to hydrophobic interactions. Water with its relatively high dielectric constant overcomes the coulombic repulsion of cationic and anionic dyes.[71] Dimerization and aggregation are crucial to supramolecular photochemistry due to the way in which absorption and fluorescence properties can be engineered by changing the surrounding environment.

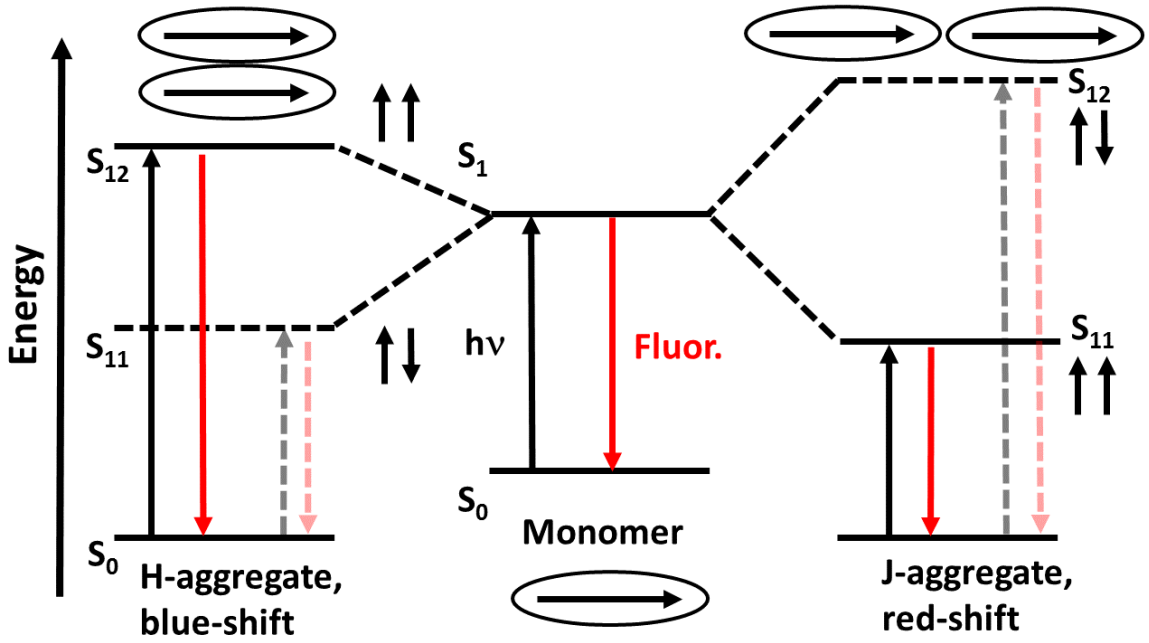

Figure 1.10. Schematic energy level description of aggregation. Within the semi-classical description of Kasha's exciton model, the description works for dimers and aggregates. Forbidden transitions correspond to faded lines

A second fundamental process which many cyanine dyes undergo is cis-trans isomerization.[72-74] Cis-trans isomerization, a fundamental process in biology related to the chemical origin of animal vision with retinal,[75] occurs readily in cyanine dyes upon exposure to light. Rotation adjacent to double bonds on the polymethine backbone results in distorted stereoisomers, which rapidly undergo equilibrium back to the all-trans ground state by thermal equilibriation or photo-induced back isomerization. Although the isomers are rarely isolated, they have been detected by flash photolysis[76] and fluorescence correlation spectroscopy.[77] This isomerization can be seen as fluctuations in fluorescence intensity and there has been some interest in studying this phenomenon further as a means of on/off fluorescence modulation, although many attribute the dark state to subsequent transitions into the triplet manifold.[78] Furthermore, isomerization is an important deactivation pathway of the singlet-excited state, often occurring in high yield and is an important consideration for similar systems. Isomerization also has implications for the photostability of chromophores.

Overall, cyanine dyes have served as a rich basis for studying fundamental photophysical phenomena, which has been closely related to their widespread use in industry. There is no sign that their use will diminish in the future.

1.4.2 Case Study 2: BODIPY Dyes

BODIPY (*4,4-difluoro-4-bora-3a,4a-diaza-s-indacene)* dyes represent a new wave of versatile, highly fluorescent, highly tuneable dyes.[79,80] Over the past 15 years research into these compoiunds has seen an explosion of new derivatives with photophyical properties to suit most imaginable applications. Characteristic of BODIPY are high fluorescence quantum yields, low Stokes' Shifts, minimal intersystem crossing yields, and good solubility in a large range of solvents with limited solvatochromism. Substitution of the core BODIPY structure (Figure 1.11) leads to virtually limitless possibilities and applications as functional derivatives.

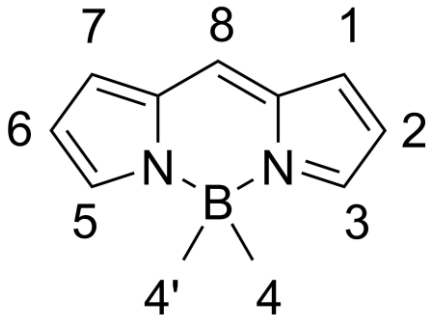

Figure 1.11. Core BODIPY structure.

The BODIPY family has found applications as environmental probes[81], biolabels[82], photodynamic therapy[83] and laser dyes[84]. Perhaps one of the more simple 4,4-difluoro BODIPY derivatives, where methyl groups are substituted at 1,3,5,7 positions, has an absorption maximum at ca. 490 nm and a fluorescence yield of unity.[84] Substituting the methyl groups for aryl rings predictably results in absorption and emission into the near-IR region, but with lower fluorescence yields.[85] Aza-BODPY dyes afford an approx. 100 nm red-shift in absorption and emission with less of a penalty in fluorescence yield. The details of this are discussed in Chapter 3.

Other BODIPY derivatives display functionality demonstrating important photophysical mechanisms such as photo-induced electron transfer, charge transfer and resonance energy transfer.[81] More recently, studies into the molecular rotor effect for substituents at the *meso*-position (position 8) has led to new fluorescent viscosity probes.[86]

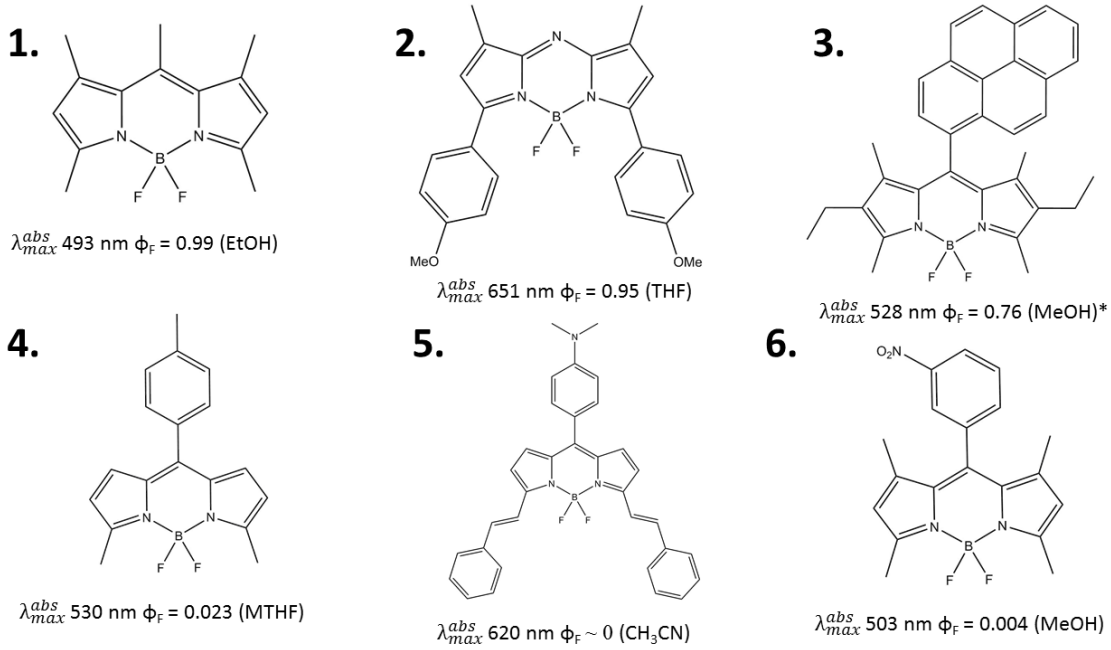

*Figure 1.12. A small selection of BODIPY derivatives from the scientific literature (*when excited into the pyrene).*[80,82,87,88,89]

Designing an effective molecular indicator for sensing analytes in real time or for fluorescence imaging *in vivo* requires careful consideration of all the photophysical phenomena mentioned previously. Figure 1.12 illustrates the relative ease with which BODIPY can be altered to suit the purpose. Dye 1 represents one of the simplest stable BODIPY dyes and has a near quantitative fluorescence yield at around 500 nm.[81] Addition of the aza-nitrogen and aryl functionality results in the far-red emitting derivative of dye 2.[88]

Dye 3 is an ideal illustration of efficient energy transfer from pyrene to BODIPY via Förster resonance energy transfer.[88] Here, one can still irradiate into the BODIPY chromophore with a high fluorescence yield, but excitation into the pyrene (which remains spectroscopically distinct) results in 100% of the excitation energy being transferred to BODIPY. This type of system is ideal when one needs to effectively separate the excitation from emission (by a large virtual Stokes' Shift).

A molecular rotor effect is observed in dye 4. Now the fluorescence yield is nearly zero in a solvent of low viscosity, with the main non-radiative pathway being rotation of the *meso* aryl group.[89] There are many subtleties affecting the rotation of the *meso*-substituent though, stemming from steric hindrance from other substituents and

structural distortion of the BODIPY core structure. Dyes 5 and 6 show examples of intramolecular charge transfer and photo-induced electron transfer (PET), respectively.[81] Charge transfer occurs due to the presence of an amine. Instead of emitting a photon from the S_1 state, there is competition from transitions to charge-transfer states, which often have a strong absorption in the visible spectrum in the case of metal complexes. The energy of the CT state will be sensitive to the polarity of the solvent so that in a non-polar environment the energy of the CT state may rise to such an extent that fluorescence once again becomes the dominant deactivation pathway. Alternatively, protonation of the amine in dye 5 will eliminate charge transfer, providing the makings of an environmental probe. Formation of charge-separated states in such donor-acceptor systems has found use in dye sensitized solar cells where the flow of current relies in effectively separating the positive and negative charges.

Photo-induced electron transfer may take place where there is a suitable thermodynamic driving force between the donor and acceptor. Where PET is possible, fluorescence is quenched. This is because at the excited state level an electron is either efficiently transferred to an electron withdrawing moiety (oxidative PET) or the excited fluorophore is reduced by electron transfer from a suitable donor (reductive PET). PET may occur by bimolecular contact or as an intramolecular process as per dye 6. In the intramolecular case, systems often have a bridge between donor and acceptor to electronically decouple the two. In the case of BODIPY dye 6, substitution at the *meso*-position achieves the same effect due to the orthogonal geometry between core and substituent. Marcus theory famously is able to predict the rate constant for PET in such systems.[90] The thermodynamic driving force for outer-sphere PET (no chemical bonds broken) can be determined from electrochemical measurements of the donor and acceptor using Equation 1.7. The electron transfer efficiency increases with increasing ergonicity only up to a point due to the increase in activation energy. This leads to the bell-shaped graph showing the Marcus inverted region for electron-transfer rates.

$$\Delta G_{PET} = E_{\frac{1}{2}}(D^+/D) - E_{\frac{1}{2}}(A^-/A) - \Delta E_{00} - C \qquad (1.7)$$

Here, $E_{1/2}$ refers to the electrochemical half-wave potentials for the donor and acceptor, ΔE_{00} is the excitation energy and C describes a term for the electrostatic

stabilization of the charge-separated state. PET becomes very useful in indicator probes because a change in environment can block the PET pathway by co-ordinating to donor or acceptor.

It is reasonable to propose that, based on the sheer diversity of applications and accessible photophysical properties, BODIPY dyes are among the most versatile fluorophores available. This is unlikely to change in the near future as yet more applications are proposed. The examples shown here are relatively simple systems. Elaborate supramolecular systems have also emerged based on BODIPY, including complex light harvesting arrays.[91] For researchers, this has resulted in a rich tapestry of mechanistic understanding to build on. The next step is now starting to emerge in the form of BOPHY dyes, an analogue on the BODIPY core (where two dipyrromethene units are merged).[92]

1.5 Taking Advantage of Molecular Photophysics in New Technologies

The applications for fluorescent dyes are numerous, as has been stressed earlier. To illustrate where the field is heading, we now explore the photophysical rational for two cutting edge techniques studied later in this thesis. Singlet-exciton fission is pertinent to understanding triplet state dynamics. Super-resolution fluorescence microscopy requires a thorough understanding of how fluorescence can be reversibly switched on and off. Interest in both topics has expanded markedly over the past decade and both are linked by emission in the red region, which itself presents challenges for photophysical measurements.

1.5.1 Singlet-Exciton Fission

Singlet-exciton fission (SEF)[93,94] is a form of exciton multiplication sometimes seen in organic chromophores whereby the singlet excited state can split into a pair of triplets possessing less than half the energy of the original singlet excited state. One fundamental condition for this process to occur is that two interacting chromophores have a singlet-excited state, S_1, energy at least twice that of the lowest-energy triplet T_1. Singlet fission competes efficiently with radiative decay in cases where the environment is favourable and neighbouring chromophores can interact. SEF was first observed in crystals of acenes (anthracene, tetracene, pentacene) in the 1960s[95,96] and 1970s, but

there was little interest in exploiting the phenomenon. Singlet fission is now associated with enhanced intersystem crossing and triplet yields up to 200%.

It is generally suggested that SEF is spin allowed under the scheme shown in Figure 1.13. One mechanism is based on the formation of a spin-correlated triplet pair, that dissociates into two equivalent triplet species.[97] Since the energy gap between the S_1 and T_1 states is so large in this case, it is logical to invoke rapid internal conversion to an intermediate energy state to account for the enhanced intersystem crossing. It has long been thought that charge-transfer states might play an important role in SEF. Indeed, more recently this has been established in some systems.[98] For pentacene though, it is apparent that charge-transfer states lie well above the singlet and triplet excited states. This may not be the case in other systems.

An alternative mechanism rationalizing efficient singlet fission in pentacene invokes super-exchange interactions, a form of indirect coupling which populates the triplet via virtual intermediate states (i.e., the high-energy charge-transfer states) with a single rate constant.[99] Excimer formation has likewise been suggested as a very short-lived intermediate.[100] In general for other SEF system, it appears these processes can be in competition. SEF does not happen in all systems where the energetic requirement is satisfied. The pigment indigo, perhaps the oldest known dyestuff, has been shown to satisfy the energetic demands for SEF, but other non-radiative processes, such as rapid internal conversion, appear to outcompete singlet fission in solution.[101]

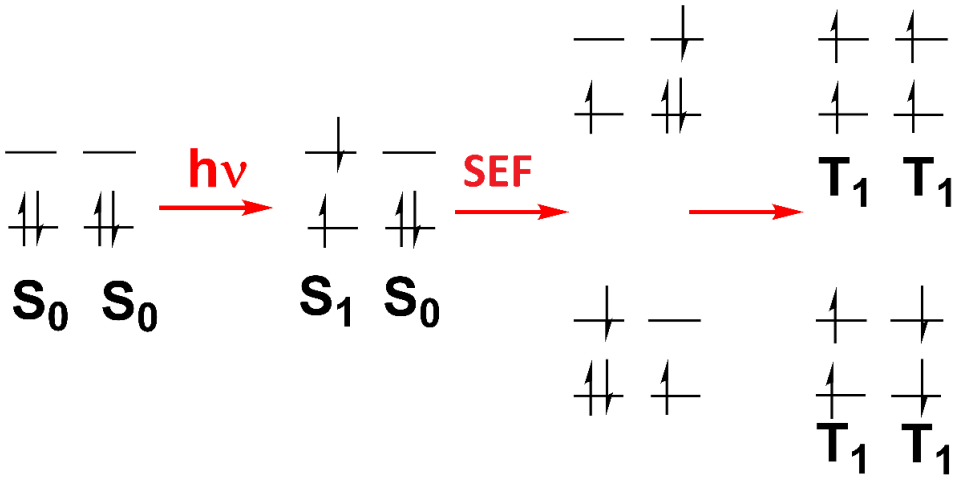

Figure 1.13. Scheme illustrating the formation of correlated triplet pairs by the process of singlet exciton fission.

During the past decade, interest in singlet fission has surged because effective harvesting of twice the number of triplets per photon increasing is envisaged as a means of increasing the number of charge carriers in organic solar cells or sensitizing a silicon solar cell.[102] This would rely on effective separation of the triplet pair so as to achieve efficient charge separation in an organic solar cell. Alternatively, it has been envisaged that singlet fission compounds (which do not phosphoresce) could transfer excitons to emissive nanoparticles in an additional layer within a silicon solar cell, thus making better use of the solar spectrum. The exciton multiplication strategy is a means of overcoming the Shockley–Queisser limit of 33% solar cell power conversion efficiency of a single junction solar cell.[103]

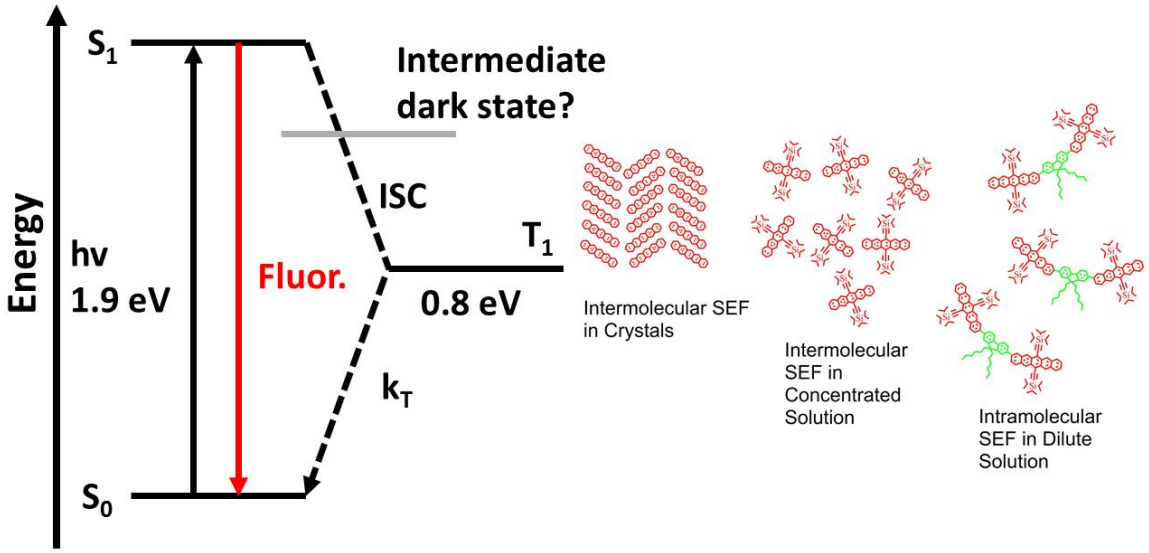

Figure 1.14. Scheme illustrating the energetic requirements for singlet fission in TIPS-pentacene (left panel). The various systems in which SEF has been reported for pentacene and its derivatives is shown on the right.

Current research into SEF revolves particularly around pentacene (where the process can occur spontaneously). Notable progress in exploiting SEF came when this process was observed in concentrated solutions of TIPS-pentcene.[104] Further stimulus was provided by the observation of SEF when pentacene moieties were linked in bichormophores,[105,106] resulting in intramolecular SEF (iSEF). In the latter case, the effect is no longer dependent on local order. Some conjugated polymers have also shown promise as singlet fission systems.[107] Although pentacene is the best characterized singlet fission chromophore, its triplet energy has been difficult to identify with high accuracy. Older literature has however established the triplet energy at approx. 0.9 eV

by indirect comparison with other compounds.[108] Addition of tri-isopropyl groups to pentacene is important in enhancing the stability of the compound and improving solubility, hence it is the most commonly used derivative.

SEF in covalently-linked pentacene-based bichromophores has enabled study of the intramolecular process in dilute solution. This makes investigating such systems with optical spectroscopy more straightforward. Having a spacer group between the two singlet fission chromophores allows also for fine tuning of the effect, changing the amount of through-bond communication between the SEF units by restricting the geometry. Due to the vast number of SEF bichromophores based on TIPS-pentacene in particular, there is a wealth of information upon which to base observations on the likely mechanism behind iSEF.

Although the mechanisms governing a dramatically enhanced rate of intersystem crossing have not yet fully been explained, a number of plausible justifications have been published for individual systems. Pentacene remains a popular basis for bichromophore SEF systems, but heterodimer systems have also been explored, as have other organic chromophores. This growth in the library of available singlet fission compounds will continue to contribute to the mechanistic understanding and no doubt see a push towards solar devices which exploit the effect, studies into which have been so far largely preliminary.[109,110]

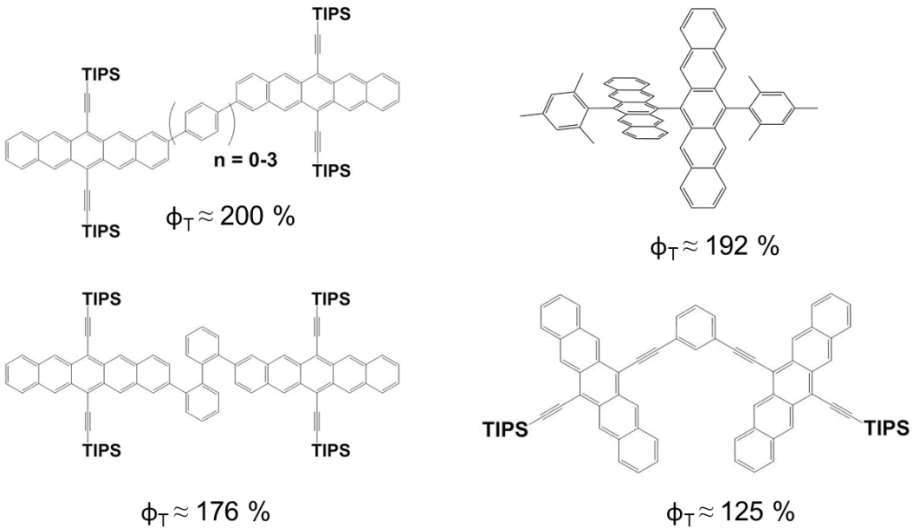

Figure 1.15. Examples of pentacene-based singlet fission compounds reported in the literature with corresponding triplet quantum yields.[105,106,111,112]. TIPS = tri-isopropylsilyl.

1.5.2 Super-Resolution Fluorescence Microscopy

Super-resolution imaging of biological samples using fluorescence microscopy has developed quite dramatically over the past twenty years or so to the point where the field is rather well established.[113-117] By definition, these techniques surpass the fundamental optical diffraction limit first described by Ernst Abbe in 1873.[118] Although super-resolution microscopy itself is a far broader field, and nanometre resolution has long been routine in the semiconductor industry for example with electron microscopy, biomedical imaging is largely limited to fluorescence microscopy which allows for a non-destructive, dynamic, imaging platform.

Nanometre-scale fluorescence microscopy has been propelled forward by technical innovation in the form of new instruments which work attempt to circumvent the ~200 nm lateral diffraction-limited resolution barrier. This has been accomplished in a variety of ways where a laser provides excitation of the fluorescent cell label. Confocal and two-photon excitation microscopes contributed moderate refinements to traditional far-field microscopy without addressing the fundamental optical limitation. Progress was nonetheless made by removing out-of-focus light and axial resolution in particular was improved by imaging above and below the sample.[119-122] Near-field microscopy affords a sizeable improvement in lateral resolution, down to tens of nanometres, by foregoing use of an objective. Instead, a pinhole detector on a sharp tip scans the surface of the sample. This is the case with SNOM/NSOM (scanning near-field optical microscopy).[123] Near-field techniques are, however, technically challenging to implement and limited to scanning surface features.

A different optical method, stimulated emission depletion microscopy STED[124], sharpens the point-spread function (the smallest spot a microscope can resolve) by stimulated emission of the fluorophore with a second high power excitation laser. Within the doughnut-shaped stimulated emission area most of the fluorophores are forced back to the ground state, leaving a very small spot of fluorescence at the focal point. With most of the fluorophores in the ground state, individual spots can be better localized without the problem of overlapping fluorophores blurring the image. Resolutions of tens of nanometres have been obtained with STED.[114]

More recently, the dominant strategy towards obtaining nanometre resolution has been to detect fluorescence from single fluorophores and reconstruct the image in a layered approach by stochastic activation of different subsets of fluorophores. Better-recognized single fluorophore detection techniques include photoactivated localization microscopy PALM, fluorescence photoactivation localization microscopy FPALM, and stochastic optical reconstruction microscopy STORM.[115,125,126] Broadly speaking these far-field methods work by forcing the vast majority of fluorescent labels in a cell back to the ground-state using a single excitation laser. By now the most advanced techniques have obtained a lateral resolution of around 20 nm while an additional benefit is the possibility of three-dimensional imaging in combination with confocal methods.[127,128] Multi-colour methods, which utilize more than one type of fluorophore, allows for greater selectivity and has contributed to better imaging.[114,117] This latter technique is limited by the availability of suitable fluorophores.

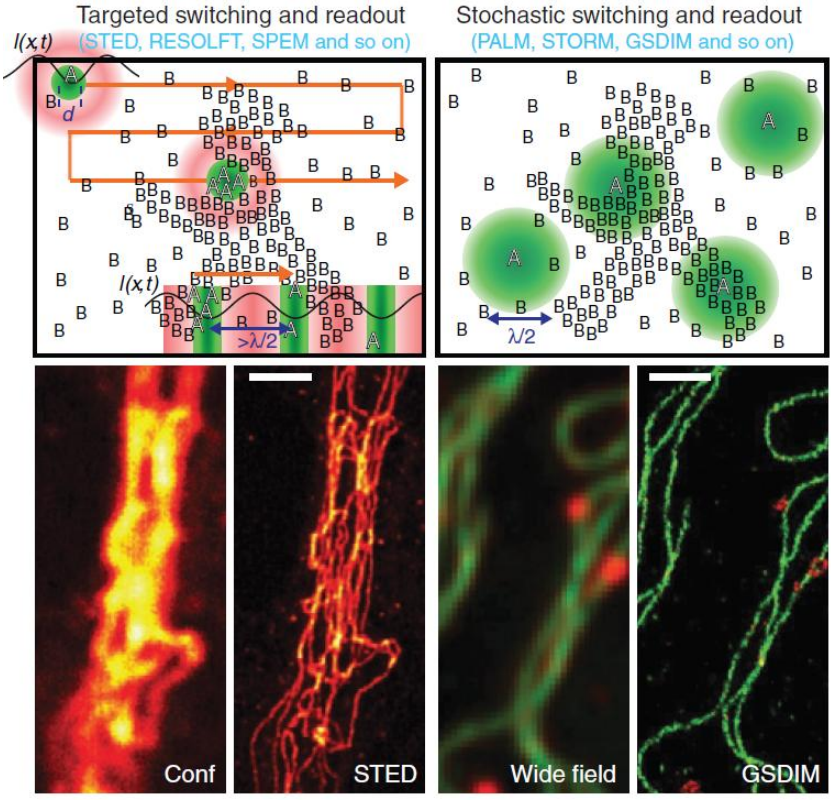

Figure 1.16. Illustration of the principle of super-resolution fluorescnece microscopy. Image adapted from reference 131.

Various derivative super-resolution techniques utilizing either near-field or far-field localization methods now exist. Most are covered extensively in various review articles.[116,129-132] To capture the smaller-cell structures in biological samples, one would ideally obtain as close to nanometre resolution images as possible. Single-fluorophore methods have shown promise in this regard. The diameter of the average organic fluorophores might be considered to be approximately 2 nm, which is perhaps the ultimate limit on image resolution.

So far, standard fluorescent dyes have mostly been used in super-resolution techniques. Stochastic techniques, including PALM and STORM, rely on on/off fluorescence "blinking" of the labelling fluorophores. These techniques seem to be dependent on the redox conditions imported by the accompanying buffer solutions which promote reversible fluorescence blinking. Commonly used small-molecule fluorophores include cyanine, rhodamine and ATTO dyes.[133-135] For example, Cy3, Cy5 and Cy7 dyes as well as Alexa Fluor cyanine probes are used for STORM and PALM as they are known to undergo "photoswitching". The STORM approach was originally implemented with two dyes (Cy3-Cy5) alternately excited so that Cy5 dyes are deactivated with a red laser-pulse and fluorescence is re-activated via resonance energy transfer by exciting Cy3 with a UV-pulse.[115] Note that dSTORM has a simpler arrangement, namely deactivating only a single dye and relying on spontaneous fluorescence recovery of sparse subsets of fluorophores.[136] In contrast, STED counts more on high fluorescence yields and resistance to permanent photobleaching under high energy excitation; ATTO dyes have therefore been singled out for this technique.[114,137] Fluorescent protein probes are also used, particularly for PALM.[125,128]

It is apparent that while fluorescence microscopy has developed rapidly, and some of the above techniques are certain to become mainstays in biomedical research with commercial setups now widely available, research into the fluorescent dyes has not received as much attention. In particular, the mechanism governing fluorescence blinking has not been rationalized fully. Cyanine dyes in the particular case of STORM imaging perform well in terms of fluorescence blinking and resistance to permanent photo-bleaching. Without a detailed understanding of how the use of a particular fluorescent dye leads to improved optical resolution, it is difficult to imagine how to

optimise systems with respect to photophysical properties. New dyes are being proposed as alternative fluorophores mainly on the basis of their absorption profile. This situation can only lead to confusion. Because the Newcastle Medical School has an advanced microscopy group, it seems logical to enquire whether we can improve the level of understanding about the role of the emissive dyes in one or more of these modern techniques. Assessing the above methods, STORM stands out as perhaps the most promising due to the rational control of emitters used to obtain a high-resolution image. For all single fluorophore localization methods, the resolution is limited by the number of photons detected per fluorescent spot. Since STORM is orientated towards the use of small organic fluorophores, more so than other techniques (PALM is associated more with fluorescent proteins and STED places high demands on stability against photobleaching), it seems reasonable to focus on developing an understanding of fluorescence blinking for this technique.

1.6 Future Trends

Organic dyes show great promise in opto-electronic applications. Organic light emitting diodes (OLED) in particular have become a successful technology, where small organic emitters and polymers form the basis of electroluminescent lights and displays.[138] Both fluorescent and phosphorescent materials have been used.[139] Recently, researchers have utilized delayed fluorescence in enhancing the efficiency of triplet emitters.[140] More exotic devices have emerged including organic semiconductor lasers.[141]

The drive towards employing organic compounds in electronic devices is driven by a number of factors revolving around manufacturing and efficiency. Precious rare-earth triplet emitting complexes (Ru, Ir, Pt) although effective emitters (up to 100% due to increased spin-orbit coupling in OLEDs) are too expensive for sustainable usage. Organic semiconductors are solution-processable and can be made in thin, flexible layers. Favourable photophysical properties can lead to high efficiency and the library of organic emitters is growing rapidly. There is certainly a trend towards all-organic semiconductor based light-emitting and photon-harvesting devices in industry and this has been reflected in the amount of fundamental research. However, organic dyes are

more susceptible to photo-fading, which requires a fundamental understanding of photobleaching mechanisms in order to produce suitable countermeasures.

The need for organic dyes absorbing and emitting in the red region is highlighted by the sections on fluorescence microscopy and singlet fission. For organic solar cells, generating excitons from photonic energy in the red is a strategy towards utilizing more of the solar spectrum.

Overall, there will be an ongoing need to rationally design chromophores for absorption and emission because the requirements set by new technologies are becoming ever-more specific. An observable trend has been the re-introduction of classic photophysical concepts such as delayed fluorescence and singlet fission to achieve these goals. Many new chromophores emit in the red region, where quantitative measurements of emission efficiency are hard to establish. This is considered to be a problem for devices such as OLEDs where knowledge of the overall light emitting efficiency is key to successful performance.

1.7 References

1. Krause, G.H.; Weis, E. *Annu. Rev. Plant Biol.* **1991**, 42, 313-349.

2. Andrews, D.L., 2014. *Molecular Photophysics and Spectroscopy*. Morgan & Claypool Publishers.

3. Valeur, B.; Berberan-Santos, M.N., 2012. *Molecular Fluorescence: Principles and Applications*. John Wiley & Sons.

4. Blankenship, R.E., 2013. *Molecular Mechanisms of Photosynthesis*. John Wiley & Sons.

5. Soffer, B.H.; McFarland, B.B. *Appl. Phys. Lett.* **1967**, 10, 266-267.

6. Duarte, F.J.; Kelley, P.; Hillman, L.W.; Liao, P.F., 1990. Dye Laser Principles: With Applications. Academic Press.

7. Lichtman, J.W.; Conchello, J.A. *Nat. Methods*, **2005**, 2, 910-919.

8. Huang, B.; Bates, M.; Zhuang, X., 2009. *Annu. Rev. Biochem*. **2009**, 78, 993-1016.

9. Hoppe, H.; Sariciftci, N.S. *J. Mater. Res*. **2004**, 19, 1924-1945.

10. Hagfeldt, A.; Boschloo, G.; Sun, L.; Kloo, L.; Pettersson, H. *Chem. Rev.* **2010**, 110, 6595-6663.

11. Dolmans, D.E.; Fukumura, D.; Jain, R.K., *Nat. Rev. Cancer*, **2003**, 3, 380-387.

12. Ochsner, M. *J. Photochem. Photobiol. B.* **1997**, 39, 1-18.

13. Ueno, T.; Nagano, T. *Nat. Methods*, **2011**, 8, 642-645.

14. Lim, M.H.; Lippard, S.J. *Acc. Chem. Res.* **2007**, 40, 41-51.

15. Baldo, M.A.; O'Brien, D.F.; You, Y.; Shoustikov, A. *Nature*, **1998**, *395*, 151-154.

16. Zhang, Q.; Li, B.; Huang, S.; Nomura, H.; Tanaka, H.; Adachi, C. *Nat. Photonics*, **2014**, 8, 326-332.

17. Gust, D.; Moore, T.A.; Moore, A.L. *Acc. Chem. Res.* **2009**, 42, 1890-1898.

18. Tachibana, Y.; Vayssieres, L.; Durrant, J.R. *Nat. Photonics*, **2012**, 6, 511-518.

19. Lewis, N.S.; Nocera, D.G., *Proc. Natl. Acad. Sci.* **2006**, 103, 15729-15735.

20. De Silva, A.P.; Gunaratne, H.N.; Gunnlaugsson, T.; Huxley, A.J.; McCoy, C.P.; Rademacher, J.T.; Rice, T.E. *Chem. Rev*. **1997**, 97, 1515-1566.

21. Allen, B.D.; Benniston, A.C.; Harriman, A.; Rostron, S.A.; Yu, C. *Phys. Chem. Chem. Phys.* **2005**, 7, 3035-3040.

22. Hasegawa, M.; Sugimura, T.; Suzaki, Y.; Shindo, Y.; Kitahara, A. *J. Phys. Chem.* **1994**, 98, 2120-2124.

23. Akemann, W.; Mutoh, H.; Perron, A.; Rossier, J.; Knöpfel, T. *Nat. Methods*, **2010**, *7*, 643-649.

24. Koev, S.T.; Dykstra, P.H.; Luo, X.; Rubloff, G.W.; Bentley, W.E.; Payne, G.F.; Ghodssi, R. *Lab Chip*, **2010**, 10, 3026-3042.

25. Burns, A.; Ow, H.; Wiesner, U. *Chem. Soc. Rev.* **2006**, 35, 1028-1042.

26. Ware, W.R. *J. Phys. Chem.* **1962**, 66, 455-458.

27. Boaz, H.; Rollefson, G.K. *J. Am. Chem. Soc.* **1950**, *72*, 3435-3443.

28. Vavilov, S.I.; Levishin, V.L. *Z. Phys.* **1923**, *16*, 136.

29. Thulstrup, E.W. and Michl, J., 1989. *Elementary Polarization Spectroscopy*. John Wiley & Sons.

30. Lewis, G.N.; Kasha, M. *J. Am. Chem. Soc.* **1944**, *66*, 2100-2116.

31. El-Sayed, M.A. *Acc. Chem. Res.* **1968**, *1*, 8-16.

32. Andrews, D.L. and Demidov, A.A., 1999. Resonance Energy Transfer (Vol. 2). New York: Wiley.

33. Förster, T. *Faraday Discuss.* **1959**, 27, 7-17.

34. Dexter, D.L. *J. Chem. Phys.* **1953**, 21, 836-850.

35. Faure, S.; Stern, C.; Guilard, R.; Harvey, P.D. *J. Am. Chem. Soc*. **2004**, 126, 1253-1261.

36. Porter, G. *Proc. Roy. Soc. A.* **1950**, 200, 284-300.

37. Porter, G.; Topp, M.R. *Proc. Roy. Soc. A.* **1970**, 315, 163-184.

38. Wasielewski, M.R. *Chem. Rev*. **1992**, 92, 435-461.

39. Emiliani, C.; Bé, A.W.H.; Ramsay, A.T.S *Nature*, **1980**, 286, 254-256.

40. Guldi, D.M. and Martin, N. eds., 2013. Fullerenes: From Synthesis to Optoelectronic Properties (Vol. 4). Springer Science & Business Media.

41. Gust, D.; Moore, T.A.; Moore, A.L. *Acc. Chem. Res.* **2001**, 34, 40-48.

42. Guldi, D.M. *Chem. Soc. Rev.* **2002**, 31, 22-36.

43. Kuciauskas, D.; Lin, S.; Seely, G.R.; Moore, A.L.; Moore, T.A.; Gust, D.; Drovetskaya, T.; Reed, C.A.; Boyd, P.D. *J. Phys. Chem. A*, **1996**, 100, 15926-15932.

44. Kodis, G.; Liddell, P.A.; De la Garza, L;, Clausen, P.C.; Lindsey, J.S.; Moore, A.L.; Moore, T.A.; Gust, D. *J. Phys. Chem. A,* **2002**, 106, 2036-2048.

45. Ziessel, R.; Ulrich, G.; Haefele, A.; Harriman, A. *J. Am. Chem. Soc.* **2013**, 135, 11330-11344.

46. Murov, S.L., Carmichael, I. and Hug, G.L., 1993. *Handbook of Photochemistry*. CRC Press.

47. Englman, R.; Jortner, J. *Mol. Phys.* **1970**, *18*, 145-164.

48. Kepler, R.G.; Caris, J.C.; Avakian, P.; Abramson, E. *Phys. Rev. Lett.* **1963**, 10, 400.

49. Perrin, F. *Ann. Phys*. **1929**, 10, 169-275.

50. Velusamy, M.; Justin Thomas, K.R.; Lin, J.T.; Hsu, Y.C.; Ho, K.C. *Org. Lett.* **2005**, *7*, 1899-1902.

51. Burke, A.; Schmidt-Mende, L.; Ito, S.; Grätzel, M. *Chem. Comm.* **2007**, 3, 234-236.

52. Kolmakov, K.; Belov, V.N.; Bierwagen, J.; Ringemann, C.; Müller, V.; Eggeling, C.; Hell, S.W. *Chem. Eur. J.* **2010**, *16*, 158-166.

53. Rockley, M.G.; Waugh, K.M. *Chem. Phys. Lett.* **1978**, 54, 597-599.

54. Brannon, J.H.; Magde, D. J. *Phys. Chem.* **1978**, 82, 705-709.

55. Caspar, J.V.; Meyer, T.J. *J. Phys. Chem.* **1983**, 87, 952-957.

56. Bixon, M.; Jortner, J.; Cortes, J.; Heitele, H.; Michel-Beyerle, M.E. *J. Phys. Chem.* **1994**, 98, 7289-7299.

57. Wilson, J.S.; Chawdhury, N.; Al-Mandhary, M.R.; Younus, M.; Khan, M.S.; Raithby, P.R.; Köhler, A.; Friend, R.H. *J. Am. Chem. Soc.* **2001**, 123, 9412-9417.

58. Oevering, H.; Paddon-Row, M.N.; Heppener, M.; Oliver, A.M.; Cotsaris, E.; Verhoeven, J.W.; Hush, N.S. *J. Am. Chem. Soc.* **1987**, 109, 3258-3269.

59. Bixon, M.; Jortner, J.; Verhoeven, J.W. *J. Am. Chem. Soc.* **1994**, 116, 7349-7355.

60. Kramers, H.A. *Physica* **1940**, 7, 284-304.

61. Fleming, G.R.; Courtney, S.H.; Balk, M.W. *J. Stat. Phys.* **1986**, 42, 83-104.

62. Williams, C.H.G. *Trans. Roy. Soc. Edinburgh*, **1856**, 21, 377.

63. Hamer, F.M. ed., 2009. The Chemistry of Heterocyclic Compounds: The Cyanine Dyes and Related Compounds (Vol. 18). John Wiley & Sons.

64. Mishra, A.; Behera, R.K.; Behera, P.K.; Mishra, B.K.; Behera, G.B. *Chem. Rev.* **1990**, 100, 1973-2012.

65. Mujumdar, R.B.; Ernst, L.A.; Mujumdar, S.R.; Lewis, C.J.; Waggoner, A.S. *Bioconjugate Chem.* **1993**, 4, 105-111.

66. Kuhn, H. 1949. *J. Chem. Phys.* **1949**, 17, 1198-1212.

67. Benson, R.C.; Kues, H.A. *J. Chem. Eng. Data*, **1977**, 22, 379-383.

68. James, T.H., The Theory of the Photographic Process, 1977. Research Laboratories Eastman Kodak Company, Rochester, pp.437-447.

69. Eisfeld, A.; Briggs, J.S. *Chem. Phys.* **2006**, 324, 376-384.

70. Kasha, M.; Rawls, H.R.; Ashraf El-Bayoumi, M. *Pure Appl. Chem.* **1965**, 11, 371-392.

71. West, W. and Pearce, S. *J. Phys. Chem.* **1965**, 69, 1894-1903.

72. Zechmeister, L.; Pinckard, J.H. *Cell. Mol. Life Sci.* **1953**, 9, 16-17.

73. Sundström, V.; Gillbro, T. *J. Phys. Chem.* **1982**, 86, 1788-1794.

74. Dietz, F.; Rentsch, S.K. *Chem. Phys.* **1985**, 96, 145-151.

75. Wang, Q.; Schoenlein, R.W.; Peteanu, L.A.; Mathies, R.A.; Shank, C.V. *Science*, **1994**, 266, 422-422.

76. Kuzmin, V.A.; Darmanyan, A.P. *Chem. Phys. Lett.* **1978**, 54, 159-163.

77. Widengren, J.; Schwille, P. *J. Phys. Chem. A.* **2000**, 104, 6416-6428.

78. Köhn, F.; Hofkens, J.; Gronheid, R.; Van der Auweraer, M.; De Schryver, F.C. *J. Phys. Chem. A.* **2002**, 106, 4808-4814.

79. Ulrich, G.; Ziessel, R.; Harriman, A. *Angew. Chem. Int. Ed.* **2008**, 47, 1184-1201.

80. Loudet, A.; Burgess, K. *Chem. Rev*. **2007**, 107, 4891-4932.

81. Boens, N.; Leen, V.; Dehaen, W. *Chem. Soc. Rev.* **2012**, *41*, 1130-1172.

82. Ni, Y.; Wu, *J. Org. Biomol. Chem.* **2014**, 12, 3774-3791.

83. Kamkaew, A.; Lim, S.H.; Lee, H.B.; Kiew, L.V.; Chung, L.Y.; Burgess, K. *Chem. Soc. Rev.*, **2013**, 42, 77-88.

84. Boyer, J.H.; Haag, A.M.; Sathyamoorthi, G.; Soong, M.L.; Thangaraj, K.; Pavlopoulos, T.G. *Heteroatom Chem.* **1993**, 4, 39-49.

85. Ni, Y.; Wu, J. *Org. Biomol. Chem*, **2014**, 12, 3774-3791.

86. Bahaidarah, E.; Harriman, A.; Stachelek, P.; Rihn, S.; Heyer, E.; Ziessel, R. *Photochem. Photobiol. Sci*. **2014**, 13, 1397-1401.

87. Karlsson, J.K.; Harriman, A. *J. Phys. Chem. A.* **2016**, 120, 2537-2546.

88. Ziessel, R.; Goze, C.; Ulrich, G.; Césario, M.; Retailleau, P.; Harriman, A.; Rostron, J.P. *Chem. Eur. J.* **2005**, 11, 7366-7378.

89. Bahaidarah, E.; Harriman, A.; Stachelek, P.; Rihn, S.; Heyer, E.; Ziessel, R. *Photochem. Photobiol Sci.* **2014**, 13, 1397-1401.

90. Marcus, R.A. *Annu. Rev. Phys. Chem.* **1964**, 15, 155-196.

91. Ziessel, R.; Ulrich, G.; Haefele, A.; Harriman, A. *J. Am. Chem. Soc.* **2013**, 135, 11330-11344.

92. Woodford, O.; Harriman, A.; McFarlane, W.; Wills, C. *ChemPhotoChem*, **2017**, 1, 317-325.

93. Smith, M.B.; Michl, J. *Chem. Rev.*, **2010**, 110, 6891-6936.

94. Smith, M.B.; Michl, J. *Annu. Rev. Phys. Chem*. **2013**, 64, 361-386.

95. Merrifield, R.E., Avakian, P.; Groff, R.P. *Chem. Phys. Lett.* **1969**, 3, 386-388.

96. Tomkiewicz, Y.; Groff, R.P.; Avakian, P. *J. Phys. Chem.* **1971**, 54, 4504-4507.

97. Chan, W.L.; Berkelbach, T.C.; Provorse, M.R.; Monahan, N.R.; Tritsch, J.R.; Hybertsen, M.S.; Reichman, D.R.; Gao, J.; Zhu, X.Y. *Acc. Chem. Res*. **2013**, 46, 1321-1329.

98. Margulies, E.A.; Miller, C.E.; Wu, Y.; Ma, L.; Schatz, G.C.; Young, R.M.; Wasielewski, M.R. *Nat. Chem.* **2016**, 8, 1120-1125.

99. Berkelbach, T.C.; Hybertsen, M.S.; Reichman, D.R. *J. Chem. Phys.* **2013**, 138, 114103.

100. Zimmerman, P.M.; Zhang, Z.; Musgrave, C.B. *Nat. Chem.* **2010**, 2, 648-652.

101. Seixas de Melo, J.S.; Burrows, H.D.; Serpa, C.; Arnaut, L.G. *Angew. Chem., Int. Ed.*, **2007**, 46, 2094-2096.

102. Xia, J.; Sanders, S.N.; Cheng, W.; Low, J.Z.; Liu, J.; Campos, L.M.; Sun, T. *Adv. Mater.* **2017**, 29, 1-11.

103. Shockley, W.; Queisser, H.J *J. Appl. Phys.* **1961**, 32, 510-519.

104. Walker, B.J.; Musser, A.J.; Beljonne, D.; Friend, R.H. *Nat. Chem.* **2013**, 5, 1019-1024.

105. Sanders, S.N.; Kumarasamy, E.; Pun, A.B.; Trinh, M.T.; Choi, B.; Xia, J.; Taffet, E.J.; Low, J.Z.; Miller, J.R.; Roy, X.; Zhu, X.Y. *J. Am. Chem. Soc.* **2015**, 137, 8965-8972.

106. Zirzlmeier, J.; Lehnherr, D.; Coto, P.B.; Chernick, E.T.; Casillas, R.; Basel, B.S.; Thoss, M.; Tykwinski, R.R.; Guldi, D.M. *Proc. Natl. Acad. Sci.* **2015**, 112, 5325-5330.

107. Musser, A.J.; Al-Hashimi, M.; Maiuri, M.; Brida, D.; Heeney, M.; Cerullo, G.; Friend, R.H.; Clark, J. *J. Am. Chem. Soc.* **2013**, 135, 12747-12754.

108. Gijzeman, O.L.J.; Kaufman, F.; Porter, G. *J. Chem. Soc. Faraday Trans. II*, **1973**, 69, 708-720.

109. Congreve, D.N.; Lee, J.; Thompson, N.J.; Hontz, E.; Yost, S.R.; Reusswig, P.D.; Bahlke, M.E.; Reineke, S.; Van Voorhis; T.; Baldo, M.A. *Science* **2013**, 340, 334-337.

110. Ehrler, B.; Walker, B.J.; Böhm, M.L.; Wilson, M.W.; Vaynzof, Y.; Friend, R.H.; Greenham, N.C. *Nat. Commun.* **2012**, 3, 1019.

111. Lukman, S.; Musser, A.J.; Chen, K.; Athanasopoulos, S.; Yong, C.K.; Zeng, Z.; Ye, Q.; Chi, C.; Hodgkiss, J.M.; Wu, J.; Friend, R.H. *Adv. Funct. Mater.* **2015**, 25, 5452-5461.

112. Sakuma, T.; Sakai, H.; Araki, Y.; Mori, T.; Wada, T.; Tkachenko, N.V.; Hasobe, T. *J. Phys. Chem. A.* **2016**, 120, 1867-1875.

113. Hell, S.W. *Nat. Biotechnol.* **2003**, 21, 1347-1355.

114. Huang, B.; Bates, M.; Zhuang, X. *Ann. Rev. Biochem.* **2009**, 78, 993-1016.

115. Rust, M. J.; Bates, M.; Zhuang, X. *Nat. Methods.* **2006**, 3, 793-796.

116. Schermelleh, L.; Heintzmann, R.; Leonhardt, H. *J. Cell Biol*. **2010**, 190, 165-175.

117. Bates, M.; Huang, B.; Dempsey, G. T.; Zhuang, X. *Science*, **2007**, 317, 1749-1753.

118. Abbe, E. *Arch. Mikroskop. Anat.* **1873**, 9, 413-418.

119. Webb, R. H. *Rep. Prog. Phys.* **1996**, 59, 427-471.

120. Denk, W.; Strickler, J. H.; Webb, W. W. *Science,* **1990**, 248, 73-76.

121. Hell, S.; Stelzer, E. H. *Opt. Commun.* **1992**, 93, 277-282.

122. Gustafsson, M. G. L.; Agard, D. A.; Sedat, J. W. *J. Microsc*. **1999**, 195, 10-16.

123. Heinzelmann, H.; Pohl, D. W. *Appl. Phys. A.* **1994**, 59, 89-101.

124. Hell, S. W.; Wichmann, J. *Opt. Lett.* **1994**, 19, 780-782.

125. Betzig E.; Patterson G. H.; Sougrat R.; Lindwasser O. W.; Olenych S.; Bonifacino J. S.; Davidson M. W.; Lippincott-Schwartz J.; Hess H. F. *Science* **2006**, 313, 1642-1645.

126. Hess, S. T.; Girirajan, T. P.; Mason, M. D. *Biophys J.* **2006**, 91, 4258-4272.

127. Huang, B.; Wang, W.; Bates, M.; Zhuang, X. *Science*, **2008**, 319, 810-813.

128. Owen, D. M.; Rentero, C.; Rossy, J.; Magenau, A.; Williamson, D.; Rodriguez, M.; Gaus, K. *J. Biophotonics* **2010**, 3, 446-454.

129. Leung, B. O.; Chou, K. C. *Appl. Spectrosc.* **2011**, 65, 967-980.

130. Hell, S. W. *Science*, **2007**, 316, 1153-1158.

131. Hell, S. W. *Nat. Methods*, **2009**, 6, 24-32.

132. Huang, B. *Curr. Opin. Chem. Biol.* **2010**, 14, 10-14.

133. Fernández-Suárez, M.; Ting, A. Y. *Nat. Rev. Mol. Cell Biol.* **2008**, 9, 929-943.

135. Heilemann, M.; Van De Linde, S.; Schüttpelz, M.; Kasper, R.; Seefeldt, B.; Mukherjee, A.; Tinnefeld, P.; Sauer, M. *Angew. Chem., Int. Ed.* **2008**, 47, 6172-6167.

135. Vogelsang, J.; Steinhauer, C.; Forthmann, C.; Stein, I. H.; Person-Skegro, B.; Cordes, T.; Tinnefeld, P. *ChemPhysChem,* **2010**, 11, 2475-2490.

136. van de Linde, S.; Löschberger, A.; Klein, T.; Heidbreder, M.; Wolter, S.; Heilemann, M.; Sauer, M. *Nat. Protocol* **2011**, 6, 991-1009.

137. Meyer, L.; Wildanger, D.; Medda, R.; Punge, A.; Rizzoli, S. O.; Donnert, G.; Hell, S. W. *Small* **2008**, 4, 1095-1100.

138. Müllen, K. and Scherf, U. eds., 2006. Organic Light Emitting Devices: Synthesis, Properties and Applications. John Wiley & Sons.

139. Chou, P.T.; Chi, Y. *Chem. Eur. J.*, **2007**, 13, 380-395.

140. Dias, F.B.; Penfold, T.J.; Monkman, A.P. *Methods Appl. Fluoresc.* **2017**, 5, 012001.

141. Samuel, I.D.W.; Turnbull, G.A. *Chem. Rev.* **2007**, 107, 1272-1295.

Chapter 2: Experimental Methods

2.1 Materials

Dye samples were obtained from various collaborators and were used as received after characterization and extensive checks for impurities. Many samples were analyzed with 700 MHz ^{1}H NMR as an additional check for purity. We thank Dr. Corinne Wills and Prof. William McFarlane for conducting these NMR experiments. Dr. Michael Hall (Newcastle University, School of Chemistry) is gratefully acknowledged for donating samples of aza-BODIPY dyes. The equivalent BODIPY dye lacking the aza-nitrogen was donated by Dr. Raymond Ziessel (Universitè Louis Pasteur de Strasbourg). The bridged bis-pentacene compound (BBP) and TIPS-pentacene were synthesized by Dr. Alparslan Atahan (Department of Polymer Engineering, Duzce University, Turkey). The series of cyanine dyes proposed as fluorescence quantum yield standards were donated by Dr. Heinz Mustroph (Few Chemicals GmbH, Germany). Aluminium phthalocyanine tetrasulfonate was donated by Dr. F. Hardy of The Procter & Gamble Co. Alexa Fluor 647 NHS ester was donated by Dr. Alex Laude (Newcastle University Medical School Bio-Imaging Unit) and originally purchased from Thermo Fisher Scientific. Brilliant Green was purchased from Acros Organics.

Additional commercially available dyes were used for the purpose of fluorescent standards either for determining the fluorescence quantum yield or as a reference for frequency-domain fluorescence lifetime measurements. Such dyes include *meso*-tetraphenyl porphyrin, cresyl violet, and Nile Blue. These dyes are well-characterized in the literature. Reference to critical photophysical values is made in the relevant chapters.

All solvents used for spectroscopic studies were of spectroscopic grade and were checked for fluorescent impurities prior to use. Solvents were obtained either from Sigma Aldrich or Thermo Fischer and usually stored in the cold, shielded from light. Freshly distilled solvents were used for electrochemical measurements.

2.2 Experimental Error and Reproducibility

Due consideration was given to minimizing experimental error throughout. Reported error values represent standard deviations of multiple experiments. This is the case for routine spectroscopic measurements such fluorescence quantum yield and fluorescence decay lifetimes. Fluorescence yield measurements for example were often run on more than one instrument, sometimes even with a complementary technique such as thermal blooming spectroscopy or using an integrating sphere. This is addition to running multiple measurements at different concentrations of dye in solution, as per a typical ratiometric fluorescence measurement. Fluorescence lifetime measurements were run multiple times and often using both TCSPC and frequency domain measurements (described later). Where values are obtained from fitting data to a model, the quality of the result is judged against visual inspection of model vs data, chi-squared values and by plotting residuals. Other sources of error such as the resolution limit of spectrophotometers and limits on accurately weighing out materials were considered where appropriate.

2.3 Steady-State Absorption and Emission Spectroscopy

UV-visible absorption spectroscopic measurements were performed either on a Hitachi U3310 or a Perkin-Elmer Lambda 35 spectrophotometer. Matched 1 cm quartz cuvettes were typically used for recording solution samples. Slow scan rates, with and a narrow slit width (<1 nm), were used to obtain high quality absorption spectra with a good signal to noise ratio. The typical concentration for the dyes examined here with molar absorption coefficients in the range of several tens of thousands was the micromolar range. Care was taken not to exceed an absorbance value of 1.5 under any circumstance as this constitutes transmission of only 3 % light. At higher absorbance, measurements become inaccurate. Routine molar absorption coefficient measurements were obtained using the Beer-Lambert Law (Equation 2.1) where A is absorbance (log of ratio between the incident light intensity (I_o) and the intensity of light passing through the sample (I)). Concentration of sample is c, in mol dm^{-3}. The cell path length l is in cm and ε is the molar absorption coefficient where the units are mol^{-1} dm^3 cm^{-1}. Since special emphasis

is given to sample purity over quantity, it was not always possible to weigh out several separate stock solutions for absorption coefficient measurements.

$$\log\left(\frac{I_o}{I}\right) = A = c * l * \varepsilon \qquad (2.1)$$

Fluorescence measurements were primarily recorded using a Horiba Fluorolog Tau-3 spectrophotometer system as it has the highest quality optics available and utilizes dual grating monochromators, which minimize stray light. Two types of detector were used depending on the nature of the dye being examined. Where samples displayed fluorescence not exceeding 830 nm, a R928 photomultiplier tube (PMT) was used. For dyes emitting beyond this range, a water-cooled R2658P PMT was used. This extends the practical emission detection range to 900 nm. As the majority of dyes examined here are in the red region for fluorescence (650-800 nm), it is important to take careful note of the limits of detections for the instrument. As Figure 2.1 demonstrates, the detector response drops off precipitously towards the red region for the R928 detector (common in many commercial instruments). For fluorescence anisotropy measurements, the instrument's built-in autopolarizers were used after following the manufacturer's instructions for calibration. Corrected fluorescence spectra were obtained in all instances. Great care was taken at all times to ensure solution samples were properly dissolved in the solvent. This involves appropriate choice of solvent at the first instance and sonication of the sample to break up solids where necessary. Additional fluorescence measurements were recorded on a Hitachi F-4500 instrument. As a general rule, an excitation and emission slit width of 2.5 nm was used for solution samples and 5 nm slits, if necessary, for solids and transparent films.

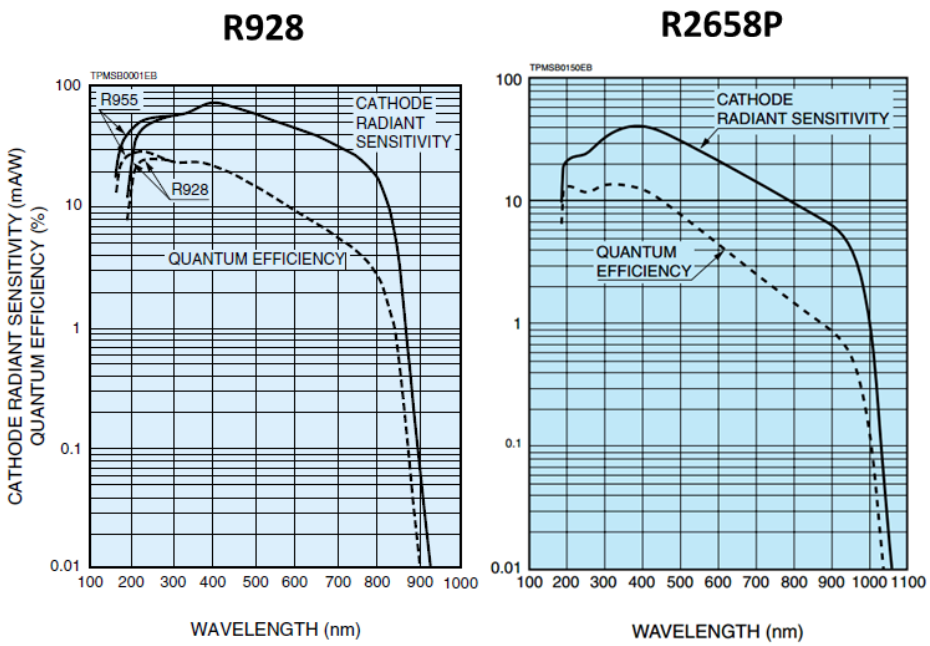

Figure 2.1. Spectral response curves for the two types of photomultiplier tube used to record fluorescence spectra. Graphs obtained from Hamamatsu Photonics.

Fluorescence quantum yields measured on a fluorescence spectrophotometer were obtained using the classical comparative method[1,2] whereby a well-characterized fluorescence standard was measured against the unknown sample fluorescence. Care was taken to choose a standard which had as closely matching fluorescence profile to the sample as possible. All measurements were repeated several times and samples were prepared in optically thin solutions to avoid artifacts due to the inner filter effect (absorbance at the excitation wavelength <0.08). Suitable cut-off filters were used to exclude stray excitation light and consideration given to tests for further artifacts from Raman and Rayleigh scattering. Fluorescence yields were always recorded in air-equilibrated solution at room temperature for consistency unless otherwise specified in the relevant chapter.

2.4 Time-Resolved Absorption and Emission Spectroscopy

Time-resolved spectroscopic measurements were used to obtain vital kinetic data, leading to a better understanding of the photophysical mechanisms governing the chromophores studied within. Time-resolved fluorescence measurements enable one to measure the fluorescence decay lifetime, τ_{s1}, which is necessary for determining the nonradiative rate constant of a fluorophore. Transient absorption measurements allow for characterization of many species across timescales spanning piscoseconds to milliseconds. Transient species of particular interest here include radicals, triplet states and isomers.

2.4.1 Fluorescence Lifetime Measurements

Broadly speaking there are two established methods for determining the fluorescence lifetime of a fluorophore; namely, time-domain and frequency-domain measurements. Both obtain the same result but use very different approaches, although neither records the fluorescence decay directly as it happens.[3,4] Time-domain measurements record fluorescence events as a function of time by obtaining signals from a large number of channels, each a specific delay after the excitation pulse. These are sometimes referred to as “bins”. The fluorescence decay can be imagined as being divided into a number of slices, each a signal measuring the number of photons at a given delay. The more channels recording photons at each delay, the more accurate the measurement. Time-correlated single photon counting (TCSPC)[5] is a common time-domain technique for determining the fluorescence lifetime and the primary method used in the work described in this thesis. It assigns each channel to a specific time. A high repetition of the excitation source (invariably a laser diode) sees the gradual build-up of individual photons detected at each channel. As the experiment progresses, a histogram of photon intensities at different time delays is built up, leading to a fluorescence decay curve. The time measurement is dictated by the excitation pulse, characterized by the instrument response function (IRF). The IRF is measured by recording emission from a scattering non-fluorescent sample, commonly colloidal silica or ethylene glycol, which establishes time zero.

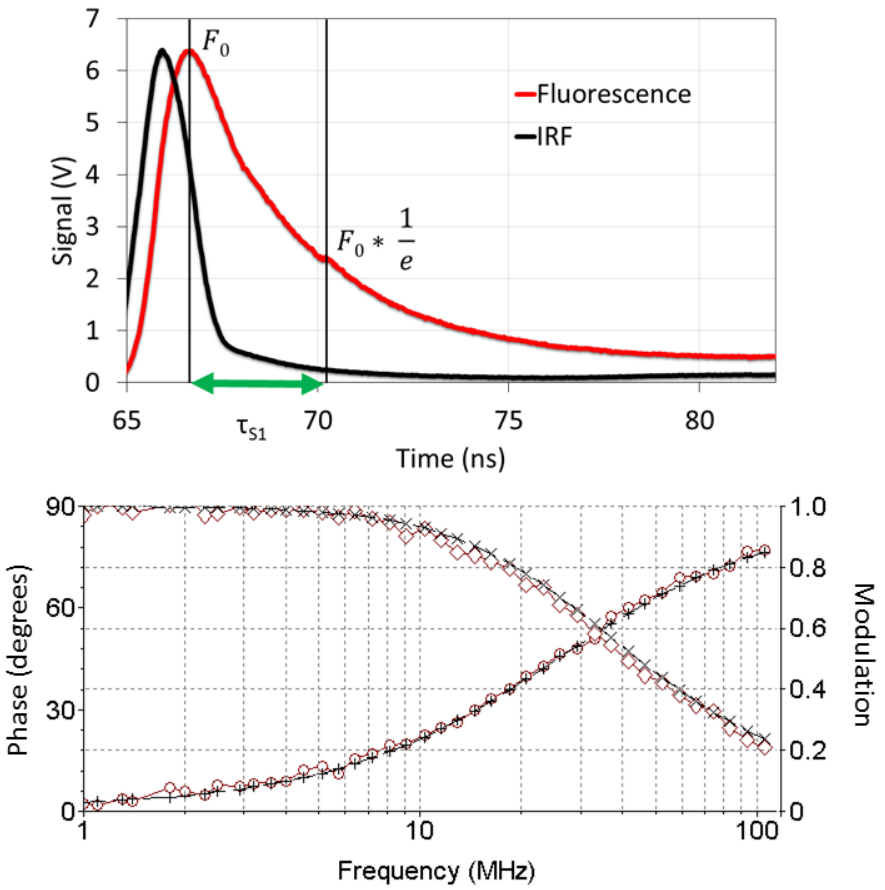

Figure 2.2. Representative examples of single exponential fluorescence decay output by TCSPC (upper panel), and the phase modulation technique (lower panel).

Frequency-domain fluorescence lifetime measurements involve continuous excitation of the sample with a sinusoidally modulated light beam.[6] The phase and modulation of the fluorescence are measured at a series of frequencies (typically in 1-500 megahertz range). The greater the phase shift, the longer the lifetime. Fluorescence emitted will have the same sinusoidal character, but there will be a phase shift associated to it, corresponding to the fluorescence lifetime (Figure 2.3). Like TCSPC, the technique is a Fourier transform of the fluorescence detected. Although both methods should produce the same results, TCSPC has become more common due to advances in fast detector electronics and inexpensive laser diodes with short excitation pulse widths (down to picoseconds). In our work, TCSPC fluorescence lifetime measurements were performed using a PTI EasyLife2 single photon counting instrument with several short-duration laser diode pulse excitation sources spanning the UV-visible range (full-width half maximum of excitation pulse = 0.5 ns). Complementary phase modulated lifetime measurements

were performed using the Horiba Fluorolog Tau-3 system, where excitation was with a 450 Watt xenon arc lamp. The excitation light is modulated with a Pockels Cell.

In most cases, TCSPC was the method of choice. With both instruments analysis of the fluorescence decay data was performed with the software provided by the manufacturer, namely Felix32 and Datamax for the EasyLife2 and Fluorolog systems respectively. In nearly all cases encountered the TCSPC fluorescence decay data was fitted to a single exponential using a least-squares fit. The phase modulated technique uses a standard with a known fluorescence lifetime for instrument response. The work here used either colloidal silica (scattering sample, τ_{s1} = 0 ns), Nile Blue (τ_{s1} = 1.42 ns in EtOH)[7] or cresyl violet (4.17 ns in THF measured in our laboratory) as a standard.

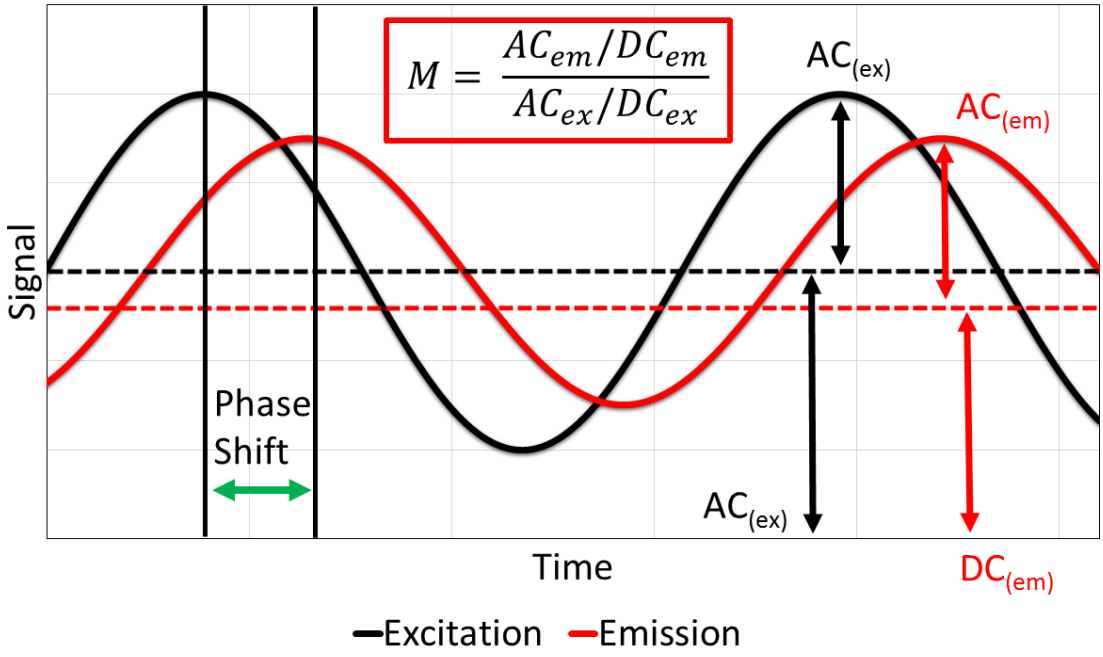

*Figure 2.3. Illustration of the principle behind frequency-domain fluorescence lifetime measurements. The modulation **M** is determined by taking the ratio of AC and DC signals for both the excitation and emission beams.*

2.4.2 Flash Photolysis and Pulse Radiolysis

Flash photolysis is a pump-probe experiment whereby the absorption of rapidly evolving photochemical intermediates can be tracked.[8,9,10] The method was pioneered by Porter and Norrish in the 1950s and 1960s[11,12] and became more popular with the advent of lasers, which could be used to excite the sample with a very short pulse and high intensity. Conventional laser flash photolysis allows for measuring the formation and decay of transient species from the nanosecond timescale to milliseconds. Nanosecond laser flash photolysis is particularly suited to measuring species such as triplets, radical species and isomers. Figure 2.4 shows a typical laser flash photolysis experimental setup.

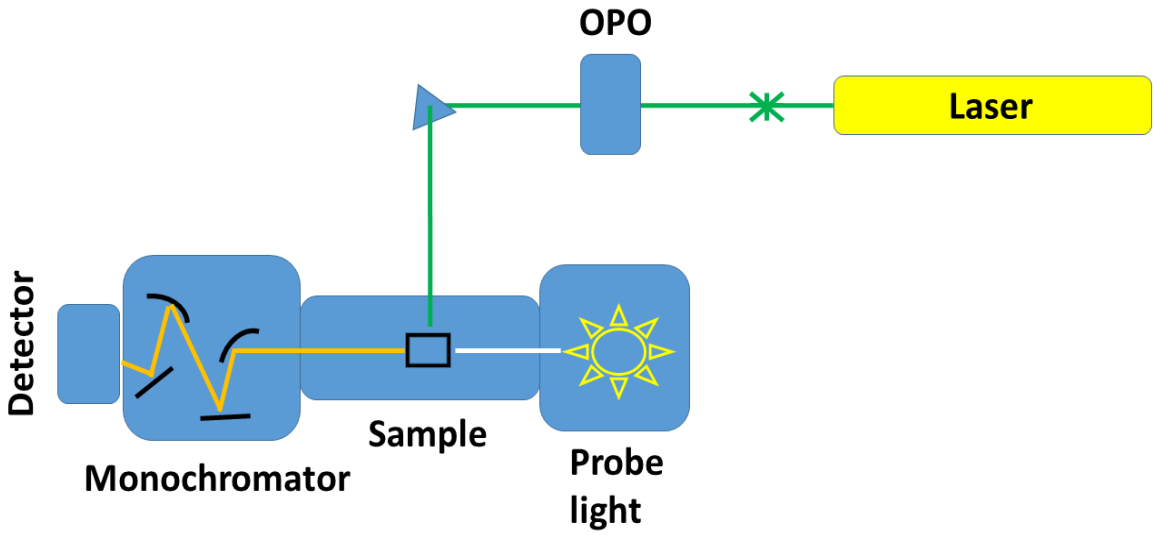

Figure 2.4. Block diagram of a conventional laser flash photolysis experimental setup.

The flash photolysis setup involves two "pulses of light". First the sample (liquid, film or solid) is irradiated by a short, high-intensity laser pulse (typically a few nanoseconds in duration). Immediately after the excitation pulse, a probe light (with a broadband spectrum, i.e. white light) is used to record the absorbance as one would with a steady-state UV-visible absorption spectrophotometer. In essence the system is perturbed by an intense light burst and the reaction monitored until an equilibrium is restored. The output is a decay trace of the transient light absorbing species at a wavelength selected by a monochromator (Figure 2.5). Light is detected either by a photomultiplier tube or a charge-coupled device (CCD). By recording transient decay signals at numerous wavelengths, it is possible to build up a decay profile for an entire absorption spectrum where global analysis is used for interpreting the data (Figure 2.5 right-hand panel).

Global analysis of transient spectra can yield a wealth of kinetic information, which in turn builds a description of the excited state decay processes in a given system.

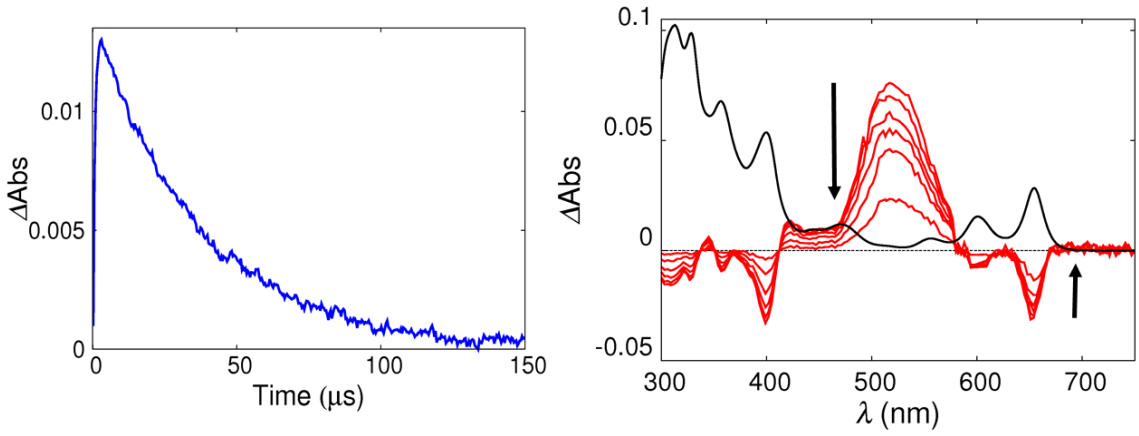

Figure 2.5. Example data output from a nanosecond laser flash photolysis experiment. The left-hand panel shows a decay trace for the absorption feature centred at 510 nm in the red spectrum (right-hand panel). The individual red traces in the right-hand panel show evolution of the transient absorption spectrum over the time-scale of the trace in the left-hand panel. The black trace corresponds to the ground-state absorption.

Nanosecond laser flash photolysis measurements in the work here were performed on an Applied Photophysics LKS-70 setup. The outline of the instrument matches that of the block diagram in Figure 2.4. Excitation was with a Nd:YAG laser at 1064 nm where the excitation pulse width was approximately 4 ns operating at a repetition rate of 10 Hz. A selection of excitation wavelengths was made available with the use of the second and third harmonic generators, allowing excitation at 532 and 355 nm respectively. An optical parametric oscillator (OPO) provided tunable excitation wavelengths from 610 to 680 in principle when used in conjunction with the second harmonic generator. Detection was with a R928 photomultiplier tube. The useful time domain for flash photolysis experiments is from tens of nanoseconds to the millisecond range. Measurements involving long-lived triplet species always involved purging the sample from oxygen (unless there was a deliberate intention not to do so), which was done by bubbling the solution sample with dry N_2 for at least 15 minutes using the capillary technique. Typical transient decay traces were averaged over at least 10 repeats.

To complement laser flash photolysis measurements of TIPS-pentacene and bis-pentacene compounds additional pulse radiolysis experiments were conducted by collaborators, Sachiko Tojo, Mamoru Fujitsuka, and Prof. Tetsuro Majima at Kyoto University, Japan. Pulse radiolysis[13,14] is a variation on laser flash photolysis where the excitation source is a high energy electron pulse from a particle accelerator instead of a laser. In this case benzene was ionized by the excitation pulse (27 MeV, 8 ns, 0.87 kGy per pulse from a linear accelerator at Osaka University), generating ionized benzene species. Recombination of the charged species generates triplet benzene[15], which transfers triplet excitation energy to the analyte by triplet energy trasnfer[16] in order to probe the sample's triplet absorption characteristics. All samples were saturated with Ar gas for a minimum of 15 min before an experiment. The kinetic measurements were performed using a nanosecond photoreaction analyzer system (Unisoku, TSP-1000). The probe light was from a 450-W Xe arc lamp (Ushio, UXL-451-0), which was operated by a large current pulsed-power supply that was synchronized with an electron pulse. The probe light was passed through an iris with a diameter of 2 mm and sent into the sample solution at a perpendicular intersection to an electron pulse. The monitor light passing through the sample was focused on the entrance slit of a monochromator (Unisoku, MD200) and detected with a photomultiplier tube (Hamamatsu Photonics, R2949). The transient absorption spectra were measured using a photodiode array (Hamamatsu Photonics, S3904-1024F) with a gated image intensifier (Hamamatsu Photonics, C2925-01) as a detector.

2.4.3 Ultra-Fast Transient Absorption Spectroscopy

Nanosecond laser flash photolysis experiments can yield a wealth of kinetic data on the molecular excited state. However such an instrument cannot detect sub-nanosecond processes, which eliminates many interesting transient species that might be involved in the reaction mechanism. The fluorescence decay lifetime of a typical organic fluorophore is usually between one and ten nanoseconds. Therefore, kinetic properties of the singlet excited state are lost in the conventional flash photolysis experiment described above because the excitation pulse width is longer than the lifetime of the singlet state. To record properties of the excited singlet state it is usually necessary to move to the picosecond timescale. In order to make such measurements, ultra-fast

transient absorption techniques are necessary.[17] This is again a pump-probe experiment akin to laser flash photolysis, but the nature of the excitation laser is different. Ultrafast transient measurements use femtosecond lasers (10^{-15} s) to excite the sample, allowing detection of transient absorption on the sub-nanosecond timescale. This allows for observation of the singlet excited state absorption, its decay and formation of subsequent species such as the triplet-excited state. Intermediate species such as radical anions, cations, excimers and exciplexes can also be detected[18], yielding yet more information on the nature of excited state dynamics. Again a wealth of kinetic information is obtained, analysis of which requires global methodology.

Access to ultra-fast transient absorption measurements was provided by collaboration with Prof. Nikolai Tkachenko (Tampere University of Technology, Finland). The experimental setup is described in the scientific literature[19], but the main components of the instrument comprise a mode-locked Coherent Libra F Ti:Sapphire 1 kHz femtosecond laser where excitation wavelength was tunable by a Coherent Topaz C optical parametric amplifier (OPA). The pulse energy was approximately 1 mJ with pulse width of 100 fs. The probe light was produced by generation of a white light supercontinuum from either water or sapphire. Detection was made with silicon photodiode array (ExciPro, CDP Inc.) in the UV-visible range and with an InGa diode detector for measurements in the near infrared region. Measurements with this technique record signals from 0 ps to approximately 6 ns achieved by an optical delay line. In contrast to the laser flash photolysis measurements on the LKS-70 system, which detects a decay at a single wavelength at a time, the ultra-fast system takes a snapshot of the entire transient spectrum at a given delay time. Multiple averages were run for each sample. Data analysis was performed with global fitting software developed at Tampere University of Technology.

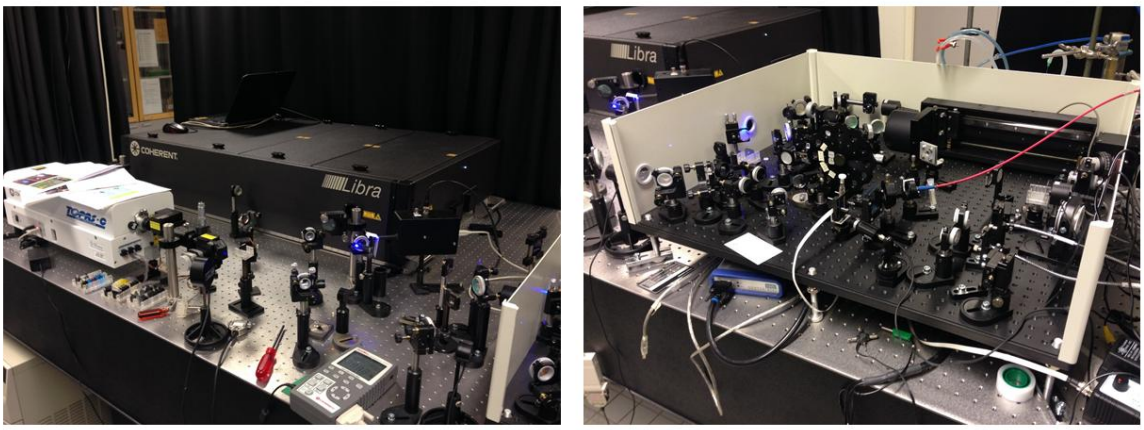

Figure 2.6. Photographs of the picosecond transient absorption spectroscopy instrumentation used at Tampere University of Technology, Finland. The left-hand panel shows the laser and optical parametric amplifier. The right-hand panel shows the optics leading to the detector and the laser pulse delay line.

2.5 Temperature-Dependent Spectroscopic Measurements

Various experiments in the work reported here involve controlling the temperature of a sample. This has been accomplished in two ways for the 20 to 80 ^{o}C and 20 to -196 ^{o}C temperature ranges. Elevated temperature experiments were carried out using a circulating water bath (Grant LT D6G) connected to a heater block cuvette holder. Low temperature spectroscopic measurements utilized an Oxford Instruments Optistat DN liquid nitrogen cryostat, connected to an ITC temperature controller. In both cases care was taken to give the sample enough time to equilibrate at a given temperature (10 minutes). Where a circulating water bath was used to warm a sample, a thermocouple was used to measure the temperature of the cuvette.

2.6 Thermal Blooming Spectroscopy for Measurement of Fluorescence Quantum Yields

The fluorescence quantum yield is a fundamental photophysical property and forms the basis of investigations throughout this thesis. Determining fluorescence yields accurately and consistently remains a great challenge though, despite advances in instrumentation and methodology. Although typically fluorescence yields are determined using the comparative method, where the fluorescence of a well-characterized standard is measured against the unknown sample, an alternative method was sought to complement these measurements. This was in part influenced by the shortage of

reliable fluorescence yield standards in the far-red region. It was decided to reintroduce the relatively unexploited method known as thermal blooming (aka. thermal lensing)[20,21] spectroscopy for determining absolute fluorescence quantum yields. Thermal blooming spectroscopy for the purpose of determining fluorescence yields was introduced by Magde and co-workers in the 1970s.[22,23,24] Since then the method has not, despite being successfully demonstrated, been widely adopted.

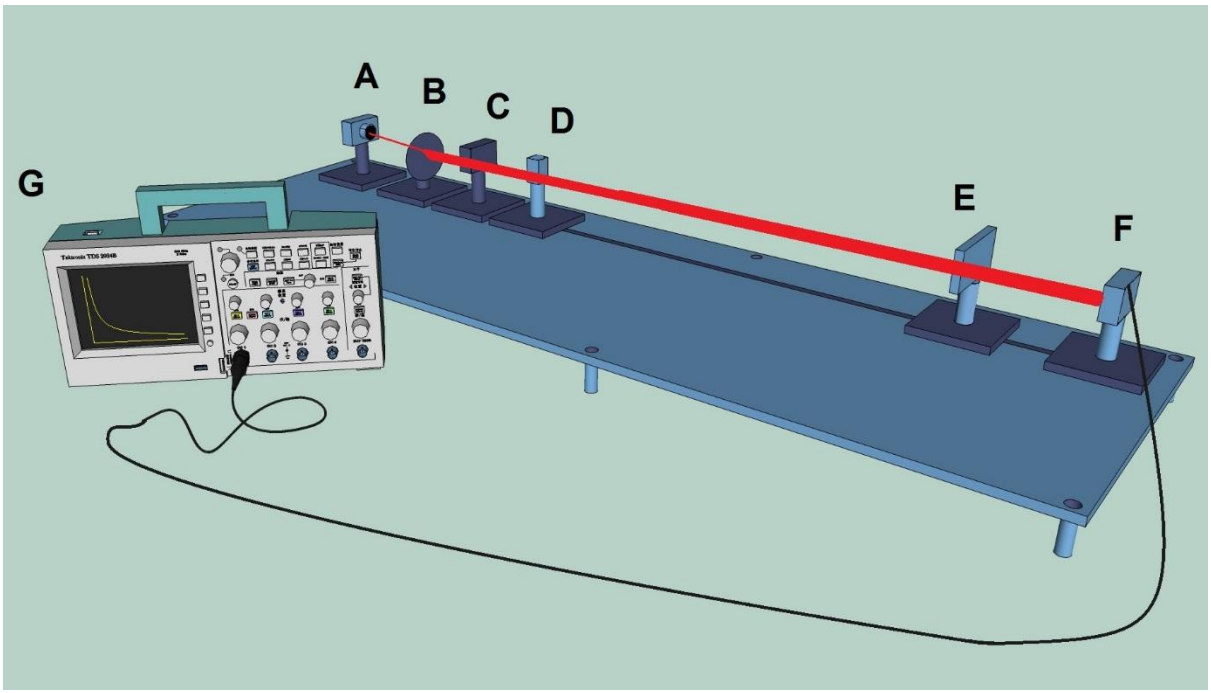

Figure 2.7. Diagram of the thermal blooming apparatus constructed to record fluorescence quantum yields. Key: A. laser, B. lens, C. shutter, D. sample cuvette, E. filter, F. photodiode detector, G. oscilloscope.

The principle of using thermal blooming to determine fluorescence quantum yields is based on recording non-radiative decay as opposed to detecting fluorescence directly, it is effectively a calorimetric technique. When a fluorophore is excited with a suitable laser for a short duration (approx. 0.5 seconds), the non-radiative component of the excited state decay transfers energy to the solvent as heat, causing a local change in the solvent refractive index before equilibrating with the environment. This change in refractive index due to the heat gradient can be visualised as the defocussing (or blooming) of a laser beam expanded on a detector. Detection is with a silicon photodiode, which records the blooming laser spot as a current decay trace.

The heat dissipated into the liquid solvent can be determined by accurately measuring the absorbance of the sample at the excitation wavelength and knowing the power of the excitation laser. Equation 2.2 shows the relationship between the incident laser power P_L, transmitted laser power P_T, fluorescence P_F and heat generated by non-radiative decay P_{TH}.

$$P_L = P_T + P_F + P_{TH} \qquad (2.2)$$

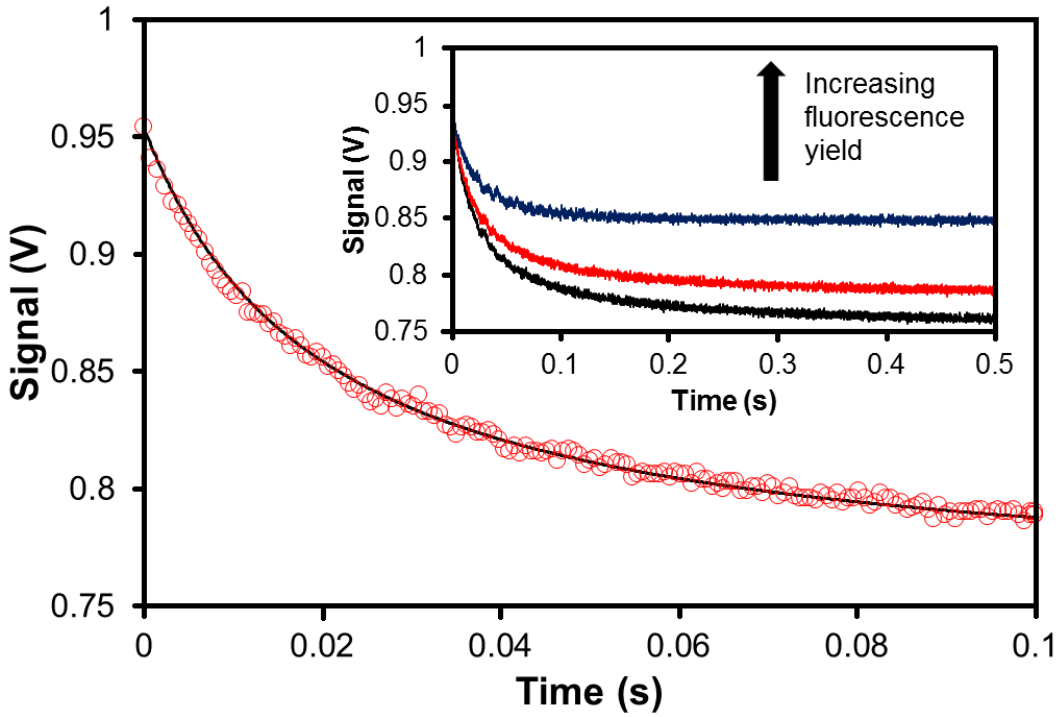

Figure 2.8. Representative example output data of a thermal blooming experiment for a chromophore in liquid solution. Red circles: raw data. Black line: experimental fit according to Equation 2.3. Inset, thermal blooming measurement followed until a steady-state equilibration has been achieved.

Figure 2.8 shows an example of the output data from a thermal blooming experiment. Equation 2.3 is used to model the data where the fit produces a parameter θ, which is directly proportional to the radiant heat. By comparing the thermal blooming data collected to that of a non-fluorescent standard under identical conditions, one can associate any change in optical properties to changes in the solvent reservoir. This is assuming the solvent is totally transparent to the excitation beam and that no chemical reaction occurs during the experiment. Experimental traces can be analyzed in terms of Equation 2.3[22] to give a value for θ. Here I_0 is initial laser intensity, t is time and t_c describes the thermal diffusivity of the solvent (specific to the solvent).

$$I(t) = I_0 \left[1 - \theta \left(1 + \frac{t_c}{2t} \right)^{-1} + \frac{1}{2}\theta^2 \left(1 + \frac{t_c}{2t} \right)^{-2} \right]^{-1} \qquad (2.3)$$

$$\Phi_F = \left[1 - \frac{A_R}{A_S}\frac{\theta_S}{\theta_R} \right] \frac{v_{ex}}{v_F} \qquad (2.4)$$

With a value of θ determined for both the non-fluorescent sample and for the unknown under identical conditions, Equation 2.4[22] can be used to determine the fluorescence quantum yield Φ_F. A refers to absorbance for the reference and sample R and S respectively. v_F is the mean fluorescence emission energy and the v_{ex} is the laser excitation energy, in wavenumber, which account for the Stokes' shift.

The number of components required for a thermal blooming spectrophotometer is few and these are relatively inexpensive in comparison to a commercial spectrophotometer (Figure 2.7). The thermal blooming apparatus must have a cw laser with Gaussian mode TEM_{00} output at a wavelength appropriate for excitation of the chromophore. A plano-convex lens is used to expand the laser beam onto the detector and a digital optical shutter used to expose the sample to the laser for a pre-determined time. A silicon photodiode detector and a digital oscilloscope are used to obtain data. It is also essential that the instrument be isolated from any vibration and that stray light from the surrounding environment is excluded. Also crucial is the location of the sample cell along the path of the laser beam. It must be centred at the point where the waist of the beam is uniform, otherwise known as the Rayleigh distance.[25] In practice this can be optimized by adjusting the distance between lens and sample until the maximum thermal blooming signal is observed.

All of these components are readily obtainable from commercial sources. Finally, an optical table is required for mounting the components. For this work an aluminium table 130 cm long and 40 cm wide with adjustable 10 cm feet was machined. This provided the necessary flexibility for measurements. Slots and threaded mounting points were cut out along the length of the table so that each component could be positioned securely and with as much adjustability as possible for alignment purposes. Each component was mounted to an aluminium rod with some degree of height adjustment. The entire instrument is enclosed with a large acrylic case to exclude stray light.

Figure 2.9. Photographs of the thermal blooming spectrometer.

Excitation was made with a cw laser diode (Coherent 3.0 mW; 635 nm; VHK Circular Beam Visible Laser Diode). A digital beam shutter (Thorlabs SC10) controls exposure of the sample to the incident laser beam. The photodiode detector used here (Thorlabs PDA100A-EC) has a detection range 400-1100 nm. The plano-convex lens used to expand the beam had a focal length of 10 cm. The detector must be sufficiently distant from the laser that the laser spot covers the entire detector surface. Output was recorded with a Tektronix DPO71254 digital oscilloscope. Brilliant Green was used as a non-fluorescent standard. All measurements were repeated in triplicate and experiments were typically repeated seven times. We thank John Corner and Gary Day of the Newcastle University School of Chemistry Mechanical Workshop for help constructing the thermal blooming instrument.

2.7 Variable Path Length Cell for Absorption and Emission Spectroscopy

There are a large number of scenarios where it is beneficial to be able to change the path length of a solution cell for absorption and emission spectroscopy, the vast majority of cells being 1 cm glass or quartz cuvettes. It was deemed desirable therefore to have a solution cell which could have as wide a range of path lengths as possible, and fit as many applications as possible. To that end, a bespoke variable path length cell was constructed (Figure 2.10).

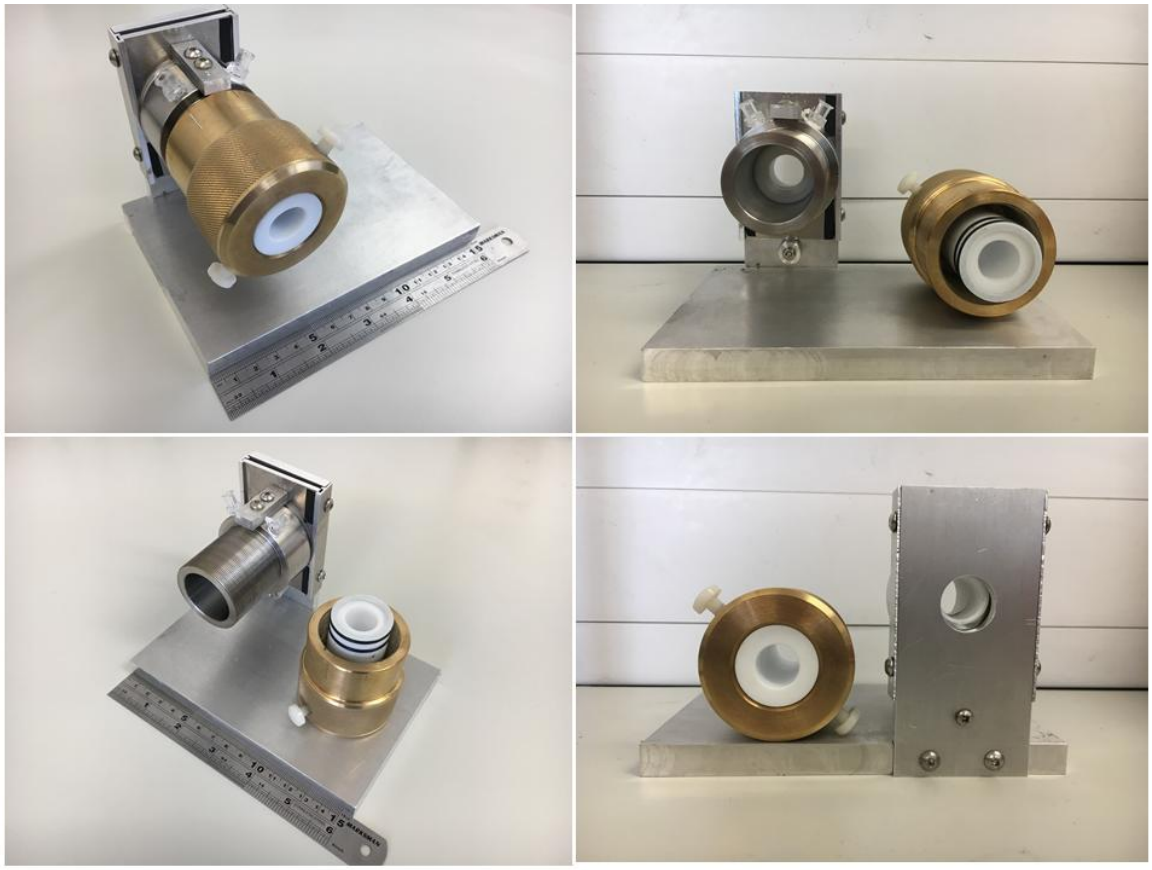

Figure 2.10. Variable path length optical cell for absorption and fluorescence measurements.

The variable path length cell is constructed as a threaded barrel, somewhat akin to a camera lens. There are two cylindrical halves which thread into each other, allowing a stepless adjustment of the path length between <0.5 mm and 4 cm. The thread was made so that one full turn of the barrel corresponds to an adjustment of 1 mm. 1 inch quartz discs obtained from Edmund Optics were used as the cell windows, which were compression fitted into PTFE (polytetrafluoroethylene) barrels, which form the inner

core of the cell. Two ports are at the top of the cell for adding/removing solution. The ports are disposable female Leur fittings, which allow for ease of cleaning and replacing parts to avoid cross-contamination. Two rubber (Viton) O-rings 26 mm internal diameter, 2 mm cross section are used to create a liquid-tight seal inside the cell between the PTFE inner barrel and the aluminium outer shell.

Calibration of the cell path length was carried upon each measurement session. This was done in two ways: First by matching the absorption of a dye measured in a 1 cm cuvette to the variable path length cell, then by confirming the concentration of a known stock solution of Rhodamine 6G in ethanol using the Beer-Lambert law. We are very grateful to Gary Day (Newcastle University School of Chemistry Mechanical Workshop) for input on the design of the cell and for its construction. The variable path length cell also provides an alternative means of measuring a dye's molar absorption coefficient where the concentration of dye is kept constant, but the path length varied.

2.8 Steady-State Photobleaching Studies

Photochemical bleaching studies were made using JCC Lighting Products IP66 floodlight operating at 400W at a distance of 85 cm to the sample. The sample was contained in 1 cm a quartz cuvette and positioned in front of the lamp. A glass cut-off filter was inserted before the sample cell to eliminate heat and to prevent illumination by near-UV light. Absorption spectra were recorded at frequent intervals in order to monitor the course of reaction. The experiments were typically repeated several times, including samples that had not been deaerated.

2.9 Fluorescence Recovery after Photobleaching: FRAP

Fluorescence recovery after photobleaching is a technique developed in the 1970s[26] used for determining the rate of diffusion of fluorophores in a two dimensional plane. It is particularly associated with bio-medical research and used to measure diffusivity though cell membranes and tissues.[27,28] FRAP instruments are in essence modified fluorescence microscopes. Here the technique was used to obtain information on how a fluorophore interacts with the solvent.

The FRAP experiment involves bleaching an area of fluorophores with high-intensity focused light (usually from a laser) and monitoring the recovery of fluorescence in the bleached area. The emission intensity is then followed while fluorophores diffuse back into the "hole" left in the wake of irradiation (Figure 2.11) allowing one to determine the translational diffusion coefficient of a fluorophore. A diffusion coefficient D is determined from the recovery of fluorescence. A method of analyzing the fluorescence recovery was developed by Axlerod *et al.*[29], and is still used to this day. Equation 2.5 describes the characteristic thermal diffusivity *D*, where ω is the bleaching radius and γ a correction factor for the amount of photobleachng. The assumption is that bleaching of the fluorophores occurs in a two-dimensional disc. This provides us with a simple way to determine diffusivity of the fluorophore, which is related to how strongly the fluorophore interacts with the surrounding environment. In the experiments here we are talking purely about a solvent interaction. Further details on this experiment are found in Chapter 3.

$$D = \frac{\omega^2 \gamma}{4t_{1/2}} \qquad (2.5)$$

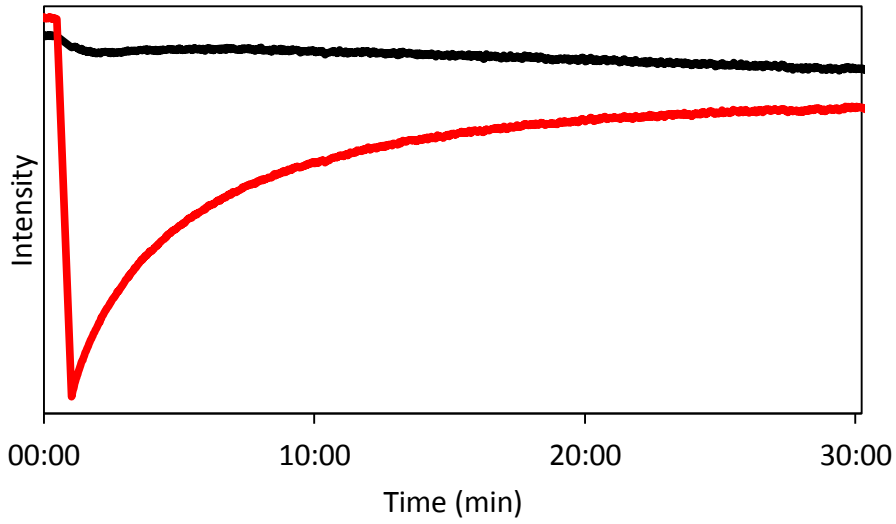

Figure 2.11. Example of FRAP experiment output. The red trace records recovery of the photobleached spot. The black trace is the fluorescecne intensity of an unbleached area of the sample, used as a reference fluorescence level.

FRAP experiments were performed with a Nikon Eclipse Ti confocal microscope at x20 magnification. Excitation was at 641 nm for aza-BODIPY and 560 nm for the non-aza BODIPY analogue. We gratefully acknowledge Dr. Alex Laude of the Newcastle University Bio-imaging Unit for access to the experiment.

2.10 Super-Resolution Fluorescence Microscopy: STORM

The theoretical principles behind stochastic optical reconstruction microscopy (STORM) are discussed in the introduction section.[30,31,32] Here the imaging protocol used in Chapter 8 is described. The photo-blinking behaviour of Alexa Fluor 647 NHS ester was analyzed from imaging with the stochastic optical reconstruction microscopy technique (STORM) using a Nikon N-STORM system based around a Nikon Eclipse Ti inverted microscope, 100x 1.49 Apo TIRF objective and Ixon DU-887 EM CCD camera (Andor). Excitation of the sample was made with a MPB VFL-P series, 647 nm 100 mW and Coherent Cube laser. Laser intensities were varied by an acousto-optical tunable filter (AOTF) as required. To increase contrast and minimize out-of-focus emission produced from mobile non-immobilised fluorophores, excitation was performed using the total internal reflectance fluorescence (TIRF) microscopy imaging technique which allows visualization of fluorophores located within 100-200 nm of the coverslip surface. Images were captured at 256 x 256 pixel resolution and at a rate of 50Hz (16 ms exposure). Any axial focal drift was corrected in real time by the Nikon 'perfect focus' system.

2.11 Cyclic Voltammetry

Electrochemical measurements were performed under a dry nitrogen atmosphere in anhydrous dichloromethane using a CH Instruments CHI600A potentiostat. Glassy carbon was used as a working electrode and platinum as the counter electrode. The reference electrode was Ag/AgCl. Ferrocene was used as an internal reference. Proprietary software was used for data collection.

2.12 Data Analysis

2.12.1 Relative Fluorescence Yield, Radiative Rate Constant and Strickler-Berg Relationship

Fundamentally the fluorescence quantum yield Φ_F is the ratio of the number of absorbed and emitted photons. Where fluorescence yields of an unknown sample (S) were determined against a well-characterized standard (R) Equation 2.6 was used.[33,34,35]

$$\Phi_F^S = \Phi_F^R \frac{1-10^{-A_R}}{1-10^{-A_S}} \frac{\int_{\lambda(em)} F^S(\lambda_{em})}{\int_{\lambda(em)} F^R(\lambda_{em})} \frac{n_R^2}{n_S^2} \qquad (2.6)$$

A refers to the absorbance, F the integrated fluorescence (the area under the fluorescence spectrum. The refractive index of the solvent is n. Where possible the same solvent was used for both sample and standard, as there has at times been debate in the literature regarding the validity of n^2correction for refractive index.[36,37,38] It must be stressed that the conditions used to measure the sample and standard should preferably be identical (i.e. same excitation wavelength, same temperature, same settings on the fluorometer).

Having obtained the fluorescence quantum yield Φ_F and singlet decay lifetime τ_{S1} by careful measurement, the radiative and non-radiative rate constants can be obtained easily by Equations 2.7 and 2.8.[39] Here the units are in s^{-1}. Knowledge of the radiative lifetime is useful for making comparisons upon modification of solvent, temperature, a quenching agent for example. Where there are extra non-radiative pathways, we can use the radiative rate constant as a marker for how the system has been perturbed.

$$k_{RAD} = \frac{\Phi_F}{\tau_{S1}} \qquad (2.7)$$

$$k_{NR} = \frac{1-\Phi_F}{\tau_{S1}} \qquad (2.8)$$

A useful tool for relating the absorption spectrum to the radiative rate constant and comparing it to experimentally obtained measurements is the Stricker-Berg relationship.[40] Where k_{RAD} is determined by experimental measurement of the fluorescence lifetime and fluorescence yield, the Strickler-Berg relationship (Equation 2.9) estimates the radiative lifetime from the nature of the absorption and fluorescence spectra. There are a number of caveats to the radiative rate constant obtained from the Strickler-Berg equation though. It assumes absolute rigidity in the system between the ground state and excited state and solvent interactions are not accounted for, i.e. there is nothing to quench the excited state. For this reason the radiative rate constant is referred to in this case as the natural radiative rate τ_n. It therefore tends to give more accurate estimates of k_{rad} where the fluorophore is highly fluorescent with strongly allowed absorption transitions and good mirror symmetry between the absorption and emission spectrum with a small Stokes shift.

$$\frac{1}{\tau_n} = 2.880 * 10^{-9} n^2 \langle v_f^{-3} \rangle_{Av}^{-1} \frac{g_l}{g_u} \int \varepsilon \, d \, lnv \qquad (2.9)$$

In Equation 2.9 n refers to the refractive index of the solvent, $\langle v_f^{-3} \rangle_{Av}^{-1}$ is the mean fluorescence energy (which can substituted for the fluorescence maximum in some cases). g_l and g_u are the degeneracies of the lower and upper states respectively. For fluorescence measurements this ratio is 1. The integral term takes the area under the molar absorptivity (ε) absorption spectrum. To obtain the mean fluorescence one must obtain the reduced fluorescence spectrum by converting the emission wavelength to wavenumber (cm^{-1}) and fluorescence intensity to $\frac{intensity}{(cm^{-1})^3}$.

2.12.2 Spectral Deconstruction of Absorption and Emission Spectra – Rational and Relationship with Molecular Dynamics

Absorption and emission spectra were routinely deconstructed into Gaussian-shaped components in order to obtain certain critical parameters such as the frequencies of nonradiative vibrational modes and the Huang-Rhys factor[41,42], *S*, which approximates the strength of electron-phonon interactions. This S-factor (Equation 2.10) is a dimensionless quantity, which describes geometry changes in the excited state therefore is therefore related to the Stokes' shift (SS). A large S-factor implies more

displacement between potential energy surfaces for ground- and excited-states and consequently a larger Stokes' shift.[43] A smaller S-factor is also indicative of extended π-conjugation.[44] Spectral deconstruction was done using commercially available software, namely PeakFit for Windows 4.0 by Jandel Scientific.

$$SS = (2S - 1)\hbar\omega \qquad (2.10)$$

The protocol for deconstructing a reduced absorption or emission spectrum was always based on fitting the spectra to the least number of Gaussian components where the resultant spectrum was in agreement with the original data with an R^2 (describing goodness of fit) value of at least 0.999. It must then be possible to reproduce this set of circumstances reliably on successive attempts. Figure 2.12 shows an example of the type of analysis carried out with this methodology. It is important to note that the wavelength scale has been converted to wavenumber here. Absorption spectra are expressed in terms of wavenumber and molar absorption coefficient. Fluorescence spectra are reduced, i.e. emission energy in wavenumber (cm^{-1}) and fluorescence intensity to $\frac{intensity}{(cm^{-1})^3}$.

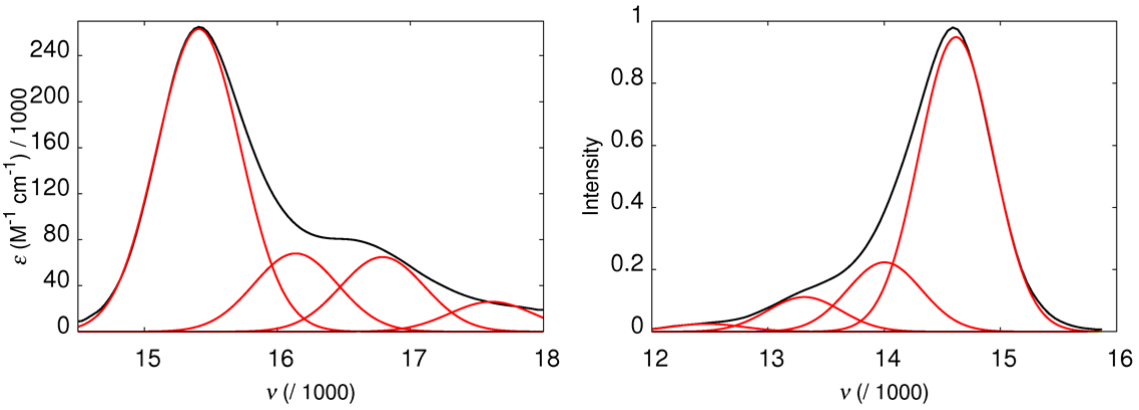

Figure 2.12. Deconstruction of the real absorption spectrum (left-hand panel) and emission spectrum (right-hand panel) for a Cy5 dye into a series of 4 Gaussian components.

With the absorption and emission spectra so deconstructed, one can obtain the true Stokes' shift (which is the difference in energy between the lowest energy Gaussian in the absorption spectrum and the highest energy Gaussian in the emission spectrum. The S-factor can be estimated from the ratio of areas of the two lowest energy Gaussians in the deconstructed spectrum.[45]

2.12.3 Analysis of Transient Absorption Spectra

Transient absorption spectra were analyzed mostly with commercial software as mentioned previously. However, some situations required manual analysis. In particular it was found that fitting nanosecond laser flash photolysis decay traces manually to a first order decay (or other differential equations as necessary) using spreadsheet software such as Microsoft Excel was often more rigorous than relying on "black box" pre-programmed fitting routines.

Determination of molar absorption coefficients for transient spectra also required manual data manipulation. This was done by taking the steady-state absorption spectrum and scaling it in magnitude such that when added back to the ground state bleach (which is a mirror image on the x-axis) no bleaching remained. At this point the appropriately scaled ground state spectrum could be directly compared with other absorption features seen in the transient spectrum (provided the absorption feature does not overlap with the ground state bleach). Assuming the molar absorption coefficient is known, the corresponding molar absorption coefficient of the transient can be estimated from a direct comparison of the heights of the absorption. This was used successfully used to estimate singlet- and triplet excited state molar extinction coefficients as well as certain light-induced isomers. Manipulation of spectra was done with freely available software.[46]

2.12.4 Computational Methods

Quantum chemical calculations were made using various items of commercial software. Preliminary geometry optimizations were made with AMPAC 10[47] using the PM6 semi-empirical method[48] with the COSMO solvation model.[49] This method was used to generate input structures for subsequent DFT calculations, carried out with TURBOMOLE V7.0.64[50] Geometry optimizations on ground-state structures was achieved using density functional theory with the CAM-B3LYP functional[51] and the cc-pVTZ basis set.[52] To model the effects of solvent on the minimized geometries re-optimization was performed using the polarizable continuum model (IEF-PCM)[53] and universal force field atomic radii with parameters set for a dielectric constant of 10. Benchmark studies were made using 1,1'-bi-2-naphthol as a model compound[54] in order to ensure comparability with the literature. Eigenvalues for the HOMO and LUMO, and the subsequent HOMO-LUMO energy gap, were computed at the B3LYP level with the 6-31G(d) basis set.

Excitation energies were calculated by time-dependent density functional theory (TD-DFT) Again, the CAM-B3LYP functional was used. Tight convergence criteria (e.g., maximum displacement of 6×10^{-7} and RMS displacement of 6×10^{-5}) were applied to both ground and excited state calculations. Additional calculations for the excited-state geometries were made with configuration interaction determined using single excitations,[55] including perturbative corrections for double excitations.[56]

2.13 References

1. Rurack, K., 2008. Fluorescence quantum yields: methods of determination and standards. In Standardization and quality assurance in fluorescence measurements I (pp. 101-145). Springer Berlin Heidelberg.

2. Fery-Forgues, S.; Lavabre, D., *J. Chem. Educ.* **1999**, 76, 1260.

3. Becker, W., 2005. *Advanced time-correlated single photon counting techniques* (Vol. 81). Springer Science & Business Media.

4. Lakowicz, J.R. and Gryczynski, I., 2002. Frequency-domain fluorescence spectroscopy. In *Topics in fluorescence spectroscopy* (pp. 293-335). Springer US.

5. Phillips, D.; Drake, R.C.; O'Connor, D.V.; Christensen, R.L. *Instrum. Sci. Technol.* **1985**, 14, 267-292.

6. Haar, H.P.; Hauser, M. 1978. *Rev. Sci. Instrum.* **1978**, 49, 632-633.

7. Sens, R.; Drexhage, K.H. *J. Luminesc.* **1981**, *24*, 709-712.

8. Andrews, D.L.; Demidov, A.A. 2012. An introduction to laser spectroscopy: second edition. Springer Science & Business Media.

9. Porter, G.; Topp, M.R. *Proc. R. Soc. A* , **1970**, 315, 163-184.

10. Bensasson, R.V.; Land, E.J.; Truscott, T.G., 2013. Flash photolysis and pulse radiolysis: contributions to the chemistry of biology and medicine. Elsevier.

11. Porter, G. *Proc. R. Soc. A*, **1950**, 200, 284-300.

12. Porter, G.; Topp, M.R. *Nature*, **1968**, *220*, 1228-1229.

13. McCarthy, R.L.; MacLachlan, A. *J. Chem. Soc. Faraday Trans.* **1960**, 56, 1187-1200.

14. Keene, J.P. *J. Sci. Instrum.*, **1964**, 41, 493-496.

15. Cooper, R.; Thomas, J.K., *J. Chem. Phys.* **1968**, 48, 5097-5102.

16. Land, E.J. *Proc. R. Soc. A*, **1968**, 305, 457-471.

17. Berera, R., van Grondelle, R.; Kennis, J.T. *Photosynth. Res.* **2009**, 101, 105-118.

18. Tkachenko, N.V., 2006. Optical spectroscopy: methods and instrumentations. Elsevier.

19. Sirbu, D.; Turta, C.; Benniston, A.C.; Abou-Chahine, F.; Lemmetyinen, H.; Tkachenko, N.V.; Wood, C.; Gibson, E. *RSC Adv.* **2014**, 4, 22733-22742.

20. Hu, C.; Whinnery, J.R. *Appl. Opt.* **1973**, 12, 72-79.

21. Swofford, R.L.; Long, M.E.; Albrecht, A.C. *J. Chem. Phys.* **1976**, 65, 179-190.

22. Brannon, J.H.; Magde, D. *J. Phys. Chem.* **1978**, 82, 705-709.

23. Magde, D.; Brannon, J.H. ; Cremers, T.L.; Olmsted, J. *J. Phys. Chem.* **1979**, 83, 696-699.

24. Magde, D.; Wong, R.; Seybold, P.G. *Photochem. Photobiol.* **2002**, 75, 327-334.

25. Pearson, J.E., *Opt. Lett.* **1978**, 2, 7-9.

26. Peters, R.; Peters, J.; Tews, K.H.; Bähr, W. *Biochim. Biophys. Acta*, **1974**, 367, 282-294.

27. Meyvis, T.K.; De Smedt, S.C.; Van Oostveldt, P.; Demeester, *J. Pharm. Res.* **1999**, 16, 1153-1162.

28. Reits, E.A.; Neefjes, J.J. *Nat. Cell Biol.* **2001**, 3, 145-147.

29. Axelrod, D.; Koppel, D.E.; Schlessinger, J.; Elson, E.; Webb, W.W. *Biophys. J.* **1976**, 16, 1055-1069.

30. Rust, M.J.; Bates, M.; Zhuang, X. *Nat. Methods*, **2006**, 3, 793-795.

31. Van De Linde, S.; Löschberger, A.; Klein, T.; Heidbreder, M.; Wolter, S.; Heilemann, M.; Sauer, M. *Nat. Protoc*. **2011**, 6, 991-1009.

32. Hell, S.W. *Nat. Methods*, **2009**, 6, 24-32.

33. Parker, C.A.; Rees, W.T. *Analyst*, **1960**, 85, 587-600.

34. Resch-Genger, U.; Rurack, K. *Pure Appl. Chem.* **2013**, 85, 2005-2013.

35. Würth, C.; Grabolle, M.; Pauli, J.; Spieles, M.; Resch-Genger, U. *Nat. Protoc.* **2013**, 8, 1535-1550.

36. Busselle, F.J.; Haig, N.D.; Lewis, C. Chem. Phys. Lett. **1980**, 72, 533-535.

37. Ediger, M.D.; Moog, R.S.; Boxer, S.G.; Fayer, M.D. *Chem. Phys. Lett.* **1982**, 88, 123-127.

38. Busselle, F.J.; Haig, N.D.; Lewis, C., *Chem. Phys. Lett.* **1982**, 88, 128-130.

39. Lakowicz, J.R., 2006. Principles of fluorescence spectroscopy. Springer US. New York.

40. Strickler, S.J.; Berg, R.A. *J. Chem. Phys.* **1962**, 37, 814-822.

41. Asada, K.; Kobayashi, T.; Naito, H. *Thin Solid Films*, **2006**, *499*, 192-195.

42. Lavrentiev, M.Y.; Barford, W. *J. Chem. Phys.* **1999**, 111, 11177-11182.

43. Karabunarliev, S.; Baumgarten, M.; Bittner, E.R.; Müllen, K. *J. Chem. Phys.* **2000**, 113, 11372-11381.

44. Strouse, G.F.; Schoonover, J.R.; Duesing, R.; Boyde, S.; Jones, W.E.J.; Meyer, T. J. *Inorg. Chem.* **1995**, 34, 473-487.

45. de Jong, M.; Seijo, L.; Meijerink, A.; Rabouw, F.T. *Phys. Chem. Chem. Phys.* **2015**, 17, 16959-16969.

46. a|e - UV-Vis-IR Spectral Software 1.2, FluorTools, www.fluortools.com

47. AMPAC 10, 1992-2013 Semichem, Inc. 12456 W 62nd Terrace - Suite D, Shawnee, KS 66216.

48. Stewart, J.J.P. *J. Mol. Model.* **2007**, 13, 1173-1213.

49. Klamt, A. *J. Phys. Chem.* **1996**, 100, 3349-3353.

50. TURBOMOLE V7.0 2015, A development of University of Karlsruhe and Forschungszentrum Karlsruhe GmbH, 1989-2007, TURBOMOLE GmbH, since 2007.

51. Yanai, T.; Tew, D.P.; Handy, N. *Chem. Phys. Lett*. **2004**, *303*, 51-57.

52. Woon, D.E.; Dunning Jr., T.H. *Chem. Phys*. **1993**, *96*, 1358-1371.

53. Cossi, M.; Scalmani, G.; Rega, N.; Barone, V. *J. Chem. Phys.* ***2002***, 117, 43-54.

54. Sahnoun, R.; Koseki, S.; Fujimura, Y. *J. Mol. Struct.* **2005**, *735*, 315-324.

55. Foresman, J.B.; Head-Gordon, M.; Pople, J.A.; Frisch, M.J. *J. Phys. Chem*. **1992**, *96*, 135-149.

56. Head-Gordon, M.; Rico, R. J.; Oumi, M.; Lee, T.J. *Chem. Phys. Lett.* **1994**, 219, 21-29.

57. Li, X.; Liang, X.; Song, T.; Su, P.; Zhang, Z. *Bioorganic Med. Chem.* **2014**, 22, 5738-5746.

58. Hosangadi, B.D.; Dave, R.H. *Tetrahedron Lett.* **1996**, 37, 6375-6378.

59. Braslau, R.; Rivera III, F.; Lilie, E.; Cottman, M. *J. Org. Chem.* **2012**, 78, 238-245.

60. Swartz, C.R.; Parkin, S.R.; Bullock, J.E.; Anthony, J.E.; Mayer, A.C.; Malliaras, G.G. Org. Lett. **2005**, 7, 3163-3166.

61. Kitamura, C.; Taka, N.; Kawase, T. *Res. Chem. Intermed.* **2013**, 39, 139-146.

62. Sanders, S.N.; Kumarasamy, E.; Pun, A.B.; Trinh, M.T.; Choi, B.; Xia, J.; Taffet, E.J.; Low, J.Z.; Miller, J.R.; Roy, X.; Zhu, X.Y. *J. Am. Chem. Soc.* **2015**, 137, 8965-8972.

Chapter 3: On the Origin of the Red-Shifted Optical Spectra Recorded for aza-BODIPY Dyes

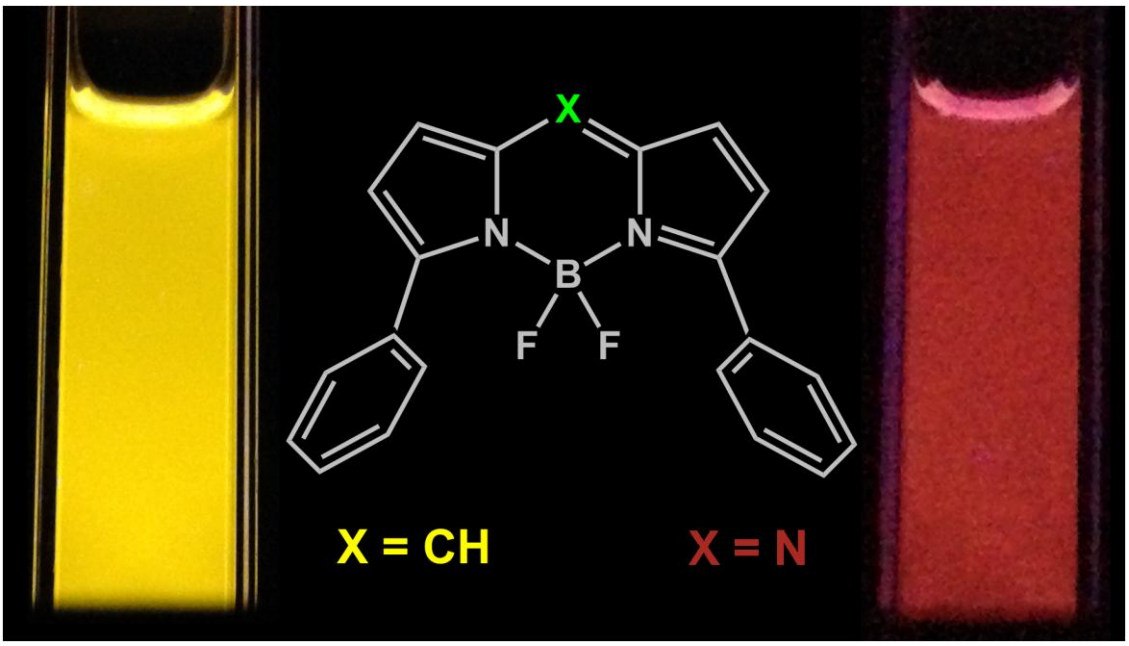

3.1 Introduction

As has been stressed in the main introduction, BODIPY dyes are well established in the scientific literature with their reputation cemented as being highly versatile, small fluorophores suitable for use in a wide range of applications from fluorescent indicators to biological probes.[1,2] Those BODIPY derivatives analogous to the core structure (the unsubstituted parent boron-dipyrromethene core itself being unstable) have absorption/emission maxima centered at approximately 500 nm and a fluorescence quantum yield approaching unity.[3] The optical properties of BODIPY dyes are readily modified by substitution at any position on the dipyrromethene backbone. Those BODIPY derivatives with red-shifted optical properties often have extended π-conjugation where additional aryl or thiophene substituents are present.[4,5] Such a strategy results in a shift towards the near-IR region, but comes with the penalty of a decreased fluorescence quantum yield. The trend is predicted by the energy-gap law since the S_0 to S_1 energy gap is smaller at lower energies of absorption/emission. Furthermore, additional nonradiative pathways are often present resulting from vibrational modes associated with the appended functional groups.

A far less studied class of BODIPY is that possessing an aza-nitrogen at the *meso*-position instead of the *meso*-methine carbon, so called "aza-BODIPY" (aza-difluoroboradiaza-s-indacene).[6,7] It has been reported in the literature that aza-BODIPY dyes possess substantially red-shifted spectra (ca. 100 nm red-shift due to aza-nitrogen alone) in comparison to the corresponding non-aza analogues. The electronic origin of this dramatic red-shift for aza-BODIPY has not been systematically investigated. While numerous aza-BODIPY dyes have been reported, many have extended conjugation due to the presence of ancillary aryl groups attached to the periphery, which contribute to red-shifted absorption/emission spectral profiles. Consequently it is difficult to resolve any spectroscopic shifts arising solely because of the aza-nitrogen atom.

Because of the considerable interest in dyes emitting in the red region, the aza-BODIPY dyes look to be promising candidates for use as bio-conjugate labels. It might be stressed that the red-shifted spectra are not associated with substantial changes in the Stokes' shift. The present study accounts for the origin of the reported optical red-shift for aza-BODIPY through a detailed photophysical investigation of appropriate dyes. The target compounds correspond to two previously reported dyes BOD[8] and aza-BOD[9] (Figure 3.1), which differ only by the presence of aza-N and para-methoxy on the 3,5-phenyl substituents. Steady-state and time-resolved absorption/emission measurements, as well as computer simulations, are the primary means for data acquisition.

Our results reveal that the aza-nitrogen atom has the effect of lowering the energy of the LUMO while having little or no effect on the corresponding HOMO energy. It is also noted that there is a significant decrease in the excited singlet-to-triplet energy gap, but no concurrent enhancement of intersystem crossing to the triplet manifold. The use of dyes emitting in the near-IR region has been discussed previously, indeed a water-solubilized derivative of aza-BOD has been reported[9], a potential probe for fluorescence microscopy. Similar systems have been proposed as near-IR probes and for use as sensitizers for photodynamic therapy.[6,10]

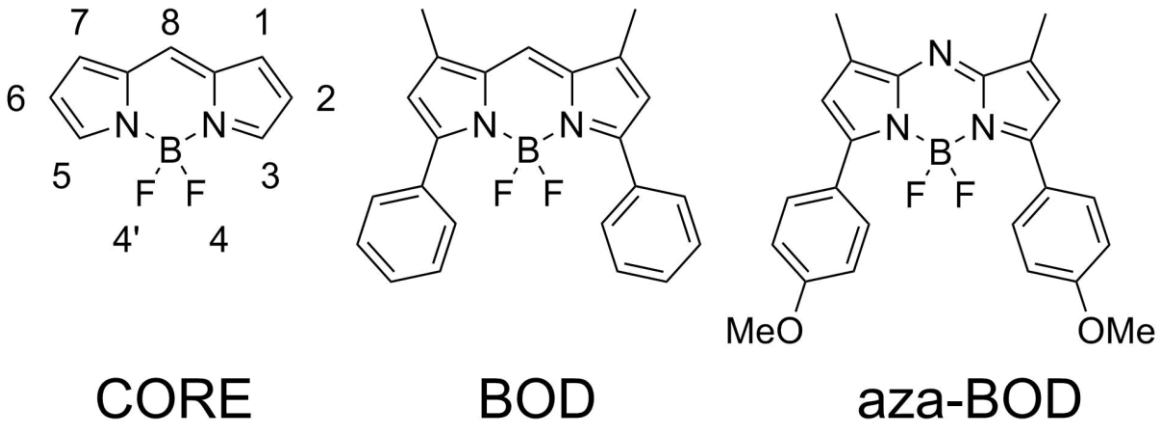

Figure 3.1. Molecular formulae for BODIPY core structure (CORE) and the two derivatives studied here, BOD and aza-BOD.

3.2 Results and Discussion

3.2.1 Steady-State Spectroscopic Measurements

The room temperature optical properties recorded for both the aza-BODIPY dye and the corresponding non-aza analogue (henceforth referred to as aza-BOD and BOD respectively as per Figure 3.1) are summarized in Table 3.1. Both dyes are readily soluble in 2-methyltetrahydrofuran (MTHF), with no evidence of aggregation at the micromolar concentration range, and are highly fluorescent. The most notable result is the 100-nm red-shift observed for aza-BOD. The fluorescence quantum yield for aza-BOD was determined against a fluorescent standard with emission in the same region (*meso*-tetraphenylporphyrin, Φ_F = 0.12 in DMF)[11] and with an appropriate detector (R928 photomultiplier tube). The high fluorescence yield for aza-BOD shows how the absence of multiple flexible substituents around the dipyrromethene core is reflected in the photophysical properties, despite the relatively low emission energy. With BOD and aza-BOD, there are relatively few nonradiative decay pathways brought about by stretching and twisting of styryl and aryl groups seen in other near-IR absorbing BODIPY derivatives.[12] Room temperature absorption and fluorescence for the two compounds is depicted in Figure 3.2.

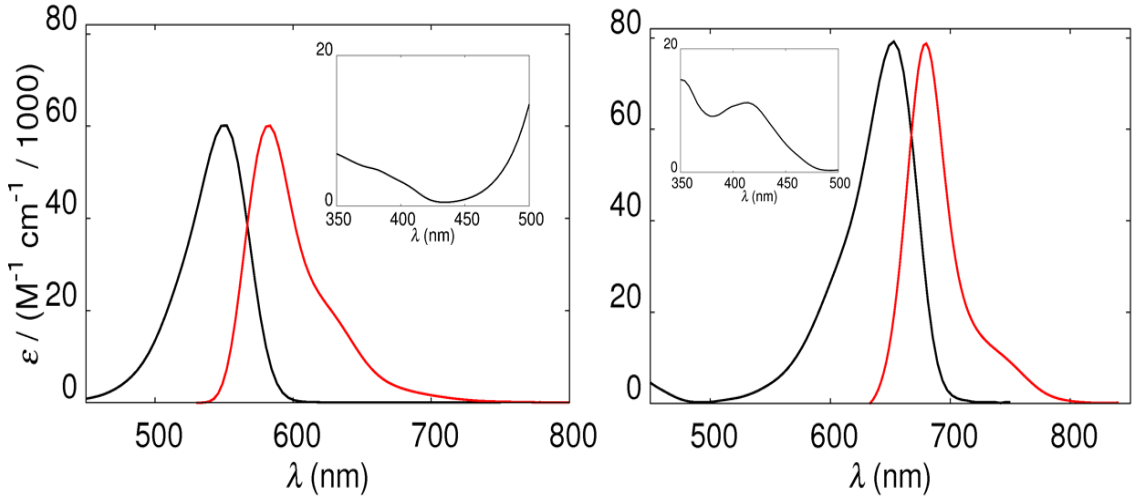

Figure 3.2. Normalized room temperature absorption and emission spectra for BOD (left panel) and aza-BOD (right panel) in MTHF. The insets emphasize absorption features in the UV-region.

Table 3.1. Compilation of the spectroscopic properties recorded for the target dyes in MTHF at ambient temperature.

Property	BOD	aza-BOD
λ_{MAX} / nm	549 ± 1	651 ± 1
ε_{MAX} / $M^{-1}cm^{-1}$	62,100 ± 5,000	81,000 ± 7,000
f [(a)]	0.50 ± 0.04	0.58 ± 0.06
λ_{FLU} / nm	585 ± 3	680 ± 3
Φ_F	0.92 ± 0.05	0.95 ± 0.05
τ_S / ns	6.6 ± 0.2	4.3 ± 0.2
E_{SS} / cm^{-1} [(b)]	585 ± 25	395 ± 15
k_{RAD} / 10^7 s^{-1} [(c)]	13 ± 2	7.0 ± 1
S [(d)]	0.20	0.12
ν_M / cm^{-1}	1,050 ± 200	1,375 ± 150
ν_L / cm^{-1}	530 ± 100	570 ± 100
k_{NR} / 10^7 s^{-1}	1.2 ± 0.2	1.2 ± 0.2

(a) Oscillator strength calculated for the lowest-energy absorption transition; (b) Stokes' shift calculated after deconstruction of the absorption and emission spectra into Gaussian components; (c) Radiative rate constant calculated from the Strickler-Berg expression; (d) Huang-Rhys factor calculated from fitting the low-temperature emission spectrum to a series of five Gaussian components.

Time-resolved fluorescence decay curves are mono-exponential for both dyes and there is very good agreement between absorption and excitation spectra. The derived radiative rate constants (k_{RAD}) are in reasonable agreement with those calculated on the basis of the Strickler-Berg expression[13] (Table 3.1). Note that k_{RAD} found experimentally for aza-BOD is relatively high for a BODIPY dye (22 x 10^7 s^{-1}) especially when taking into consideration the low energy of the fluorescence transition. Nonradiative decay, as characterized by the corresponding rate constant ($k_{NR} = \frac{1-\Phi_F}{\tau_{S1}}$), does not make a significant contribution to the overall excited-state deactivation under these conditions.

An additional nonradiative decay pathway can be introduced for aza-BOD when a hydrogen-bonding solvent is present. Thus, when ethanol was added as a co-solvent at varying mole fractions in chloroform, the fluorescence yield clearly decreased with increasing amount of the alcohol. Where the fluorescence yield in pure chloroform is

0.94, this decreases progressively to 0.60 in pure ethanol. This is matched with a shorter fluorescence lifetime for aza-BOD in C_2H_5OH and CH_3OH (τ_S = 3.5 ± 0.2 ns). The apparent trend in fluorescence yield is suggestive of the involvement of a high-energy vibronic mode due to the N-H stretching vibration where hydrogen bonding occurs at the *meso*-nitrogen atom. The effect is the same in water. The presence of hydrogen bonding will be corroborated later by way of spectral deconstruction, fluorescence anisotropy and experiments involving fluorescence recovery after photobleaching.

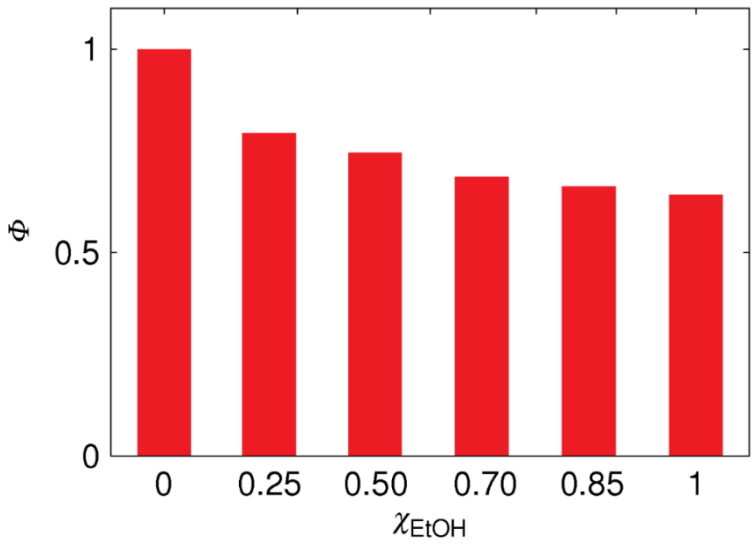

Figure 3.3. Relative fluorescence quantum yields recorded for aza-BOD in chloroform at room temperature as a function of the mole fraction χ of added ethanol.

The absorption and emission spectra recorded for BOD and aza-BOD can be deconstructed into a minimum of five Gaussian-shaped components of common full-width at half-maximum (fwhm). Examples of such deconstructions are show in Figure 3.4 for spectra obtained at 77K in a rigid MTHF glass, due to the better resolved vibrational fine structure seen at lower temperature. From the relevant spectra, we note there are a number of vibronic satellites at higher energies. There are also weaker transitions seen in the UV-region of the absorption spectrum. Estimation of the Stokes' shift (E_{SS}) is also possible as a result of the spectral deconstruction of the room temperature absorption and fluorescence since the energy of the 0-0 transition is defined more clearly. Stokes' shifts for both compounds are relatively small, indicating only minor structural distortions following excitation. We also obtain an accurate estimate for the red-shift between BOD and aza-BOD, this now being refined as 2,855 cm^{-1}.

Table 3.2. Energies and relative weightings of the Gaussian components used to reconstruct the emission spectra of aza-BOD (left) and BOD (right). These data correspond to Figure 4.

# Gaussian	λ_{max} / cm^{-1}	Rel. Area
1	12631	0.01
2	13160	0.04
3	13545	0.05
4	14006	0.10
5	14576	0.81

# Gaussian	λ_{max} / cm^{-1}	Rel. Area
1	15695	0.02
2	15974	0.06
3	16318	0.07
4	16745	0.14
5	17273	0.71

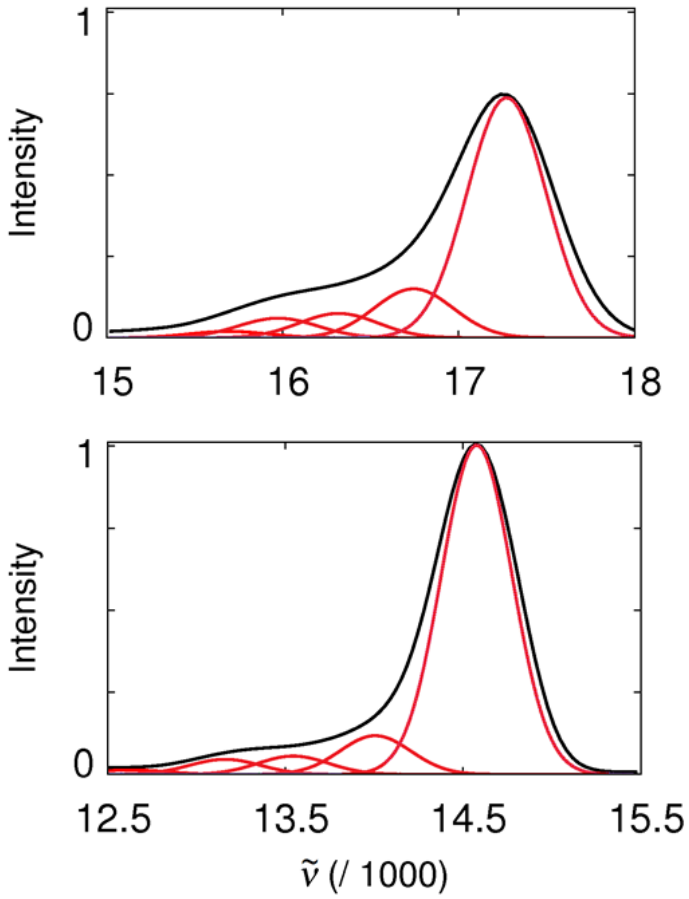

Figure 3.4. Low-temperature emission spectra in MTHF for BOD (top panel) and aza-BOD (lower panel) overlaid with the minimum number of Gaussian components necessary to fully reconstruct the spectrum.

The spectral deconstruction analysis detailed above gives a quantitative description of those vibronic modes which accompany nonradiative deactivation of the excited state. This also allows for calculation of the Huang-Rhys factor[14] (S-factor), which provides a measure of the strength of electron-phonon interactions and of the displacement between potential energy surfaces for the respective electronic states.[15] A higher S-factor is indicative of more displacement between potential energy surfaces for ground- and excited states[16], and hence a larger Stokes' shift. The S-factor derived for aza-BOD at 77K (Table 3.2) is smaller than that for BOD, although both values are small and are indicative of π,π^* transitions in conjugated systems.[17] A smaller S-factor is also consistent with more extended π-conjugation.[18] Indeed this corresponds to the observed red-shift seen for aza-BODIPY. At room temperature, the S-factor for aza-BOD increases to 0.26 which would be consistent with the greater degree of rotational freedom of the aryl substituents present on the BODIPY nucleus.

It is clear that the Gaussian components derived for BOD (FWHM = 965 cm^{-1}) are broader than those for aza-BOD (FWHM = 770 cm^{-1}). In both cases, spectral reconstruction requires the introduction of low- (ν_L) and medium-frequency (ν_M) modes. The low energy modes can be assigned to structural distortions of the dipyrrin backbone. High energy modes can be accounted for by stretching of C=C and C=N bonds during relaxation. The values of the vibronic transitions derived from the Gaussian contributions can be referenced against typical infrared absorption frequencies in organic compounds.[19] One noteworthy difference in the vibronic progression seen with aza-BOD is a vibronic mode with a frequency of 1375 cm^{-1}. The corresponding mode in BOD is 1050 cm^{-1}. This difference could be rationalized as a difference in the way the dipyrrin backbone distorts in the two dyes. The higher frequency mode for aza-BOD would fall in the region associated with a C-N stretch, implying that aza-BOD has a slightly buckled backbone. The corresponding lower frequency mode in BOD is more suggestive of an alkene bending mode.[19] The buckling of the dipyrrin unit in aza-BOD supports quantum chemical geometry calculations discussed later in this chapter.

Implementing the same spectral analysis for aza-BOD dyes in methanol, one can observe a high frequency mode of ca. 3100 cm^{-1}. This feature can most probably be assigned to an N-H stretch associated with specific hydrogen bonding to the *meso*-nitrogen atom. This coincides with the moderate decrease in the fluorescence quantum yield and excited singlet lifetime noted above. Recovering the absorption and fluorescence spectra for aza-BOD in deuterated methanol, and once again implementing spectral deconstruction using the same parameters, there is little change in vibronic progression but the fluorescence lifetime of aza-BOD in deuterated methanol-D1 is 4.2 ± 0.2 ns. This increase in fluorescence lifetime for the deuterated solvent can be accounted for with a contribution from a lower frequency N-D stretching mode relative to an N-H stretch (one would expect the N-D stretch to have a frequency of approx. 2100-2600 cm^{-1}).[20] The absence of a perceivable change in the optical spectra of aza-BOD on moving to a deuterated solvent is consistent with this hypothesis. Moreover, the isotope effect on the fluorescence lifetime provides strong evidence for the notion of selective hydrogen bonding.

3.2.2 Stability Against Photobleaching

Photostability of organic dyes is of major concern for all compounds proposed for use in applications such as solar cells, laser dyes and fluorescent probes.[21,22] The photostabilities of BOD and aza-BOD were tested in solution under steady-state illumination with light at wavelengths longer than 495 nm for BOD or 550 nm for aza-BOD. The photobleaching kinetics were monitored by recording absorption spectra at regular time intervals. After 6 hours continuous irradiation with a 400 W floodlamp positioned 85 cm from a solution of the dye in a cuvette, approximately 30% loss of the aza-BOD chromophore in de-aerated N,N-dimethylformamide solution was recorded. Under comparable conditions, illumination of BOD for more than 12 hours caused no significant (i.e., <5%) bleaching of the sample. The presence of oxygen did not have an appreciable effect on the rate of photobleaching in either case. The bleaching process follows first-order kinetics (Figure 3.5), but does not lead to products detectable by UV-visible absorption measurements. Light intensities at the two excitation regions are comparable.

There is no recovery of a partially bleached sample upon standing in the dark. Somewhat related aza-BODIPY dyes were found to exhibit similar levels of photoactivity in deaerated solution and it is clear that these compounds possess reasonably good levels of photostability; bleaching is too inefficient for quantum yield measurements. The aza-N atom therefore appears to weakly promote instability under continuous illumination with visible light.

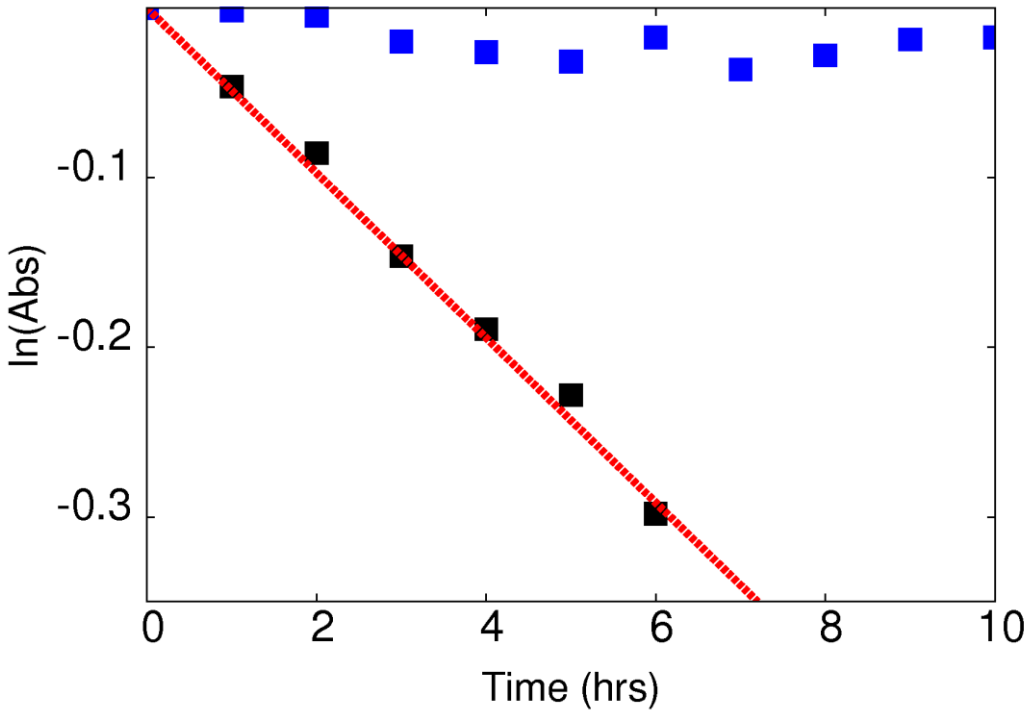

Figure 3.5. Plot showing steady-state photobleaching of BOD (blue squares) and aza-BOD (black squares) monitored with absorption spectroscopy. The red line represents a fit assuming first order kinetics for aza-BOD predicting a rate constant for photobleaching of 6.0 x 10^{-7} M h^{-1} ± 10%.

3.2.2 Characterization of the aza-BODIPY Triplet

BODIPY dyes are not normally known for having any appreciable yield of intersystem crossing into the triplet manifold. This is also the case for BOD and aza-BOD due to their high fluorescence quantum yields. It is possible, however, to induce transitions to the triplet state by promotion of intersystem crossing using an external heavy atom.[23] Some similar compounds in the literature have employed this as an internal effect, by attaching iodine or bromine substituents to the BODIPY core, in which case triplet yields usually increase.[24,25] To have a more complete description of the photophysics of aza-BODIPY, it seems appropriate to characterize the triplet state.

Nanosecond transient absorption measurements of aza-BOD in deoxygenated dimethylsulfoxide (Figure 3.6) gave no detectable triplet signal upon excitation at 610 nm. On addition of 20% v/v iodomethane, however, a transient absorption signal centred at 660 nm was observed and assigned to the triplet (T_1-T_0) transition. This transient signal corresponded to a first-order bleaching of the ground state with a lifetime of 6.0 ± 1.2 μs. Upon aeration of the same sample, the lifetime fell to 1.2 ± 0.06 μs. Aza-BOD in MTHF solution containing 50% v/v iodomethane also produced the same transient signal with a lifetime of 1.20 ± 0.06 μs. The triplet energy was confirmed by detection of very weak phosphorescence at 77 K, again in the presence of iodomethane, with an emission maximum located at 775 nm.

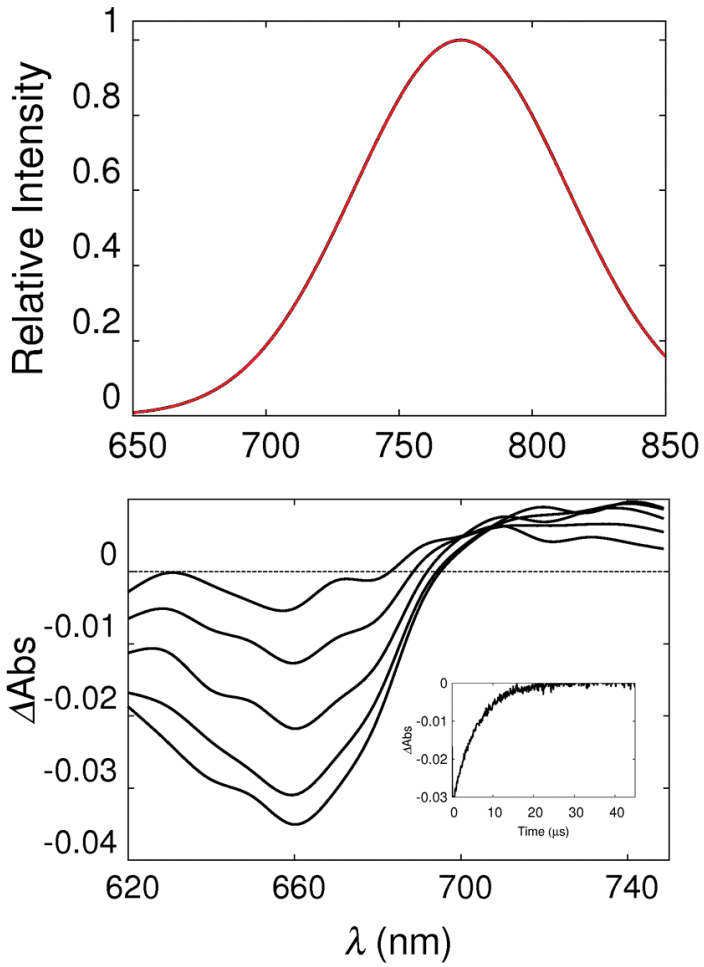

Figure 3.6. Upper panel: Phosphorescence spectrum recorded for aza-BOD at 77K in an ethanol glass containing 20% v/v iodomethane. Lower Panel: Transient absorption spectra recorded for aza-BOD in MTHF containing 20% v/v iodomethane with laser excitation at 610 nm. The time resolved spectra were recorded at delay times of 1, 2, 10 and 20 μs. The inset shows a typical kinetic trace recorded at 650 nm.

Based on the fact that phosphorescence was detected corresponding to the transient absorption signal at 660 nm, which is sensitive to the presence of oxygen as well as external heavy atom perturber, it is reasonable to associate these measurements with the triplet. The observed triplet energy is approximately 1.6 eV (i.e. 12,900 cm^{-1}), therefore the singlet to triplet S_1-T_1 energy gap is determined to be 1,800 cm^{-1}. The corresponding triplet energy for non-aza BODIPY is very hard to determine due to the lack of intersystem crossing, but has been reported in the literature with phosphorescence emission at ca. 750 nm.[26] Therefore the S_1-T_1 energy gap is significantly smaller in aza-BOD, yet there is no appreciable enhancement of the rate of intersystem crossing in the absence of spin-orbit coupling.

3.2.4 Anisotropy Data and Fluorescence Recovery after Photobleaching

The steady-state fluorescence anisotropies for both BOD and aza-BOD were determined in glycerol between 20 and 60 °C.[27] Results obtained from the fluorescence depolarization measurements are summarized in Tables 3.3 and 3.4. The anisotropy <r> is defined by Equation 3.1. Here $I_{\|}$ is fluorescence intensity with excitation and emission polarizers parallel to each other while $I_{\perp}$ refers to the fluorescence intensity with the excitation polarizer horizontal and the emission polarizer vertical. The term G represents a correction factor for bias in the detector.

$$< r > = \frac{I_{\|} - GI_{\perp}}{I_{\|} + 2GI_{\perp}} \qquad (3.1)$$

The time it takes for the fluorophore to tumble in the solvation sphere, the reorientation time τ_R, can be derived from Equation 3.2. Where the fluorescence decay is a single exponential, τ_f is the fluorescence lifetime, r the anisotropy and the limiting anisotropy r_0 in a frozen solution. The limiting anisotropy was derived from the temperature dependence of the steady-state anisotropy, which displayed a linear relationship.

$$\tau_R = \frac{\tau_f}{[(r_0/< r >) - 1]} \qquad (3.2)$$

Given the structural similarities of the two fluorophores, the hydrodynamic radius of the molecule can be considered the same for both emitters. Despite this, there was a marked difference in the recorded fluorescence anisotropy. At room temperature, BOD had a measured anisotropy of 0.24 whereas for aza-BOD it was 0.29. Higher anisotropy values are associated with slower fluorescence depolarization (i.e., a slower molecular reorientation time).[28] The result here is consistent with aza-BOD undergoing hydrogen bonding to the glycerol solvent, effectively increasing the volume of the tumbling chromophore and thereby resulting in a slower reorientation time.

Table 3.3. Steady-state fluorescence anisotropy data for BOD in glycerol.

Temperature / ^{o}C	Anisotropy <r>	Viscosity of Glycerol / Pa s	Reorientation Time τ_R / ns	Error / %
20	0.24	1410	12.3	0.2
25	0.23	949	10.8	0.5
30	0.21	612	8.9	0.5
35	0.19	403	7.2	0.5
40	0.17	284	5.5	1.0
45	0.14	192	4.1	0.8
50	0.11	142	2.8	1.2
55	0.08	121	1.9	1.7
60	0.06	81	1.2	1.8

Table 3.4. Steady-state fluorescence anisotropy data for aza-BOD in glycerol.

Temperature / ^{o}C	Anisotropy <r>	Viscosity of Glycerol / Pa s	Reorientation Time τ_R / ns	Error / %
20	0.29	1410	16.8	2.2
25	0.28	949	13.4	1.9
30	0.27	612	10.9	3.3
35	0.25	403	8.90	3.6
40	0.23	284	7.2	2.5
45	0.21	192	5.7	2.4
50	0.20	142	5.2	2.6
55	0.18	121	3.8	3.0
60	0.16	81	3.3	3.4

The same trend can be observed from complementary experiments made using a fluorescence microscope. Here, the technique is known as fluorescence recovery after photobleaching (FRAP).[29] An intense laser beam suitable for exciting the sample causes permanent photobleaching of a small volume of sample under the microscope, allowing the time taken for the recovery of fluorescence into that spot to be monitored. Recovery of the fluorophores into the bleached spot occurs by one of two processes, flow and diffusion. Although the technique is more commonly used for determining whether fluorophores are immobilized in living cells, bleaching a spot in viscous media will allow the determination of the diffusion coefficient D using Equation 3.3.[30,31]

$$D = \frac{\omega^2 \gamma}{4 t_{1/2}} \qquad (3.3)$$

Here ω refers to the bleaching radius while γ is a correction factor for the amount of photobleaching. The bleaching radius can be determined directly from the instrument. We can set $t_{1/2}$ as being the half-life taken for full recovery of the steady-state fluorescence (obtained from a simple three-point fit of the FRAP trace (Figure 3.7)). The assumption for these measurements is that the primary process of fluorescence recovery is due to diffusion into a two-dimensional disc with an area corresponding to the laser spot incident on the sample. Since the two dyes are studied in the same medium and the bleaching spot size is the same, this allows for a valid comparison of the two (flow is proportional to ω and diffusion proportional to ω^2). In these calculations, γ is taken as 0.88 for a circular, Gaussian laser beam.[31] Under standard experimental conditions, the derived diffusion coefficient is 0.32 μm^2 /s for aza-BOD where the equivalent value is 1.23 μm^2 /s for BOD. The perceived anisotropy in the diffusion of the two fluorophores can be rationalized in terms of hydrogen bonding to the solvent, which is consistent with the steady-state fluorescence anisotropy data.

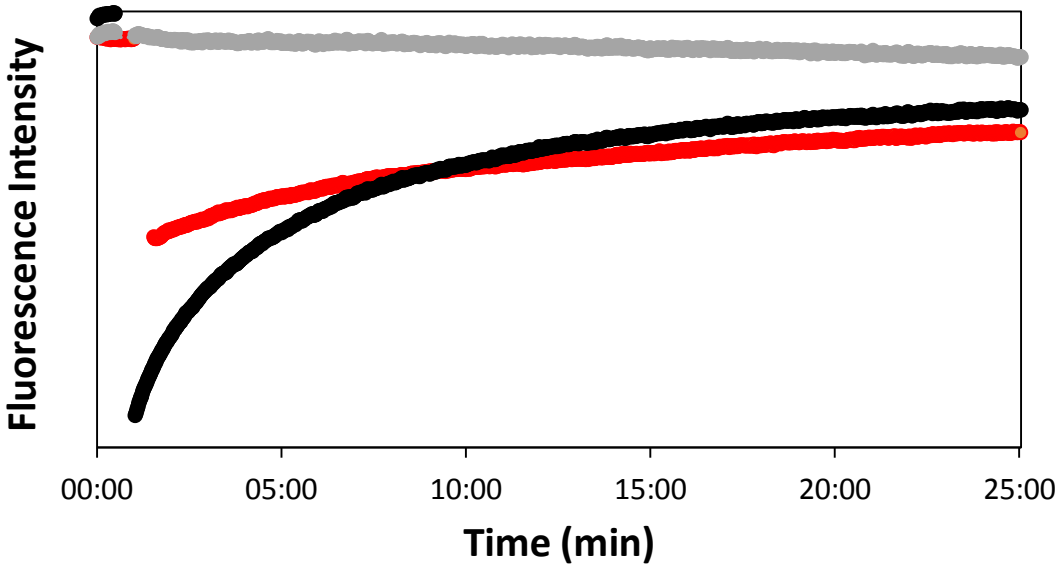

Figure 3.7. FRAP experimental traces for BOD (black trace) and aza-BOD (red trace). A reference area of the sample is also tracked during the experiment to reflect the change in intensity of fluorescence outside the area of photobleaching.

3.2.5 Quantum Chemical Calculations

Quantum chemical calculations were performed in order to clarify the apparent differences in HOMO, LUMO and triplet energies for the two BODIPY dyes. Density functional and time-dependent density functional theory calculations were performed using a 6-31G(d) basis set with the CAM-B3LYP functional. The results are summarized in Table 3.5. The data presented here illustrate a consistent trend in excited state properties in general agreement with the prior experimental measurements.

Table 3.5. Summary of the structural data derived from computer modelling of the target compounds in a solvent reservoir having a dielectric constant of 10.

Property	BOD	aza-BOD
λ_{MAX} / nm	533	619
f	0.51	0.47
μ_{TD} / D	2.6	2.29
$S_0 \rightarrow T_1$ / nm	790	855
E_{HOMO} / eV	-5.46	-5.31
E_{LUMO} / eV	-3.19	-3.45
C-X-C / $^{0\,(a)}$	121.6	120.1
N-B-N / $^{0\,(b)}$	110.1	108.5
F-B-F / $^{0\,(c)}$	104.8	105.1
N-C-aryl / $^{0\,(d)}$	59	54
C-X / Å	1.389	1.332
N-B / Å	1.564	1.570
X-B / Å $^{(e)}$	3.031	3.029
B-F / Å	1.380	1.377
C_1-C_7 / Å $^{(f)}$	5.921	5.696

(a) Angle around the meso-site. (b) Angle around the boron atom. (c) Angle around the F-B-F unit. (d) Dihedral angle between the dipyrrin unit and the appended aryl ring. (e) Distance between the meso-atom (C or N) and the boron atom. (f) Distance between the methyl C atoms appended at the 1,7-positions.

The geometries of the two molecules show some consistent differences, namely in the fact that BOD is apparently a more planar molecule than is aza-BOD. With a dihedral angle of 59^0 for the 3,5-appended aryl groups for BOD, it is necessary for the dipyrrin backbone to distort. This is because there is a rotational barrier (E_0) for reaching the

planar structure, which amounts to 15.9 kcal/mol, arising from repulsion between the *ortho*-H atom on the rotor and a fluorine atom (Figure 3.8). For both molecules there is an additional barrier of ca. 1.5 kcal/mol at 90^0 due to the loss of π-electron delocalization when the aryl substituents are orthogonal to the dipyrrin unit. The 4-methoxy substituent makes a small contribution to the disparity in rotational barriers noted between BOD and aza-BOD. The corresponding aza-BODIPY lacking this substituent exhibits E_0 and E_{90}, respectively, of 12.6 and 0.90 kcal/mol. Simulations of the unsubstituted aza-BODIPY show a slightly higher dihedral angle and at a value of 56^0, than found for aza-BOD (Table 3.5). Overall there is no clear structural feature accounting for the 4-methoxy substituent, suggesting an electronic effect has role.[32,33]

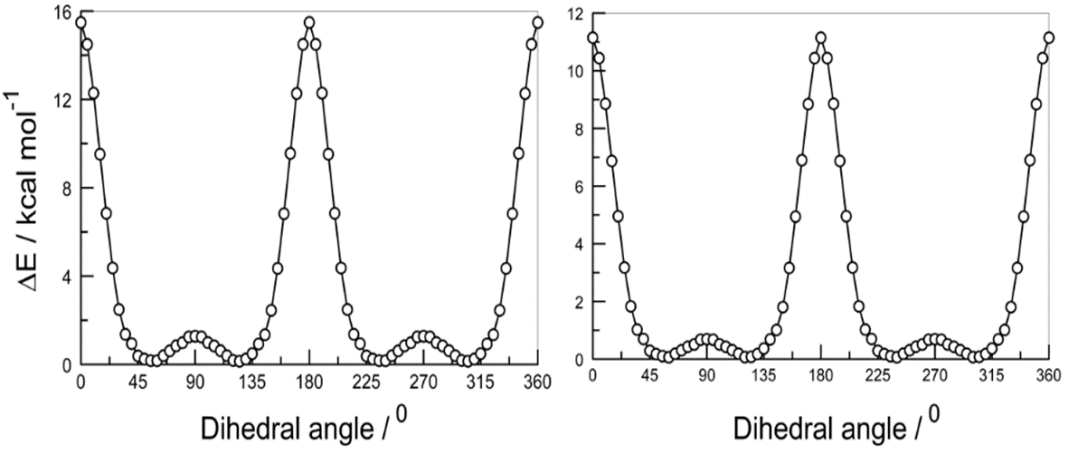

Figure 3.8. Effect of dihedral angle on the total energy calculated for ground state BOD (left panel) and aza-BOD (right panel) in a solvent reservoir with dielectric constant equal to 10.

The energy-minimized structure calculated for aza-BOD also shows a slightly distorted dipyrrin nucleus with a smaller bite angle around the aza-N atom. Insertion of the aza-N leads to a reduction in the overall length of the dipyrrin upper rim. This distortive effect can be illustrated by comparing the distances between the carbon atoms on C1 and C7 appended methyl groups; the distance being reduced from 5.92 Å for BOD to only 5.70 Å for aza-BOD (Table 3.5). This observation is possibly supported by an associated C-N vibrational mode seen in the deconstructed spectra for aza-BOD (see earlier). The geometry around the boron atom shows a greater N-B-N angle for BOD. The mean dihedral angle for the 3,5-aryl substituents is marginally smaller for aza-BOD but for aza-BOD there are reduced barriers for ring rotation (E_0 = 11.2 kcal/mol; E_{90} = 0.70 kcal/mol)

(Figure 3.8). The variations in barrier energies are likely due to the change of geometry in the dipyrrin unit brought about by replacing C-H with N at the *meso* site. The larger C-X-C and N-B-N angles seen for BOD stretch the molecule down the longest axis and result in changes to the 3,5-aryl substituent rotational barriers. For aza-BOD, the F-H distances are elongated relative to BOD, with values of 1.787 and 1.897 Å, respectively, but again the dipyrrin unit has to distort in order to accommodate this structure.

The dihedral angles about the 3,5-aryl groups likely play an important role in determining the absorption and emission maxima of the two BODIPY dyes. Aza-BODIPY dyes having constrained aryl groups at the 3,5-positions, i.e. dihedral angles are close to zero, are known to have further red-shifted absorption and fluorescence transitions.[12] This observation follows on with the calculated HOMO-LUMO energy gap, which has been observed to be sensitive to the size of the dihedral angle in comparable dyes.[34-36]

Far more than any other feature in aza-BOD, the aza-N atom has a large effect on the energies of both the LUMO and the HOMO (Table 3.5). In aza-BOD, the HOMO-LUMO energy gap is reduced to 1.86 eV, corresponding to an optical transition of 665 nm, which is very close to the experimental value. It is therefore the main conclusion here that the red-shifted absorption and fluorescence are as a consequence of the effect of the aza-N atom on the HOMO and LUMO energies. To a far lesser extent, the difference in dihedral angle of the 3,5-aryl substituents contributes to the red-shift. This effect is quite subtle since the dihedral angle for the aryl rings is reduced only from 59^0 to 54^0.

Figure 3.9 shows how the energy of the HOMO and LUMO in BOD change as a function of the dihedral angle of the 3,5-aryl substituents. These simulations culminate in the energy-minimized geometry computed HOMO-LUMO energy gap as being 2.27 eV, corresponding to an optical transition of 546 nm. This is in excellent agreement with experimental observations and shows that an appreciation of planarity in aryl substituted BODIPY dyes is important in predicting the optical properties. It is notable that for aza-BOD the dihedral angle has more effect on the HOMO than on the LUMO energy. The angular effect on the HOMO energy is greatly enhanced for aza-BOD compared to BOD. The LUMO energy varies in a similar fashion for the two compounds.

For aza-BOD, the effect of increased planarity noted for aza-BOD corresponds to a red-shift of ca. 10 nm.

Calculations were also performed for the aza-BODIPY derivative lacking the 4-methoxy substituents. The resulting HOMO and LUMO at the energy-minimized geometry were found to be -5.45 and -3.52 eV, respectively. The HOMO-LUMO energy gap (ΔE = 1.93 eV) corresponds to an optical transition of 643 nm. Therefore, we can conclude that the 4-methoxy groups contribute a red-shift of around 22 nm. The effect of the dihedral angle (Figure 3.9) on the HOMO and LUMO energies follows the pattern established for aza-BOD, again the effect on the HOMO energy dominating over the LUMO.

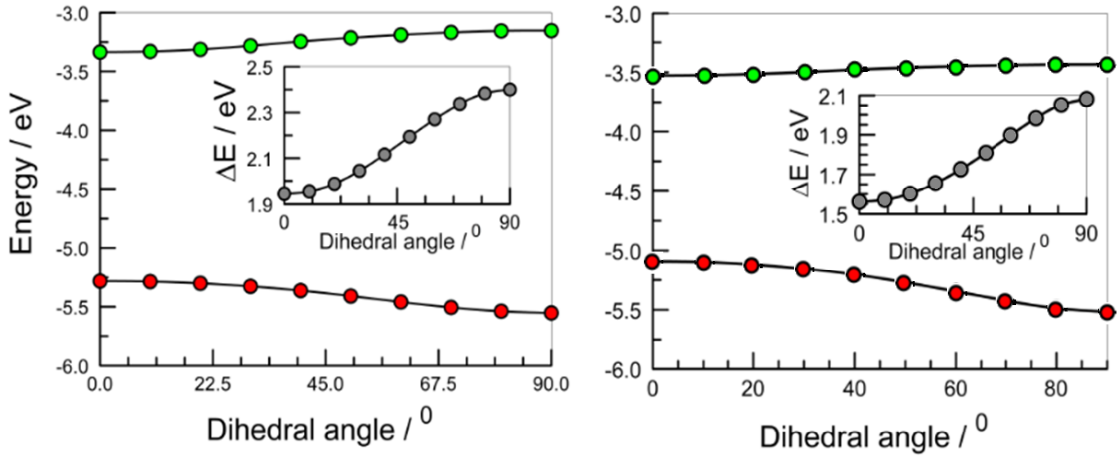

Figure 3.9. Left panel: effect of dihedral angle on the calculated energies of the LUMO (green points) and HOMO (red points) for BOD. The inset shows the calculated HOMO-LUMO energy gap (in units of eV) as a function of the same dihedral angle range. Same scheme for aza-BOD.

Kohn-Sham contour plots[37] indicate that the electronic distributions for the HOMO and LUMO for BOD are centred mainly on the BODIPY nucleus. For both dyes, a fraction of the overall distribution is off-loaded to the appended aryl rings at the energy-minimized configuration (Figure 3.10). It is also apparent that the influence of the *meso*-site plays little role in the HOMO (E_{HOMO}), but is important for the LUMO (E_{LUMO}). This is the case whether there is a methine-carbon or aza-nitrogen at the *meso*-position. With the 4-methoxy substituent present on aza-BOD there is a lowering of the E_{HOMO}, but in contrast little effect on the E_{LUMO}. Also the HOMO of aza-BOD has more electron density drawn to the aryl substituents. As was pointed out above, altering the dihedral angle of

the 3,5-aryl substituent mainly effects E_{HOMO}. This highlights the role of various substituents in fine-tuning orbital energies in BODIPY.

Comparison of the calculated orbital energies with electrochemical measurements was not possible because some of the electrochemical processes were irreversible. For BOD, there is a reversible, one-electron oxidation step ($E_{1/2}$ = 1.11 V vs SCE). The corresponding one-electron reduction step is electrochemically irreversible in CH_2Cl_2 and shows a peak potential of -0.98 V vs SCE. Electrochemical measurements with aza-BOD under identical conditions, show a reversible, one-electron reduction ($E_{1/2}$ -1.00 V vs SCE), but oxidation involves an irreversible, two-electron step.

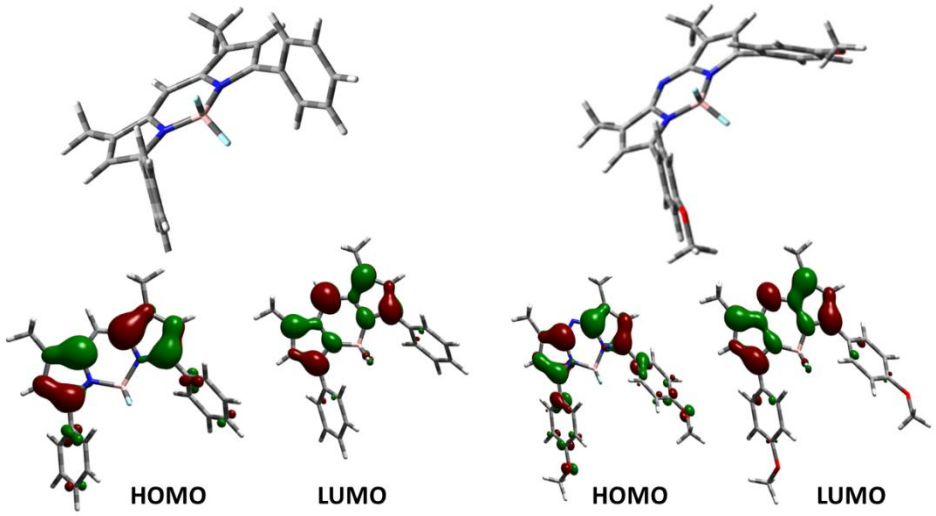

Figure 3.10. *Optimized geometries and HOMO/LUMO Kohn-Sham distributions for BOD (left) and aza-BOD (right).*

TD-DFT calculations show that the potential energy surfaces of the triplet-excited states are similar to those derived for the corresponding ground states. For the S_1 surface, the aryl rings are more planar with the dipyrrin unit by ca. 5^0 and there are slight changes in geometry around the *meso*-site (Table 3.6). At room temperature (k_BT = 208 cm^{-1}), an exciton at the S_1 level can sample a wide variance in dihedral angle for aza-BOD, with a high fraction being able to traverse the barrier (E_{90} = 245 cm^{-1}) for reaching the perpendicular geometry. Due to the higher energy barrier for rotation of the aryl substituents noted earlier for BOD (E_{90} = 455 cm^{-1}), the S_1 excited BOD has less of a chance to change geometry. This might explain the observation that under cryogenic

conditions aza-BOD undergoes a red-shift whereas BOD exhibits a small blue-shift on cooling to this temperature.

The final set of calculations address the S_1-T_1 energy gap. It is clear that the relatively small S_1-T_1 gap is a feature brought about by introducing the aza-nitrogen. Table 3.6 summarizes the structural parameters of the two dyes at the triplet state level. Indeed, manipulating the S_1-T_1 energy gap is an important design consideration for other photophysical processes such as delayed fluorescence and singlet fission.[38] An aza-derivative of pentacene has been considered as a singlet fission compound.[39] Some compounds in the literature show a similar decrease in the S_1-T_1 gap due to insertion of an aza-nitrogen atom. For example, phosphorescence from the N,N'-diazapyrenium dication occurs some 15-nm to the blue compared[40] to pyrene. The S_0-T_1 absorption transition computed[41] for zinc(II) tetraazaporphyrin lies 0.07 eV to the blue of that calculated for zinc(II) porphyrin.

Table 3.6. Structural parameters calculated for the target dyes at the ground state and excited state levels. Calculations in a solvent reservoir with dielectric constant of 10.

Parameter	**BOD (S_0)**	**BOD (S_1)**	**BOD (T_1)**	**aza-BOD (S_0)**	**aza-BOD (S_1)**	**aza-BOD (T_1)**
C-X-C / ^{0}	121.6	121.7	119.2	116.2	119.6	116.8
N-B-N / ^{0}	110.1	109.1	107.7	108.3	107.3	106.0
F-B-F / ^{0}	104.8	106.8	106.7	105.3	107.1	107.2
N-C-Ph / ^{0}	59.3	55.4	60.2	54.1	52.0	57.3
C-X / Å	1.398	1.389	1.403	1.332	1.330	1.364
N-B /Å	1.564	1.572	1.573	1.570	1.575	1.578
B-F / Å	1.380	1.373	1.372	1.377	1.370	1.369
X-B / Å	3.002	3.034	3.034	3.030	3.045	3.077
C_1-C_7 / Å	5.921	5.932	5.930	5.700	5.701	5.697

The S_1-T_1 energy gap is related to the extent of HOMO-LUMO spatial separation[42], which sets the mutual overlap and corresponds to twice the electron exchange energy.[43] A greater overlap of HOMO and LUMO and a smaller spatial separation leads to an increase in the S_1-T_1 energy gap. Qualitatively speaking we can see from Figure 3.10 that a greater portion of the HOMO in aza-BOD is directed to the 3,5-aryl substituents, lowering the effective HOMO-LUMO overlap while simultaneously increasing their separation. Turning this concept into a quantitative description is difficult due to the lack of computational tools for the task. Transition density cube methodology has been

offered as a promising solution[44], but more work is required to refine such concepts. Despite lacking quantitative information on the HOMO-LUMO separation, it appears likely that the change in orbital overlap between HOMO and LUMO accounts for the decrease in the S_1-T_1 energy gap reported for aza-BOD.

3.3 Conclusions

The present study has systematically evaluated the photophysical properties of a BODIPY dye against an aza-BODIPY analogue in an attempt to account for the large red-shift in optical properties brought about by substituting aza-nitrogen at the *meso*-position of the BODIPY core. The predominant cause for the reported red-shift is attributed to an effect of the aza-nitrogen atom on the LUMO energy and that the 3,5-aryl substituents present in both dyes orient themselves in a way which has a bearing on the HOMO-LUMO energy gap. It is noted that the 4-methoxy substituents present in aza-BOD but not BOD has an effect on the overall spectral red-shift, but the effect can be delineated from contributions due solely to the aza-nitrogen atom by way of computational methods. The presence of these substituents highlights the subtleties in fine-tuning the optical properties of aza-BODIPY, particularly by affecting the dihedral angle of the dipyrrin core and and any appended aryl-groups.

It is important to note the decrease in S_1-T_1 energy gap observed for aza-BOD, which does not correspond with an in increase in triplet yield. The role of hydrogen bonding to the *meso*-N atom in aza-BOD was highlighted. From the perspective of applying the dye in bio-medicinal applications, say as a probe for fluorescence microscopy, it presents a potential obstacle. This is because the resultant N-H hydrogen bond activates nonradiative decay in accordance with the Englman-Jortner energy-gap law.[45] The detrimental effect of this hydrogen bonding should not be over-emphasized on the other hand, since aza-BOD is exceptionally fluorescent for a dye emitting in the red and the dye remains relatively fluorescent in the presence of mildly hydrogen bonding solvents such as methanol and ethanol.

Strategies for inhibiting hydrogen bonding at the aza-nitrogen could be implemented to eliminate this problem. This might be accomplished by adding bulky substituents at the 1,7 positions. The diminished fluorescence due to hydrogen bonding to aza-nitrogen could also be used to advantage in a probe to detect atomic hydrogen under catalyzed conditions. These dyes remain viable alternatives for applications in fluorescence microscopy and indeed a (poorly) water solubilized version of aza-BOD[9] was measured and shown to have a fluorescence quantum yield of 0.12 in water.

3.4 References

1. Boens, N.; Leen, V.; Dehaen, W. *Chem. Soc. Rev*. **2012**, *41*, 1130-1172.

2. Ulrich, G.; Ziessel, R.; Harriman, A. *Angew. Chem. Int. Ed.* **2008**, 47, 1184-1201.

3. Boyer, J.H.; Haag, A.M.; Sathyamoorthi, G.; Soong, M.L.; Thangaraj, K.; Pavlopoulos, T.G., *Heteroatom Chem.* **1993**, 4, 39-49.

4. Chen, J.; Burghart, A.; Derecskei-Kovacs, A.; Burgess, K. *J. Org. Chem.* **2000**, 65, 2900-2906.

5. Bura, T.; Hablot, D; Ziessel, R. *Tetrahedron Lett.* **2011**, 52, 2370-2374.

6. Zhao, W.; Carreira, E.M. *Angew. Chem. Int. Ed.* **2005**, 44, 1677-1679.

7. Gresser, R.; Hummert, M.; Hartmann, H.; Leo, K.; Riede, M. *Chem. Eur. J.* **2011**, 17, 2939-2947.

8. Bahaidarah, E.; Harriman, A.; Stachelek, P.; Rihn, S.; Heyer, E; Ziessel, R. *Photochem. Photobiol. Sci.* **2014**, *13*, 1397-1401.

9. Wu, D.; O'Shea, D. F. *Org. Lett.* **2013**, 15, 3392-3395.

10. Batat, P.; Cantuel, M.; Jonusauskas, G.; Scarpantonio, L.; Palma, A.; O'Shea, D.F.; McClenaghan, N.D. *J. Phys. Chem. A.* **2011**, 115, 14034-14039.

11. Owens, J. W.; Smith, R.; Robinson, R.; Robins, M. *Inorg. Chim. Acta.* **1998**, *279*, 226-231.

12. Loudet, A.; Bandichhor, R.; Burgess, K.; Palma, A.; McDonnell, S. O.; Hall, M. J.; O'Shea, D. F. *Org. Lett.* **2008**, *10*, 4771-4774.

13. Strickler, S. J.; Berg, R. A. *J. Chem. Phys.* **1962**, 37, 814–822.

14. Huang, K.; Rhys, A. *Proc. Royal Soc. A.* **1950**, 204, 406-423.

15. Asada, K.; Kobayashi, T.; Naito, H. *Thin Solid Films,* **2006**, 499, 192-195.

16. Karabunarliev, S.; Baumgarten, M.; Bittner, E.R.; Müllen, K. *J. Chem. Phys.* **2000**, 113, 11372-11381.

17. Bässler, H.; Schweitzer, B. *Acc. Chem. Res.* **1999**, 32, 173-182.

18. Strouse, G. F.; Schoonover, J. R.; Duesing, R.; Boyde, S.; Jones, W. E. Jr; Meyer, T. J. *Inorg. Chem.* **1995**, 34, 473-487.

19. Silverstein, R.M., Webster, F.X., Kiemle, D.J.; Bryce, D.L. 2014. Spectrometric Identification of Organic Compounds. John Wiley & Sons.

20. Socrates, G., 2004. Infrared and Raman Characteristic Group Frequencies: Tables and Charts. John Wiley & Sons.

21. Woodford, O.; Harriman, A.; McFarlane, W.; Wills, C. *ChemPhotoChem*, **2017**, 1, 317-325.

22. Karlsson, J.K. Woodford, O.J. Al-Aqar, R.A.; Harriman, A. *J. Phys. Chem. A.* **2017**, 121, 8569-8576.

23. McGlynn, S.P.; Sunseri, R.; Christodouleas, N. *J. Chem. Phys.* **1962**, 37, 1818-1824.

24. Adarsh, N.; Avirah, R.R.; Ramaiah, D. *Org. Lett.* **2010**, 12, 5720-5723.

25. Yogo, T.; Urano, Y.; Ishitsuka, Y.; Maniwa, F.; Nagano, T. *J. Am. Chem. Soc.* **2005**, 127, 12162-12163.

26. Singh-Rachford, T. N.; Haefele, A.; Ziessel, R.; Castellano, F. N. *J. Am. Chem. Soc*., **2008**, 130, 16164-16165.

27. Dutt, G.B.; Krishna, G.R. *J. Chem. Phys.* **2000**, 112, 4676-4682.

28. Lakowicz, J. R., 2006. Principles of Fluorescence Spectroscopy. Springer Science & Business Media. New York.

29. Reits, E.A.; Neefjes, J.J. *Nat. Cell Biol.* **2001**, 3, E145-E147.

30. Yguerabide, J.; Schmidt, J.A.; Yguerabide, E.E. *Biophys. J.* **1982**, 40, 69-75.

31. Axelrod, D.; Koppel, D.E.; Schlessinger, J.; Elson, E.; Webb, W.W. *Biophys. J.* **1976**, 16, 1055-1069.

32. Dumas-Verdes, C.; Miomandre, F.; Lépicier, E.; Galangau, O.; Vu, T. T.; Clavier, G., Méallet-Renault, R.; Audebert, P. *Chem. Eur. J*. ***2010,*** 13, 2525-2535.

33. Zatsikha, Y. V.; Yakubovskyi, V. P.; Shandura, M. P.; Dubey, I. Y.; Kovtun, Y. P. *Tetrahedron*, **2013**, 69, 2233-2238.

34. Brownell, L. V.; Robins, K. A.; Jeong, Y.; Lee, Y.; Lee, D. C. *J. Phys. Chem. C.* **2013**, 117, 25236-25247.

35. Omomo, S.; Furukawa, K.; Nakano, H.; Matano, Y. *J. Porphyrins Phthalocyanines,* **2015**, 19, 775-785.

36. Bura, T.; Retailleau, P.; Ulrich, G.; Ziessel, R. *J. Org. Chem.* **2011**, 76, 1109-1117.

37. Baerends, E. J.; Ricciardi, G.; Rosa, A.; van Gisbergen, S. J. A. *Coord. Chem. Rev*. **2002**, 230, 5-27.

38. Dias, F.B.; Bourdakos, K.N.; Jankus, V.; Moss, K.C.; Kamtekar, K.T.; Bhalla, V.; Santos, J.; Bryce, M.R.; Monkman, A.P *Adv. Mater.* **2013**, 25, 3707-3714.

39. Herz, J.; Buckup, T.; Paulus, F.; Engelhart, J.; Bunz, U.H.; Motzkus, M. *J. Phys Chem. Lett.* **2014**, *5*, 2425-2430.

40. Brun, A. M.; Harriman, A. *J. Am. Chem. Soc.* **1991**, 113, 8153-8159.

41. Nguyen, K. A.; Pachter, R. *J. Chem. Phys.* **2003**, 118, 5802-5810.

42. Wasserberg, D.; Marsal, P.; Meskers, S. C. J.; Janssen, R. A. J.; Beljonne, D. *J. Phys. Chem. B.* **2005**, *109*, 4410-4415.

43. Karsten, B. P.; Viani, L.; Gierschner, J.; Cornil, J.; Janssen, R. A. J. *J. Phys. Chem. A*. **2008**, 112, 10764-10773.

44. Chen, T.; Zheng, L.; Yuan, J.; An, Z.; Chen, R.; Tao, Y.; Li, H.; Xie, X.; Huang, W. *Nature Scientific Rep*. **2015**, *5*, 10923.

45. Englman, R.; Jortner, J. *Mol. Phys*. **1970**, *18*, 145-164.

Chapter 4: On the Triplet-Excited State of TIPS-Pentacene

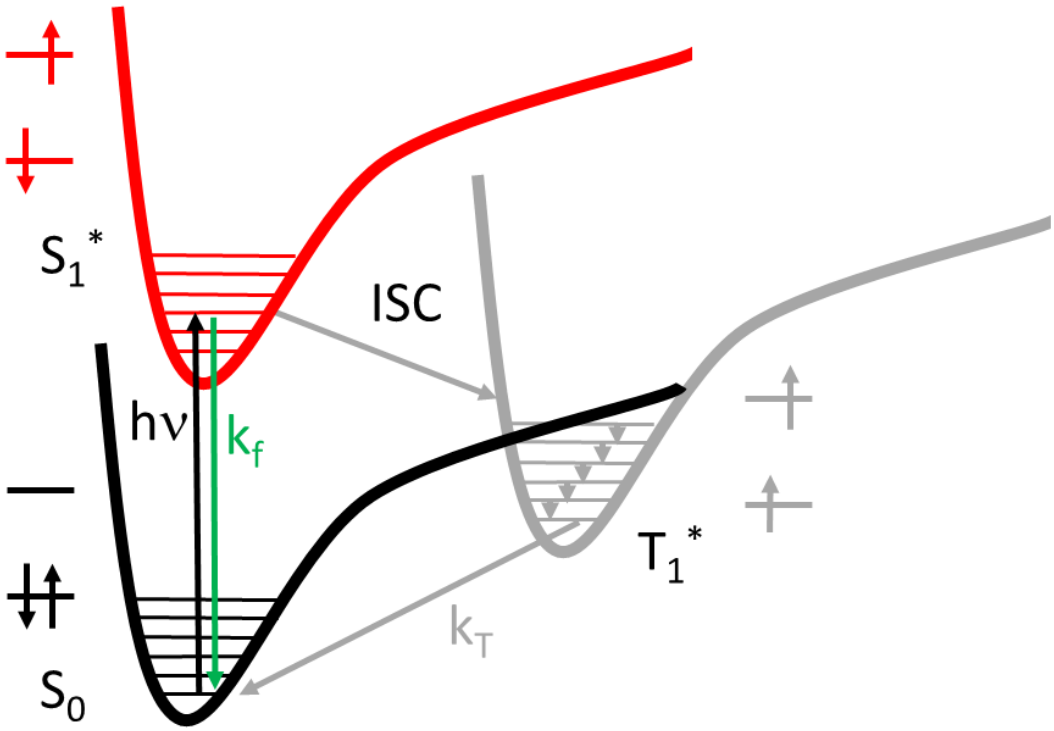

4.1 Introduction

Investigations into the triplet-excited states of organic chromophores have been pertinent since the seminal work of Lewis and Kasha, who first defined this *meta*-stable state as originating from spin-forbidden electronic transitions.[1-3] Before their work, it was known only that, in certain organic chromophores, there were two disparate emission bands present at low temperature (one with a short lifetime and the second lifetime being milliseconds or even seconds). Phosphorescence had not been explained, at the time, by a quantum mechanics description. Indeed, from a mechanistic standpoint, both processes were fluorescence, because a change in spin multiplicity had yet to be invoked. Figure 4.1 is used to illustrate the luminescence from anthracene, showing both fluorescence and phosphorescence at low temperature. Aryl hydrocarbons have figured prominently in establishing the basic rules of photophysics, most notably because of the work of Birks, and are blessed with well-structured absorption and emission bands that aid analysis.[4-6]

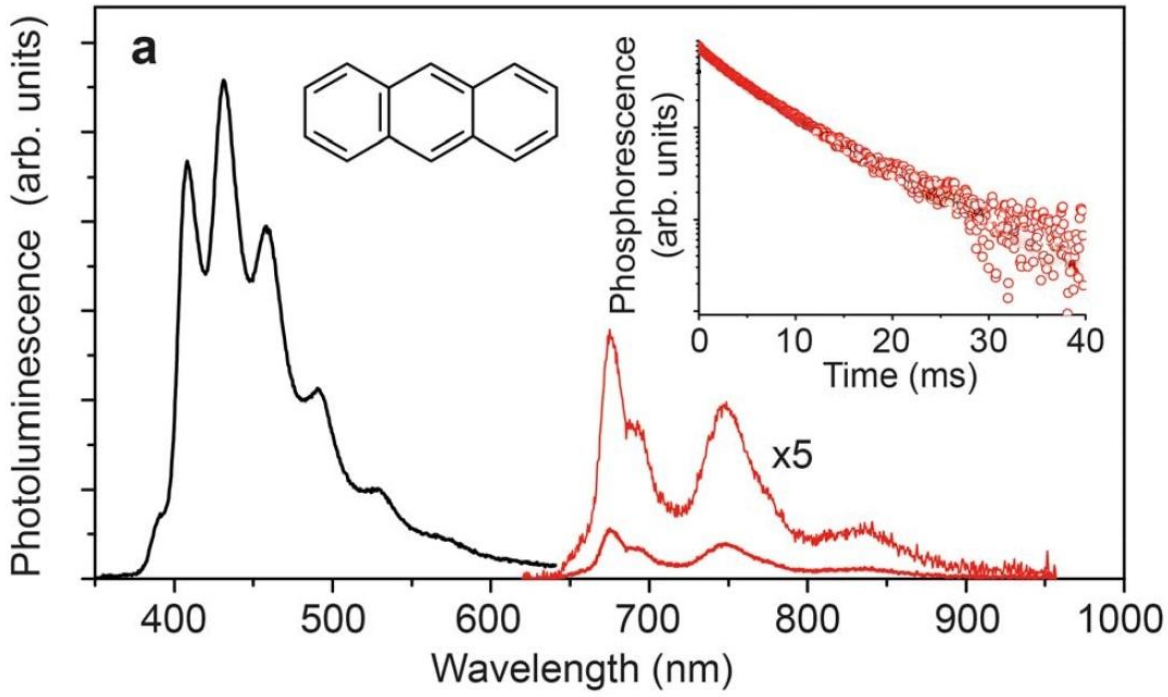

Figure 4.1. Steady-state emission spectrum of anthracene in a brominated polymer matrix. The black trace is fluorescence and the red is phosphorescence. Inset: decay curve for the phosphorescence shows this process occurs over tens of milliseconds. Figure adapted from reference 7.

Nowadays, the triplet state is a key concept in photochemistry, as it gives access to a relatively long-lived (at least in terms of diffusion in fluid solution), redox-active species for many different classes of molecule. Triplet excitons can be used to sensitize photochemical reactions; probably the best known example being benzophenone, where intersystem crossing from the singlet-excited state to the lowest-energy triplet is rapid and occurs with unity quantum yield.[8] The resulting diradical will abstract a hydrogen atom from a suitable donor, such as an alcohol, to give the highly reducing ketyl radical.[9] It is important to note from a historical perspective that the excited-triplet state gained immense importance following the introduction of the flash photolysis technique by Norrish and Porter. Indeed, the early instruments had limited time resolution but this was sufficient to monitor reactions of the triplet-excited state. Many such species were examined in deoxygenated solution, including triplet states of relevance to natural photosynthesis, and a catalogue of triplet-triplet absorption spectra began to evolve.

Other examples highlighting the importance of the triplet-excited state are found in artificial photosynthesis and in certain areas of medicine. Many photochemical systems for hydrogen evolution, or water oxidation, make use of the water-soluble *tris*(2,2'-bipyridyl)ruthenium(II) complex ($[Ru(bpy)_3]^{2+}$) as a sensitizer, triggering photo-induced electron transfer from an electron donor or acceptor to a suitable catalyst.[10-12] In the case of $[Ru(bpy)_3]^{2+}$, the chromophore absorbs visible light between about 370 and 600 nm, with a maximum at 450 nm. This latter transition corresponds to a spin-allowed, metal-to-ligand, charge-transfer state, which undergoes rapid intersystem crossing to the corresponding excited-triplet state. The triplet is long-lived in de-aerated water (over 1 μs)[12] and shows weak phosphorescence centred at around 600 nm. Such a long excited-state lifetime is sufficient for the dye either to be oxidized or reduced by suitable species. In the case of oxidative quenching by a sacrificial electron acceptor, such as the persulfate ion, the relatively stable $[Ru(bpy)_3]^{3+}$ cation so produced can abstract electrons from water in the presence of a suitable catalyst.[13] Much of our current understanding of the photophysics of luminescent transition metal complexes of this type is derived from the pioneering studies of Meyer.[14]

Systems based on organic dyes such as metallo-porphyrins, and to a lesser extent metallo-phthalocyanines, can be used for the same purpose due to their high triplet quantum yields.[15] An important criterion to note is that whereas the singlet-excited state rarely gives charge-separated redox species by way of diffusional quenching, the triplet-excited state tends to favour charge separation. A photosensitizer, electron relay and catalyst form the basis of the well-known three-component system for photochemical water oxidation (Figure 4.2) or proton reduction.[16] Unfortunately these systems rely on the use of a sacrificial electron donor/acceptor.

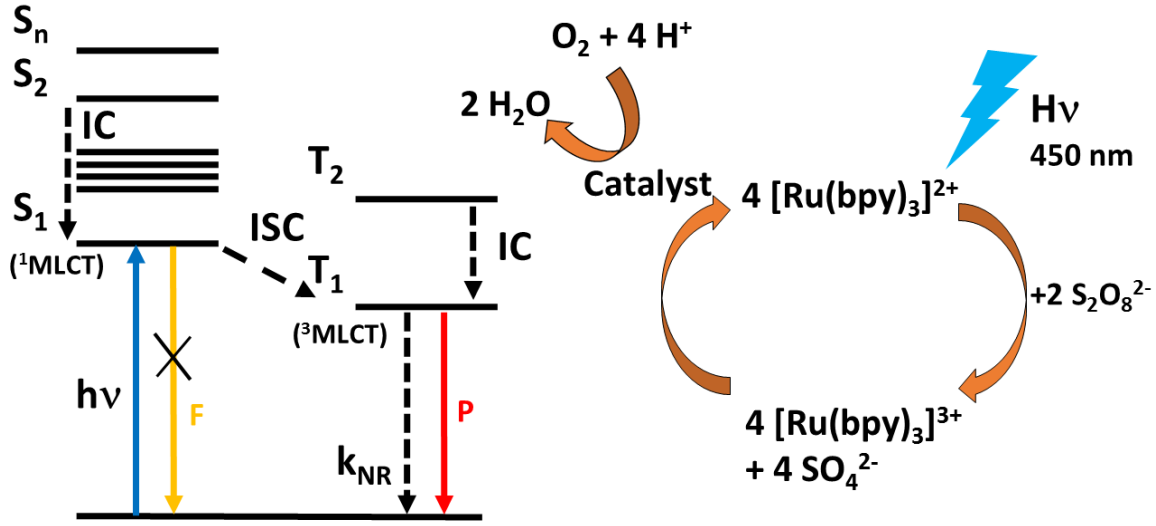

Figure 4.2. Schematic illustration of how the triplet-excited state is populated in a model system, ruthenium(II) tris(2,2'-bipyridine). A scheme for photocatalytic oxidation of water is presented on the right. Note as a side reaction the reduced acceptor will decompose as well. Key: IC (internal conversion), ISC (intersystem crossing), F (fluorescence), P (phosphorescence).

In photodynamic therapy, porphyrins or metallo-phthalocyanines are used to sensitize the formation of the reactive oxygen species known as singlet molecular oxygen.[17,18] This activation process occurs by way of triplet-triplet energy transfer from the chromophore triplet state to ground-state oxygen (which is also a triplet state). The net result is formation of singlet oxygen, with the chromophore being restored to its ground state. In principle, the sensitizer can recycle numerous times. The reactive singlet oxygen can attack cancerous cells and bacteria *in situ* but its lifetime is quite short and it needs to be generated close to the target. Nonetheless, photodynamic therapy is a useful alternative treatment for certain infections under illumination with light of an

appropriate wavelength as long as sufficient concentrations of molecular oxygen are present. The same process dominates in the photo-initiated fading of organic dyes. A good model example of this latter reaction is the common food dye Erythrosine, which generates ~100% triplet state from the S_1 state.[19] In the presence of molecular oxygen, the resultant singlet oxygen will attack the dye, leading to loss of colour.[20] Under these circumstances, one might wish to avoid using dyes with high triplet quantum yields or to ensure that the triplet lifetime is kept short. Organic dyes are particularly susceptible to quenching by molecular oxygen, which puts the emphasis on understanding the photophysical properties of functional chromophores. Such considerations are important for those investigating the use of organic dyes in opto-electronics, organic solar cells and light-emitting devices.

There is no doubt that understanding the triplet-state dynamics for organic dyes in fluid solution is important given their numerous practical applications. If there is not a direct application for the triplet, then it will be a hindrance in most cases. Although it is more common to see the triplet state populated readily in transition metal complexes, such as $[Ru(bpy)_3]^{2+}$, due to the increased spin-orbit coupling[21] from the metal centre, there is a drive towards having sensitizers based entirely on organic molecules. These are inevitably more abundant and less expensive.[22] In this chapter, we consider how the triplet-excited state is populated in organic dyes and how control of the prevailing conditions affects the rate of intersystem crossing. This follows from our investigation of the photophysics of aza-BODIPY where the S_1-T_1 energy gap was found to decrease on aza-substitution. We now move to the opposite end of the scale and consider the photophysics of pentacene, which is a member of the linear series of polyacenes known since the early work of Clar.[23] The special, but not unique, feature of interest for pentacene is that the S_1-T_1 energy gap is very wide. In fact, the triplet energy falls below half that of the corresponding excited-singlet state and this situation facilitates the process known as singlet exciton fission. First recognized by Jundt *et al*.[24] in thin films of microcrystalline pentacene, singlet exciton fission allows a singlet exciton to split into two triplet excitons, each localized on a separate molecule. For pentacene, this process occurs without activation and triplet yields up to 200% have been reported. This curiosity of molecular photophysics has gained tremendous appeal of late in terms of

the potential to increase the number of charge carriers in organic opto-electronic devices. Of course, singlet exciton fission demands the close proximity of two or more chromophores and was originally devoted to processes occurring in crystals. This has been extended to solid films and, quite remarkably, to concentrated liquid solutions. Further impetus was provided by the observation of Guldi *et al.*[25] that singlet exciton fission could be engineered in carefully designed molecular bis-pentacene derivatives. Indeed, intramolecular singlet exciton fission has now been extended to other aryl polycycles such as rylene, tetracene, rubrene and diketopyrrolopyrrole derivatives, although details of the mechanism are still under debate and some systems need thermal activation.[26-29] Pentacene nicely complements our work with aza-BODIPY and so here we look at triplet formation in solution phase. In a separate chapter, we present our own results relating to intramolecular singlet exciton fission in a bis-pentacene dyad.

4.2 Results and Discussion

The commercially available dye TIPS-pentacene (TIPS-P), for which the molecular formula is shown below in Figure 4.3, was synthesized by Dr. Alparslan Atahan of the Molecular Photonics Laboratory, Newcastle University, according to a previously reported procedure.[30] The purity of this sample was confirmed by high resolution 700 MHz NMR spectroscopy and by mass spectrometry measurements.

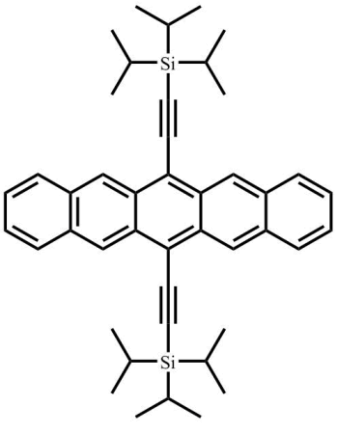

Figure 4.3. Molecular formula for TIPS-pentacene (TIPS-P).

4.2.1 Steady-State Spectroscopic Measurements

In common with many polycyclic aryl hydrocarbons, pentacene (Pc) is susceptible to self-association in solution at modest concentration. It has limited solubility in most organic solvents, benzene and 1-chloronaphthalene being the most suitable solvents. It is also considered to be carcinogenic. Early reports have described the absorption spectral properties and have identified the lowest-energy, spin-allowed transition as being located at 17,000 cm^{-1}. The corresponding excited-singlet state is of ^1L_a configuration and the radiative lifetime in solution has been reported as 7 ns[31], although later work increased this value to 22 ns.[32] Interestingly, this study reported[30] that intersystem crossing in pentacene is symmetry forbidden. Other features of the absorption spectrum recorded in nonpolar solvents locate the ^1L_b state at 23,200 cm^{-1} while the more intense transition to the $^1B_{1u}$ state is found at 33,050 cm^{-1}. The same study gave a calculated triplet energy of 7,700 cm^{-1}, with the lowest-energy triplet-excited state being of ^3L_a configuration. In nonpolar solvent, the fluorescence quantum yield was reported as being 0.08 and it was concluded that the main deactivation route for the S_1 state involved internal conversion.

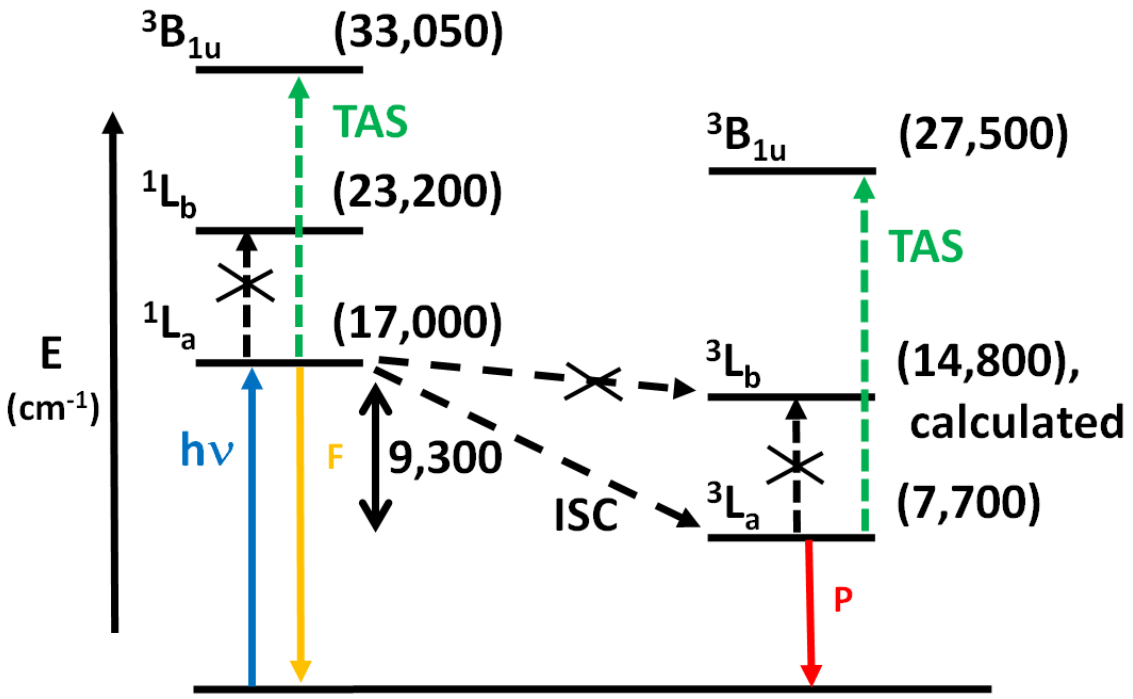

Figure 4.4. Schematic energy level diagram for pentacene. Transitions seen in transient absorption spectroscopy are in green. Energy values obtained from references 31 and 33.

Porter *et al*.[34] reported the triplet lifetime for pentacene to be 120 μs in thoroughly outgassed benzene. For this experiment, a long (i.e., 20 cm) optical path length was used together with a 5 μs flash lamp as excitation source. The very low concentration of triplet pentacene present under such conditions helps to minimize bimolecular quenching processes and, as a consequence, long triplet lifetimes are observed. Indeed, Lindquist *et al*.[35] studied triplet pentacene at higher concentrations and observed quenching by both ground-state Pc and triplet-triplet annihilation (*vide infra*). This investigation reported the effect of temperature on the triplet decay rate where excitation was made with a 4 μs white-light pulse and the solute concentration was around 3 μM with a path length of 20 cm. The solution in benzene was thoroughly de-aerated by the freeze-pump-thaw protocol. The first-order decay rate constant for triplet pentacene was determined to be 1.43 x 10^4 s^{-1} (i.e., τ_T = 70 μs) and independent of temperature over a wide range. Self-quenching by ground-state Pc was evident with a bimolecular rate constant of 3.6 x 10^8 M^{-1} s^{-1}. Interestingly for our work, triplet-triplet annihilation was observed with a bimolecular rate constant of 1.1 x 10^9 M^{-1} s^{-1}. It was considered[31] that this latter value was anomalously low when compared to other aromatic molecules under the same conditions. This effect was attributed to the relatively low triplet energy of pentacene. Finally, Lindquist *et al*.[35] estimated the molar absorption coefficient for triplet pentacene at 505 nm to be 120,000 M^{-1} cm^{-1}, on the basis of complete conversion of the ground state into the triplet. Both Porter and Lindquist observed the main T_1-T_n absorption transition to be located at 505 nm.

Further work by Lindquist *et al*.[36] aimed to establish the quantum yield for formation of the pentacene triplet-excited state. This experiment concluded that the triplet state was generated with a quantum yield (Φ_T) of 0.16 in de-aerated 1-chloronaphthalene solution. It is difficult, however, to prevent recycling of the chromophore under these conditions because the excitation pulse had an average FWHM of ca. 500 ns (1-12 mJ per pulse delivered with a tunable dye laser). Under these conditions, the excited-singlet state is expected to absorb several photons and thereby amplify the population of the *meta*-stable triplet state. The reported triplet yield,[36] therefore, should be treated cautiously; a further problem concerns the molar absorption coefficient of 9,900 M^{-1} cm^{-1} used to calculate the triplet concentration, as determined by complete bleaching of the

chromophore. This latter value differs markedly from the 120,000 M^{-1} cm^{-1} reported[35] elsewhere.

Because of the great interest being shown in singlet exciton fission, where measuring the triplet yield requires accurate knowledge of the underlying photophysical properties, it is important to quantify the processes leading to excited-state deactivation under controlled conditions. This is our intention here but, to overcome any limitations of poor solubility, we have used TIPS-P rather than pentacene. The photophysical properties of TIPS-P are available in the literature[37], but several important parameters need further scrutiny. Indeed, in recent years, TIPS-P has become the preferred Pc derivative due to its enhanced solubility in organic solvents and greater stability against photo-induced dimerization in the presence of oxygen.[38] In summary, Table 4.1 compiles the results of our studies made with TIPS-P in toluene at room temperature. The findings are in general agreement with previously reported results. In particular, absorption (λ_{ABS} = 643 nm) and fluorescence (λ_{FLU} = 650 nm) maxima match expected values (Figure 4.5) while the fluorescence quantum yield (Φ_F = 0.75) is high in dilute (i.e., μM) aerated solution. In de-aerated toluene solution the fluorescence yield increases to unity. The fluorescence spectral profile sharpens and undergoes a slight red-shift on cooling to 77K in 2-methyltetrahydrofuran solution (Figure 4.6). The excitation spectrum was found to agree well with the absorption spectrum over most of the visible region.

A Beer-Lambert plot for TIPS-P in toluene is linear over quite a wide concentration range (Figure 4.5). Indeed, there is no evidence for aggregation of the chromophore at concentrations below 10^{-4} M. This range covers that used in our photophysical investigations. The resistance towards self-association might be attributed to steric effects imposed by the TIPS units but it should also be stressed that the ethyne groups could perturb the electronic properties of the chromophore (*vide infra*). We now outline how these results were obtained and where inconsistencies might exist.

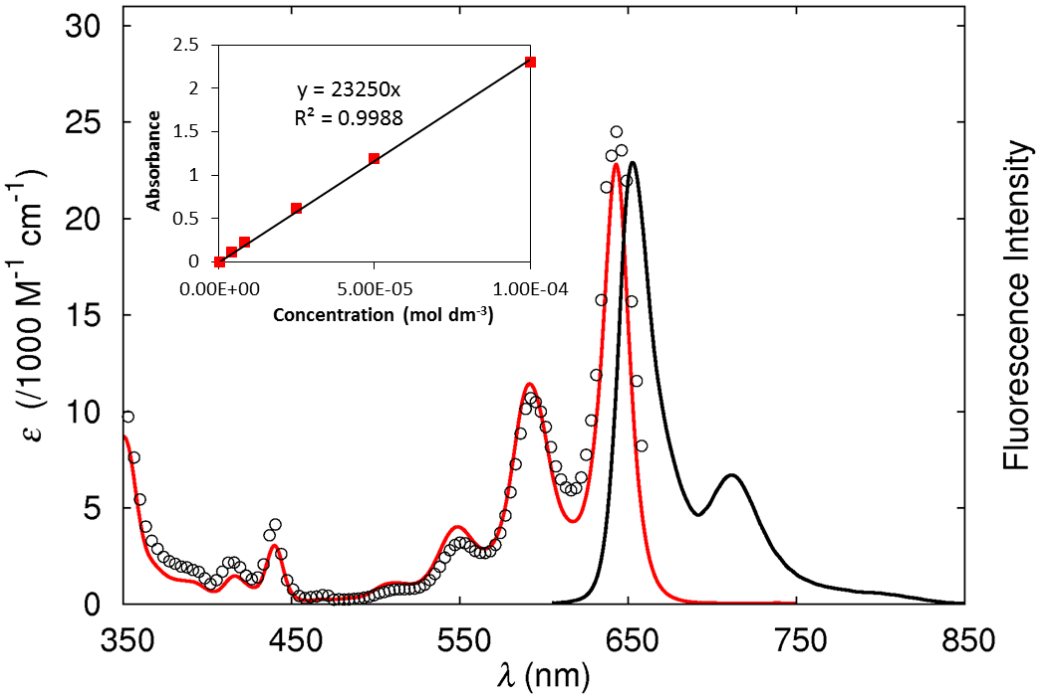

Figure 4.5. Steady-state absorption and fluorescence spectra for TIPS-P (2 μM) in toluene solution. The excitation spectrum is overlaid on the absorption spectrum with circles. Inset: Beer-Lambert plot showing the molar absorption coefficient of the dye.

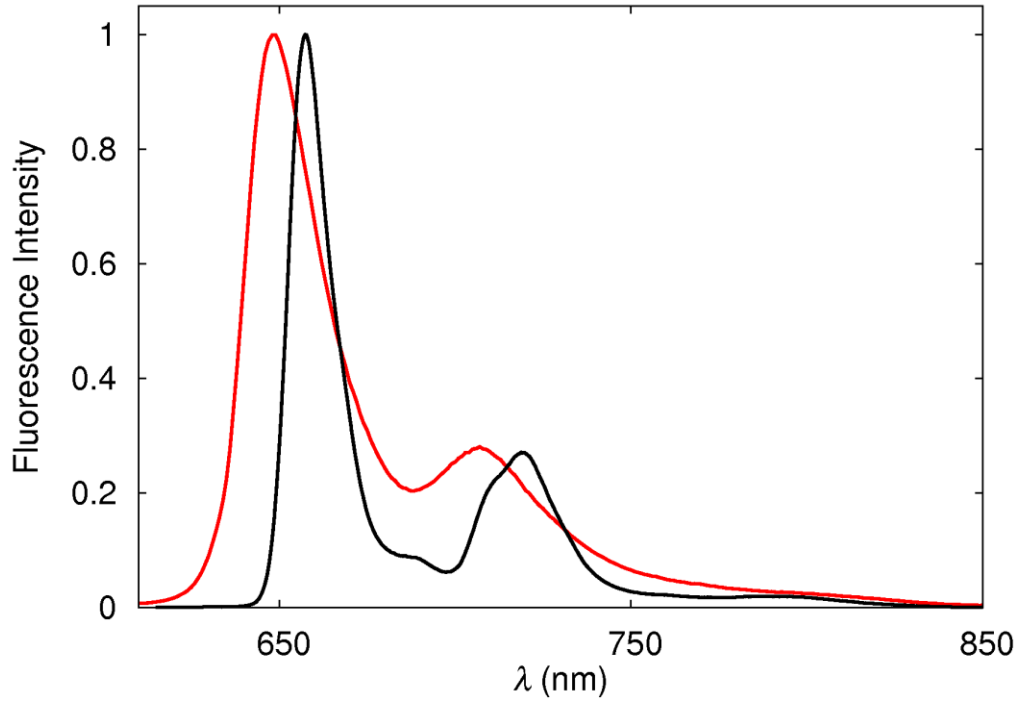

Figure 4.6. Low-temperature emission spectrum of TIPS-P obtained at 77K in an MTHF glass (black trace) overlaid with the room temperature spectrum (red trace).

4.2.2 Transient Absorption Spectroscopy

The excited-singlet state lifetime (τ_S) is 22 ns in deoxygenated toluene but falls to 15 ns on aeration when measured by time-correlated, single photon counting (635 nm laser excitation). Ultrafast laser (λ = 590 nm, FWHM = 150 fs) excitation of TIPS-P in toluene solution provides the differential absorption spectrum for the first-allowed, excited-singlet state (S_1). This spectrum is contaminated with stimulated emission and strong bleaching of the ground-state absorption bands (Figure 4.7). Correction for these effects gives the absolute S_1-S_n absorption spectrum, with a derived molar absorption coefficient (ε_{MAX}) of 36,000 M^{-1} cm^{-1} at 453 nm, as determined by iterative spectral curve fitting. To obtain this value, it was assumed that the transient differential absorption spectrum at early times (i.e., before significant deactivation has occurred) is compiled from ground-state bleaching, stimulated emission and excited-state absorption. Furthermore, we assume that the spectral signature for stimulated fluorescence is equivalent to that for normal emission and that there is no significant contribution from anti-Stokes emission. On this basis, iterative reconvolution of the observed spectrum together with the inverted fluorescence and excitation spectra leads to the best estimate for the "true" excited-state absorption spectrum. Comparison of the ground-state bleaching with excited-state absorption, in conjunction with the absence of triplet population at this time, allows estimation of the molar absorption coefficient for the excited-singlet state. This procedure was used for multiple spectra and at different delay times in order to establish an average value for ε_{MAX}. It might be noted that transient differential absorption spectra for the S_1 state of TIPS-P reported in the scientific literature[25] are in good agreement with that given in Figure 4.7. However, less attention has been given to the molar absorption coefficient of the S_1 excited state spectrum.

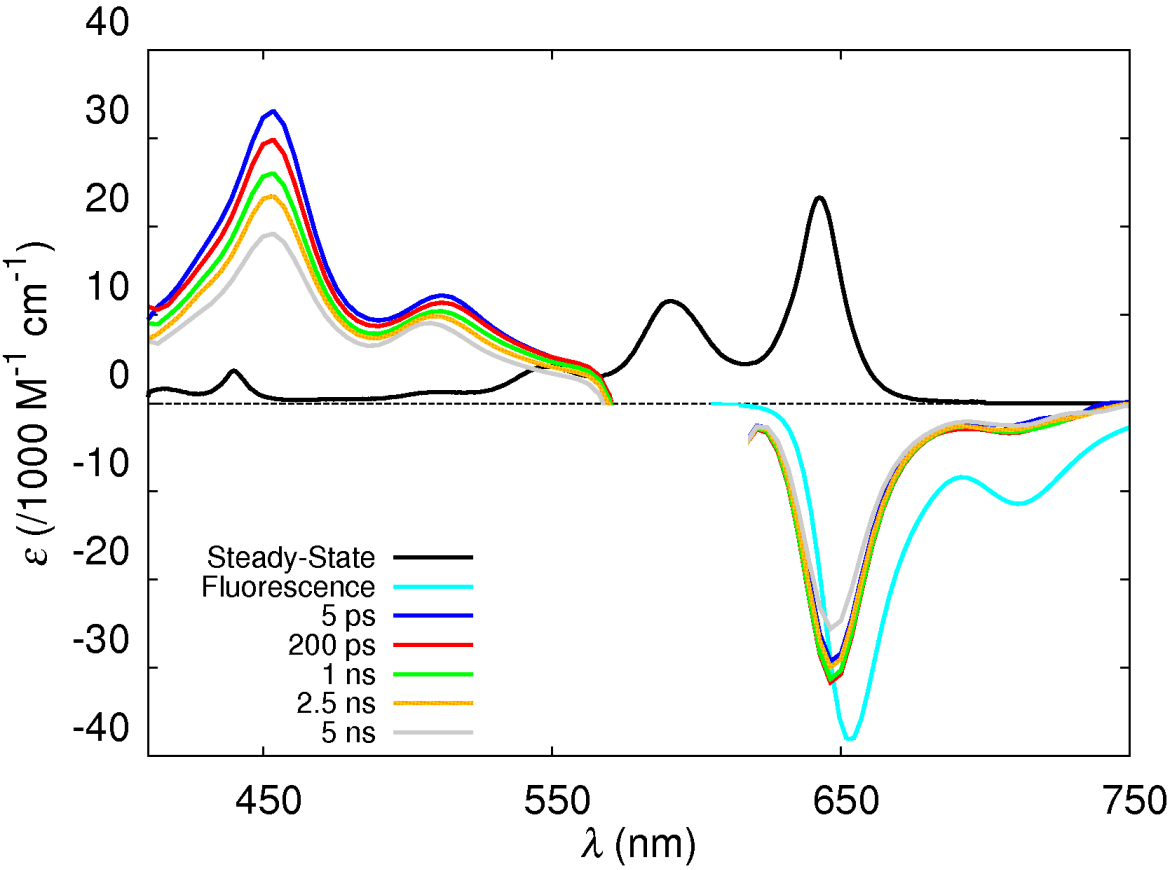

Figure 4.7. Transient differential absorption spectra recorded for TIPS-P in aerated toluene following excitation with an ultra-short laser pulse. The concentration was kept in the low μM range where singlet exciton fission is not expected. The steady-state fluorescence is overlaid to highlight the stimulated emission seen at about 700 nm. Sections of the ultrafast transients have been removed due to pump light scatter.

Under the conditions of the experiment, the S_1 state returns to the ground state with a lifetime of ca. 12 ns in aerated toluene; this lifetime being in acceptable agreement with that determined by time-correlated, single photon counting. The triplet state is not detected under these conditions. Reportedly, it is only when the concentration of TIPS-P is in excess of 1 mM that the triplet yield increases above a few percent.[37] The optical properties of such a strongly absorbing solution are not easily examined with conventional transient spectroscopy and require the use of short path lengths. We found no discernable difference in the appearance of the transient absorption spectra when changing the solvent from toluene to tetrahydrofuran (THF). It should be emphasized that the maximum delay time for these studies was 6 ns and therefore the transient decay records are dominated by residual S_1-S_n absorption. It is inappropriate to conclude, on these spectral studies alone, that triplet population is ineffective for TIPS-P.

Excitation of TIPS-P in de-aerated 2-methyltetrahydrofuran (MTHF) with a 4-ns laser pulse delivered at 532 nm (80 mJ) also generates the characteristic S_1-S_n differential absorption spectrum. Under these conditions, no triplet state is observed on timescales up to a few hundred nanoseconds. Addition of iodoethane (20% v/v), which quenches fluorescence from TIPS-P by way of a non-linear Stern-Volmer plot (*vide infra*), promotes intersystem-crossing to the triplet manifold. Now, transient absorption spectroscopy clearly shows the presence of a long-lived *meta*-stable species that displays a well-defined absorption band centred at 505 nm. This latter transition corresponds to the differential absorption spectrum previously assigned for Pc as being the T_1 to T_3 transition (Figure 4.8).[39]

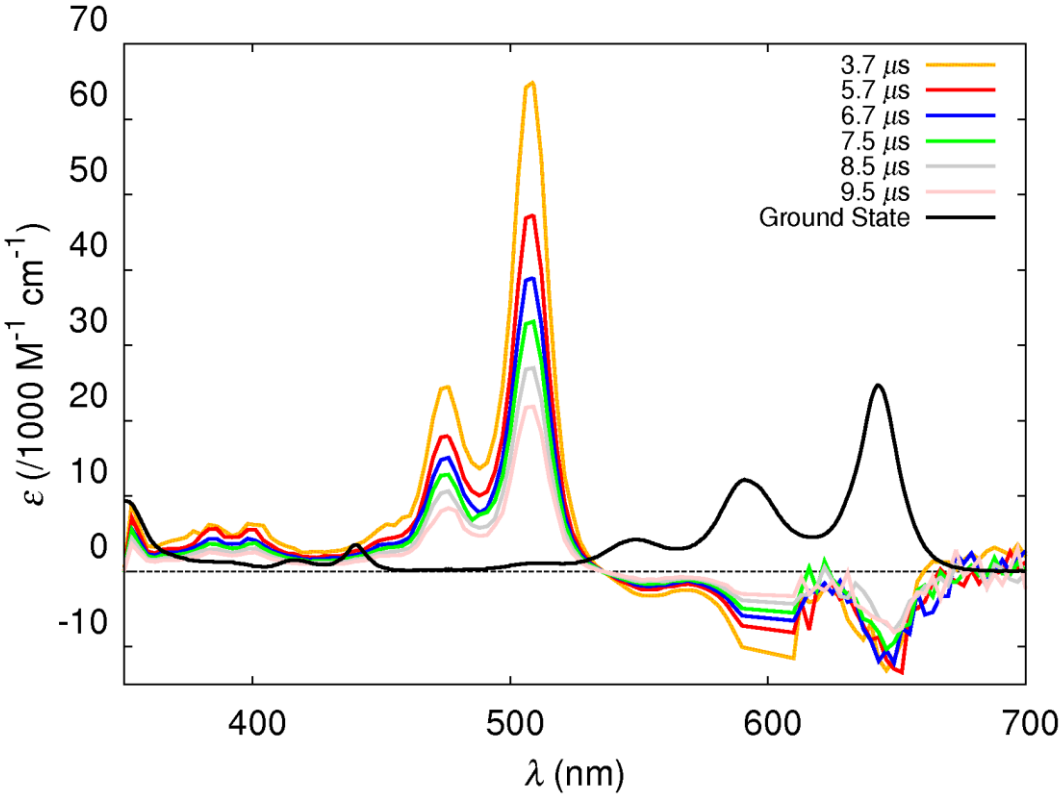

Figure 4.8. Transient differential absorption spectrum recorded for TIPS-P in deaerated toluene in the presence of 20% v/v iodoethane following excitation with a 4-ns laser pulse at 532 nm.

The derived nanosecond differential absorption spectrum resembles that reported by Porter *et al*. in the 1950s[3] using pentacene and is ascribed to the triplet-excited state. Our spectra remain in general agreement with literature reports. While the triplet lifetime (τ_T) measured in deoxygenated toluene is ca. 10 μs; the actual value being

highly sensitive to the level of residual molecular oxygen. The triplet decays *via* first-order kinetics to restore the pre-pulse baseline at low excitation energies. The triplet is quenched by addition of oxygen with a bimolecular rate constant of 1.1 x 10^9 M^{-1} s^{-1}. This value is below the diffusion controlled rate limit for toluene at room temperature (1.1 x 10^{10} M^{-1} s^{-1}).[40] Oxygen quenching of the singlet-excited state is effectively diffusion-controlled. Both these observations are in line with expectations where molecules with low triplet energies are expected to be quenched at 1/9th the diffusion controlled bimolecular limit, due to spin restriction rules.[41]

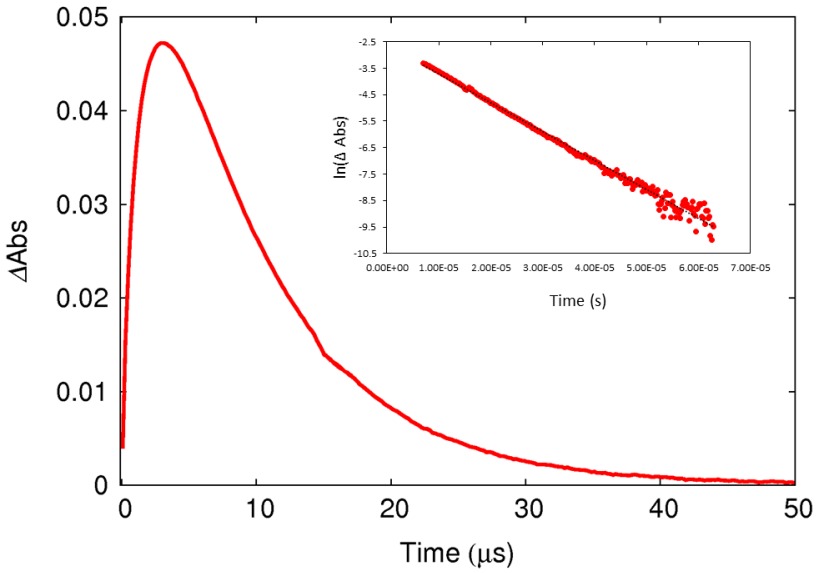

Figure 4.9. Decay of the TIPS-pentacene triplet absorption band centred at 505 nm seen in Figure 4.8 (inset: semi-log plot of decay shows conformity to first-order kinetics). The rise time at the beginning is due to saturation of the detector with strong fluorescence.

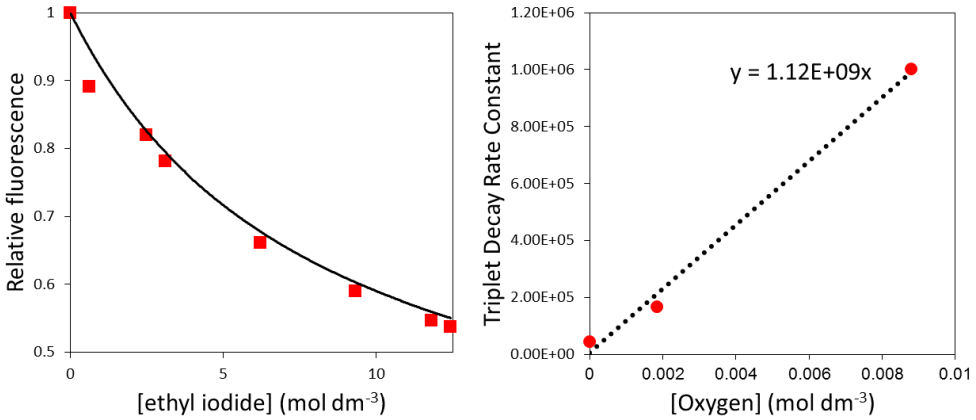

Figure 4.10. Left panel: fluorescence quenching of TIPS-P fluorescence with concentration of iodoethane in MTHF (solid line is a fit corresponding to a static quenching model).[42] *Right panel: triplet decay rate in MTHF plotted against concentration of dissolved oxygen.*[40]

In principle, the effects of an external spin-orbit promoter can be used to estimate the triplet quantum yield under any particular set of experimental conditions. This requires certain assumptions to be raised. The main condition to be imposed is that fluorescence quenching leads directly and quantitatively to triplet population. Thus, varying the concentration of iodoethane leads to a progressive decrease in Φ_F and a corresponding increase in the triplet quantum yield (Φ_T). The decrease in Φ_F is exactly balanced by the increase in Φ_T. Now, by calibrating the laser excitation energy using zinc *meso*-tetraphenylporphyrin, and the parameters established by Linschitz *et al*,[43] we can convert the absorbance change for the triplet state at 505 nm to a concentration change. Doing so for a series of iodoethane concentrations leads to an estimate for the molar absorption coefficient of the triplet state (ε_{TRIP}) at 505 nm of 72,000 M^{-1} cm^{-1}. In many cases, our estimate for ε_{TRIP} would be acceptable, naturally it falls between the two limits for ε_{TRIP} reported for Pc, but this is not the case for singlet exciton fission where the triplet yield needs to be measured with high precision. The assumption that the external heavy-atom effect leads exclusively to enhanced triplet population is an obvious weakness. Attention turned, therefore, to other ways to determine ε_{TRIP} for TIPS-P in fluid solution. Initially, we attempted to use a very dilute solution of TIPS-P in benzene and completely convert the ground state into the triplet but the incident laser flux proved to be insufficient.

The triplet differential absorption spectrum was also recorded by pulse radiolysis of TIPS-P in deoxygenated benzene solution (Figure 4.12). This work was carried out in collaboration with Prof T. Majima and his group at Osaka University [We thank the RSC and Newcastle University for providing the travel grant that facilitated visiting Osaka University]. Now, the triplet state is produced *via* electronic energy transfer from the benzene triplet state generated at the end of the pulse of ionizing radiation (Figure 4.11). Details of the methodology are provided in the experimental methods chapter and outlined here. Ionizing radiation is absorbed by the solvent and, within the 8-ns pulse, generates the respective benzene radical ions. These ions undergo geminate recombination on a fast timescale to generate a mixture of benzene singlet- and triplet-excited states. As is now well known in the field of organic-based OLEDs, three triplet species are produced for each singlet species. In fact, the singlet-excited state of liquid benzene in an inert solvent such as cyclohexane has an average lifetime of 30 ns while the lifetime of the excited-triplet state is highly concentration dependent. This latter value falls from 470 ns in dilute cyclohexane to only 26 ns in pure benzene.[44] None-the-less, at high solute concentrations, singlet-singlet and triplet-triplet energy transfer occurs to generate the excited states of TIPS-P (Figure 4.12). By measuring the absorbance at 505 nm *versus* solute concentration, it should be possible to completely trap the benzene excited states. However, very high concentrations of TIPS-P are needed to ensure that energy transfer competes with decay of the benzene excited states and we cannot be sure that the reaction is quantitative.

It is possible to determine the average radiation dose delivered in a pulse using a standard dosimeter, in our case benzophenone (ε_{TRIP} at 530 nm is taken as 7,220 M^{-1} cm^{-1}).[45] The concentration of benzophenone (BP) was varied to ensure complete trapping of the excited-state benzene molecules; the appropriate concentration was <5 mM. The ratio of initial absorbance values for the excited-singlet at 453 nm and the excited-triplet at 505 nm, measured for TIPS-P, is approximately 0.55. Now, the same ratio of molar absorption coefficients for the corresponding differential absorption spectra in toluene solution, as reported by Guldi *et al*., is ca. 0.57. This means that the concentrations of excited-singlet and excited-triplet states of TIPS-P produced by pulse radiolysis are roughly equal.

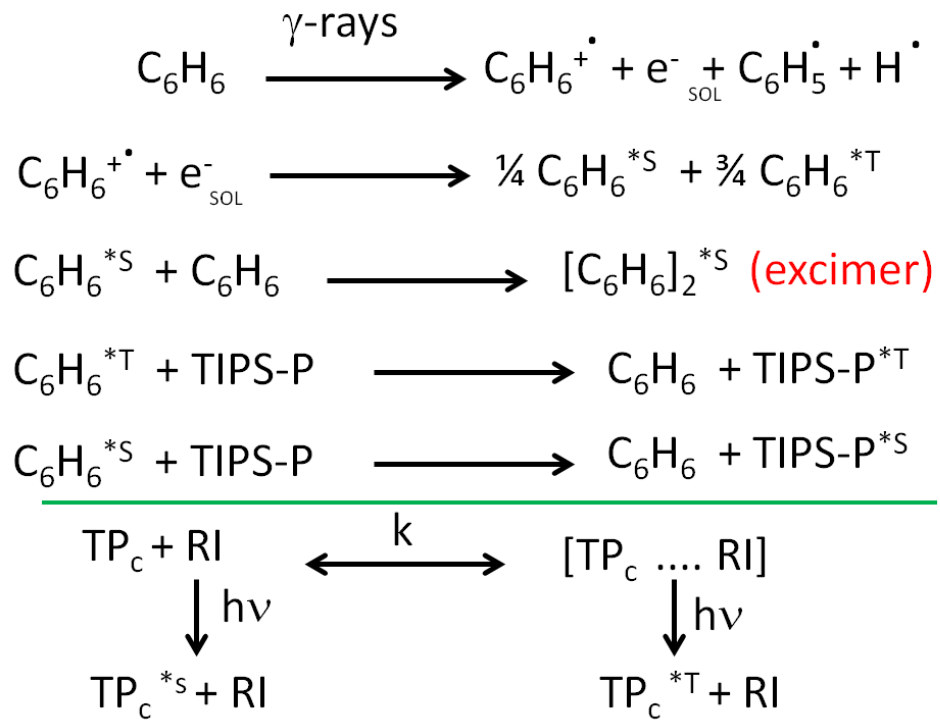

Figure 4.11. Schematic representation showing pathways to generating the triplet in TIPS-P (TPc) by pulse radiolysis[46] (top) and by using an external heavy atom perturber (bottom).

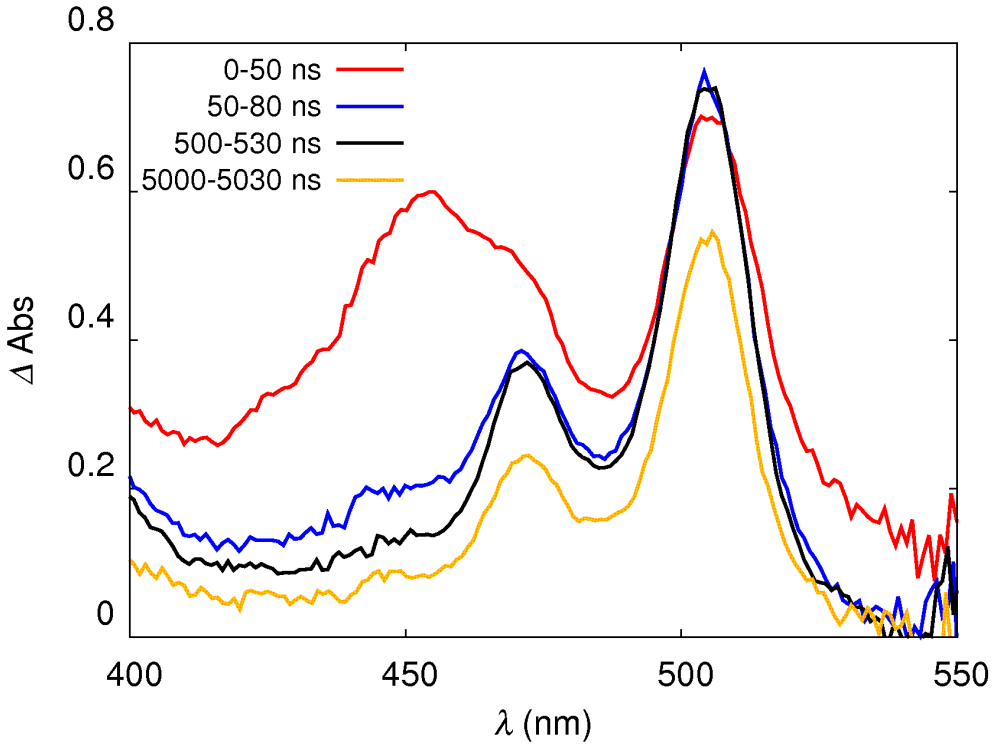

Figure 4.12. Transient absorption data for TIPS-P from pulse radiolysis experiments in toluene (1.2 mM concentration). At early times the excited singlet state can be seen (red trace).

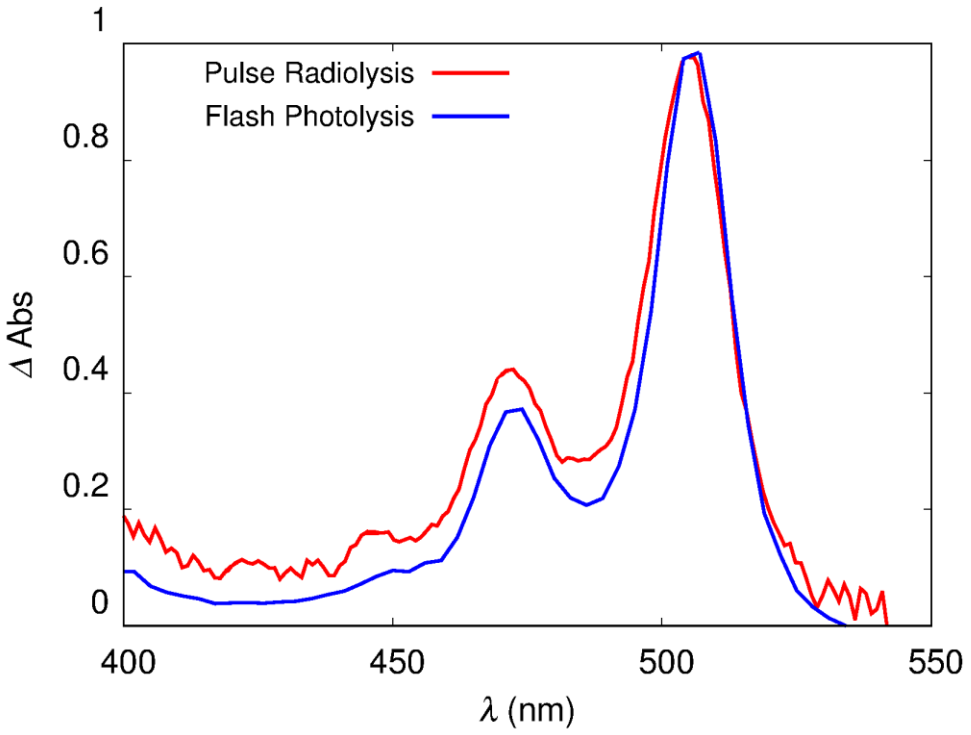

Figure 4.13. Normalized TIPS-P triplet spectra in deoxygenated toluene generated by pulse radiolysis and laser flash photolysis (with 20% v/v iodoethane) at 5 μs.

The triplet differential absorption spectra obtained on exposure to ionizing radiation and by laser flash photolysis agree quite well (Figure 4.13). It is clear that the spin-orbit promoter catalyzes intersystem crossing to the triplet manifold. Comparing ε_{TRIP} measured by the two techniques shows the two values to be in good agreement, with the higher value being obtained using a spin orbit promoter. This suggests that iodoethane promotes internal conversion from S_1 to S_0 states as well as catalyzing intersystem crossing. The triplet lifetime recorded under ionizing radiation, which is free from any effects associated with the heavy-atom spin promoter, is 20 μs in de-aerated benzene. Using ε_{TRIP} measured by pulse radiolysis in conjunction with the laser flash photolysis studies made in the absence of iodoethane, we conclude that the quantum yield for direct formation of the triplet-excited state in TIPS-P is less than 3%.

A third way to determine ε_{TRIP} for TIPS-P is to employ a triplet sensitizer of appropriate excitation energy. Sensitizers that immediately spring to mind as potential energy donors are zinc(II) tetraphenylporphyrin (ZnTPP) and benzophenone (BP) because of their well-characterized photophysical properties. However, the main difficulty with these sensitization experiments is to identify an excitation wavelength that allows

unique illumination of the sensitizer. Our original experiments used Zn-TPP in de-aerated toluene. Although triplet-triplet energy transfer was observed for this system, quantitative measurements were unconvincing because of strongly overlapping transient spectra. We identified a promising alternative in a halogenated bacteriochlorin reported by Arnaut *et al.*[47] but were not able to obtain a sample for our experiments at the time. Subsequent collaboration with the Arnaut group showed that conventional triplet-state sensitizers, such as per-chlorinated tetraphenylporphyrin, transferred triplet excitation energy to TIPS-P at rates well below the diffusion-controlled rate limit. The bimolecular rate constant for triplet-triplet energy transfer increases with decreasing triplet energy of the donor, in line with energy transfer lying within the Marcus inverted region. This indicates that the triplet energy of TIPS-P is, indeed, very low.

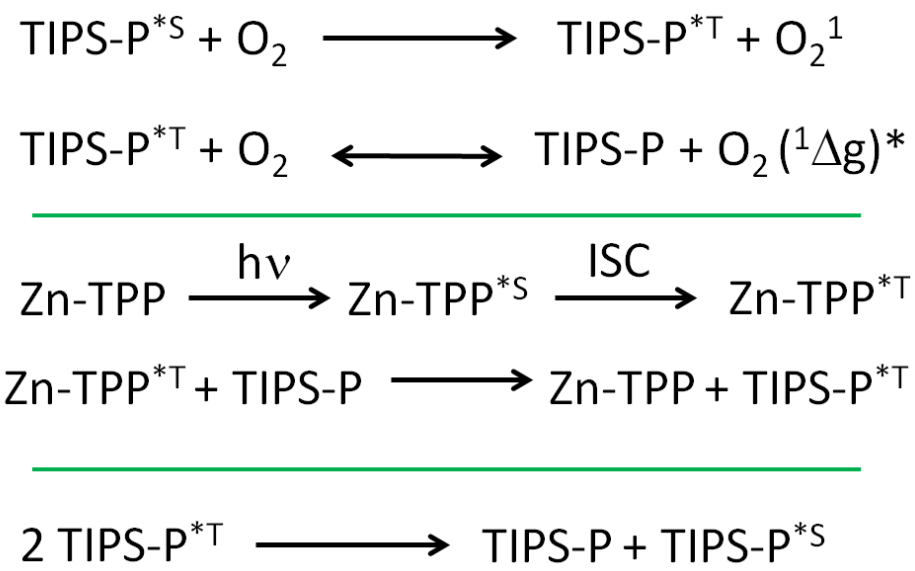

Figure 4.14. Schemes illustrating triplet sensitization and triplet quenching either by contact with molecular oxygen or by way of triplet-triplet annihilation.

In summary, at this point, we are confident that we have obtained appropriate optical absorption spectra for the lowest-energy excited-singlet and excited-triplet states of TIPS-pentacene in fluid solution. Excited-state lifetimes have been determined by way of several complementary experimental techniques and are shown to be mutually consistent. Values derived for the molar absorption coefficients at selected wavelengths for the ground, excited-singlet and excited-triplet states also appear to be reasonably sound. There is no reason to doubt the claim that intersystem crossing is inefficient for

TIPS-P in dilute, de-aerated fluid solution. There is a need, however, to establish the excitation energies for this compound with a high degree of confidence. This remains the outstanding objective.

4.2.3 Energy Levels

The intersection point between normalized absorption and fluorescence spectra, as recorded under high resolution, allows establishment of the singlet excitation energy (E_S) as being 15,445 cm^{-1} (i.e., 1.92 eV) for TIPS-P in dilute toluene solution. It has been possible to detect fluorescence from the S_1 state and also to record S_1-S_N absorption, together with stimulated emission. In particular, it should be noted that TIPS-P is a strong emitter when present in dilute liquid solution, although the excited-state lifetime is sufficiently long for diffusional quenching by oxygen to be a problem. Indeed, the excited-singlet state lifetime recorded in de-aerated solution (i.e., 22 ns) is remarkably close to that calculated using the Stricker-Berg expression[48] (i.e., 24 ns). This finding confirms our claim that fluorescence is almost quantitative in the absence of molecular oxygen and at high dilution. Fluorescence is also evident from μM concentrations of TIPS-P dispersed in a non-polar polymer matrix, namely Zeonex 480, which has obvious red emission that is clearly visible to the naked eye.

Figure 4.15. Photograph of a drop-cast Zeonex 480 film doped with TIPS-P. Lower panel shows the fluorescence under illumination with a mercury-vapour lamp (365 nm).

Spin-orbit coupling is rather ineffective for TIPS-P but we have successfully characterized the triplet-excited state in terms of its T_1-T_3 absorption spectrum. The excited-triplet state is quenched by molecular oxygen but this is not an indication for triplet-triplet energy transfer to form singlet molecular oxygen. This latter species shows weak luminescence centred at 1260 nm (i.e., 7,935 cm^{-1} or 0.98 eV).[49] Molecular oxygen can interact with triplet-excited states by the so-called paramagnetic effect, which enhances spin-orbit coupling and promotes formation of the ground state. If quenching is solely due to the paramagnetic effect, then the same trend would be seen by saturating TIPS-P solutions with nitric oxide (NO), which has a much higher excited state energy at approx. 35,000 cm^{-1}.[50] This experiment was not performed, however, due to unavailability of a suitable sample of NO. During the triplet quenching studies with molecular oxygen, we saw no indication for a plateau that might indicate reversible triplet energy transfer (Figure 4.14). This suggests to us that the triplet energy of TIPS-P is less than ca. 7,800 cm^{-1}. For effective singlet exciton fission, the triplet energy would need to be below ca. 7,700 cm^{-1}.

Early literature work has estimated the triplet energy of pentacene on the basis of the bimolecular triplet quenching rate constants of a series of organic chromophores with molecular oxygen. Here, the triplet energy of Pc was estimated at approximately 8,000 cm^{-1}.[51] All our attempts to record phosphorescence from TIPS-P at 77K were unsuccessful, even in the presence of 60% v/v iodoethane. Direct observation of phosphorescence from an organic chromophore in the near-infrared region is experimentally challenging because of the relative insensitivity of most detectors. A recent report[25] describes the phosphorescence spectrum of TIPS-P, this being centred at approximately 6,300 cm^{-1}, which corresponds to a triplet energy much less than one half the excitation energy of the excited-singlet state.[31] A further report of phosphorescence from TIPS-P in de-oxygenated 2-methyltetrahydrofuran at 77K places the emission maximum at 1580 nm (i.e., 6,330 cm^{-1}) but does not provide a supporting excitation spectrum.[52]

Our results suggest that the triplet quantum yield will be less than 3% under these conditions so it is difficult to imagine how a phosphorescence signal might be observed. Nonetheless, the two reported phosphorescence maxima are in excellent agreement and place the triplet energy in the expected region on the basis of successful singlet exciton fission. There are no reported determinations of the phosphorescence lifetime for TIPS-P and no measurements of the quantum yield or excitation spectra. We should be cautious about using the data to establish the triplet energy, even though the experiments match our expectations.

Plotting the singlet excitation energy against triplet excitation energy for the series of linear polyacenes (i.e., benzene to hexacene) gives an indication of the trend in triplet energy (Figure 4.16). There does appear to be a linear correlation, which would suggest that the estimate for Pc (E_T = 6,330 cm^{-1}) is appropriate. However, this is not a rigorous relationship and there is no real support for the veracity of a linear correlation between the two excitation energies. Pentacene and TIPS-P have become well known as chromophores capable of singlet exciton fission in the crystal phase, in concentrated solution[37,53] and where the two pentacene units are held in close proximity by way of covalent links. In such systems, fluorescence is quenched and triplet quantum yields can exceed 100%.[54-56] We can assume therefore that estimates of the triplet energy being less than half that of the singlet-excited state, this being a necessary requisite for effective singlet exciton fission, are correct. It is counterintuitive to envisage populating the triplet state effectively when the energy gap between S_1 and T_1 is very large and earlier work referred to symmetry restrictions for intersystem crossing in pentacene.[57] In fact, a well-known route to enhance the rate of intersystem crossing involves reducing the singlet-to-triplet energy gap.[58,59] This was observed with aza-BODIPY (Chapter 3), although we did not see a perceivable increase in triplet yield.

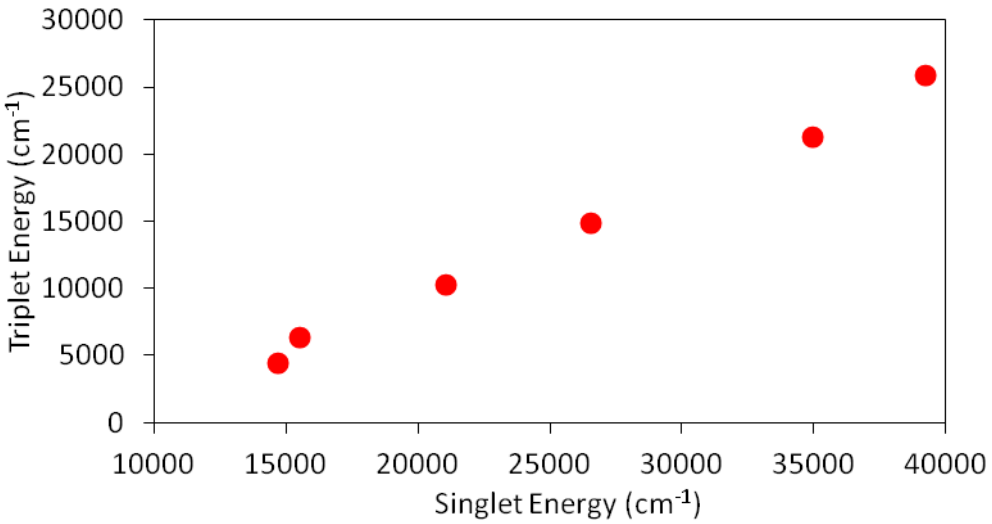

Figure 4.16. Relationship between singlet and triplet energies of the acene series from benzene to hexacene from a literature survey[38,40,54] Here a singlet energy of 15,445 cm^{-1} and triplet energy of 6,330 cm^{-1} are used for pentacene.

Other ways to quantify the triplet energy include searching for delayed fluorescence. The most direct method is based on E-type delayed fluorescence – nowadays popularly called thermally-activated delayed fluorescence[60] – where the emitting S_1 state is repopulated from a lower-lying triplet state. Unfortunately, this approach works only if the S_1 and T_1 states are quite close in energy and this is certainly not the case for TIPS-P. The alternative type of delayed fluorescence is known as P-type and arises from triplet-triplet annihilation (TTA).[61] In fact, TTA can be achieved by bimolecular diffusion of two triplet states or by excitation of a bis-chromophore with an intense laser pulse. For TIPS-P in de-aerated toluene we observed no evidence of a signal corresponding to delayed fluorescence. As was mentioned earlier, Lindquist *et al*. reported TTA for pentacene in liquid benzene and noted that the relatively low bimolecular rate constant was consistent with a low triplet energy relative to that of the singlet state. It is not possible, however, to use this information in a more quantitative sense.

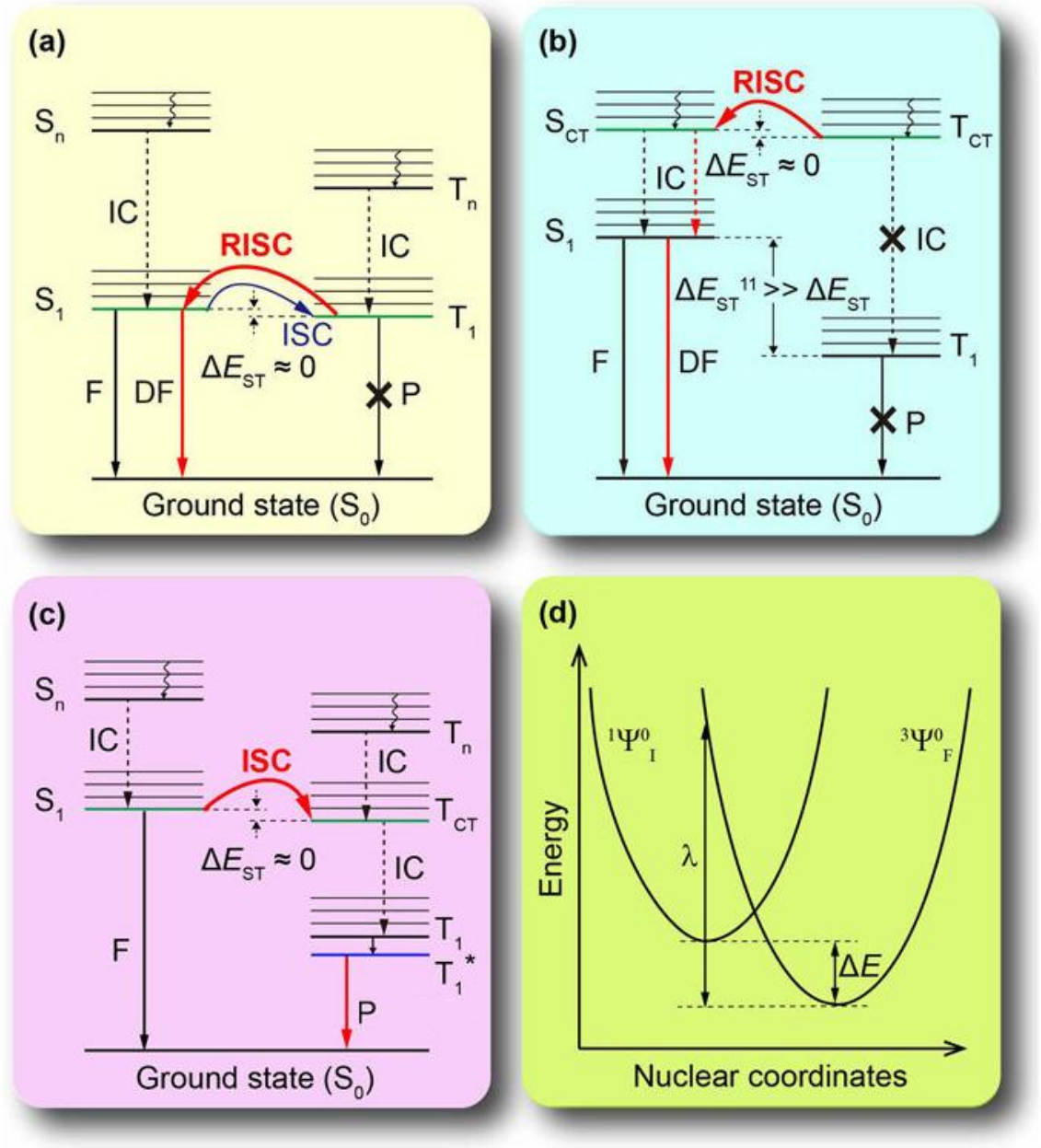

Figure 4.17. Pathways to increased intersystem crossing for organic chromophores: ***(a)*** *thermally-activated delayed fluorescence or E-type delayed fluorescence (DF)* ***(b)*** *reverse intersystem crossing by closely matched charge-transfer excited states,* ***(c)*** *charge transfer mediated intersystem crossing* ***(d)*** *classical view of intersystem crossing highlighting the importance of the singlet-triplet energy gap. Figure adapted from reference 62.*

At this point we still lack an independent estimate of the triplet energy for TIPS-P in fluid solution. In part, the problem revolves around the poor efficacy for intersystem crossing inherent to pentacene in fluid solution. Incorporating an internal heavy atom should help overcome this problem but we have not taken this route. It is well-known that one

can enhance the rate of intersystem crossing via a charge-transfer state.[63-65] Long-lived, charge-separated states can recombine to yield the triplet state, this works well in donor-acceptor dyads as originally predicted by Rehm and Weller.[63,66] Complexes between excited donor and ground-state acceptor, for example, are often termed "exciplexes" and can also occur when the donor and acceptor are separated in the ground state. The exciplex, like the excimer, has played an important role in photophysics and many examples have been well documented.[67-68] However, formation of a homo-exciplex is unlikely to arise with dilute solutions of TIPS-P due to the lack of bimolecular contact; the same situation is so for formation of an excimer.

A further way to measure the triplet excitation energy for TIPS-P is based on the technique known as photoacoustic calorimetry (PAC)[70], which in a crude sense is an adaptation of the thermal blooming procedure described in Chapter 7. Time-resolved PAC is a technique that allows one to measure, in the same experiment, both the rate and the enthalpy of a photochemical or photophysical event. The basic principle of PAC is that the heat released in the course of a reaction produces a transient heating of the local environment. When contained in a closed system, this thermal gradient creates a pressure wave that is transmitted across the cell and can be detected by a high-frequency transducer. It is common practice to use a laser pulse as excitation source, allowing times as short as 10 ns to be monitored. This may be a useful means of determining the triplet energy for TIPS-P independently of any phosphorescence measurement. To undertake such measurements would necessitate construction of new instrumentation, however, which is beyond the scope of this study.

In summary, there is good indirect evidence to establish the triplet energy of pentacene somewhere below half that of the singlet-excited state. Phosphorescence measurements for TIPS-P do exist, but there is no alternative to corroborate these measurements. The field would benefit from independent measurements using an alternative technique and we propose photoacoustic calorimetry for this purpose. A second alternative measurement, albeit indirect, would be to establish whether TIPS-P generates singlet oxygen in solution. For this, a very sensitive singlet oxygen detector would be required. If however, TIPS-P were found to generate singlet molecular oxygen

by energy transfer then it would reposition the estimate of the triplet energy back to the ~8,000 cm^{-1} suggested by Porter *et al*.[52] Until these highly specialized experiments can be done, one cannot establish the triplet energy of this system with a high degree of precision or confidence.

4.2.4 Redox Chemistry

Charge-transfer states have been suggested to play a role in singlet exciton fission in certain cases.[71,72] With this in mind, we set out to better characterize the redox chemistry of TIPS-P in solution. To convert TIPS-P to the corresponding π-radical cation, the chromophore was dissolved in MTHF containing a few percent of carbon tetrachloride and illuminated for 5 minutes with a floodlight. The sample quickly lost fluorescence and turned colourless. The course of reaction was subsequently followed by steady-state absorption spectroscopy. During reaction, the excited-singlet state of TIPS-P transfers an electron to CCl_4. Geminate charge recombination is prohibited by rapid loss of a chloride ion (since the carbon is highly oxidized), followed by addition of molecular oxygen to form the trichloromethyl peroxyl radical. This oxygen-centred radical is a powerful oxidant and oxidizes a further molecule of TIPS-P (Figure 4.18). The π-radical anion was generated by irradiating TIPS-P in a de-aerated solution of 3:1 THF-propan-2-ol containing benzophenone (1 mM) and a small amount of base. Illumination of benzophenone under these conditions produces two ketyl radicals by way of hydrogen atom abstraction from the alcohol. The presence of the base favours deprotonation of these radicals, thereby preventing mutual addition reactions, to give the corresponding ketone π-radical anions (Figure 4.18). These latter species are powerful reductants and transfer an electron to TIPS-P. Subtracting the initial ground-state spectra from those generated during early stages of illumination gives rise to the spectra for the π-radical ions (Figure 4.19). These species are essentially colourless, with the cation having prominent absorption features further into the UV-region and a transition at about 410 nm.

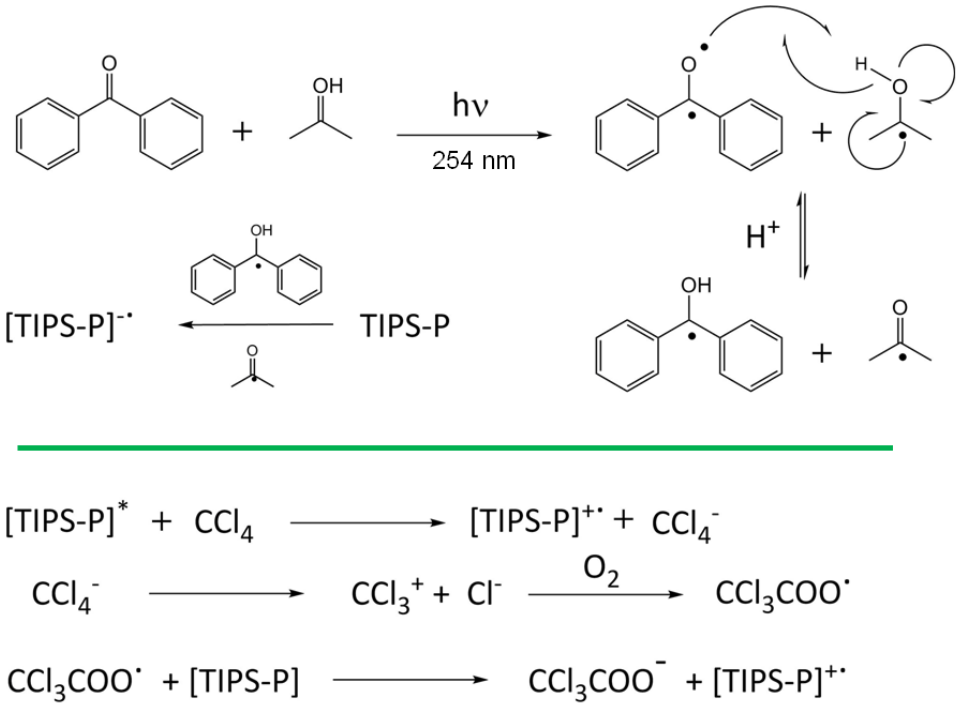

Figure 4.18. Schemes showing how to generate the π-radical anion (top) and cation (bottom) species of TIPS-P in by steady state irradiation.

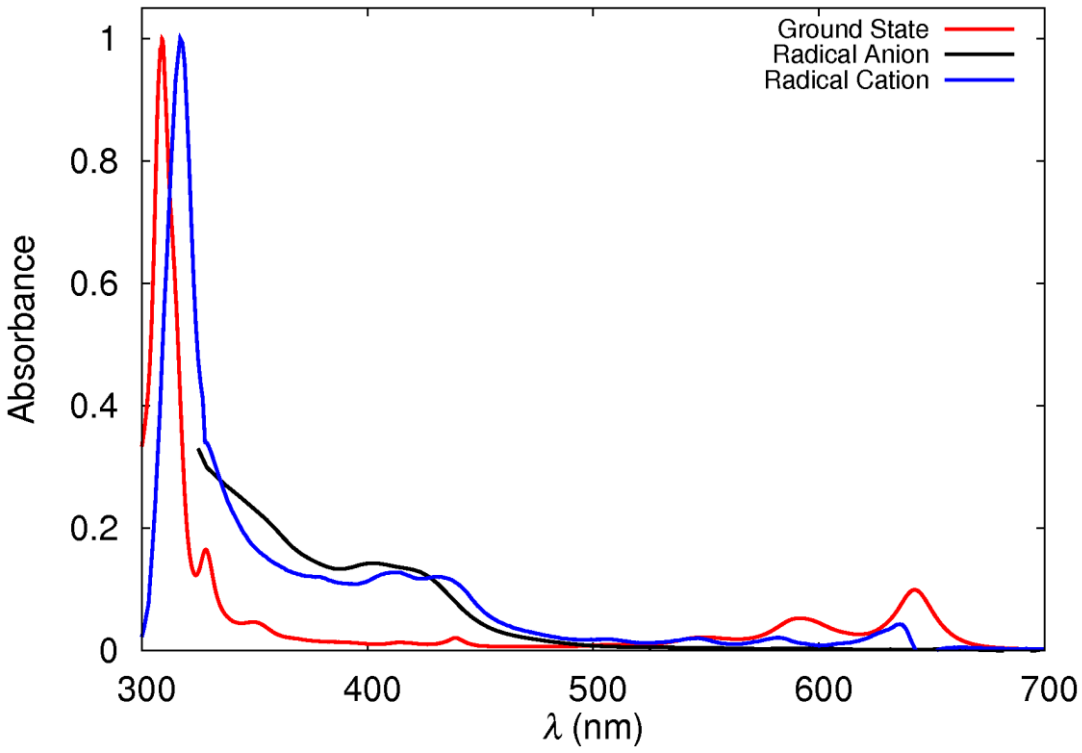

Figure 4.19. Normalized steady-state absorption spectra for TIPS-P derived π-radical anion and cation species.

Polycyclic aryl hydrocarbons are well known to undergo multiple oxidation and reduction processes in liquid solution. Indeed, such compounds tend to possess a rich redox chemistry, but it is important to prevent association reactions accompanying the electron-transfer chemistry. For example, one-electron oxidation of pyrene forms the expected π-radical cation but the electrode reaction is irreversible due to attachment of a second pyrene molecule.[40] The net product is the π-radical cation of a pyrene dimer. Electrochemical studies have been reported for several derivatives of pentacene, including TIPS-P, in different environments. Thus, for TIPS-P in de-aerated tetrahydrofuran, half-wave potentials of -1.32, -1.87 and +0.78 V vs Ag/Ag^+ have been reported.[73]

We recorded cyclic voltammograms for TIPS-P in de-aerated CH_2Cl_2 containing tetra-N-butylammonium hexafluorophosphate (0.2 M) as background electrolyte. The voltammogram indicates two oxidation and two reduction steps over the accessible potential window. The first reduction step involves a *quasi*-reversible (by comparison of the electron transfer rate constant of ferrocene electrochemistry), one-electron process to form the corresponding π-radical anion. The half-wave potential for this process is -1.26 V vs Ag/Ag^+. This is followed by a further one-electron reduction step that is poorly reversible in electrochemical terms. Here, the peak potential occurs at -1.8 V vs Ag/Ag^+, with the degree of reversibility increasing somewhat with increasing scan rate. Re-oxidation of the two-electron reduced product occurs with a peak potential of -1.0 V vs Ag/Ag^+. According to our analysis of this voltammogram, the π-radical anion should be stable with respect to disproportionation. Our values seem to be fully consistent with the literature data, especially considering the change in solvent and reference electrode.

On oxidative scans, TIPS-P undergoes a *quasi*-reversible oxidation step with a half-wave potential of +0.56 V vs Ag/Ag^+. This process forms the corresponding π-radical cation and should be compared with the literature value of +0.78 V vs Ag/Ag^+ reported for TIPS-P in tetrahydrofuran. At higher potentials, there is a two-electron oxidation process that is only partially reversible in electrochemical terms. The peak potential for this latter process is +1.27 V vs Ag/Ag^+. Again, the wide spacing between these two oxidation steps suggests that the π-radical cation should be stable against thermal disproportionation.

Recording the cyclic voltammogram over a restricted potential range confirms that the first reduction and oxidation steps can be termed *quasi*-reversible. Comparison to the literature suggests that TIPS-P is somewhat harder to oxidize than is the unsubstituted pentacene.[74] This could be because the TIPS groups provide a significant electronic effect or because they help solubilize the solute and thereby minimize self-association in solution.

The difference between the first oxidation and first reduction potentials observed for TIPS-P in CH_2Cl_2 corresponds to an energy gap of 1.84 eV. This is substantially reduced relative to the optical band gap taken from the absorption spectrum where the onset of absorption occurs at 1.93 eV in toluene. Normally, we would expect the electrochemical and optical band gaps to be in closer agreement and with the former value being the higher. This is the case in THF solution where the electrochemical band gap is 2.1 eV.

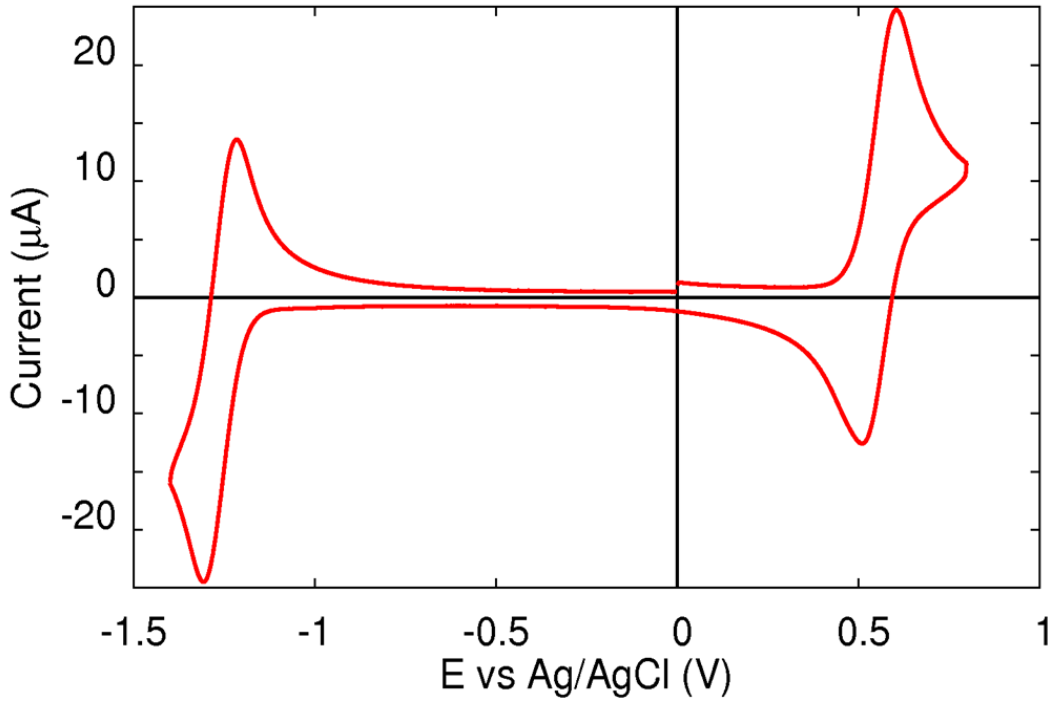

Figure 4.20. Cyclic voltammogram of TIPS-pentacene in dichloromethane. Scan speed 0.05 V/s.

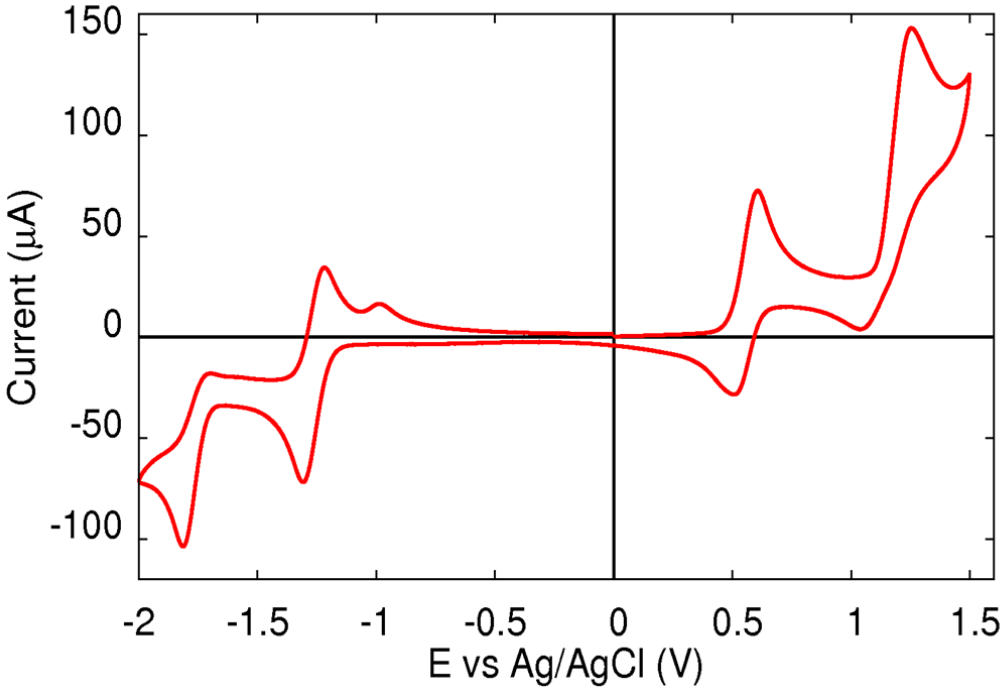

Figure 4.21. Expanded view of TIPS-P electrochemistry showing non-reversible processes.

It seems important at this stage to comment on the possible role, if any, of the TIPS groups in modulating the electronic properties of pentacene. It was shown previously that attaching an ethyne residue to pyrene at the 1-position renders the molecule slightly easier to reduce than the parent pyrene while making oxidation much easier.[75] This seems to be much the same situation as found with TIPS-P. Earlier work has used DFT calculations to compare the effect of TIPS substitution on the optical properties of small acenes.[76] Upon TIPS-functionalisation, there is a generic lowering of the ionisation potential and a small rise of the electron affinity. This leads to a systematic decrease of the HOMO-LUMO energy gap across the series of acenes, a general trend that is reflected in the computed optical absorption spectra. In all cases, the onset of absorption for the TIPS-acene is red-shifted compared to the respective parent. We have observed this same effect when comparing the absorption onset for pentacene (ΔE = 17,000 cm^{-1}) and TIPS-P (ΔE = 15,555 cm^{-1}). The TIPS groups are expected to hinder formation of an endoperoxide by attack from singlet molecular oxygen and limit the significance of photo-dimerisation.

Frontier molecular orbital calculations made for TIPS-P lend some evidence to support our electrochemical measurements. Here, the HOMO and LUMO molecular orbitals show that electron density is being shifted to the alkyne bond of the TIPS-groups, serving to somewhat deactivate the central benzene ring. This would explain the increase in electrochemical oxidation potential and the decrease in tendency to form endoperoxides. It has also been reported that the TIPS-groups improve the photo-stability of pentacene some 50-fold.[38] It is important to note that a proposed reason for this is a considerable lowering of the triplet energy for TIPS-P relative to pentacene, which would prevent energy transfer to molecular oxygen and consequently greatly reduce the rate of photobleaching.

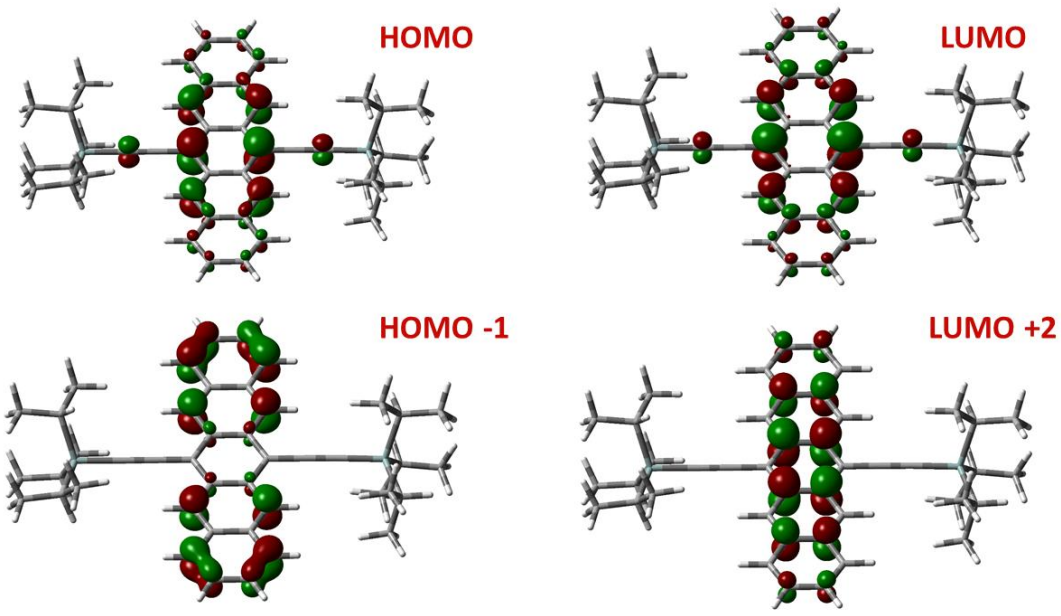

Figure 4.22. Frontier molecular orbitals calculated for TIPS-P. Calculations used density functional theory with the B3LYP functional with a 6-311d basis set. The solvent was chloroform.

Table 4.1. Summary of the photophysical properties for TIPS-pentacene in dilute toluene solution.

λ_{max}^{abs} / nm	643 ± 1
λ_{max}^{fluor} / nm	652 ± 1
$\varepsilon_{643\ nm}$ / M^{-1} cm^{-1}	23 250 ± 2325
$f^{(a)}$	0.090 ± 0.009
E_{SS} / $cm^{-1(b)}$	215
ϕ_{fluor}	$0.75^{(c)}$ ± 0.04
k_{RAD} / * 10^7 s^{-1}	3.4 ± 0.3
k_{NR} / * 10^7 s^{-1}	1.1 ± 0.1
τ_{S1} / $ns^{(e)}$	22.3 ± 1.0
τ_{T1} / $\mu s^{(e)}$	9.0 ± 0.9
E_{T1-T3} / M^{-1} cm^{-1} (at 505 nm)	$65300^{(g)}$ ± 3,250

(a) Oscillator strength, (b) Estimated Stokes' Shift from deconstruction of the absorption and emission spectra into the minimum number of Gaussian components (c) Fluorescence yield in sub-micromolar concentration (aerated) solution, (e) Solution was purged with dry N_2 for at least 15 minutes prior to measurement. (g) Triplet extinction coefficient determined from pulse-radiolysis experiments in benzene.

4.3 Conclusions

This chapter has characterized the photophysical properties of a topical polyacene chromophore, TIPS-pentacene, under carefully controlled conditions with particular emphasis on the excited-triplet state. Although pentacene is well known as a potential singlet exciton fission chromophore, with triplet yields approaching 200% under some conditions, the chromophore is highly fluorescent in dilute solution and intersystem crossing inefficient. Under our conditions, the triplet state can only be populated by means of an external heavy atom or by sensitization. The TIPS-P monomer triplet is much longer-lived than the pairs of triplets produced by singlet exciton fission either in the crystal phase[77] or in pentacene dyads.[25,78] No short-lived transient species were observed as part excited state dynamics in dilute solution ruling out excimers or exciplexes. It appears then that populating triplet state of TIPS-P by singlet fission is heavily driven by close proximity electronic communication, as expected, but the spectroscopic signature of the TIPS-P triplet closely matches reports of some pentacene dyads, where two triplets are produced on the same molecule.[79]

An independent, clear-cut, measurement of triplet energy remains an outstanding problem, although indirect measurements suggests this falls well within the energetic requirement for singlet exciton fission (i.e. half the energy of the singlet) at approx. 6,300 cm^{-1}. Since singlet fission relies so heavily on knowing the energy of the triplet, it calls for rigorous experimental procedure for measuring near-IR phosphorescence or another approach. An alternative means to quantifying the triplet energy was proposed, this being photoacoustic calorimetry and future studies will surely address this issue. The results obtained here will be used to aid in characterizing the excited state properties a new bridged pentacene bichromophore, examined in Chapter 5, in order to better understand intramolecular singlet fission.

4.4 References

1. Lewis, G.N.; Kasha, M. *J. Am. Chem. Soc.* **1944**, 66, 2100-2116.

2. McClure, D.S. *J. Chem. Phys.* **1949**, 17, 905-913.

3. Porter, G.; Windsor, M.W. *Proc. Royal Soc. A* **1958**, 245, 238-258.

4. Birks, J.B.; Dyson, D.J.; Munro, I.H. *Proc. Royal Soc. A*, **1963**, 275, 575-588.

5. Birks, J.B. *Nature*, **1967**, 214, 1187-1190.

6. Birks, John B. 1970. Photophysics of aromatic molecules. Wily-Interscience.

7. Reineke, S.; Baldo, M.A. *Sci. Rep.* **2014**, 4, 3797.

8. Ledger, M.B.; Porter, G. *J. Chem. Soc., Faraday Trans.1* **1972**, 68, 539-553.

9. Porter, G.; Wilkinson, F. *J. Chem. Soc. Faraday Trans. 1* **1961**, 57, 1686-1691.

10. Kiwi, J.; Grätzel, M. *Nature* **1979**, 281, 657-658.

11. Gust, D.; Moore, T.A.; Moore, A.L. *Acc. Chem. Res*. **2009**, 42, 1890-1898.

12. Van Houten, J.; Watts, R.J. *J. Am. Chem. Soc.* **1976**, 98, 4853-4858.

13. Hara, M.; Waraksa, C.C.; Lean, J.T.; Lewis, B.A.; Mallouk, T.E. *J. Phys. Chem. A.* **2000**, 104, 5275-5280.

14. Caspar, J.V.; Meyer, T.J. *J. Am. Chem. Soc.* **1983**, 105, 5583-5590.

15. Darwent, J.R.; Douglas, P.; Harriman, A.; Porter, G.; Richoux, M.C. *Coord. Chem. Rev*. **1982**, 44, 83-126.

16. Pellegrin, Y.; Odobel, F. *C. R. Chim.* **2017**, 20, 283-295.

17. Bonnett, R. *Chem. Soc. Rev.* **1995**, 24, 19-33.

18. Macdonald, I.J.; Dougherty, T.J. *J. Porphyrins Phthalocyanines*, **2001**, 5, 105-129.

19. Bowers, P.G.; Porter, G. *Proc. Royal Soc. A*. **1967**, 299, 348-353.

20. Karlsson, J.K.; Woodford, O.J.; Al-Aqar, R.; Harriman, A. *J. Phys. Chem. A*. **2017**, 121, 8569-8576.

21. McGlynn, S.P.; Reynolds, M.J.; Daigre, G.W.; Christodoyleas, N.D. *J. Phys. Chem*. **1962**, 66, 2499-2505.

22. Sun, Y.; Giebink, N.C.; Kanno, H.; Ma, B.; Thompson, M.E.; Forrest, S.R. *Nature*, **2006**, 440, 908-912.

23. E. Clar; F. John. Ber. *Dtsch. Chem. Ges. B.* **1930**, 63, 2967.

24. Jundt, C.; Klein, G.; Sipp, B.; Le Moigne, J.; Joucla, M.; Villaeys, A.A. *Chem. Phys. Lett.* **1995**, 241, 84-88.

25. Zirzlmeier, J.; Lehnherr, D.; Coto, P.B.; Chernick, E.T.; Casillas, R.; Basel, B.S.; Thoss, M.; Tykwinski, R.R.; Guldi, D.M. *Proc. Natl. Acad. Sci. U.S.A*, **2015**, 112, 5325-5330.

26. Eaton, S.W.; Shoer, L.E.; Karlen, S.D.; Dyar, S.M.; Margulies, E.A.; Veldkamp, B.S.; Ramanan, C.; Hartzler, D.A.; Savikhin, S.; Marks, T.J.; Wasielewski, M.R. *J. Am. Chem. Soc.* **2013**, 135, 14701-14712.

27. Burdett, J.J.; Bardeen, C.J. *Acc. Chem. Res.* **2013**, 46, 1312-1320.

28. Ma, L.; Zhang, K.; Kloc, C.; Sun, H.; Michel-Beyerle, M.E.; Gurzadyan, G.G. *Phys. Chem. Chem. Phys*. **2012**, 14, 8307-8312.

29. Eaton, S.W.; Shoer, L.E.; Karlen, S.D.; Dyar, S.M.; Margulies, E.A.; Veldkamp, B.S.; Ramanan, C.; Hartzler, D.A.; Savikhin, S.; Marks, T.J.; Wasielewski, M.R. *J. Am. Chem. Soc.* **2013**, 135, 14701-14712.

30. Fudickar, W.; Linker, T. *J. Am. Chem. Soc.* **2012**, 134, 15071-15082.

31. Nijegorodov, N.; Ramachandran, V.; Winkoun, D.P. *Spectrochim. Acta A*, **1997**, 53, 1813-1824.

32. Kryschi, C.; Fleischhauer, H.C.; Wagner, B. *Chem. Phys.* **1992**, 161, 485-491.

33. Chakraborty, H.; Shukla, A. *J. Chem. Phys.* **2014**, 141, 164301.

34. Porter, G.; Wilkinson, F. *Proc. Royal Soc. A.* **1961**, 264 1316, 1-18.

35. Hellner, C.; Lindqvist, L.; Roberge, P.C. *J. Chem. Soc. Faraday Trans. 2*, **1972**, 68, 1928-1937.

36. Soep, B.; Kellmann, A.; Martin, M.; Lindqvist, L. *Chem. Phys. Lett.* **1972**, 13, 241-244.

37. Walker, B.J.; Musser, A.J.; Beljonne, D.; Friend, R.H. *Nat. Chem.* **2013**, 5, 1019-1024.

38. Maliakal, A.; Raghavachari, K.; Katz, H.; Chandross, E.; Siegrist, T. *Chem. Mater*. **2004**, 16, 4980-4986.

39. Musser, A.J.; Liebel, M.; Schnedermann, C.; Wende, T.; Kehoe, T.B.; Rao, A.; Kukura, P. *Nat. Phys.* **2015**, 11, 352-357.

40. Murov, S.L.; Carmichael, I.; Hug, G.L., 1993. Handbook of Photochemistry. CRC Press.

41. Patterson, L.K.; Porter, G.; Topp, M.R. *Chem. Phys. Lett.* **1970**, 7, 612-614.

42. Bowen, E.J.; Metcalf, W.S. Proc. Royal Soc. A, **1951**, 206, 437-447.

43. Hurley, J.K.; Linschitz, H.; Treinin, A. *J. Phys Chem.* **1988**, 92, 5151-5159.

44. Hentz, R.R.; Thibault, R.M. *J. Phys. Chem.* **1973**, 77, 1105-1111.

45. Hurley, J.K.; Sinai, N.; Linschitz, H. *Photochem. Photobiol.* **1983**, 38, 9-14.

46. Thomas, J.K.; Mani, I. *J. Chem. Phys.* **1969**, 51, 1834-1838.

47. Pereira, M.M.; Monteiro, C.J.; Simões, A.V.; Pinto, S.M.; Abreu, A.R.; Sá, G.F.; Silva, E.F.; Rocha, L.B.; Dąbrowski, J.M.; Formosinho, S.J.; Simões, S.; L.G. Arnaut. *Tetrahedron*, **2010**, 66, 9545-9551.

48. Strickler, S.J.; Berg, R.A. *J. Chem. Phys.* **1962**, 37, 814-822.

49. Krasnovsky, A.A. *Photochem. Photobiol.* **1979**, 29, 29-36.

50. Gijzeman, O.L.J.; Kaufman, F.; Porter, G. *J. Chem. Soc. Faraday Trans.* **1973**, 69, 727-737.

51. Gijzeman, O.L.J.; Kaufman, F.; Porter, G. *J. Chem. Soc. Faraday Trans.* **1973**, 69, 708-720.

52. Busby, E.; Berkelbach, T.C.; Kumar, B.; Chernikov, A.; Zhong, Y.; Hlaing, H.; Zhu, X.Y.; Heinz, T.F.; Hybertsen, M.S.; Sfeir, M.Y.; Reichman, D.R. *J. Am. Chem. Soc.* **2014**, 136, 10654-10660.

53. Wilson, M.W.; Rao, A.; Clark, J.; Kumar, R.S.S.; Brida, D.; Cerullo, G.; Friend, R.H. *J. Am. Chem. Soc.* **2011**, 133, 11830-11833.

54. Busby, E.; Berkelbach, T.C.; Kumar, B.; Chernikov, A.; Zhong, Y.; Hlaing, H.; Zhu, X.Y.; Heinz, T.F.; Hybertsen, M.S.; Sfeir, M.Y.; Reichman, D.R. *J. Am. Chem. Soc.* **2014**, 136, 10654-10660.

55. Zimmerman, P.M.; Bell, F.; Casanova, D.; Head-Gordon, M. *J. Am. Chem. Soc.* **2011**, 133, 19944-19952.

56. Sakuma, T.; Sakai, H.; Araki, Y.; Mori, T.; Wada, T.; Tkachenko, N.V.; Hasobe, T. *J. Phys. Chem. A*. **2016**, 120, 1867-1875.

57. Kryschi, C.; Fleischhauer, H.C.; Wagner, B. *Chem. Phys.* **1992**, 161, 485-491.

58. Lamola, A.A.; Hammond, G.S. *J. Chem. Phys.* **1965**, 43, 2129-2135.

59. Beljonne, D.; Cornil, J.; Friend, R.H.; Janssen, R.A.J.; Brédas, J.L. *J. Am. Chem. Soc.* **1996**, 118, 6453-6461.

60. Parker, C.A.; Hatchard, C.G. *J. Chem. Soc. Faraday Trans*, **1961**, 57, 1894-1904.

61. Sternlicht, H.; Nieman, G.C.; Robinson, G.W. *J. Chem. Phys.* **1963**, 38, 1326-1335.

62. Chen, R.; Tang, Y.; Wan, Y.; Chen, T.; Zheng, C.; Qi, Y.; Cheng, Y.; Huang, W. *Sci. Rep.* **2017**, 7, 6225.

63. Knibbe, H.; Rehm, D.; Weller, A. *Ber. Bunsenges. Phys. Chem.* **1968**, 72, 257-263.

64. Uoyama, H.; Goushi, K.; Shizu, K.; Nomura, H.; Adachi, C. *Nature*, **2012**, 492, 234-238.

65. Bhattacharyya, K.; Chowdhury, M. *Chem. Rev.* **1993**, 93, 507-535.

66. Liddell, P.A.; Kuciauskas, D.; Sumida, J.P.; Nash, B.; Nguyen, D.; Moore, A.L.; Moore, T.A.; Gust, D. *J. Am. Chem. Soc.* **1997**, 119, 1400-1405.

67. Jenekhe, S.A.; Osaheni, J.A. *Science*, **1994**, 265, 765-768.

68. Kesti, T.J.; Tkachenko, N.V.; Vehmanen, V.; Yamada, H.; Imahori, H.; Fukuzumi, S.; Lemmetyinen, H. *J. Am. Chem. Soc.* **2002**, 124, 8067-8077.

69. Wasielewski, M.R. *Chem. Rev.* **1992**, 92, 435-461.

70. Rudzki, J.E.; Goodman, J.L.; Peters, K.S. *J. Am. Chem. Soc.* **1985**, 107, 7849-7854.

71. Margulies, E.A.; Miller, C.E.; Wu, Y.; Ma, L.; Schatz, G.C.; Young, R.M.; Wasielewski, M.R. *Nat. Chem.* **2016**, 8, 1120-1125.

72. Monahan, N.; Zhu, X.Y. *Annu. Rev. Phys. Chem*. **2015**, 66, 601-618.

73. Swartz, C.R.; Parkin, S.R.; Bullock, J.E.; Anthony, J.E.; Mayer, A.C.; Malliaras, G.G. *Org. Lett.* **2005**, 7, 3163-3166.

74. Sakamoto, Y.; Suzuki, T.; Kobayashi, M.; Gao, Y.; Fukai, Y.; Inoue, Y.; Sato, F.; Tokito, S. *J. Am. Chem. Soc.* **2004**, 126, 8138-8140.

75. Thomas, K.J.; Kapoor, N.; Bolisetty, M.P.; Jou, J.H.; Chen, Y.L.; Jou, Y.C. *J. Org. Chem.* **2012**, 77, 3921-3932.

76. Appleton, A.L.; Brombosz, S.M.; Barlow, S.; Sears, J.S.; Bredas, J.L.; Marder, S.R.; Bunz, U.H. *Nat. Commum.* **2010**, 1, 91, 1-6.

77. Chan, W.L.; Ligges, M.; Jailaubekov, A.; Kaake, L.; Miaja-Avila, L.; Zhu, X.Y. *Science* **2011**, 334, 1541-1545.

78. Sanders, S.N.; Kumarasamy, E.; Pun, A.B.; Trinh, M.T.; Choi, B.; Xia, J.; Taffet, E.J.; Low, J.Z.; Miller, J.R.; Roy, X.; Zhu, X.Y. *J. Am. Chem. Soc.* **2015**, 137, 8965-8972.

79. Stern, H.L.; Musser, A.J.; Gelinas, S.; Parkinson, P.; Herz, L.M.; Bruzek, M.J.; Anthony, J.; Friend, R.H.; Walker, B.J. *Proc. Natl. Acad. Sci. U.S.A*, **2015**, 112, 7656-7661.

Chapter 5: Photophysics of a Bis-Pentacene Derivative in Fluid Solution – Qualitative Results

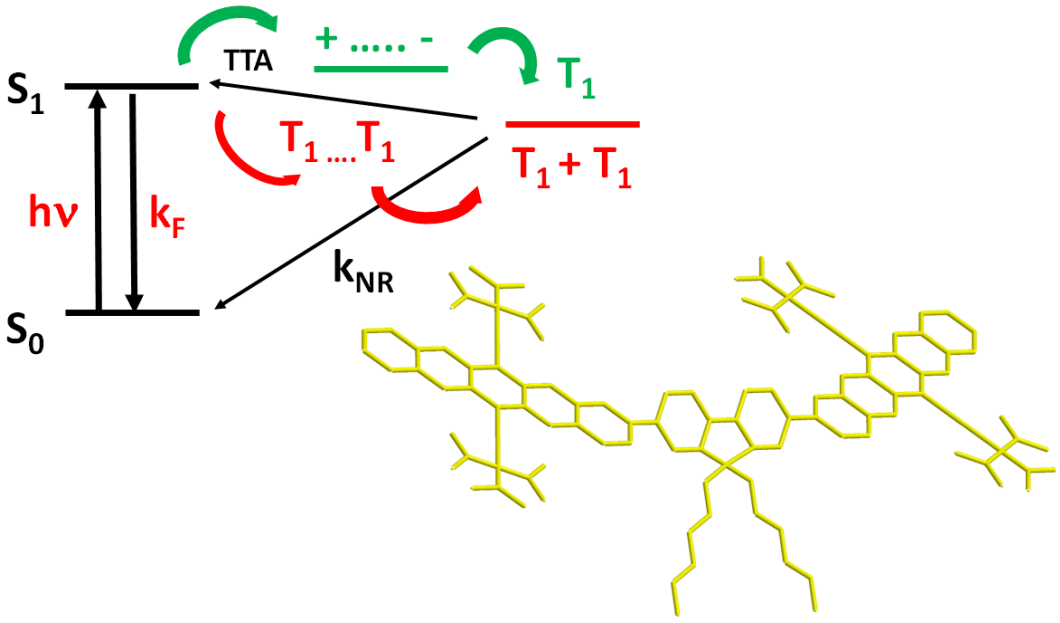

5.1 Introduction

Singlet exciton fission (SEF)[1,2] is a photophysical phenomenon whereby a pair of identical (or similar) organic chromophores, satisfying the energetic requirement that the excited singlet state energy is at least twice that of the excited-triplet state, undergoes rapid intersystem crossing into the triplet manifold. This radiationless process produces two triplet excitons (Scheme 1). As has been discussed elsewhere in this thesis, SEF was originally reported in justification of the anomalously low fluorescence yield seen in the crystal phase for certain polyacenes, such as tetracene and pentacene.[3,4] It is essentially the reverse of triplet-triplet annihilation. Singlet exciton fission is known to compete efficiently with radiative decay, under carefully controlled conditions, and triplet yields up to 200% have been observed in certain systems. It goes without saying that the two chromophores must reside within rather close proximity or be subject to quite pronounced electronic coupling.

After a period of inactivity, interest in the topic has been revived and the past few years have witnessed a massive escalation in publications dedicated to the subject. Recent investigations have focused on monitoring the process in fluid solution,[5] where two chromophores are covalently linked by way of a spacer unit. Both conjugated and non-conjugated bridges have been used for this purpose. To distinguish such systems from a condensed state of the chromophore, such as crystals or thin films, the covalently-linked analogues give rise to intramolecular singlet exciton fission (iSEF).[6-10] The advantage of this latter approach is that optical spectroscopic measurements can be made under conventional conditions, notably in dilute solution, thereby facilitating deep probing of the reaction mechanism and energetics. The intramolecular approach also allows greater control over electronic communication between the two proximal chromophores. Many singlet exciton fission bichromophores are based on TIPS-pentacene (see Chapter 4), this being perhaps the best-understood SEF compound to date. Pentacene itself is an archetypal organic semiconductor, which makes it a relevant model system for use in various opto-electronic applications.[5,11]

$$S_1 + S_0 \underset{k_{TTA}}{\overset{k_{SEF}}{\rightleftharpoons}} T_1 + T_1 \qquad (1)$$

Investigations into SEF have sought to expand the library of compounds available and to evaluate the underlying mechanism(s). There are now many bichromophores known to undergo singlet exciton fission in dilute solution or in thin films. An important characteristic of these bichromophores is that triplet quantum yields exceed 100% in the absence of an added spin-orbit coupling promoter. The topic is dynamic and highly active at the present time. Indeed, chromophores other than polyacenes have now been proposed for singlet exciton fission.[12,13] Some donor-acceptor polymers have also been shown to display the same generic effect.[14,15]

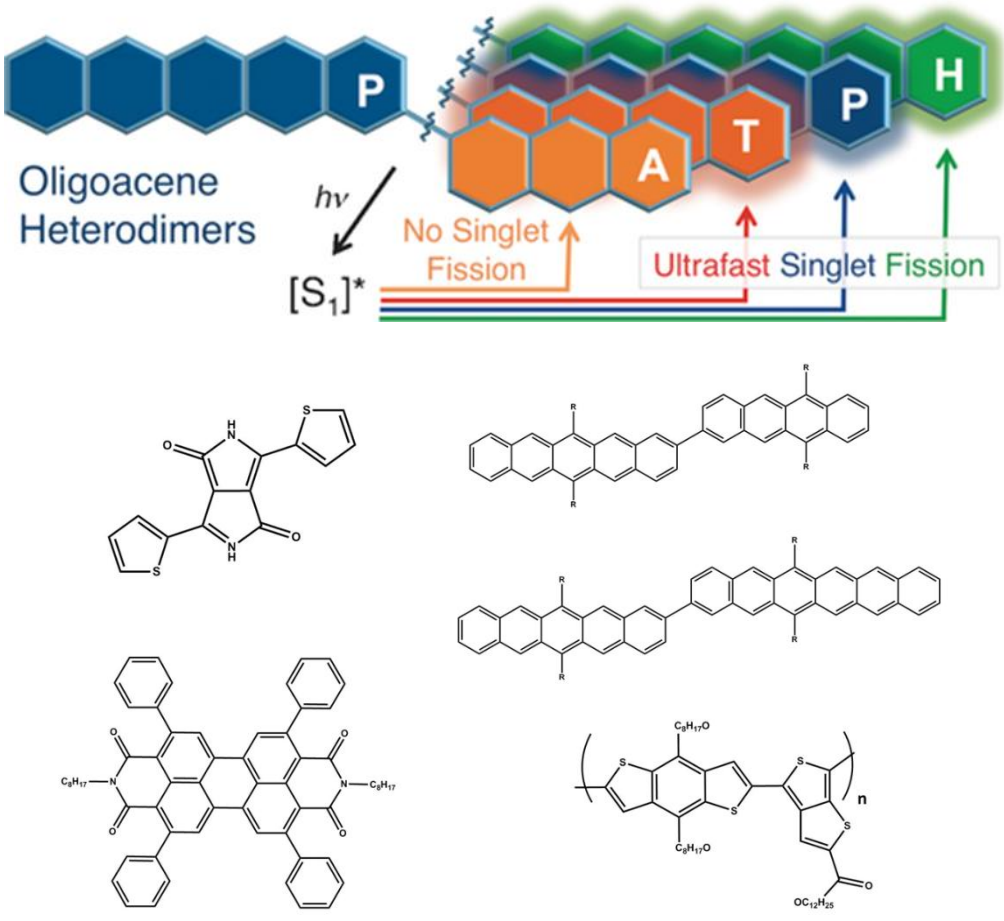

Figure 5.1. Examples of singlet exciton fission chromophores reported in the scientific literature.[16-19] Top panel adapted from reference 16.

Along with experimental studies, theoretical models abound as efforts to predict the likely efficacy increase in scope. The primary motivation for exploring SEF stems from the possibility of increasing the density of charge carriers in organic opto-electronic devices. The field, although now very active, has not yet progressed to the point where actual devices can exploit the triplet excitons. Singlet fission has been suggested as a means of enhancing solar cell efficiency by doubling the photocurrent per absorbed photon.[20,21] One of these strategies involves coupling SEF compounds to emissive nanoparticles, thereby transferring the non-emissive triplet exciton energy to an adjacent silicon solar cell as an additional layer. Such a system could utilize otherwise wasted parts of the solar spectrum.[22,23] Another putative method involves incorporating SEF compounds into organic solar cells as sensitizers.[24] Whatever the application, realizing quantitative singlet fission will be important. In the case of organic solar cells, long-lived triplets may be important for achieving efficient charge separation. Harvesting the triplet excitons presents challenges, however, due to rapid triplet-triplet annihilation. More work is surely required to fully understand the underlying mechanism(s) and compounds would need to become available on a commercial scale.

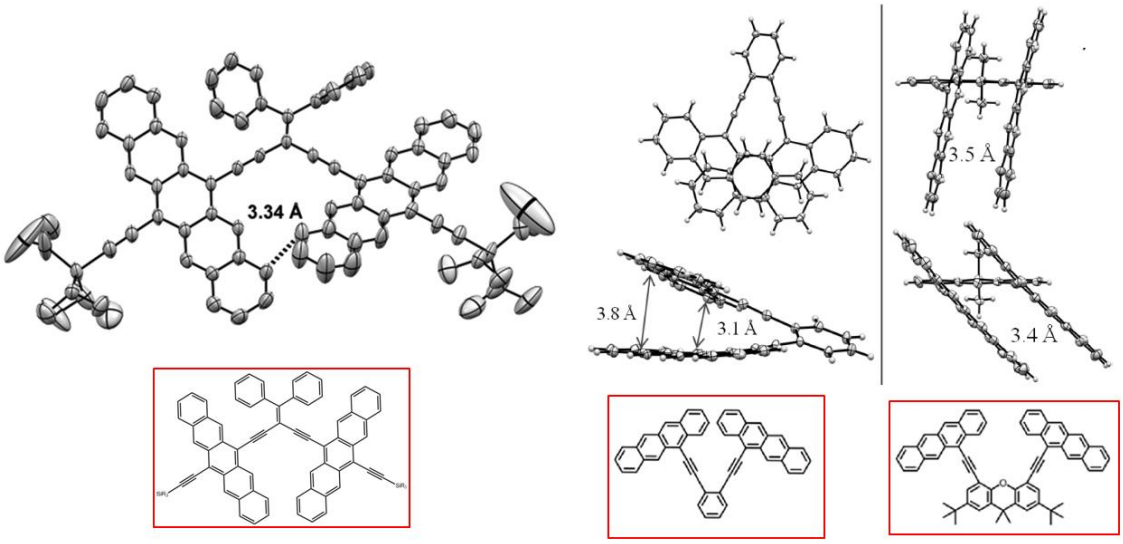

Figure 5.2. Example of literature iSEF compounds where obtained crystal structures highlight the geometry between polyacene units, mediating singlet fission.[9,25]

In this chapter, we are primarily concerned with intramolecular singlet exciton fission, but a few words are in order regarding crystalline materials. In crystalline pentacene, the lowest-lying excited state is understood to localize on a pair of pentacene monomers.[26] There is some debate as regards how this dark state dephases into a pair of triplets, but it is known that the process occurs very quickly (<1 ps), with minimal stimulated emission.[27-29] In pentacene, the process is thought to be spontaneous due to the energy of the singlet-excited state being slightly more than twice that of the lowest-lying triplet (although the energy of the pentacene triplet is not known with certainty, as discussed in Chapter 4). The energetics also allow for triplet-triplet annihilation, and the decay rate of the triplet is controlled, in part, by morphology.[30] The role of inter-chromophore coupling is just as important as the energetic requirement, but this is not thoroughly understood in the crystal phase. The main advantage of studying iSEF in bichromophores is the relative ease with which spectroscopic characterization can be undertaken.

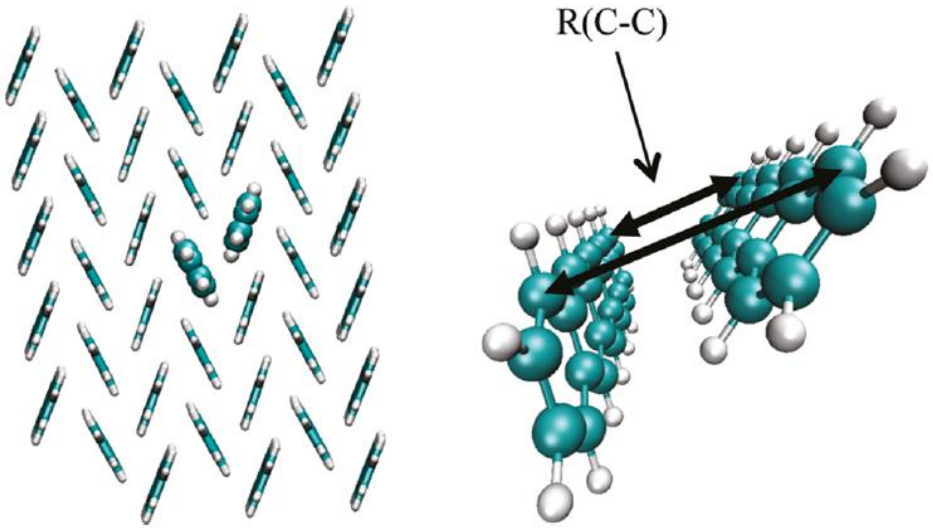

Figure 5.3. Illustration of packing in crystalline pentacene. The close proximity of pentacene molecules in the solid allows for effective intermolecular singlet fission.[26]

Progress in understanding the mechanistic origin of SEF has been rapid, but we still lack a thorough comprehension of this process. A set of guidelines for rational design of singlet exciton fission chromophores seems far off. Subtleties in different SEF systems are introduced by restricted geometry and by altering the bridging ligand. Super-exchange interactions and charge-transfer states have been implicated as playing a role in enhancing intersystem crossing. It therefore seems unlikely that there will be a unified

model for singlet fission across a wide range of compounds.[26,31,32] What is apparent in covalently-linked, singlet exciton fission is that the nature of the bridging group has a pivotal role in mediating the rate of intersystem crossing and intramolecular triplet-triplet annihilation. Many publications refer to the formation of a spin-correlated triplet pair which dephases into two separate triplets. The identity of the triplet pair is difficult to establish with classical optical spectroscopy.[33] Electron paramagnetic resonance measurements have been used as an alternative means of analyzing the triplet.[1,34] The kinetics of iSEF are further complicated by the complementary influences of through-space and through-bond interactions. These uncertainties combine to make an extremely challenging and attractive subject.

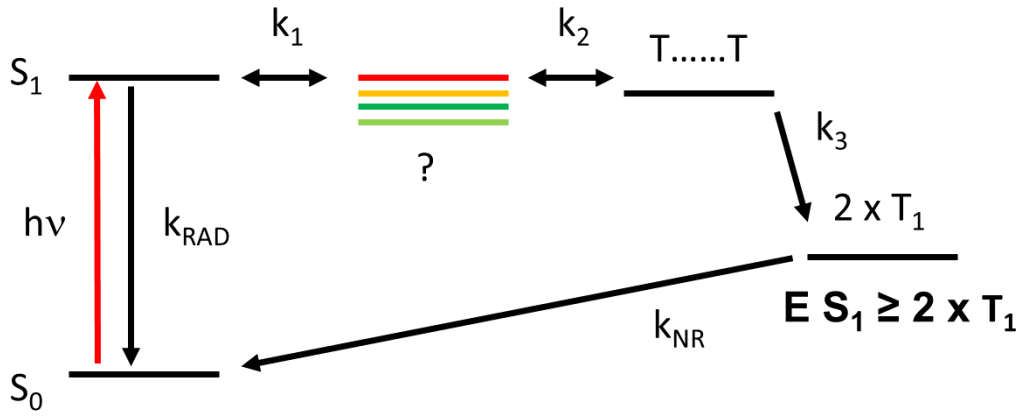

Figure 5.4. A schematic energy level diagram for the singlet fission process. Many investigators have invoked an intermediate state between the singlet- and triplet excited states to account for the high rate of intersystem crossing.

This chapter introduces a new iSEF bichromophore based on TIPS-P and following what might be termed conventional lines. The compound was synthesized and characterized in the Molecular Photonics Laboratory by Dr. Alparslan Atahan and the chemical formula is sketched in Figure 5.5. It will be recalled that Chapter 4 contains a summary of the photophysics of the monomer in fluid solution. An important feature of this compound relates to the rather large spacer group used to connect the two pentacene chromophores. The spacer is formed from a fluorene residue, suitably derivatized to improve solubility, which is rigid but allows rotations about the terminals. We do see triplet yields in excess of 100% following excitation into the pentacene chromophore but, to our surprise, we observed that the absorption spectra recorded for both excited-

singlet and excited-triplet states differ from those reported earlier for TIPS-P. This disparity suggests that delineating the level of communication between the pentacene-based end-groups might be less than straightforward.

[*NB The concept of intramolecular singlet exciton fission was expanded greatly in recent years and it is no longer interesting to simply report one more example. We have tried, therefore, to dig deeper into the accompanying processes and avoid emphasizing the yield of triplet. The downside of this approach is the length of the chapter. To aid the reader, the work has been split into two more manageable drafts. Chapter 5 deals with the basic results while Chapter 6 covers more advanced features.*]

5.2 Results and Discussion

Synthetic procedures for the target dye, the bridged bis-pentacene bichromophore (BBP), were devised by Dr. Atahan of this Laboratory and will be reported in full in a forthcoming publication. The purity of the compound was confirmed by way of high-resolution NMR and mass spectrometry. The compound was found to have good solubility in toluene, the solvent of choice for this work, and reasonable solubility in other solvents such as MTHF. In all cases, the solution was checked to ensure full solubility before undertaking any measurements. Solutions were prepared fresh and used within a few hours. A computerized model constructed for BBP shows an extended geometry with the two pentacene units being held at an oblique angle. Rotation around the connecting C-C bonds at the chromophore-spacer interface is possible.

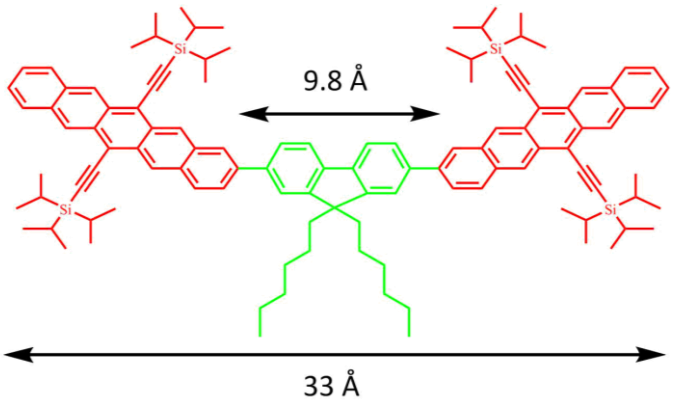

Figure 5.5. Molecular formula for BBP. The mean dihedral angle between fluorene bridge (green) and TIPS-pentacene units (red) is 36^{o} as determined by ab initio molecular dynamics simulations in the gas phase.

5.2.1 Steady-State Spectroscopic Measurements

The bis-pentacene bichromophore was interrogated under the same conditions as reported earlier for TIPS-pentacene (TIPS-P) in Chapter 4. Steady-state absorption and emission spectra show the lowest-energy π-π* transition to have the same spectral profile as for TIPS-P, but red-shifted by 280 cm^{-1}. This shift can be explained in terms of extended conjugation with the fluorene spacer group and has been reported for other non-orthogonal bis-pentacene compounds.[16,35] Additional higher-energy bands can be seen at wavelengths below 450 nm. The excitation spectrum is considered to be in good agreement with the absorption spectrum. Also, the molar absorption coefficient approximately doubles from ~ 20,000 for TIPS-P to 40,000 M^{-1} cm^{-1} for BBP. These features are suggestive of electronic coupling between spacer and chromophore or even between chromophores. The new absorption bands appear in the excitation spectrum and, therefore, are not due to impurities in the sample. Indeed, samples were subjected to extensive TLC purification immediately before recording the spectra but this had no effect on the spectral profile. At least two separate batches of BBP were used for these trials, with no obvious difference.

The fluorescence quantum yield (Φ_F) is drastically reduced relative to TIPS-P under closely comparable conditions; Φ_F is measured to be 3% in dilute toluene solution (determined relative to *meso*-tetraphenylporphyrin).[36] The emission spectral profile remains similar to that of TIPS-P, apart from the red-shift. In toluene, the excited-singlet state lifetime is decreased (from 14 ns) to 200 ps, a result obtained both by TCSPC and ultra-fast transient absorption experiments. This finding indicates there is a new nonradiative process that competes effectively with radiative decay. The fluorescence quantum yield was also found to be ca. 3% in chloroform.

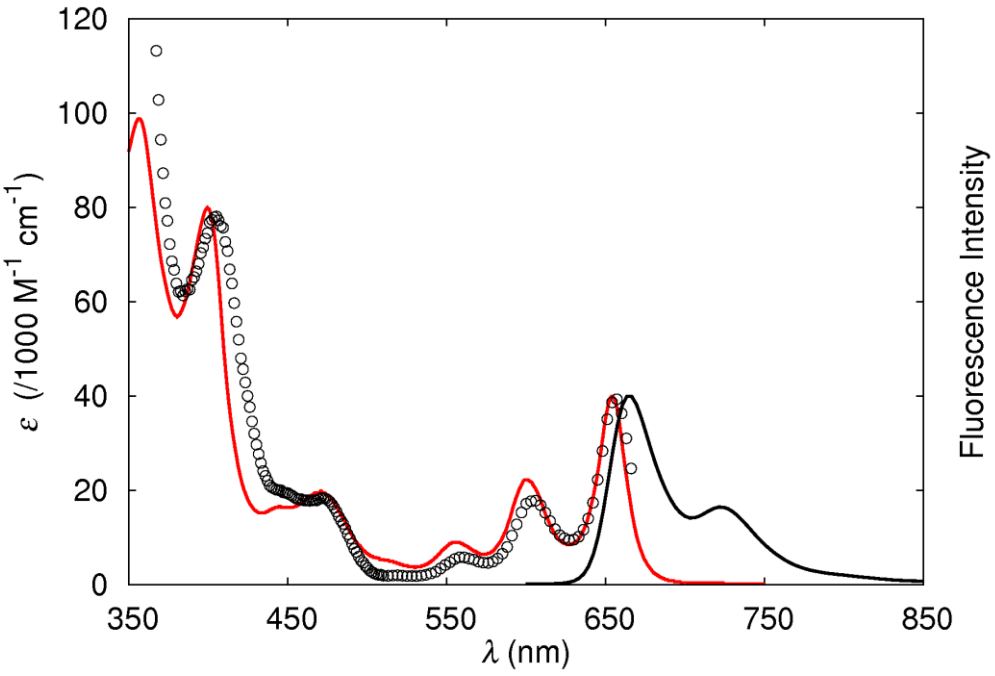

Figure 5.6. Steady-state absorption and emission spectra for BBP in μM toluene solution. The excitation spectrum is overlaid onto the absorption spectrum with circles.

Low-temperature fluorescence measurements in methylcyclohexane and 2-methyltetrahydrofuran show a slight red-shift (approx. 10 nm) and a sharpening of the spectrum upon stepwise cooling from room temperature to 80 K. The fluorescence signal was corrected for solvent contraction[37] and spectral shifts at the excitation wavelength in order to explore how the nonradiative rate constant depends on temperature. Both in the case of methylcyclohexane and MTHF, there is little change in the fluorescence quantum yield over this temperature range. We conclude therefore that the nonradiative process competing with fluorescence is essentially activationless. Slight variations in the derived fluorescence quantum yield at low temperature (Figure 5.8) correspond to previously reported changes in solvent relaxation for organic dyes in MTHF.[38]

Low-temperature fluorescence measurements made for BBP in a nonpolar film, Zeonex 480, show no red-shift relative to toluene and almost no sharpening of the spectrum upon cooling to 80 K. In agreement with the solution studies, the fluorescence yield increased by less than 2% across the full temperature range. The fluorescence yields in the film and in the frozen glass were derived from fluorescence lifetimes obtained by time-correlated, single photon counting on the basis that the radiative rate constant is

fixed. The derived activation energy for radiationless decay is 6.7 kJ mol^{-1} in Zeonex, but this is considered to be on the lower limit of what can be measured. These temperature-dependence studies suggest light-induced electron transfer is not the dominant nonradiative pathway. There is no indication for exciplex emission at any temperature. This latter observation is not surprising because, at high dilution, there is little possibility for orbital overlap between the aromatic units.

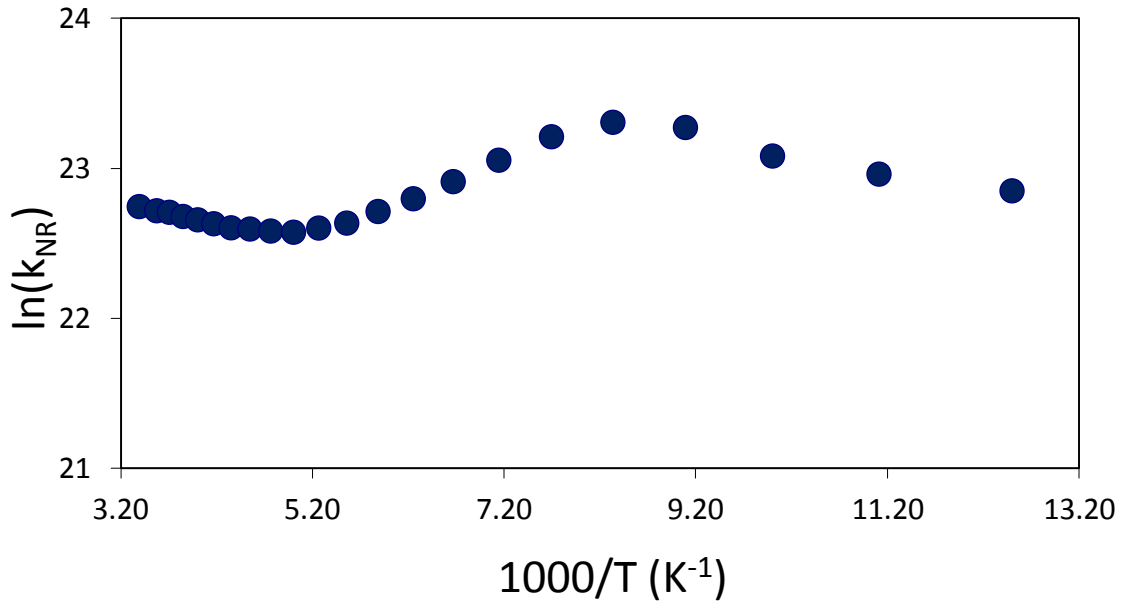

Figure 5.7. Arrhenius plot for BBP in 2-methyltetrahydrofuran between 80 and 295 K.

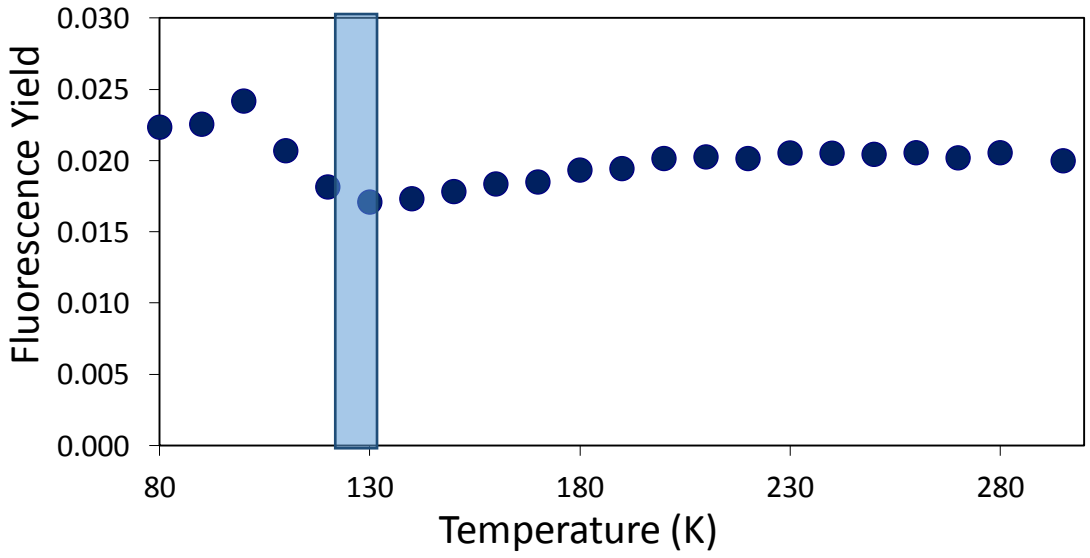

Figure 5.8. Fluorescence quantum yield of BBP in MTHF versus temperature. The solvent melts at 137 K (see blue region) and forms a rigid glass at about 100 K.

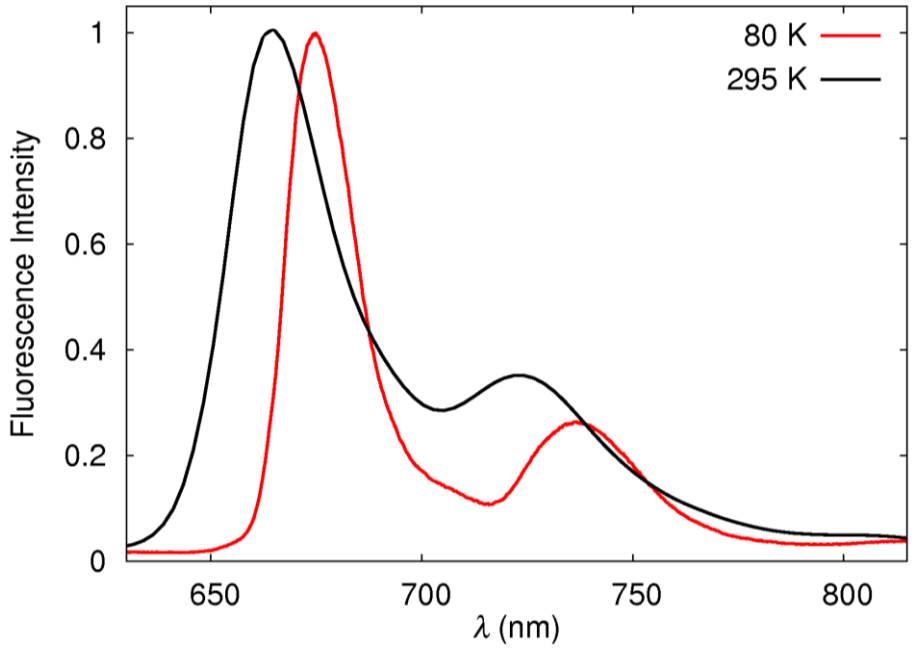

Figure 5.9. Normalized emission spectra of BBP in MTHF at room and cryogenic temperatures.

The spectral shift and band narrowing seen for BBP at low temperature is consistent with that observed earlier for TIPS-P and is a natural consequence of rigidifying the solvent. The lack of any significant temperature effect on the nonradiative decay rate constant is attributed to the main deactivation process being activationless. This finding is in line with expectations if the deactivating channel involves singlet exciton fission. Thus, Friend *et al*. reported activationless singlet exciton fission over a wide temperature range for thin films of tetracene.[39] There is, in fact, no obvious reason for singlet exciton fission involving an activation energy – although the absence of an activated barrier does not by itself prove that the enhanced nonradiative decay observed for BBP is primarily due to intramolecular singlet exciton fission. We could find no literature reports of a temperature-dependence study for intramolecular singlet exciton fission.

The rate constant for this new deactivating channel is 3.6×10^9 s^{-1}, which is low relative to values reported for crystals and thin films of pentacene. Numerous bis-pentacene derivatives have been reported to undergo intramolecular singlet exciton fission with a wide variety of rate constants. The magnitude of these rate constants reflects the

molecular topology and comparison is difficult because some structures might better facilitate through-space processes. For BBP, it seems most likely that the geometry will promote through-bond interactions between the two terminal pentacenes. The closest structural analogue to BBP that we could find in the literature is BP2 as reported by Campos *et al*.[33] Here, the rate constant for intramolecular singlet-exciton fission is 4.3 x 10^9 s^{-1}. This value is in excellent agreement with our determination for BBP.

5.2.2 Nanosecond Time-Resolved Optical Measurements

Nanosecond transient absorption experiments in toluene with excitation at 532 nm show the presence of a triplet species with an absorption maximum centred at ca. 515 nm (Figure 5.10). Contrary to TIPS-P, the excited-triplet state can be seen at low concentration in fluid solution without the aid of an external heavy-atom perturber, such as ethyl iodide. Also of note is the observation that the structured absorption of the T_1-T_3 optical transition seen for TIPS-P is replaced with a broad and featureless absorption band for BBP. The long-lived decay conforms to first-order kinetics with a lifetime of ca. 40 μs in well deoxygenated toluene. Decay of the absorption signal at 515 nm is exactly matched by the rate of recovery of the ground-state bleach. The transient absorption signal in the region around 515 nm does not shift on the microsecond timescale, but it sharpens slightly, with a shoulder becoming ever more pronounced at later times. Further bleaching signals corresponding to absorption at the high-energy bands suggest these features are part of the same electronic system and are not due to impurities. Typical energies per pulse for nanosecond excitation were varied across the range 5-80 mJ.

On focusing attention on the decay kinetics in the 0-50 ns time window, triplet-triplet annihilation (TTA) was apparent and a short-lived fluorescence signal was observed with a maximum at ca. 665 nm. We assign this latter emission signal to delayed fluorescence. An estimate of the half-life for this signal places it at around 30-50 ns. This is clearly too long for the signal to be due to prompt fluorescence but it is entirely consistent with intramolecular TTA. The half-life recorded for the delayed emission is independent of laser intensity over a wide range. For BBP in deoxygenated toluene, the appearance of the transient spectra did not change when the excitation wavelength was varied

between 530-600 nm. Previous work has recognized the importance of bimolecular TTA for tetracene[27] in thin films while intramolecular TTA has been found in certain orthogonally orientated bis-pentacene derivatives.[35] The occurrence of TTA in our bis-pentacene derivative is highly significant because it would suggest that the excitation energy of the triplet-excited state cannot be much less than one-half that of the excited-singlet state. This is believed to be the case for tetracene. We will return to the possibility of TTA in BBP later in the chapter. It is important to note, however, that the concentration of excited-triplet state found at high laser intensity is roughly 5 μM, compared to a ground state concentration of around 10 μM. This means that, at high excitation densities, about 25% of the available pentacene chromophores are promoted to the triplet state at the beginning of the experiment. The important point is to establish how these triplet states are distributed; specifically, we refer to whether both pentacenes belonging to a single BBP molecule are at the triplet level.

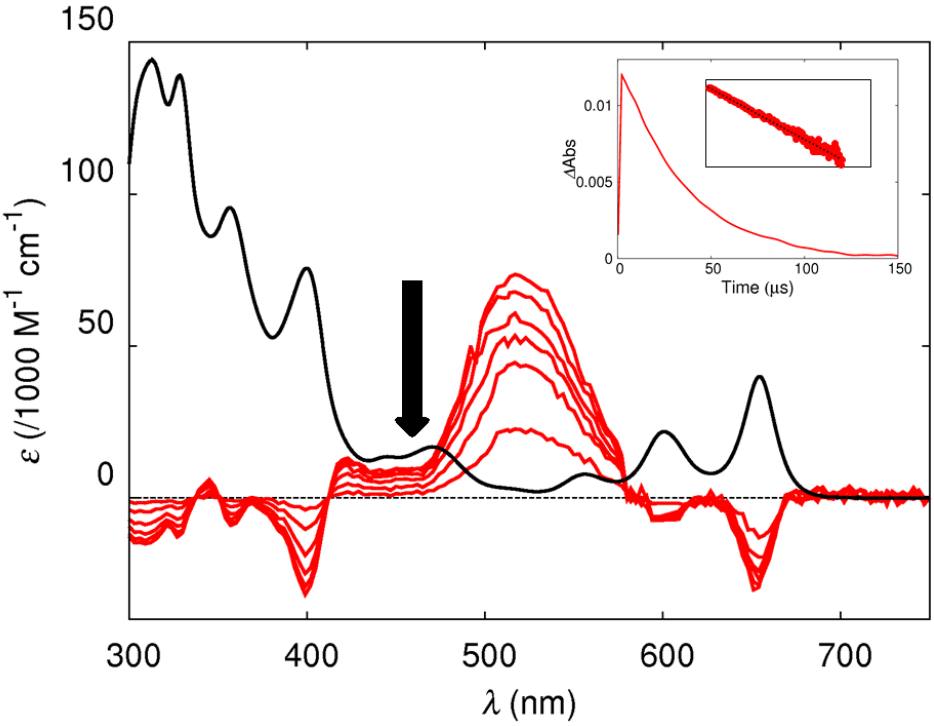

Figure 5.10. Red traces: nanosecond transient absorption spectrum recorded for BBP (between 3 and 35 μs) in deoxygenated toluene solution in terms of molar absorption coefficient. Black trace: steady-state absorption spectrum for BBP. Inset: decay of transient species at 520 nm with a semi-log plot showing decay conforms to first-order kinetics.

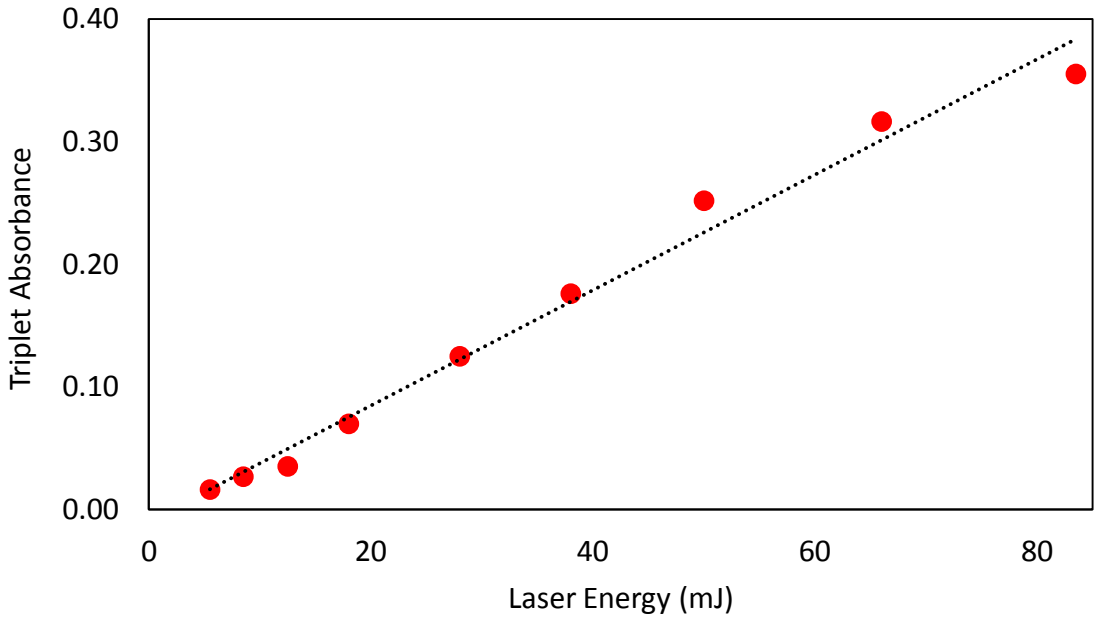

Figure 5.11. Triplet absorbance in deoxygenated toluene at 520 nm excitation vs laser energy. Excitation is at 532 nm.

In summary thus far, there are notable disparities in the optical spectra and properties between the reference compound TIPS-P and the bis-pentacene derivative BBP when measured under the same conditions. Unfortunately, we do not have access to the mono-pentacene derivative equipped with the fluorene bridge so we are not able to say if these differences are caused by the close proximity of two poly(acene) units or by interaction with the spacer. Of particular concern is the observation that the transient differential absorption spectrum recorded for the triplet-excited state is broad for BBP but well-resolved for TIPS-P. To confirm that our identification is correct, a set of pulse radiolysis experiments was made with BBP in deoxygenated benzene and toluene solution. As before, these measurements were made in the laboratory of Prof. T. Majima in Osaka. The temporal resolution of this instrument is ca. 8 ns and benzophenone in de-aerated benzene or toluene was used as the dosimeter.

The first point to note from these pulse radiolysis studies is that the broad and relatively featureless absorption profile for the *meta*-stable triplet state is similar to that observed by ns-laser flash photolysis (Figure 5.12). The spectrum evolves slightly with time, with the maximum undergoing a small shift from 525 nm to 515 nm on the timescale of the experiment. The conditions used for these pulse radiolysis experiments preclude simple determination of the concentration of the triplet-excited state by comparison to the benzophenone dosimeter. This is because, at the end of the pulse, there is a mixture of the benzene singlet- and triplet-excited states present. Both states are short lived but able to transfer excitation energy to the added BBP. We do not see the excited-singlet state of BBP but this is because its lifetime is less than the temporal resolution of the setup. We can use the pulse radiolysis data in a constructive manner but, for the moment, we draw attention only to the fact that the derived differential absorption spectrum is closely comparable to that obtained by laser flash photolysis. We will return to the pulse radiolysis experiments at a later stage in the discussion.

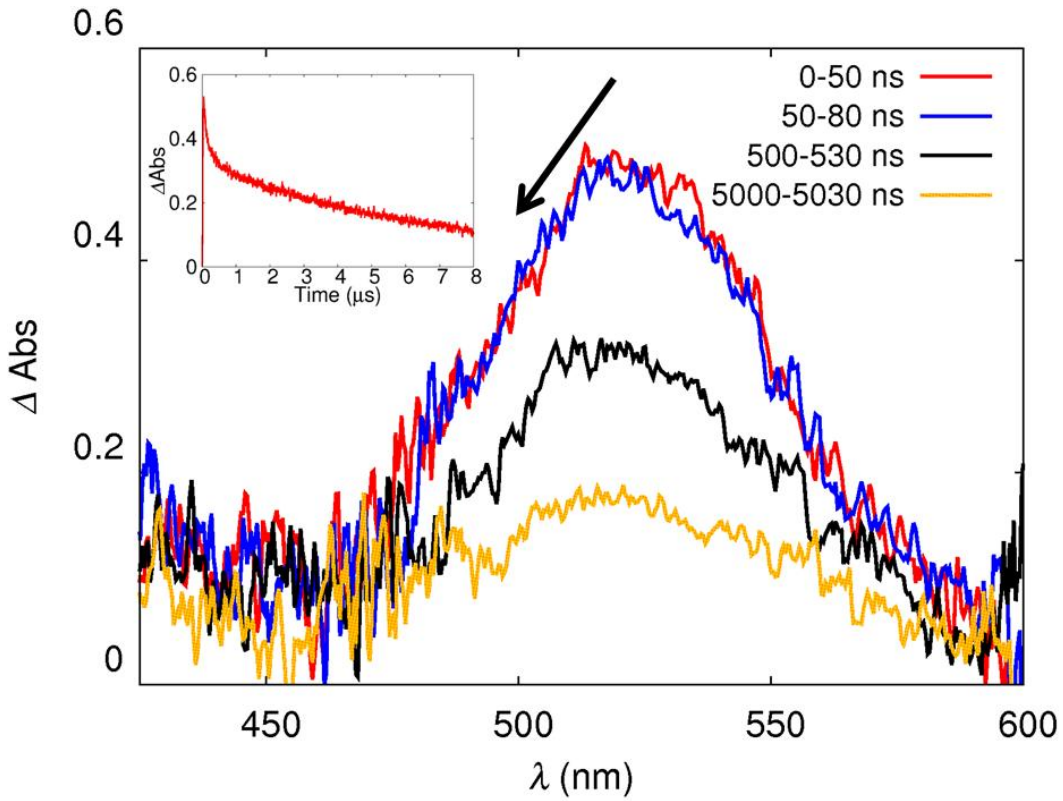

Figure 5.12. Transient absorption data for BBP from pulse radiolysis experiments in benzene (0.7 mM concentration). Decay trace at 524 nm inset showing biexponential character.

Pulse radiolysis of BBP clearly show bi-exponential character for the decay curves attributed to the triplet-excited state (Figure 5.12 inset). We see the same behavior for the triplet species generated by laser photolysis. This situation could indicate the onset of intermolecular triplet-triplet annihilation, although this was not seen for TIPS-P under the same conditions. There are many reports of triplet-excited states being quenched by the corresponding ground-state species – the first such report was by Livingston[40] and referred to the triplet state of chlorophyll-a in ethanol solution. This might also be the case for BBP but quenching by BBP molecules in the ground state would not give rise to the mixed-kinetics (i.e., a fast decay superimposed on a slower decay) observed here for the triplet-excited state.

The kinetic profile is superficially consistent with a fast decay (some tens of nanoseconds) competing with a slower exponential decay of the triplet-excited state (microseconds). This behaviour would be consistent with bimolecular TTA at early times, where the concentration of the triplet state is relatively high, followed by unimolecular deactivation of the triplet at longer times. This situation corresponds to the conventional TTA as first outlined by Birks.[41] All attempts to analyze the data as a fast second-order decay and a slower exponential decay failed in our hands. In contrast, the decay curves from both pulse radiolysis and laser flash photolysis could be analyzed satisfactorily in terms of dual-exponential fits. This situation is readily explained in terms of fast intramolecular TTA, followed by relatively show first-order decay of the remaining triplet species.

Fitting the pulse radiolysis triplet decay data observed at 524 nm to consecutive first-order components yield a lifetime for the faster process is 100 ns in de-aerated benzene with the slower component being ca. 6.5 μs. The same behaviour is observed in de-aerated toluene, with lifetimes of 90 ns and 5.3 μs. Examination of the longer decay component on a longer timebase brings the longer lifetime in line with flash photolysis experiments. This type of analysis gives a satisfactory fit to the experimental data but does not explain the underlying chemistry. That we do not see evidence for intermolecular TTA with either BBP or TIPS-P suggests that the bulky TIPS groups hinder close contact between pentacene molecules. The only reasonable explanation for

efficient intramolecular TTA in BBP is that a substantial fraction of excited-state BBP species are formed with both pentacene units promoted to the excited-triplet state. It is the dual-excited species that give rise to intramolecular TTA. The only way to generate the dual-triplet species is through intramolecular singlet exciton fission. This process can take place following both pulse radiolysis and pulsed laser excitation. If this deduction is correct, we have a simple way to distinguish between intersystem crossing (to give the mono-triplet) and singlet exciton fission (to give the dual-triplet). It is also possible that the different rates of decay of these two triplets helps account for the modest evolution of the differential absorption spectral features. The timescales are consistent with this possibility.

Our understanding of the situation is covered by Scheme 13. Here S, T and G refer to pentacene units in the excited-singlet, excited-triplet and ground states, respectively. The scheme applies to both pulse radiolysis and pulsed laser photolysis, although the Scheme emphasizes the pulse radiolysis case. Before attempting to quantify some of these processes, we draw attention to the cyclic voltammetry studies before returning to the transient absorption spectroscopy. This is to explore any possible role for light-induced electron transfer competing with the reactions illustrated in the Scheme.

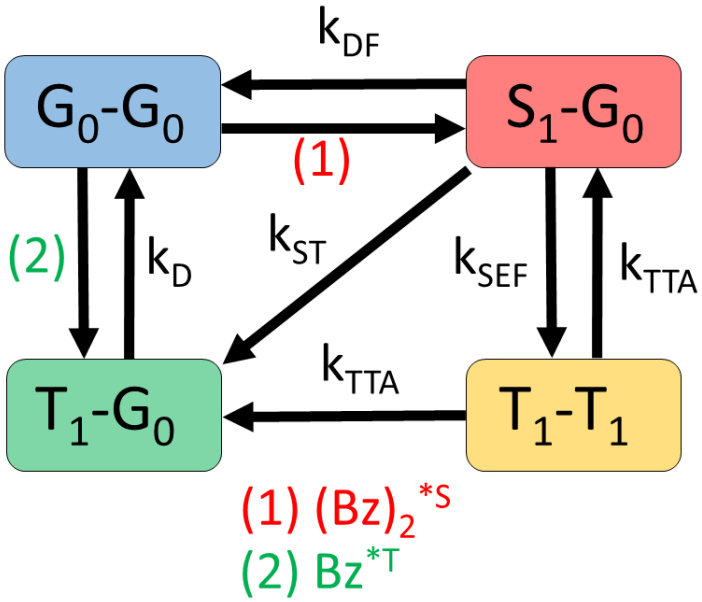

Figure 5.13. Scheme for the process of singlet fission during pulse-radiolysis experiments. SEF = intramolecular singlet-exciton fission, D = nonradiative decay, TTA = intramolecular triplet-triplet annihilation, DF = delayed fluorescence. ST = singlet to triplet.

5.2.3 Electrochemistry

Electrochemical measurements of BBP were performed under a dry nitrogen atmosphere in anhydrous dichloromethane with tetra-N-butylammonium hexafluorophosphate as the supporting electrolyte. A highly polished glassy carbon disk was used as a working electrode with a platinum wire as the counter electrode. The reference electrode was Ag/AgCl, with ferrocene as an internal reference. These are the same conditions as used for TIPS-P (Chapter 4).

For TIPS-P, the oxidation wave with a mid-point potential of +0.56 V vs Ag/AgCl can be assigned to formation of the radical cation species. For BBP one would expect an additional reversible oxidation wave for the formation of the doubly-oxidized species.[43] Indeed, literature reports show two separate one-electron oxidation waves for some bis-pentacene derivatives; splitting of the peak is a sign of electronic or electrostatic interactions between the two terminal pentacene units.[8] A small series of bis-pentacene compounds with poly(aryl) bridges has been used to show that the magnitude of through-bond electronic communication decreases with increasing length of the spacer group. Somewhat surprisingly, we observed a single peak for the first oxidation and first reduction processes for BBP, both processes being electrochemically *quasi*-reversible. That is to say, there is no splitting of the electrochemical peaks. This situation could be interpreted in terms of very strong or very weak electronic coupling between the two pentacene units. The respective half-wave potentials derived for one-electron reduction and oxidation of BBP are -1.25 and +0.56 V vs Ag/Ag^+. A second quasi-reversible reduction process is seen with a half-wave potential of -1.76 V vs Ag/Ag^+. On oxidative scans, a further oxidation step occurs with a peak potential of ca. +1.3 V vs Ag/Ag^+ but this process is electrochemically irreversible.

Table 5.1. Summary of quasi-reversible redox potentials for TIPS-P vs BBP in dichloromethane versus Ag/Ag^+. Ferrocene was used as an internal standard.

Compound	**$E_{1/2}$ OX / V**	**$E_{1/2}$ RED / V**
BBP	+0.56	-1.25

The electrostatic repulsion between two single charges located at the centre of each pentacene moiety can be estimated from Equation 5.1. Here, ε_S is the static dielectric constant of the solvent, ε_0 the permittivity of free space and d_{CC} is the estimated separation distance. For CH_2Cl_2 (ε_S = 9) and with d_{CC} = 23 Å, we would expect a repulsion energy of ca. 70 meV. This is necessarily a crude calculation but one that is used widely to explain electronic communication in many binuclear systems. As shown in Figure 5.14, BBP does not exhibit the anticipated peak splitting at either oxidation or reduction levels.

$$q = \frac{e^2}{4\pi\varepsilon_0\varepsilon_s d_{CC}} \qquad (5.1)$$

On further examination of the cyclic voltammograms recorded for BBP it can be seen that the various waves are somewhat broader than found for TIPS-P and the potential difference between peaks found for forward and reverse scans is larger than usual; typical potential splits are 200 meV at a scan rate of 200 mV/s. In fact, the difference between the peak potentials and half-wave potentials for each of the two reduction processes amounts to 60 meV at slow (i.e., 30 mV/s) scan rates. Both electrochemical steps can be attributed to the simultaneous transfer of two electrons; the same analysis made for TIPS-P under identical conditions corresponds to the transfer of a single electron. For the first oxidation process, the respective potential difference between peak and half-wave potential at very slow scan rates is 65 meV. Again, this is more consistent with the simultaneous addition of two electrons than a one-electron step. We can conclude, therefore, that each wave seen in the cyclic voltammograms for BBP corresponds to the simultaneous transfer of one electron to (or the removal of one electron from) each pentacene unit.

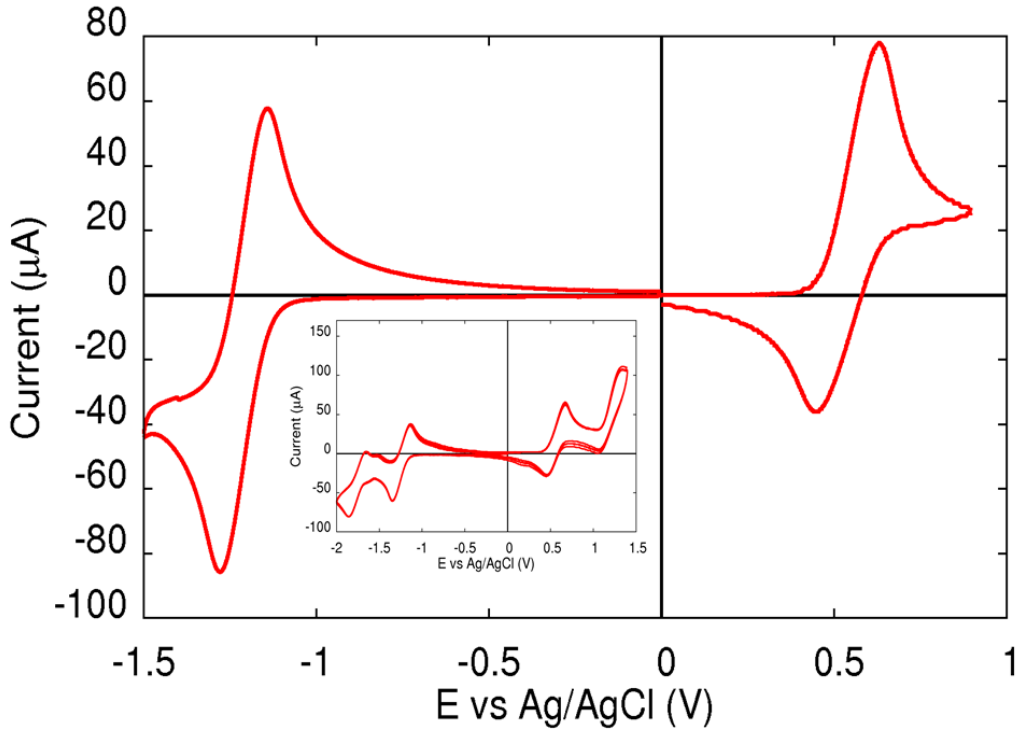

Figure 5.14. Cyclic voltammogram of BBP in de-aerated dichloromethane. Scan speed 0.08 V/s. Inset: expanded CV showing additional electrochemical processes.

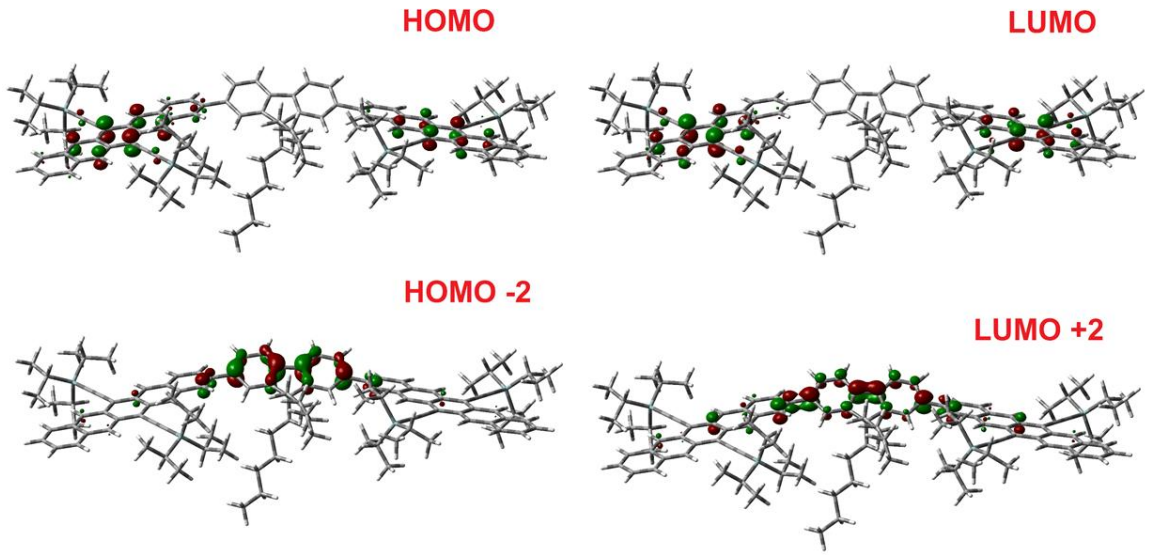

Figure 5.15. Frontier molecular orbitals for BBP calculated using density functional theory with the 6-311d basis set and B3LYP functional. The solvent was chloroform.

Frontier molecular orbital descriptions (Figure 5.15) indicate that both HOMO and LUMO correspond to localized electronic systems with the electron density distributed on the pentacene moieties. The fluorene-based bridge is not involved until much higher energies. Our failure to observe splitting of the peaks in the cyclic voltammograms is

mostly likely due to the fact that these systems cannot be regarded as point charges. The important conclusion, however, is that BBP comprises two electronically isolated pentacene units. As such, there is no reason why intramolecular singlet-exciton fission should not be detected in this compound. We now return to the transient absorption spectral studies.

Although the ultrafast transient spectra show no evidence of the formation of intermediate species such as radical cation-anion species or an exciplex, these may be obscured by the broadening of the S_1 state in the case of BBP. It was possible to obtain the steady-state absorption spectra of the radical anion and radical cation species for BBP by photochemical oxidation and reduction as it was with TIPS-P.

To obtain the radical anion and cation the same methods were used as for the TIPS-pentacene monomer (ref. Chapter 4). For BBP, as with TIPS-pentacene, the anion and cation are colourless with the cation having prominent absorption features further into the UV-region and a transition at ~ 410 nm (Figure 5.16).

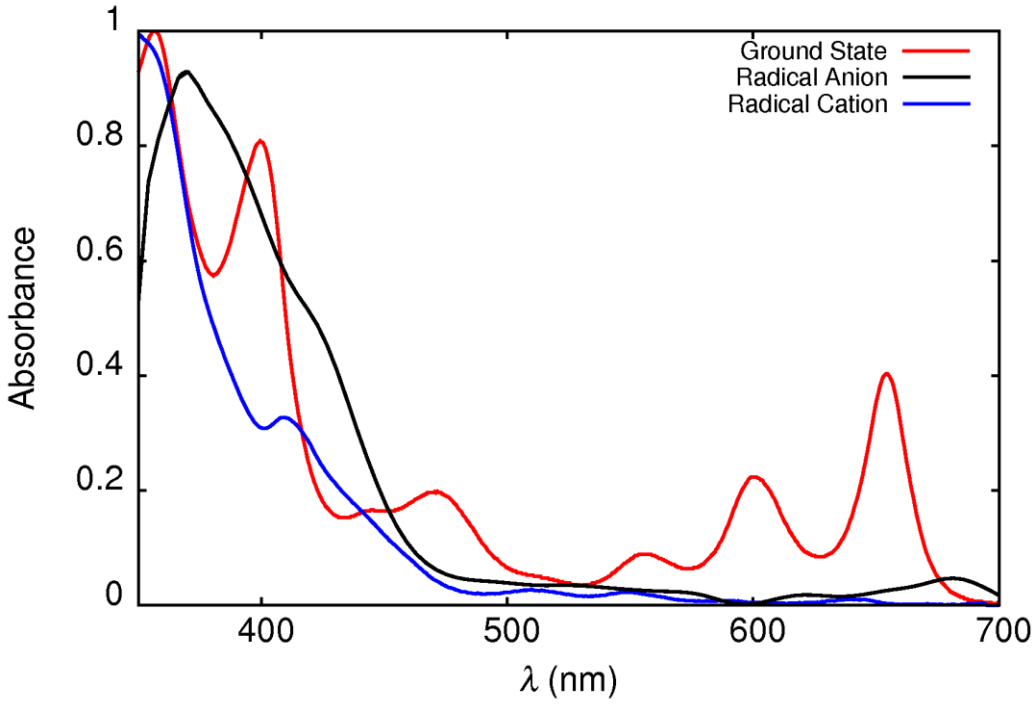

Figure 5.16. Normalized steady-state absorption spectra for BBP radical anion and cation species.

5.2.4 Ultrafast Transient Absorption Spectroscopy

Deactivation of the singlet-excited state and subsequent population of triplet excitons can be monitored by ultrafast laser transient absorption spectroscopy (Figure 5.17). Initial studies were made with laser excitation (FWHM = 150 fs) of BBP in toluene at 600 nm. This corresponds to excitation into the S_1 state and, at the end of the excitation pulse, the excited-singlet state is the sole transient species in solution. The differential absorption spectrum recorded with a delay time of a few ps comprises stimulated emission, ground-state bleaching and absorption of the S_1 state. Monitoring decay kinetics at wavelengths corresponding to each of these three processes shows that the S_1 lifetime is 200 ps under these conditions. The derived lifetime is in excellent agreement with that determined by TCSPC methods. The stimulated emission spectrum closely resembles that of prompt fluorescence while the ground-state bleaching signal clearly agrees with the ground-state absorption spectrum. However, the transient absorption spectrum differs from that recorded in Chapter 4 for TIPS-P. For BBP, the S_1-S_3 absorption spectrum is broadened and has an offset baseline relative to that of TIPS-P under identical conditions.

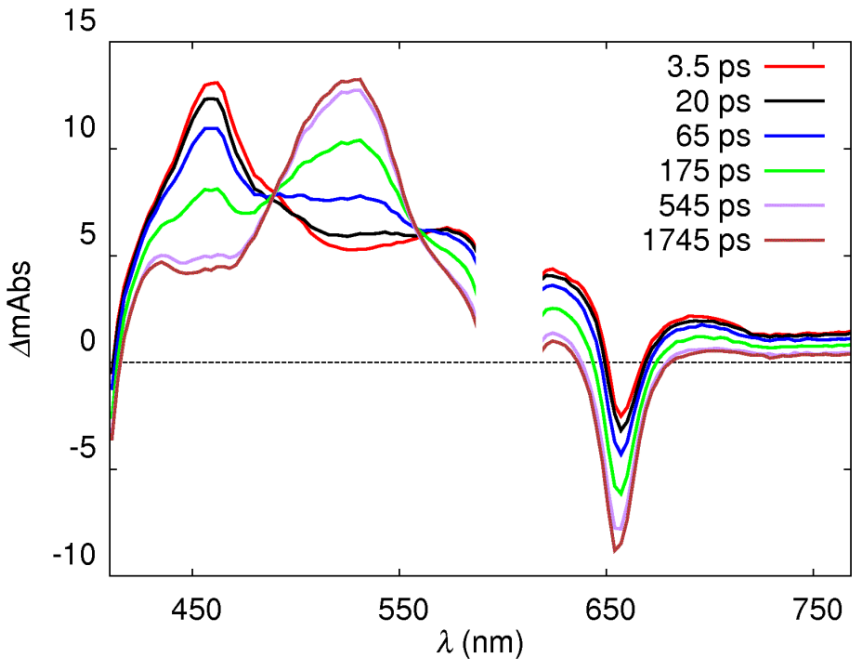

Figure 5.17. Picosecond transient spectra of BBP in toluene upon excitation at 600 nm. A section of the spectrum has been removed due to excitation scatter. Typical excitation power was ~ 1.5 mW.

At longer delay times, the triplet-excited state of BBP appears. Due to the broadening of the spectrum, it is not possible to confirm or eliminate the existence of any intermediate transient species. Formation of the excited-triplet state can be followed most conveniently at 520-525 nm, which corresponds primarily to the peak of the differential absorption spectrum. Growth of this signal follows first-order kinetics and corresponds to a lifetime of 200 ps in toluene using global fitting. Clearly, there is good agreement between decay of S_1 and formation of T_1 (Figure 5.18). This *meta*-stable species decays on a timescale far longer than can be accessed with the delay stage. We have already explained that the T_1-T_3 absorption spectrum for BBP is different to that found for TIPS-P under the same conditions. At first glance, the T_1-T_3 differential absorption spectra recorded on sub-ns and μs timescales look similar but closer inspection shows the match is imperfect. This finding is consistent with pulse radiolysis data at early times described already in this chapter (Figure 5.12). The main differences relates to a blue shift, which sees the absorption maximum move from 525 nm to 515 nm, and a modest narrowing of the entire profile. This change occurs over a period of ca. 250 ns. These absorption spectral changes are best explained in terms of two overlapping features, of which one disappears on the relevant timescale. This situation is illustrated by way of Figures 5.19 and 5.20.

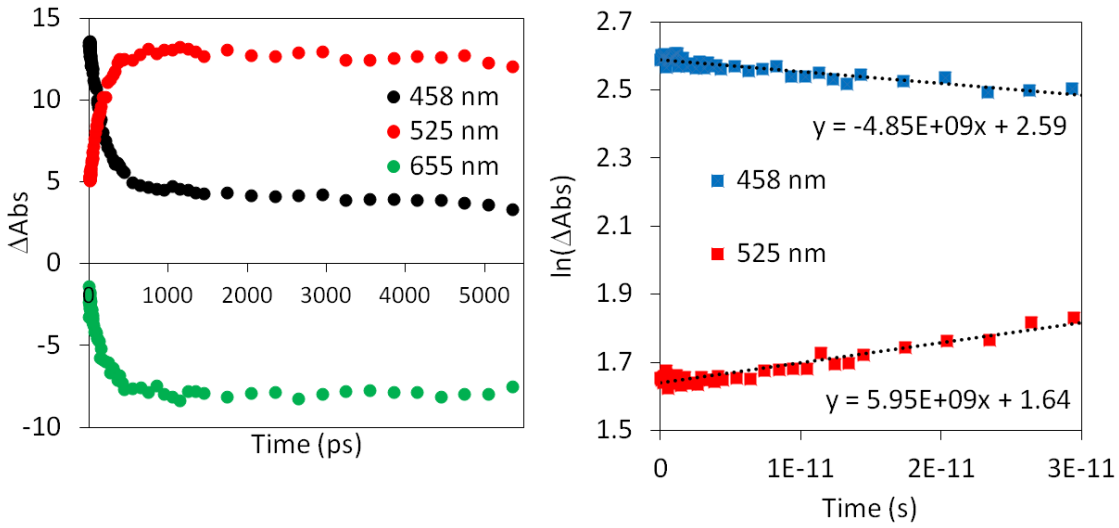

Figure 5.18. Traces of transient species for BBP obtained from femtosecond TAS experiments (corresponds to Figure 5.17) in toluene.

Thus, the transient differential absorption spectra can be considered in terms of Gaussian-shaped components. For BBP in both benzene and toluene, the spectral profiles can be analyzed reasonably well in terms of two components when examined at relatively long delay times. Under such conditions, intramolecular TTA is complete and the only excited-state species present in solution will be the mono-triplet T—G. At much shorter times, both mono- and dual-triplet species will be present, but not in equilibrium. Gaussian deconstruction of the transient differential absorption spectrum requires additional components to satisfactorily reproduce the entire spectral envelope. This can be done by adding two extra components, which we assign to the dual-triplet, T—T. The contribution of T—T decreases with increasing delay time. Although such analysis is open-to-question, it gives a useful confirmation of the kinetic effects. Furthermore, it is not unreasonable that the triplet species will show slightly different differential spectra.

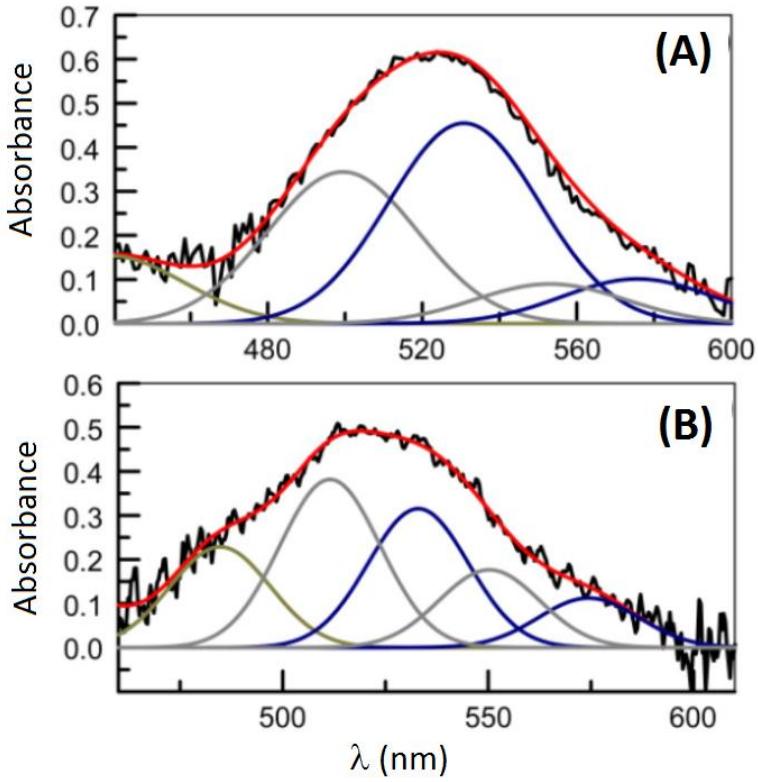

Figure 5.19. Deconstructed triplet-triplet differential absorption spectra obtained for BBP in de-aerated (a) toluene) and (b) benzene. The time window for collecting the spectrum was 0-30 ns. The black curve corresponds to the experimental spectrum while the red curve is the spectrum obtained by summation of the individual Gaussian components. The Gaussian components for $T_1—G_0$ and $T_1—T_1$, respectively, are shown as grey and blue curves. An additional Gaussian (olive curve) is required to for the high-energy region.

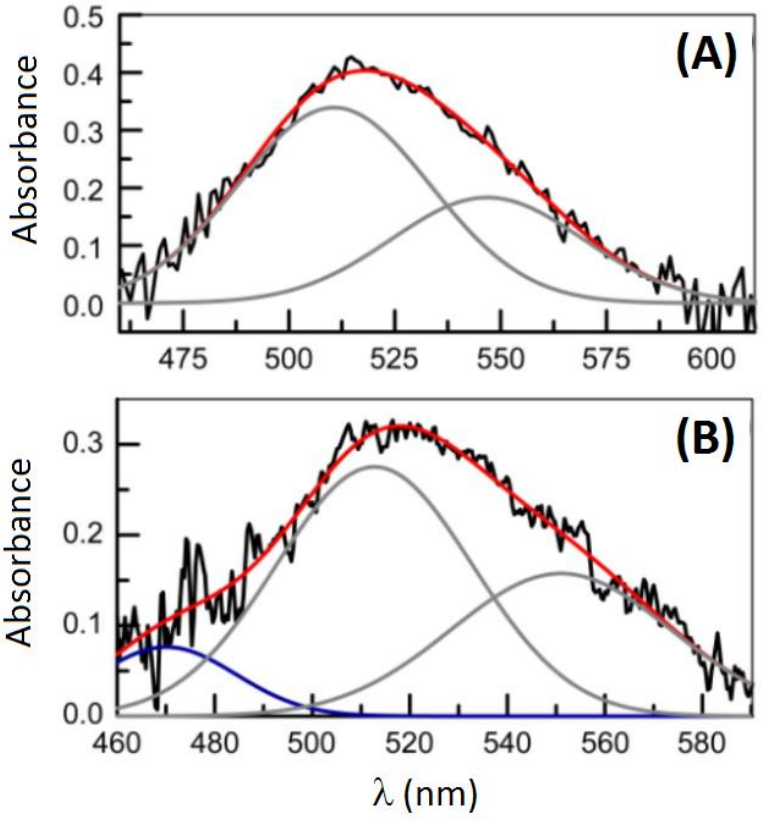

Figure 5.20. Triplet-triplet differential absorption spectra recorded at 500 ns for BBP in de-aerated (a) toluene and (b) benzene. The black curve is the experimental record and the overlaid red curve is the computed spectrum re-assembled on summation of the individual Gaussian components, which are shown as grey curves. For benzene, an addition Gaussian component, shown as a blue curve, is required to fully represent the experimental trace.

By combining the ps and ns transient absorption spectral data it becomes possible to monitor the kinetics of the triplet absorption feature from start to finish, with only a small temporal gap. Formation is fast, as stated above, but there are two decay processes, as seen with pulse radiolysis experiments earlier. The first step, which accounts for the major portion of the triplet signal, occurs over some 150 ns and has a half-life of 75 ns. The residual triplet decays slowly via first-order kinetics and has a lifetime of 1.5 μs in aerated toluene. This latter value increases to 40 μs in de-aerated solution but the faster decay is not much affected by the presence of oxygen. Our interpretation of the triplet absorption spectrum and the ancillary decay kinetics requires the presence of two species with triplet-state character. In toluene, there is little likelihood of intramolecular electron transfer and so, as a starting point, we raise the possibility that the enhanced triplet yield is a consequence of iSEF. This process

would result in the formation of a BBP molecule with both TIPS-P moieties promoted to the triplet state. Given the relatively short separation distance between the two TIPS-P residues and the strong possibility for super-exchange interactions promoted by the fluorene-based spacer, we might anticipate triplet-triplet annihilation between the two triplet species. This could be responsible for the 75 ns decay component. This would leave the longer-lived species as being a BBP molecule with only one TIPS-P unit promoted to the triplet state. This overall situation is illustrated in Figure 5.21, which mirrors the conclusions based on pulse radiolysis experiments. If correct, this explanation would require that the additional feature recognized in the $T_1 - T_3$ absorption spectrum is a signature of the doubly-excited species.

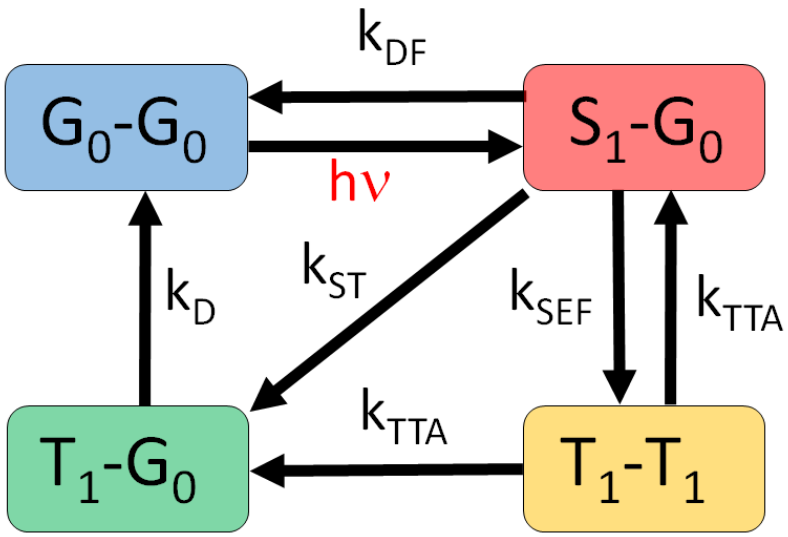

Figure 5.21. Scheme illustrating the occurrence of singlet fission and partitioning of singly and doubly excited triplets in BBP.

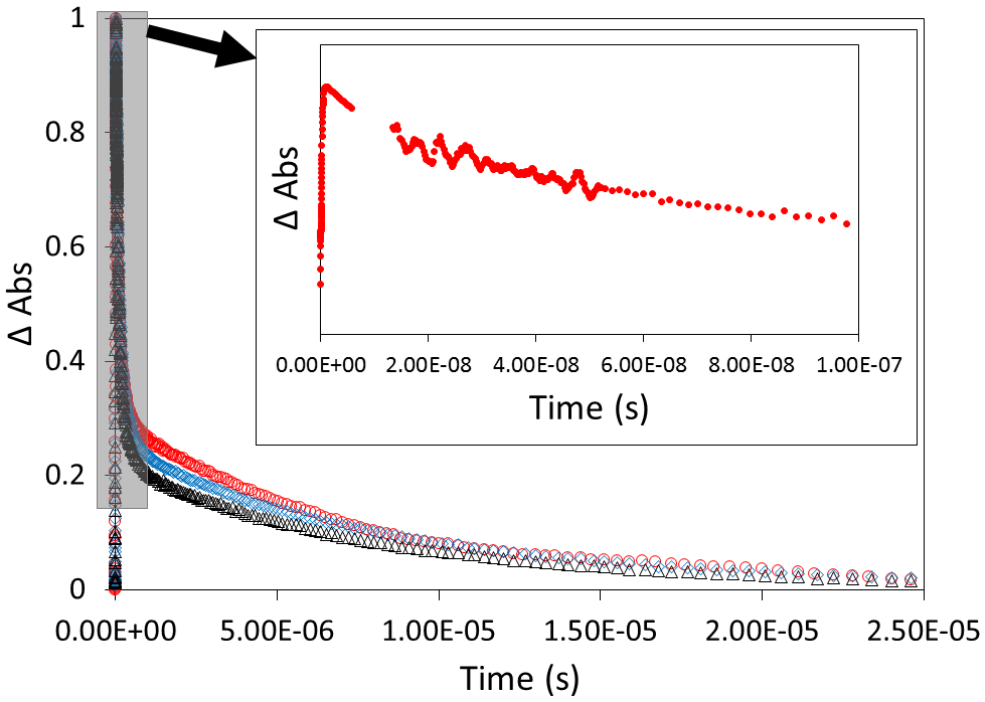

Figure 5.22. Normalized kinetic trace of BBP monitored at 520 nm from the picosecond timescale to microseconds in three solvents. Inset is the initial decay of the triplet pair in toluene (the slight gap is the boundary between ultrafast spectroscopy and nanosecond flash photolysis). Key: red - toluene; blue - cyclohexane; black - benzonitrile. Solutions were purged with nitrogen prior to measurements.

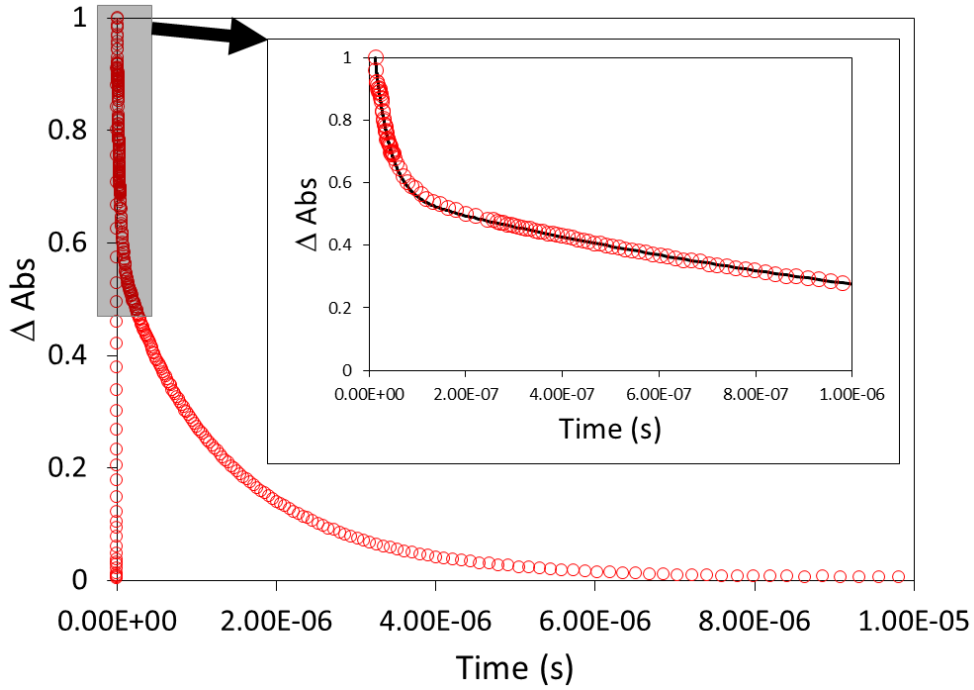

Figure 5.23. Normalized triplet decay trace monitored at 520 nm for BBP in air-equilibrated toluene solution. Inset shows decay at early times where the solid line corresponds to a biexponential fit.

In toluene, the 200 ps fluorescence lifetime can be referred to as the singlet fission time, i.e. the time taken for fluorescence to decay and a pair of equivalent triplets to form. Triplet-triplet annihilation leads to S_0, T_1 and S_1 states. Some of the S_1 can presumably once again undergo singlet fission to form a pair of triplets which will again annihilate with a set loss at each cycle. A characteristic of the decay is the long-lived triplet, which is presumably that of a mon-triplet species. It is interesting to note that in toluene, cyclohexane and benzonitrile the ratio between the initial triplet pair absorption and that of the long-lived component does not change noticeably. We return to this point later.

5.2.5 Delayed Fluorescence

Support for intramolecular TTA on the nanosecond timescale comes from our observation of weak emission occurring on a relatively long timescale (Figure 5.24). The observed fluorescence spectrum is similar, but slightly shifted, to that of the prompt fluorescence. The delayed emission decays via exponential kinetics with a lifetime of ca. 50 ns. This is consistent with the fluorescence signal arising via decay of the S—G species produced during intramolecular TTA.

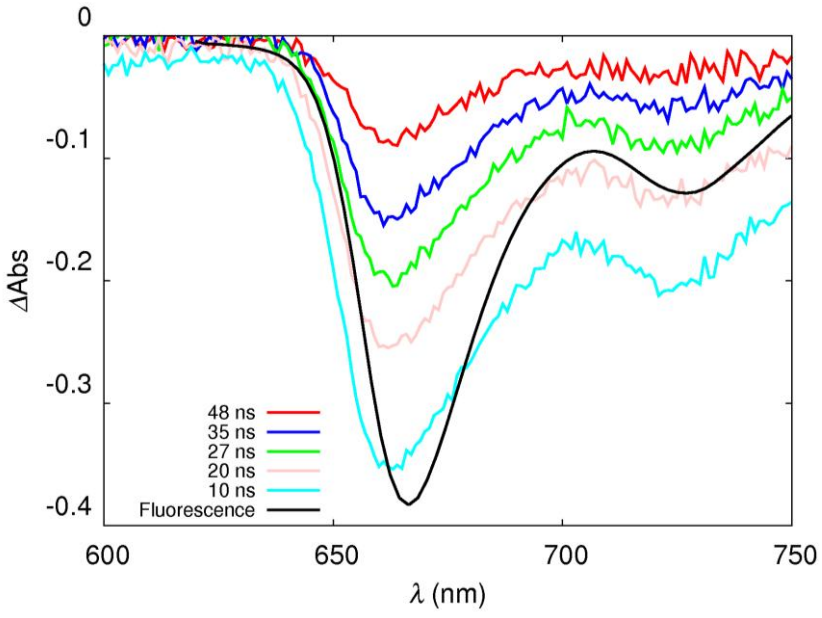

Figure 5.24. Nanosecond transient absorption spectrum of BBP in toluene between 10 and 50 ns shows the ground state bleach is dominated by delayed fluorescence. The black trace is the steady-state fluorescence spectrum.

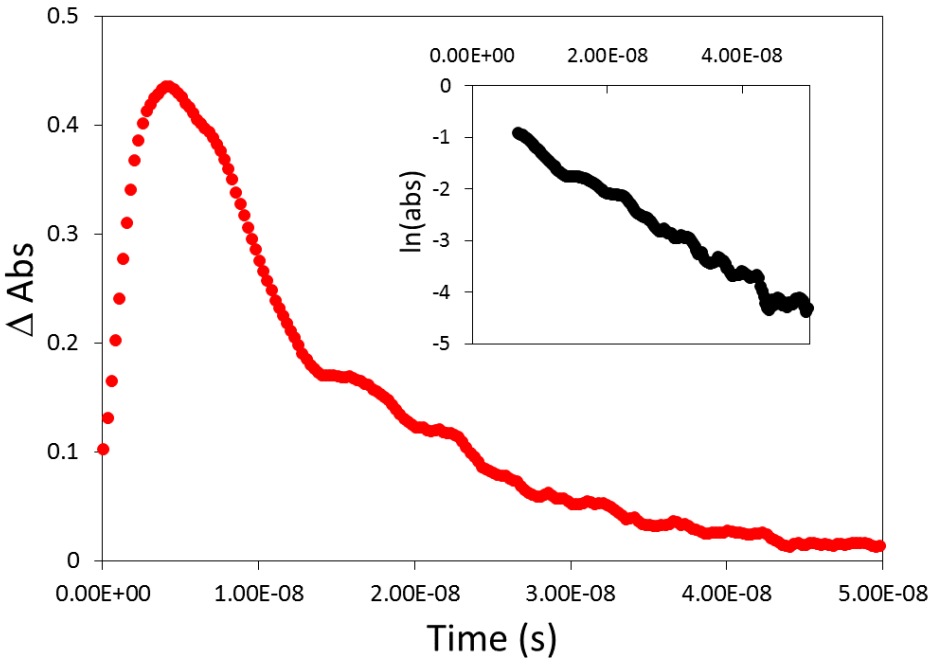

Figure 5.25. Decay of delayed fluorescence of BBP in toluene monitored by nanosecond laser flash photolysis at 725 nm. Inset semi-log plot shows decay is first order.

Triplet-triplet annihilation was further interrogated by varying the solvent viscosity. The intention behind this experiment was to elucidate whether changes in geometry contribute towards the rate of TTA. In pure mineral oil, the lifetime of the dual-triplet increased to 220 ns, independent of the excitation laser intensity. This line of investigation was taken further to examining BBP in a drop-cast Zeonex 480 film, approximately 200 μm thick, and of excellent optical quality. Under such conditions, the TTA decay lifetime increased further to approx. 300 ns. The appearance of the steady-state emission spectrum did not change when using a focused 440 nm LED beam (excitation power ranging from 10 mW to 3 W). Overall, there is little doubt that intense illumination of BBP produces delayed fluorescence due to the appearance of the long-lived transient emission spectrum. Particularly in the solid film, intense red emission can be seen upon laser excitation.

Figure 5.26. Illumination of a BBP-doped Zeonex 480 film with a focused 410 nm laser (25 mW). A 550 nm cut off filter was used to exclude excitation light.

5.3 Conclusions

In this chapter we have reported on the photophysical properties of a new bridged bis-pentacence derivative, BBP, where the individual pentacene units are kept far apart by a fluorene spacer. Steady-state absorption and fluorescence spectra suggest some degree of coupling to the spacer, causing a modest red-shift. More significantly, the bis-pentacene shows a dramatic loss of fluorescence and increase in triplet yield compared to the isolated TIPS-P chromophore. We believe that there are two triplet states formed under both laser excitation and pulse radiolysis in benzene. These triplets possess slightly different absorption spectra and decay by very different kinetic pathways. We have interpreted these triplets in terms of species where both pentacene units are simultaneously present as triplet-excited states – these we call dual-triplets – and species where only one of the pentacene units is present as a triplet – these we refer to as mono-triplets. The dual triplets show slightly red-shifted absorption spectra and decay quickly by first-order kinetics. Their lifetime is essentially unaffected by initial concentration, presence of molecular oxygen or solution viscosity. We see the same general behaviour for triplet species formed via pulsed laser illumination or by exposure to ionizing radiation. Our interpretation of the fast decay for the dual-triplet species involves intramolecular triplet-triplet annihilation. This process partitions to form the excited singlet state, the mono-triplet and the ground state.

Proof for iTTA is obtained by the observation of weak delayed fluorescence, which would give rise to a modest amount of recycling of the excited states. It follows that the energy of the excited-triplet state cannot be much less than one-half that of the corresponding singlet-excited state. This prediction is at odds with literature reports of low-temperature phosphorescence but we have not succeeded with an independent measurement of the triplet energy. On-going experiments might succeed and we remain hopeful of refining this value by way of collaboration. The mono-triplet is long-lived but quenched by molecular oxygen in fluid solution.

Our overall understanding of the photophysics of BBP in non-polar solution is summarised in Table 5.2. The accompanying processes are described in Figure 5.21. We have not, as yet, addressed the issue of the triplet yield. This is important in terms of comparison with other bis-polyacene compounds, where triplet yields well in excess of 100% have been reported. It is more of a challenge to establish the quantitative features of this system but we attempt to do so in the following chapter.

Table 5.2. Summary of the photophysical properties for BBP in dilute toluene solution.

λ_{max}^{abs} / nm	655 ± 1
λ_{max}^{fluor} / nm	664 ± 1
$\varepsilon_{643\ nm}$ / M^{-1} cm^{-1}	40 000 ± 4000
f[(a)]	0.16 ± 0.02
E_{SS} / cm^{-1}[(b)]	245
ϕ_{fluor}	0.030 ± 0.005
k_{RAD} / 10^7 s^{-1}	15 ± 1.5
k_{NR} / 10^7 s^{-1}	485 ± 48.5
τ_{S1} / ns[(e)]	0.20 ± 0.02
τ_{TTA}[(f)] / ns	150 ± 10
τ_{T1} / μs[(e)]	40 ± 5
$E_{T1\text{-}T3}$ / M^{-1} cm^{-1} (at 525 nm)	42 000 ± 4200

(a) Oscillator strength, (b) Estimated Stokes' Shift from deconstruction of the absorption and emission spectra into the minimum number of Gaussian components (c) Fluorescence yield in sub-micromolar concentration solution, (e) Solution was purged with dry N_2 for at least 15 minutes prior to measurement. (f) Intramolecular triplet-triplet annihilation of the triplet pair (g) Triplet extinction coefficient determined from pulse-radiolysis experiments.

5.4 References

1. Smith, M.B.; Michl, J. *Chem. Rev.* **2010**, 110, 6891-6936.

2. Smith, M.B.; Michl, J. Annu. Rev. Phys. Chem. **2013**, 64, 361-386.

3. Merrifield, R.E.; Avakian, P.; Groff, R.P. *Chem. Phys. Lett.* **1969**, 3, 386-388.

4. Burgos, J.; Pope, M.; Swenberg, C.E.; Alfano, R.R. *Phys. Status Solidi.* **1977**, 83, 249-256.

5. Walker, B.J.; Musser, A.J.; Beljonne, D.; Friend, R.H. *Nat. Chem.* **2013**, 5, 1019-1024.

6. Zirzlmeier, J.; Lehnherr, D.; Coto, P.B.; Chernick, E.T.; Casillas, R.; Basel, B.S.; Thoss, M.; Tykwinski, R.R.; Guldi, D.M. *Proc. Natl. Acad. Sci. U.S.A*, **2015**, 112, 5325-5330.

7. Sanders, S.N.; Kumarasamy, E.; Pun, A.B.; Trinh, M.T.; Choi, B.; Xia, J.; Taffet, E.J.; Low, J.Z.; Miller, J.R.; Roy, X.; Zhu, X.Y *J. Am. Chem. Soc.* **2015**, 137, 8965-8972.

8. Sakuma, T.; Sakai, H.; Araki, Y.; Mori, T.; Wada, T.; Tkachenko, N.V.; Hasobe, T. *J. Phys. Chem. A.* **2016**, 120, 1867-1875.

9. Zirzlmeier, J.; Casillas, R.; Reddy, S.R.; Coto, P.B.; Lehnherr, D.; Chernick, E.T.; Papadopoulos, I.; Thoss, M.; Tykwinski, R.R.; Guldi, D.M. Nanoscale, **2016**, 8, 10113-10123.

10. Kumarasamy, E.; Sanders, S.N.; Tayebjee, M.J.; Asadpoordarvish, A.; Hele, T.J.; Fuemmeler, E.G.; Pun, A.B.; Yablon, L.M.; Low, J.Z.; Paley, D.W.; Dean, J.C. *J. Am. Chem. Soc.* **2017**, 139, 12488-12494.

11. Rao, A.; Wilson, M.W.; Hodgkiss, J.M.; Albert-Seifried, S.; Bassler, H.; Friend, R.H. *J. Am Chem. Soc.* **2010**, 132, 12698-12703.

12. Johnson, J.C.; Nozik, A.J.; Michl, J. *J. Am. Chem. Soc.* **2010**, 132, 16302-16303.

13. Ryerson, J.L.; Schrauben, J.N.; Ferguson, A.J.; Sahoo, S.C.; Naumov, P.; Havlas, Z.; Michl, J.; Nozik, A.J.; Johnson, J.C. *J. Phys. Chem. C.* **2014**, 118, 12121-12132.

14. Busby, E.; Xia, J.; Wu, Q.; Low, J.Z.; Song, R.; Miller, J.R.; Zhu, X.Y.; Campos, L.M.; Sfeir, M.Y. *Nat. Mater.* **2015**, 14, 426-433.

15. Musser, A.J.; Al-Hashimi, M.; Maiuri, M.; Brida, D.; Heeney, M.; Cerullo, G.; Friend, R.H.; Clark, J. *J. Am. Chem. Soc.* **2013**, 135, 12747-12754.

16. Sanders, S.N.; Kumarasamy, E.; Pun, A.B.; Steigerwald, M.L.; Sfeir, M.Y.; Campos, L.M.; *Angew. Chem.* **2016**, 128, 3434-3438.

17. Eaton, S.W.; Miller, S.A.; Margulies, E.A.; Shoer, L.E.; Schaller, R.D.; Wasielewski, M.R. *J. Phys. Chem. A*, **2015**, 119, 4151-4161.

18. Eaton, S.W.; Shoer, L.E.; Karlen, S.D.; Dyar, S.M.; Margulies, E.A.; Veldkamp, B.S.; Ramanan, C.; Hartzler, D.A.; Savikhin, S.; Marks, T.J.; Wasielewski, M.R. *J. Am. Chem. Soc.* **2013**, 135, 14701-14712.

19. Mauck, C.M.; Hartnett, P.E.; Margulies, E.A.; Ma, L.; Miller, C.E.; Schatz, G.C.; Marks, T.J.; Wasielewski, M.R. *J. Am. Chem. Soc*. **2016**, 138, 11749-11761.

20. Congreve, D.N.; Lee, J.; Thompson, N.J.; Hontz, E.; Yost, S.R.; Reusswig, P.D.; Bahlke, M.E.; Reineke, S.; Van Voorhis, T.; Baldo, M.A. *Science,* **2012**, 340, 334-337.

21. Jadhav, P.J.; Mohanty, A.; Sussman, J.; Lee, J.; Baldo, M.A. *Nano Lett.* **2011**, 11, 1495-1498.

22. Ehrler, B.; Walker, B.J.; Böhm, M.L.; Wilson, M.W.; Vaynzof, Y.; Friend, R.H.; Greenham, N.C. *Nat. Commun.* **2012**, 3, 1019.

23. Ehrler, B.; Wilson, M.W.; Rao, A.; Friend, R.H.; Greenham, N.C. *Nano Lett.* **2012**, 12, 1053-1057.

24. Paci, I.; Johnson, J.C.; Chen, X.; Rana, G.; Popović, D.; David, D.E.; Nozik, A.J.; Ratner, M.A.; Michl, J. *J. Am. Chem. Soc.* **2006**, 128, 16546-16553.

25. Korovina, N.V.; Das, S.; Nett, Z.; Feng, X.; Joy, J.; Haiges, R.; Krylov, A.I.; Bradforth, S.E.; Thompson, M.E. *J. Am Chem. Soc.* **2016**, 138, 617-627.

26. Zimmerman, P.M.; Bell, F.; Casanova, D.; Head-Gordon, M. *J. Am. Chem. Soc.* **2011**, 133, 19944-19952.

27. Groff, R.P.; Avakian, P.; Merrifield, R.E. *Phys. Rev. B*, **1970**, 1, 815-817.

28. Zimmerman, P.M.; Zhang, Z.; Musgrave, C.B. *Nat. Chem.* **2010**, 2, 648-652.

29. Wilson, M.W., Rao, A.; Clark, J.; Kumar, R.S.S.; Brida, D.; Cerullo, G.; Friend, R.H. *J. Am. Chem. Soc.* **2011**, 133, 11830-11833.

30. Thorsmølle, V.K.; Averitt, R.D.; Demsar, J.; Smith, D.L.; Tretiak, S.; Martin, R.L.; Chi, X.; Crone, B.K.; Ramirez, A.P.; Taylor, A.J. *Physica B.* **2009**, 404, 3127-3130.

31. Basel, B.S.; Zirzlmeier, J.; Hetzer, C.; Phelan, B.T.; Krzyaniak, M.D.; Reddy, S.R.; Coto, P.B.; Horwitz, N.E.; Young, R.M.; White, F.J.; Hampel, F; Clark, T.; Thoss, M.; Tykwinski, R.R., Wasielewski, M.R.; Guldi, D.M. *Nat. Commun.* **2017**, 8, 15171.

32. Chan, W.L.; Berkelbach, T.C.; Provorse, M.R.; Monahan, N.R.; Tritsch, J.R.; Hybertsen, M.S.; Reichman, D.R.; Gao, J.; Zhu, X.Y. *Acc. Chem. Res.* **2013**, 46, 1321-1329.

33. Trinh, M.T.; Pinkard, A.; Pun, A.B.; Sanders, S.N.; Kumarasamy, E.; Sfeir, M.Y.; Campos, L.M.; Roy, X.; Zhu, X.Y. *Sci. Adv.* **2017**, 3, 1700241.

34. Tayebjee, M.J.; Sanders, S.N.; Kumarasamy, E.; Campos, L.M.; Sfeir, M.Y.; McCamey, D.R. *Nat. Phys.* **2017**, 13, 182-188.

35. Lukman, S.; Musser, A.J.; Chen, K.; Athanasopoulos, S.; Yong, C.K.; Zeng, Z.; Ye, Q.; Chi, C.; Hodgkiss, J.M.; Wu, J.; Friend, R.H. *Adv. Funct. Mater.* **2015**, 25, 5452-5461.

36. Bonnett, R.; McGarvey, D.J.; Harriman, A.; Land, E.J.; Truscott, T.G.; Winfield, U. *J. Photochem. Photobiol.* **1988**, 48, 271-276.

37. Zoon, P.D.; Brouwer, A.M. *Photochem. Photobiol. Sci.* **2009**, 8, 345-353.

38. Görlach, E.; Gygax, H.; Lubini, P.; Wild, U.P. *Chem. Phys.* **1995**, 194, 185-193.

39. Wilson, M.W.; Rao, A.; Johnson, K.; Gélinas, S.; Di Pietro, R.; Clark, J.; Friend, R.H. *J. Am. Chem. Soc.* **2013**, 135, 16680-16688.

40. Fujimori, E.; Livingston, R. *Nature*, **1957**, 180, 1036-1038.

41. Birks, J.B., 2013. The Theory and Practice of Scintillation Counting: International Series of Monographs in Electronics and Instrumentation (Vol. 27). Elsevier.

42. Bensasson, R.V., Land, E.J. and Truscott, T.G., 2013. Flash photolysis and pulse radiolysis: contributions to the chemistry of biology and medicine. Elsevier.

43. Bula, R.; Fingerle, M.; Ruff, A.; Speiser, B.; Maichle-Mössmer, C.; Bettinger, H.F. *Angew. Chem. Int. Ed.* **2013**, 52, 11647-11650.

Chapter 6: Photophysics of a Bis-Pentacene Derivative in Fluid Solution – Further Considerations

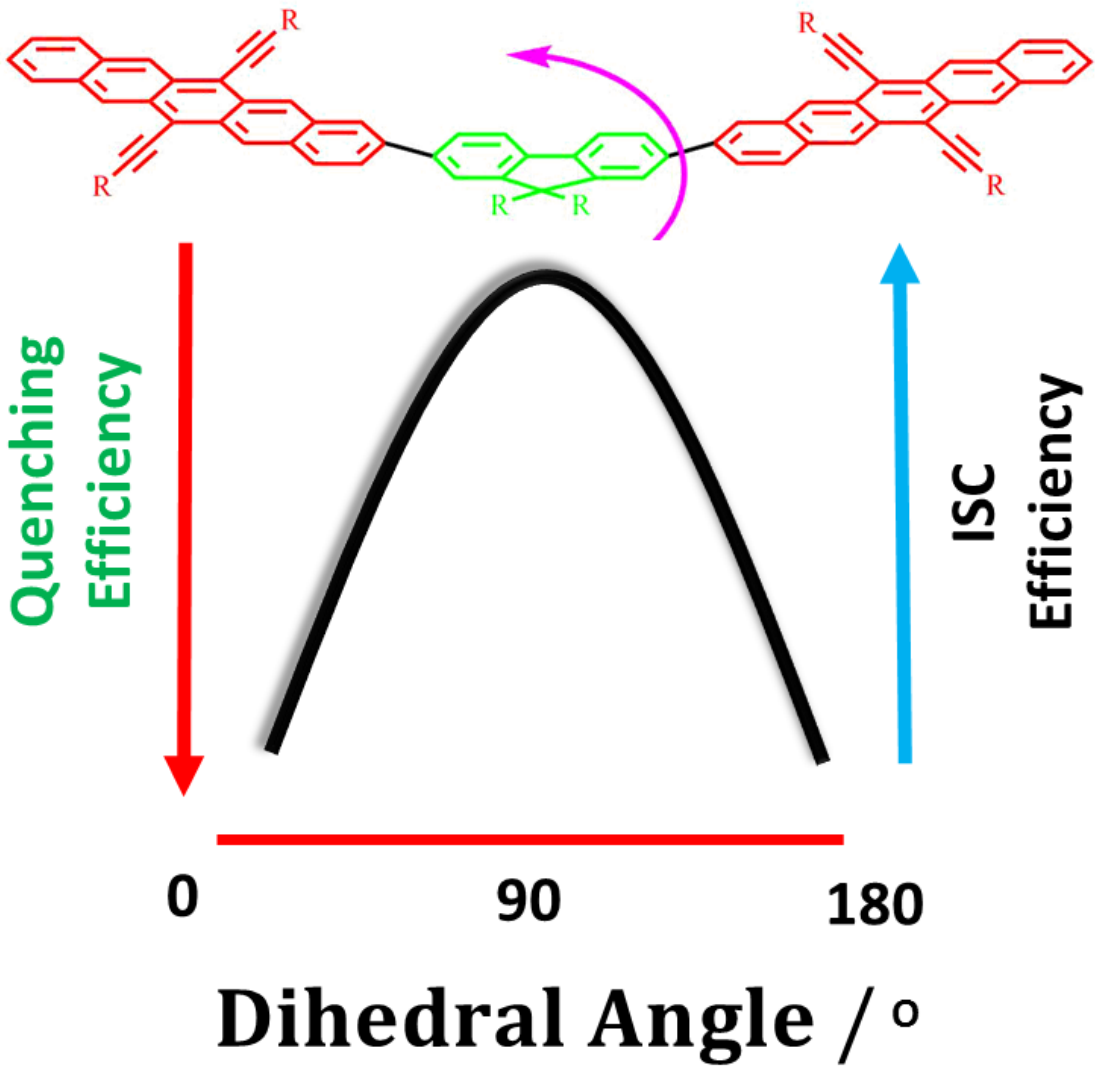

6.1 Introduction

In this chapter, we continue investigations into the origin of the enhanced intersystem crossing to the triplet manifold observed for the bridged bis-pentacene derivative, BBP. The chapter follows closely from Chapter 5 and there are obvious links to Chapter 4. For interests of brevity, and to avoid unnecessary repetition, a long introduction is not warranted. The aim of the chapter is to provide a concise quantitative estimate of the triplet yield for BBP in fluid solution. We have established that the bis-pentacene exhibits a rather drastic reduction in the fluorescence yield/lifetime and a corresponding increase in population of the triplet state. We have also noted the onset of intramolecular triplet-triplet annihilation[1], delayed fluorescence[2] and broadening of the singlet- and triplet-excited state absorption spectra. Our understanding of the system is that singlet exciton fission is responsible for the enhanced yield of the triplet state, at least in toluene. In several literature examples of singlet exciton fission occurring with polyacenes, the optimal yield of triplet-excited states approaches 200%.[3,4] This finding suggests that each excited-singlet state splits to give a pair of triplets. In other cases, the triplet yield is significantly less than 200%, although still in excess of 100%.[5,6] Here, the situation becomes more ambiguous and splitting of the singlet exciton might give a mixture of dual- and mono-triplets. Alternatively, the splitting process could give a pair of triplets and a pair of ground-state molecules. Of course, other possibilities exist…

In trying to establish the efficacy of iSEF for BBP, we return to pulse radiolysis and ultrafast transient absorption spectroscopic measurements in a more quantitative approach. An important feature of this analysis revolves around values for the various molar absorption coefficients. We have already alluded to our estimates of coefficients for the excited-singlet and -triplet differential absorption spectra. Our derived values are significantly reduced relative to those reported for TIPS-P by Guldi *et al*.[5] In fact, the ratio of derived values obtained by the two groups for singlet and triplet species is in perfect agreement. This ratio indicates that, at the respective maxima, the singlet state has an absorptivity some 55% that of the triplet state. Rather than rely on absolute molar absorption coefficients, in the first instance, our initial estimates of the iSEF partitioning will make use of the ratio. The first objective, therefore, is to obtain an

estimate of the triplet yield obtained via iSEF in toluene (or benzene) solution under ionising radiation. Later we will address the ultrafast transient absorption spectroscopic data. Finally, we move away from toluene and consider a few more polar solvents.

Ideally, the analysis would go one step further and provide an estimate of the partitioning of the excited-singlet state in nonpolar media. Thus, we can suppose that fast decay of S–G could give rise to some or all of T–T, T–G, and G–G species. We have raised the assumption that iTTA might play a critical role in the analysis. We are of the opinion that, on the nanosecond timescale, we have a mixture of mono-triplet (T–G) and dual-triplet (T–T) species present in our system. The origin of T–G depends on the history of the sample. In contrast, T–T arises uniquely from iSEF and is a signature feature. By measuring the relative concentration of triplet species undergoing iTTA, we indirectly measure the relative concentration of T–T. If this notion is correct, we can easily distinguish between mono- and dual-triplet species and thereby quantify the role of iSEF at a more demanding level.

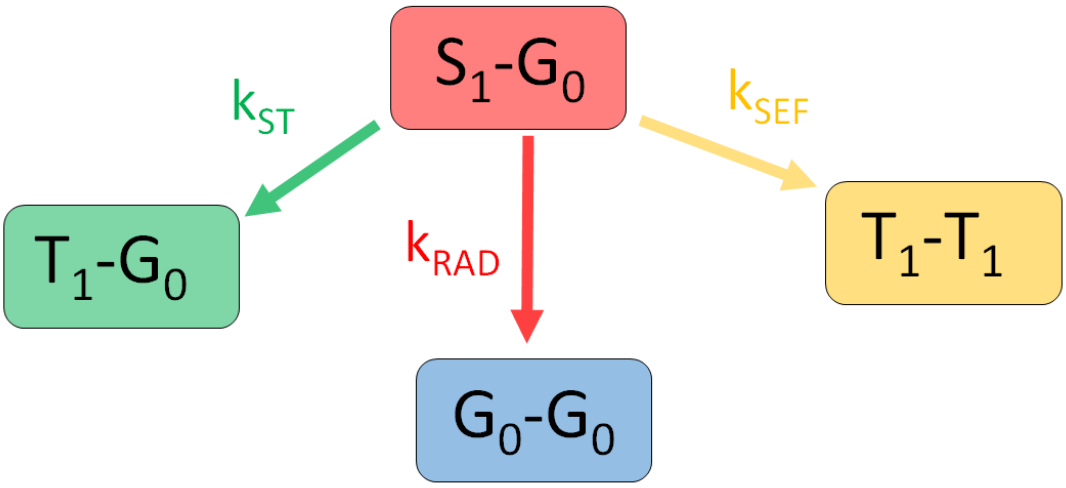

Figure 6.1. Simplified scheme illustrating the possible partitioning of the BBP singlet-excited state into mono- and dual-triplet species.

6.2 Pulse Radiolysis in De-aerated Benzene (or Toluene)

Previously, we set out to analyze the results of our pulse radiolysis studies making use of the benzophenone dosimeter[7] [These studies were carried out in collaboration with the Majima Group at Osaka University]. This analysis is based on two assumptions: namely, (i) the combined concentrations of pentacene-derived excited states exactly equals the concentration of the BP excited-triplet state and (ii) molar absorption coefficients are valid for at least one of the pentacene-derived excited states. It should be stressed that, because of the very high solute concentrations needed for pulse radiolysis, it is not possible to work in the ground-state bleaching regime. This is unfortunate because, as will be illustrated later, our most reliable analysis makes use of the transient ground-state bleaching signal. This is simply not possible with the pulse radiolysis data.

Now, Table 6.1 includes initial absorbance (A_λ) values for wavelengths corresponding to excited-singlet and excited-triplet states for TIPS-P in solution observed at the end of the pulse of ionizing radiation. Also shown are the initial concentrations of BP triplet, obtained by extrapolation of the decay curve to zero time, and the path length used for the experiment. Data entries are given for both benzene and toluene. The individual entries are used to calculate the respective absorbance (Q_λ) projected for a path length of 1 cm and a BP-triplet dosimeter concentration of 40 μM. In other words, we have simply scaled the absorbance values to match hypothetical conditions. There are no assumptions, other than scalability, in this rather straightforward analysis.

Table 6.1. Values pertaining to the iSEF partitioning under pulse radiolysis conditions, data entries refer to TIPS-P.[(a)]

Solvent	Species	A_λ	PL / cm	[BP] / μM	Q_λ
Benzene	singlet	0.394	0.5	27.3	1.115
	triplet	0.574	0.5	27.3	1.682
Toluene	singlet	0.443	0.5	32.2	1.101
	triplet	0.670	0.5	32.2	1.666

(a) Experimental values refer to zero time.

We now carry out a similar analysis for BBP, noting that the excited-singlet state makes no contribution to the signal but the triplet state shows successive fast and slow decay processes. To distinguish between these latter processes, we record absorbance values at the absorption maximum at zero time (A_0) and at a time delay of 500 ns (A_{500}). As before, we project the absorbance values that would pertain to a path length of 1 cm and a dosimeter concentration of 40 μM. In fact, the latter is not needed because the BP-triplet dosimeter was in fact 40 μM. The data are compiled in Table 6.2.

Table 6.2. Values pertaining to the iSEF partitioning under pulse radiolysis conditions, data refers to BBP.

Solvent	**A_0**	**A_{500}**	**PL / cm**	**[BP] / μM**	**Q_0**	**Q_{500}**
Benzene	0.651	0.420	0.2	40.0	3.255	2.100
Toluene	0.625	0.420	0.2	40.0	3.125	2.100

It will be noted that the projected triplet absorbance values are significantly higher for BBP than for TIPS-P. This is so for both the faster decaying triplet, assigned as T−T, and the longer-lived triplet, attributed to T−G. The latter finding indicates that somewhere within the iSEF and/or iTTA cycle, there is provision for formation of the mono-triplet. As mentioned above, there is no singlet-state contribution for BBP on the timescale of the experiment. We raise the condition that fast deactivation of the excited-singlet state of BBP is responsible for the enhanced yield of the triplet state. We have now to resort to the introduction of molar absorption coefficients for some excited-state species. This is done in two steps: Firstly, the ratio of absorbance signals for excited-singlet and excited-triplet states of TIPS-P is taken as 0.55, which is in agreement with the report of Guldi *et al.*[5] and with our own curve fitting analysis. This routine uses the molar absorption coefficient for the ground-state of TIPS-P in dilute toluene solution. Now, we can project the additional crop of triplet absorbance expected if the excited-singlet state decays exclusively to the triplet-excited state. We collect the results in Table 6.3 in the form of ΔA_0 (*calc*). Recall, these values are based on the agreed ratio of molar absorption coefficients for excited-singlet and –triplet states of TIPS-P.

Table 6.3. Analysis of the projected triplet yields related to iSEF partitioning under pulse radiolysis conditions.

Solvent	Q_0	ΔA_0 (calc)	ΔA_{BBP}	ΔA_{iSEF}	Φ_{iSEF} / %
Benzene	3.255	3.709	2.485	3.852	156
Toluene	3.125	3.678	2.465	3.821	148

This analysis underestimates the yield of triplet BBP because the differential molar absorption coefficient for the particular species is significantly less than 67,500 M^{-1} cm^{-1} at the peak. This will be covered later but it should be recalled that the absorption band in the region around 520 nm is considerably broader for triplet BBP than for triplet TIPS-P. There is the additional problem that the spectrum evolves with time but this has a relatively minor effect of the absorption coefficient. Our best estimate for the differential molar absorption coefficient for triplet BBP at 525 nm is 42,000 M^{-1} cm^{-1} (see later). Now, the ΔA_0 values calculated for Table 6.3 refer to the projection based on data for TIPS-P. Allowing for the different molar absorption coefficients for the triplet states of TIPS-P and BBP, we can revise these values. The relevant factor is 0.67. This leads to expected normalized absorbance values (ΔA_{BBP}) that are less than the "observed" (normalized) absorbance values. We can now estimate the normalized absorbance values for BBP in the event that iSEF forms the triplet state in quantitative yield. The relevant entry in Table 6.3 comes under the heading ΔA_{iSEF}. This is the absorbance we would expect to see if all the initially formed excited-singlet state decays to form a pair of triplet states. Finally, we can calculate the efficiency (Φ_{iSEF}) for production of triplet-excited states during iSEF for BBP in benzene and toluene. The derived values are added to Table 6.3.

The first point to note is that the experimentally determined triplet absorbance (Q_0), this referring to total triplet, falls someway short of that projected (ΔA_{iSEF}) if iSEF leads exclusively to formation of a triplet pair. That is to say, in this system, fast deactivation of the excited-singlet state does not appear to lead to quantitative formation of the corresponding triplet-excited state. Nonetheless, the actual triplet yield observed is very

high, being in the region of 150% for both toluene and benzene. This is in line with expectations based on literature systems.[3-6]

We can try to go further and partition the splitting of iSEF into the most likely products. Thus, the fraction of the initial triplet absorbance arising from iSEF can be calculated from the above analysis and amounts to about 65% for both benzene and toluene. Analysis of the kinetic data indicates that roughly 40% of the initial triplet absorbance decays via iTTA. Roughly speaking, the iTTA event should lose around 60% of the absorbance attributed to the excited-triplet state if the conventional statistics for TTA hold for this system.[8] This indicates that S—G decays exclusively to give T—T, without formation of the mono-triplet, T—G. The product balance (i.e., the missing 25% of S—G that does not produce T—T) is achieved on the recognition that a crop of the ground state G—G is formed in competition to T—T.

Using the above analysis, we can simulate the various concentration levels. Pulse radiolysis of BBP in benzene gives 22 μM S_1—G_0, plus a crop of 18 μM T_1—G_0. The model (Chapter 5, Figure 5.13) was used to simulate the recovered pulse radiolysis data (Figures 6.2-4).

The compartmentalized model is described by the following differential equations:

$$\frac{d[S-G]}{dt} = -k_{DF}[S-G] - k_{SEF}[S-G] - k_{ST}[S-G] + k_{TT}[T-T] \qquad (6.1)$$

$$\frac{d[G-T]}{dt} = -k_D[G-T] + k_T[T-T] + k_{ST}[S-G] \qquad (6.2)$$

$$\frac{d[T-T]}{dt} = -k_T[T-T] - k_{TT}[T-T] + k_{SEF}[S-G] \qquad (6.3)$$

With the following starting conditions, one can accurately simulate the concentration profiles for the various species generated during a pulse radiolysis experiment. [T—T] = [G—G] = 0 : [S—G] = 0.55 : [G—T] = 0.45. k_D = 1200 , k_{SEF} = 3.75 x 10^7 k_{DF} = 1 x 10^5 k_{TT} = 3 x 10^5, k_T = 1.25 x 10^7. Note the units for the various rate constants are (100 ns)$^{-1}$.

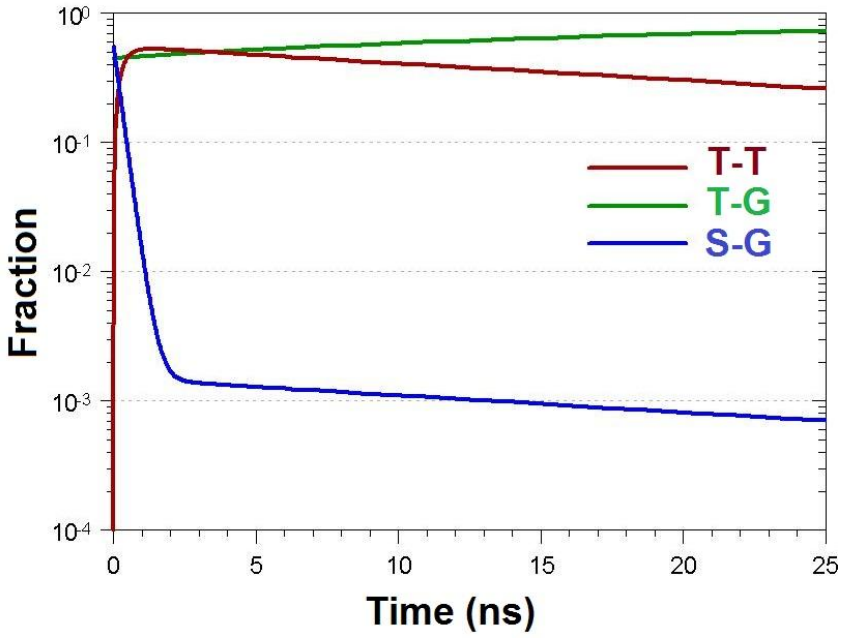

Figure 6.2. Kinetic simulation of the concentration profile evolution at short stages of the cycle. Note the introduction of delayed fluorescence. Relative fractions of species plotted on a log scale.

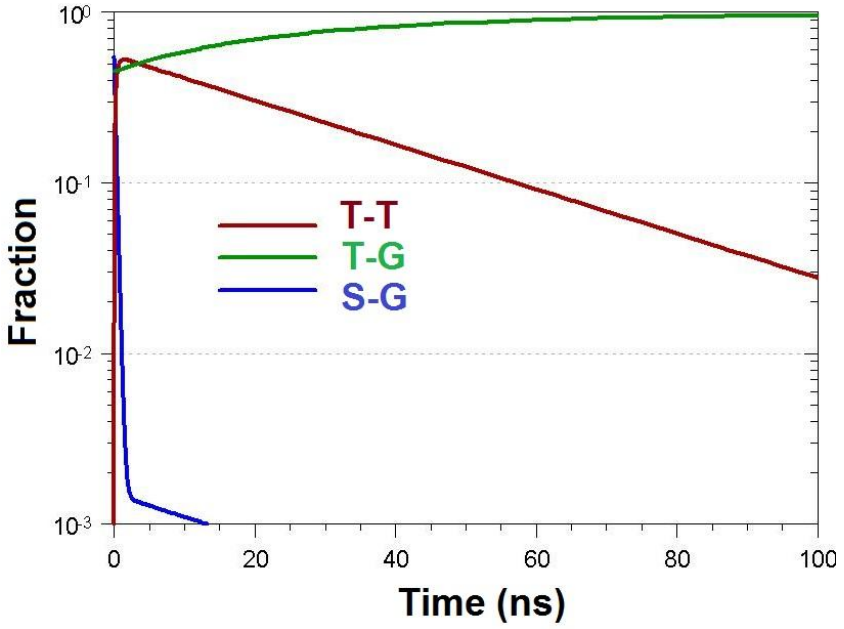

Figure 6.3. Kinetic simulation of the concentration profile evolution at intermediate stages of the cycle. This highlights the role of intramolecular triplet-triplet annihilation. Relative fractions of species plotted on a log scale.

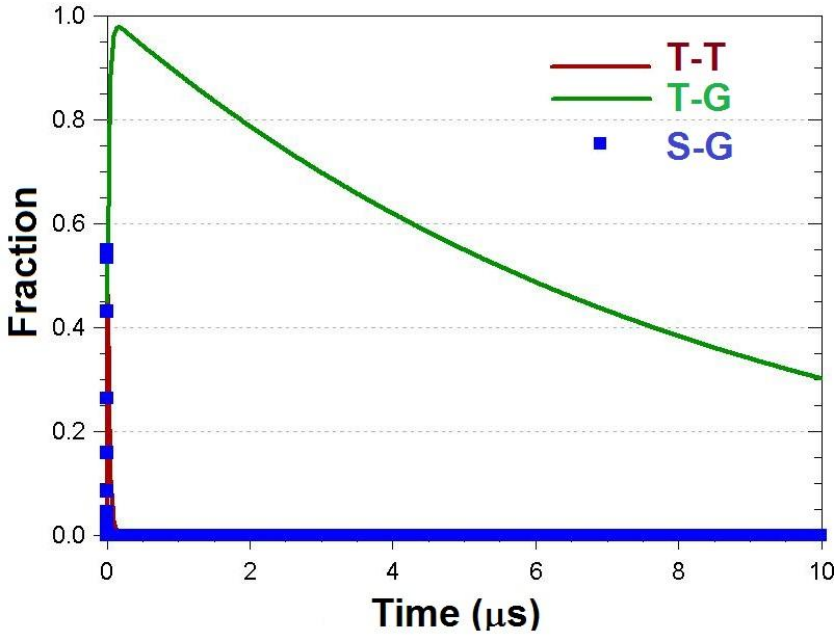

Figure 6.4. Kinetic simulation of the concentration profile evolution at long times.

6.3 Analysis of the Ultrafast Transient Absorption Spectral Data

The most common protocol for determining triplet yields for iSEF in bis-pentacene derivatives makes use of differential molar absorption coefficients measured for TIPS-P in the appropriate solvent.[3-5] For BBP, however, it is noticeable that the absorption profile for the S_1 state is somewhat broader and slightly shifted relative to that of the control compound. This broadening is more pronounced for the absorption spectrum assigned to T_1 and there is some evolution of the spectrum with time. This effect has been assigned to a mixture of T–T and T–G species at early times. There is also an effect due to mixing between orbitals on the pentacene moiety and the fluorene-based spaced unit. For this reason, it is not appropriate to employ values found for TIPS-P when calculating triplet yields for BBP, even in the same solvent. As a consequence, it is prudent to determine differential molar absorption coefficients for the excited-states of BBP (in toluene) and avoid reliance on those of the control compound.

It is evident that, on relatively long timescales, the triplet-excited state shows ground-state bleaching (GSB) in the region around 650-660 nm that is essentially free of contamination by fluorescence. On either side of the GSB signal, there is rather weak absorption due to the triplet species. Under these experimental conditions, only one of

the two pentacene chromophores will be at the excited-triplet state level. Therefore, the differential molar absorption coefficient for the triplet state (ε_{TRIP}) over this narrow wavelength region will be given approximately as the product of the ground-state molar absorption coefficient multiplied by minus one-half. Due allowance can be made for the minor absorption by the triplet state. At the maximum of the GSB in toluene (λ = 643 nm; ε_{GS} = 40,000 M^{-1} cm^{-1}), we reach a value for ε_{TRIP} of -20,000 M^{-1} cm^{-1}. Now, comparison of the magnitude of the GSB to the absorbance associated with the T_1-T_3 absorption transition centred at around 525 nm allows establishment of an averaged value for ε_{TRIP} at each wavelength. Averaging across the region around the peak absorption, we reach a value for ε_{TRIP} of 42,000 M^{-1} cm^{-1}. This value, which is the average of 5 measurements, is significantly smaller than found for TIPS-P, in line with the considerably broader spectral profile.

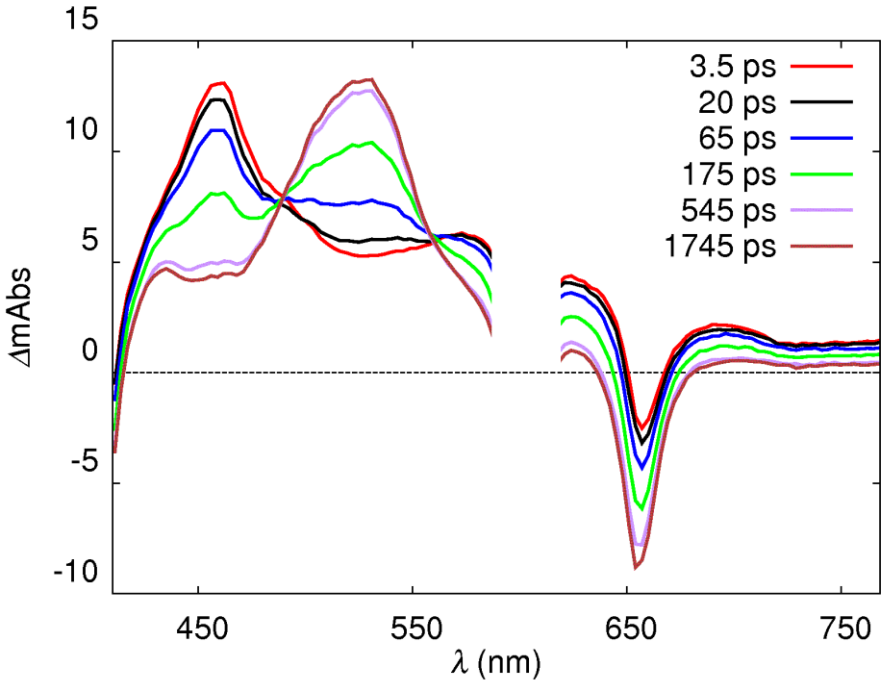

Figure 6.5. Ultrafast transient absorption spectra for BBP in toluene.

By the same set of criteria it is clear that the excited-singlet state makes a positive contribution towards the differential molar absorption coefficient (ε_{SING}) for the S_1 state in the region of GSB. However, isosbestic points are noted for the S_1-T_1 evolution at wavelengths where the ground state exhibits low absorptivity. Unfortunately, these isosbestic points are useful only if the reaction stoichiometry is beyond dispute and that

is not really the case here. Instead, we have relied on spectral curve fitting to firstly eliminate any contribution due to stimulated fluorescence in the region around 650-680 nm. Secondly, the differential absorption spectrum is regenerated by adding incremental amounts of the GSB in the region around 650-660 nm until a smooth residual curve is produced. Comparing the amount of GSB needed to produce the final spectrum gives access to the required value for ε_{SING}. The derived value is ca. 43,800 M^{-1} cm^{-1} at the differential absorption maximum of 460 nm in toluene. Now, by comparing the transient absorbance measured at short times (ca. 1-3 ps) at 460 nm with that measured at the GSB on the timescale of a few ns, we can determine the triplet yield. For toluene, we reach a value of ca. 160%. This is in excellent agreement with that estimated for iSEF accompanying the pulse radiolysis analysis.

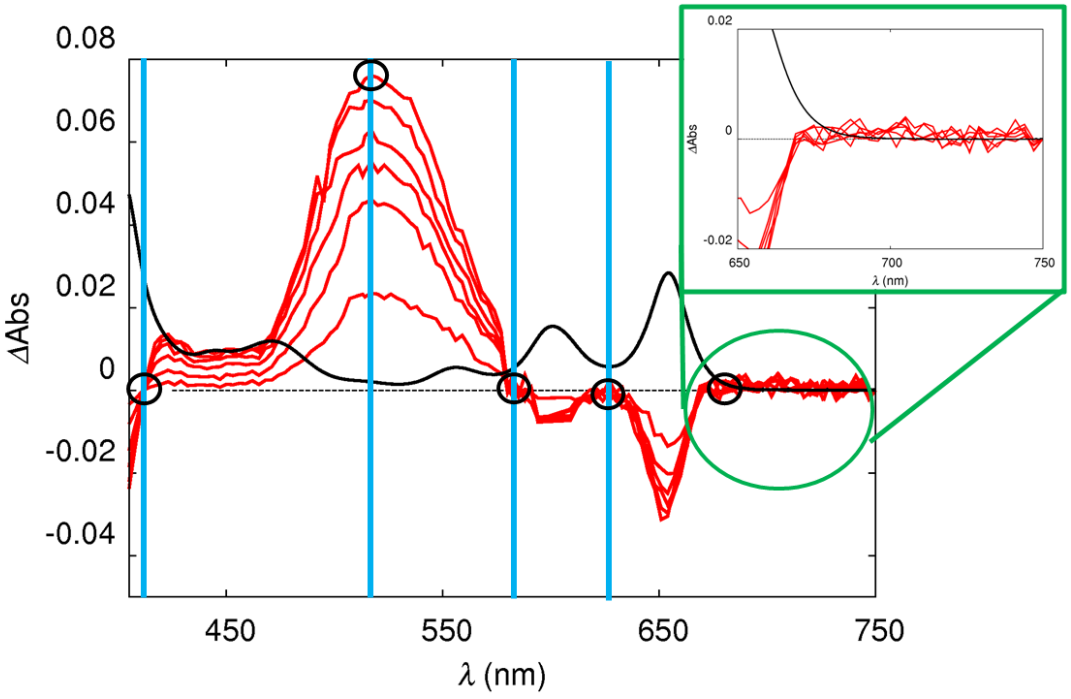

Figure 6.6. Figure illustrating how key isosbestic points in the BBP triplet spectrum can be used as reference points for obtaining the molar absorption coefficient of the triplet at 525 nm. Spectra here are of BBP in toluene. Inset shows residual positive signal past the ground state bleach.

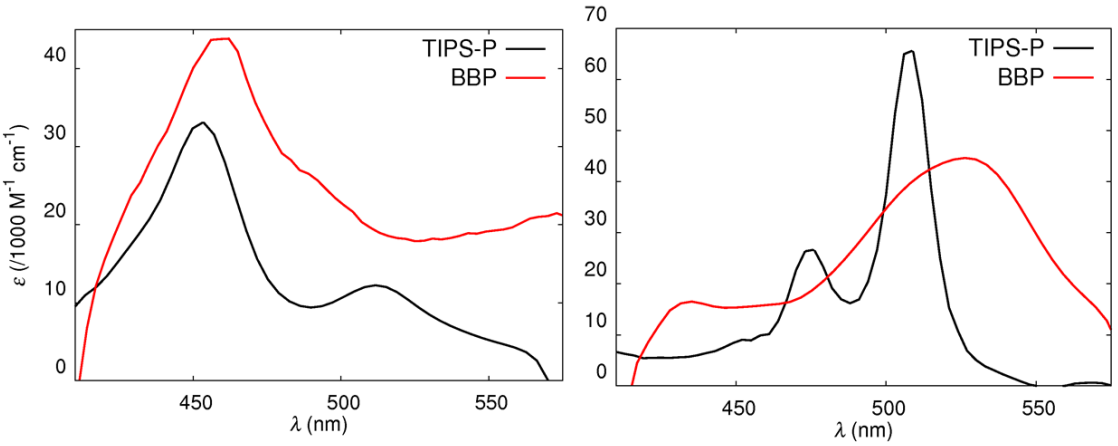

Figure 6.7. Direct comparison of the singlet-excited state spectra (left panel) and triplet-excited (right panel) spectra for BBP and TIPS-pentacene in toluene. Singlet-excited state spectra are obtained at ca. 5 ps and triplet spectra obtained at 500 ps and 1 μs for BBP and TIPS-P respectively.

Finally, the compartmental model used to simulate pulse radiolysis experiments can be applied to laser transient absorption experiments. Using the same kinetic parameters as earlier we simply alter the starting condition to reflect the fact that the excited-singlet and -triplet states are no longer populated by way of electronic energy transfer. Instead, we start with 100% S−G. By applying the differential molar absorption coefficients for the excited-triplet state as obtained in this chapter, we can simulate the triplet decay curve. With minimal optimization qualitatively comparable decay curves can be simulated against real triplet decay data over timescales spanning several orders of magnitude as can be seen from Figure 6.8.

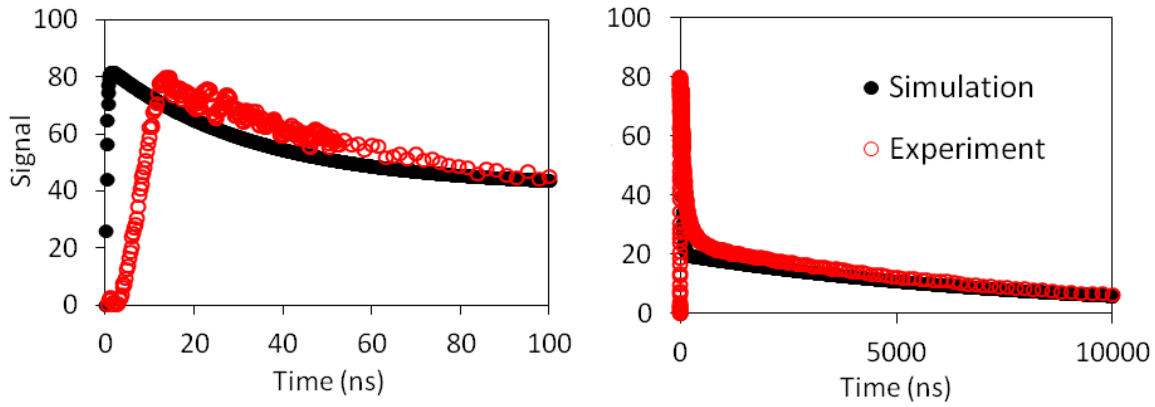

Figure 6.8. Simulation of the BBP transient triplet decay at 525 nm in toluene.

6.3.1 The Effect of Solvent Polarity on the Ultrafast Photophysics

Transient absorption spectral measurements were made for BBP in a small range of solvents with differing polarity, under otherwise identical experimental conditions. Although the general features of the various spectra were not ostensibly altered by changing the solvent polarity (apart from slight shifts in peak maxima), the reaction kinetics were modified. The most notable change in the transient spectroscopic data occurs in the rate constant for singlet-excited state deactivation. This particular feature was confirmed by ultrafast transient absorption spectroscopy. Table 6.4 summarizes the effect of solvent polarity on the excited-singlet state lifetime (τ_S) and on the quantum yield (Φ_T) for formation of the triplet-excited state. Here, the relative triplet quantum yield was determined from the ultrafast transient absorption spectra. In cyclohexane, which is the least polar of the solvents used, we find the longest fluorescence lifetime (τ_S = 280 ps) and a triplet yield of Φ_T = 150%. The two parameters appear to be correlated, although there is considerable spread of data, in that lower triplet yields appear for shorter singlet lifetimes.

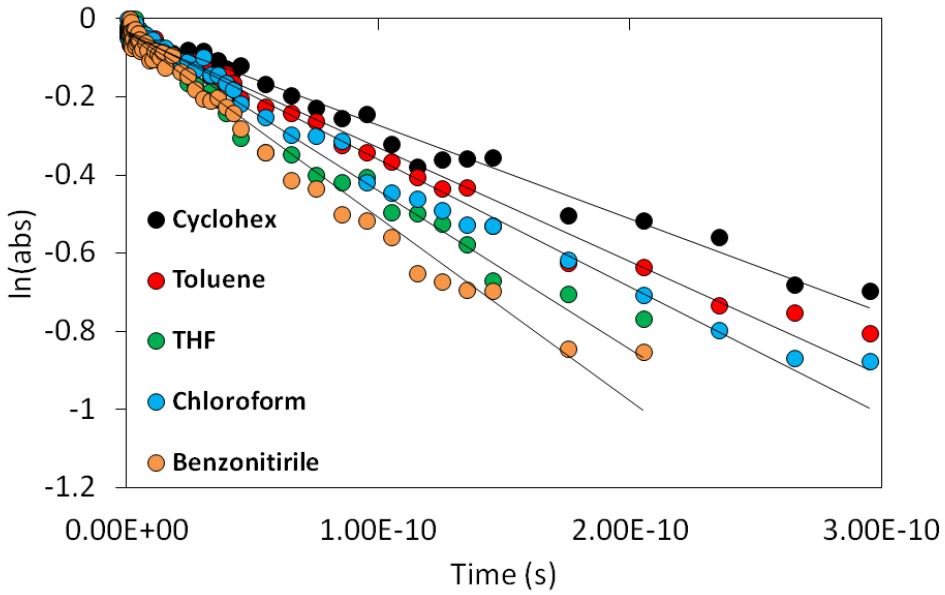

Figure 6.9. Trend of singlet-excited decay as monitored by ultra-fast transient absorption spectroscopy for BBP at 460 nm in a range of solvents.

Before exploring the solvent dependence in more detail, it is useful to establish the protocol for determining triplet quantum yields Φ_T. Earlier the triplet quantum yield was carefully established for BBP in benzene and toluene from pulse radiolysis experiments. The triplet yield in non-polar solvents (150%) is taken as the baseline for comparison with the more polar solvents. In making this analysis, it is assumed that the ratio of molar absorption coefficients for the singlet- and triplet-excited states is not sensitive to the solvent polarity. Each absorbance measurement is taken at the maximum, thereby allowing for small solvent shifts.[3,5] Finally, it should be stressed that initial studies refer only to the total triplet yield, with no attempt to partition this between T−T and T−G.

We accept that the quantum yield for formation of the excited-singlet state is unity in all solvents and that the corresponding differential molar absorption coefficient is insensitive to solvent polarity. The molar absorption coefficient of a single triplet for BBP was determined to be 42,000 M^{-1} cm^{-1} at 525 nm from pulse radiolysis measurements (using the method from Chapter 4). The absorption coefficient for the singlet-excited state at the peak maximum (approx. 460 nm) is 43,800 M^{-1} cm^{-1} in toluene. We assume that this latter value is independent of solvent polarity. Rather than use the value derived for ε_{TRIP}, we prefer to rely on the absorbance change associated with the GSB signal in the wavelength region around 650-660 nm. We fix this value at -20,000 M^{-1} cm^{-1}. Now we are able to compare the concentration of singlet and triplets and derive the triplet quantum yield using Equation 6.4. It is important to ensure the GSB signal is not contaminated by other transient species such as stimulated emission.[9]

A visual representation of how we determined the triplet yield is provided with Figures 6.10 and 6.11. In each case, the absorbance for the singlet-excited state measured at 5 ps is compared to that of the excited-triplet state measured at 5 ns. In Figure 6.11, the triplet spectra collected in several solvents are normalized to a common singlet-excited state absorbance, which allows for direct comparison of the concentration of triplet species represented by the GSB. There was some concern that the baseline might be shifting during the course of the transient spectra, but identification of isosbestic points confirms the signal at early and later times can be compared directly.

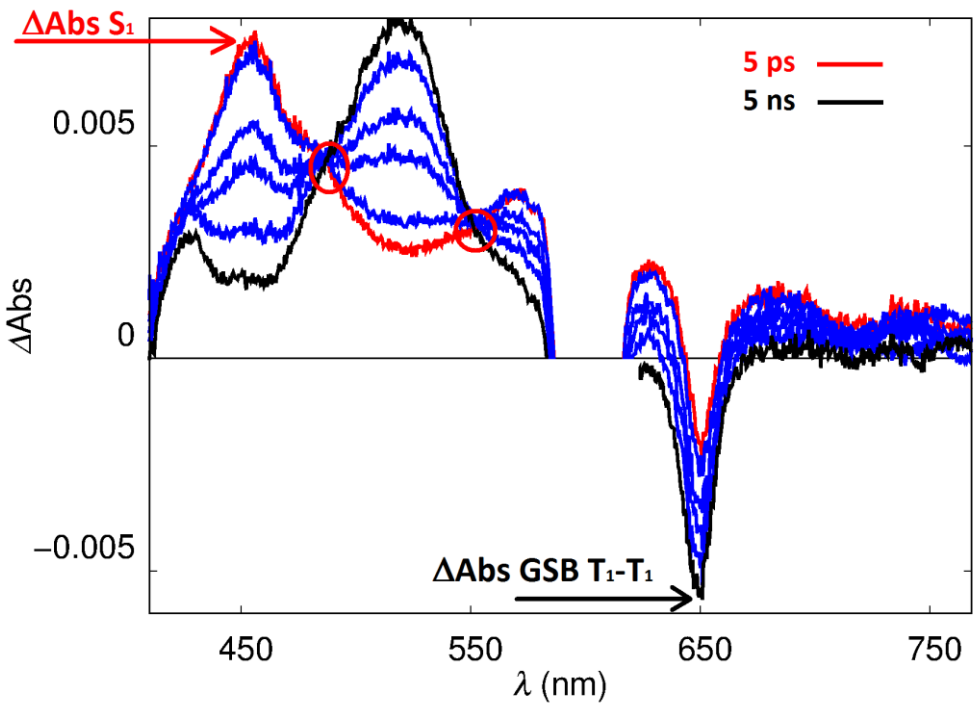

Figure 6.10. Illustration of how the triplet quantum yield for BBP was determined from the evolving ultrafast transient spectra in cyclohexane. Here the absorbance values used in Equation 6.1 are identified.

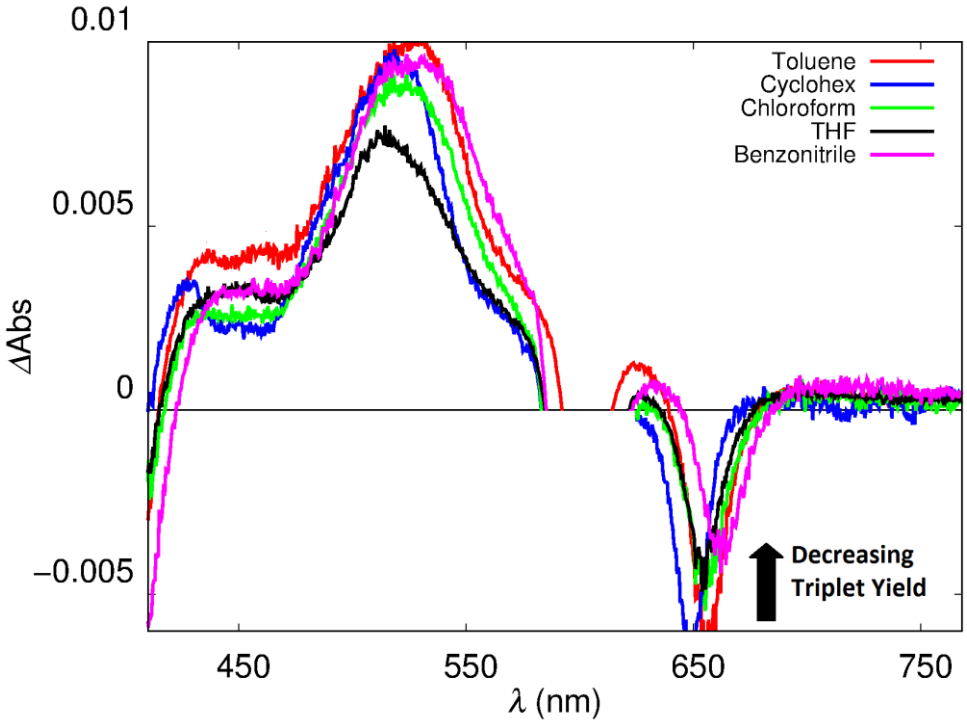

Figure 6.11. Normalized triplet absorption spectra for BBP in a selection of solvents illustrating the trend in triplet quantum yield.

The rate constant (k_S) for deactivation of the excited-singlet state is calculated as being the reciprocal of its lifetime. The derived values are listed in Table 6.4 and compared to the solvent dielectric constant. It is seen that k_S increases steadily with increasing ε_S across the solvents used. It is conceivable that the rate constant for singlet fission changes with solvent polarity, leading to an enhancement of nonradiative decay. Another possibility is a change in the partitioning in mono and dual triplets. Indeed other investigators have indicated that singlet fission is in some cases mediated by charge transfer states.[10-12] The triplet yield is clearly above 100% in all the solvents investigated, but decreases with increasing solvent polarity, as measured in terms of the static dielectric constant (Table 6.4). Somewhat surprisingly, the triplet yield evolves with the inverse of the rate constant for global decay of the S_1 state. Thus, increased rates of decay of S_1 correspond to lower triplet yields. This same effect was reported by Friend *et al.* for iSEF in an orthogonally linked bis-pentacene derivative, although only two solvents were compared.[1] It is interesting to enquire more deeply into this situation.

$$\Phi_T = \frac{\Delta Abs(_{GSB\ nm}{}^{3}BBP) * \mathcal{E}(_{nm\ max}{}^{1}BBP)}{\Delta Abs(_{nm\ max}{}^{1}BBP) * \mathcal{E}(_{GSB\ nm}{}^{3}BBP)} \qquad (6.4)$$

Table 6.4. Solvent dependence on excited-singlet state lifetime and triplet yield as recorded for BBP in dilute solution.

Solvent	τ_S (ps)	k_S (10^9 s^{-1})	ε_S	Φ_T	$\tau_{T\text{-}T}$ (ns)	$\tau_{T\text{-}G}$ (ns)
C_6H_{12}	280 ± 15	3.6	2.0	162	150	6.3
Tol	200 ± 10	5.0	2.4	160	150	6.0
$CHCl_3$	170 ± 9	5.9	4.8	145	120	5.8
THF	130 ± 7	7.7	7.6	140	-	-
BzCN	100 ± 5	10.0	25	130	100	5.5

In addition to the trend in the triplet yield there is also a small change in the triplet lifetimes. The lifetime for the mono-triplet shows only a modest dependence on solvent and appears to decrease slightly in more polar solvents. A more significant effect is observed for the lifetime of the dual-triplet, which we believe is set entirely by iTTA. Here, the lifetime shortens in the more polar solvents. It might be noted that in viscous,

non-polar environments, the rate of iTTA decreases significantly. For example, in mineral oil the lifetime is extended to ca. 200 ns while in a drop-cast Zeonex film doped with BBP the value rises to some 300 ns. In both these latter cases, decay of T−T remains as a first-order process.

For the excited-triplet state there can be no possibility for light-induced charge transfer between the pentacene units. This might not be the case for the excited-singlet state in polar solvent. However, the electrochemical data discussed earlier can be used to estimate the thermodynamic driving force (ΔG_{CT}) for intramolecular electron transfer[13] in CH_2Cl_2 solution. For this, we use Equation 6.2[14] where E_{OX} (= +0.56 V vs Ag/Ag^+) and E_{RED} (= -1.25 V vs Ag/Ag^+), respectively, are the half-wave potentials for oxidation and reduction of the TIPS-P units present in BBP. The excitation energy, E_{00} (= 1.88 eV), is determined as the intersection between normalized absorption and emission spectra. The final term of the equation accounts for the electrostatic stabilization of the radical ion pair, where e is the elementary charge of an electron, ε_0 the vacuum permittivity, ε_s the dielectric constant of the solvent and r_{DA} the distance between the two charges.

$$\Delta G_{CT} = (E_{OX} - E_{RED}) - E_{00} - \frac{e^2}{4\pi\varepsilon_0\varepsilon_s r_{DA}} \qquad (6.5)$$

$$\Delta G_d = \frac{e^2}{4\pi\varepsilon_0\varepsilon_s}\left[\frac{1}{r_p} - \frac{1}{d_{cc}}\right] - \frac{e^2}{36\pi\varepsilon_0}\left[\frac{1}{r_p}\right] \qquad (6.6)$$

The latter term is assumed to be similar to the centre-centre separation of 23 Å. The net result is an approximation that ΔG_{CT} in CH_2Cl_2 has a value of about –0.14 ± 0.02 eV. This would suggest that light-induced electron transfer is slightly favourable under these conditions. The nature of the solvent affects both the electrostatic energy and the reduction potentials. This latter effect can be calculated using the Weller equation (Equation 6.6)[15], where r_P (= 8 Å) is the approximate radius of a TIPS-P molecule, d_{cc} is the centre-centre distance of the pentacene units and ε_s' is the dielectric constant of the medium used for cyclic voltammetry measurements. The conclusion from these calculations is that ΔG_{CT} for light-induced electron transfer between TIPS-P molecules transforms from strongly positive in cyclohexane to mildly negative in benzonitrile (Figure 6.12 inset).

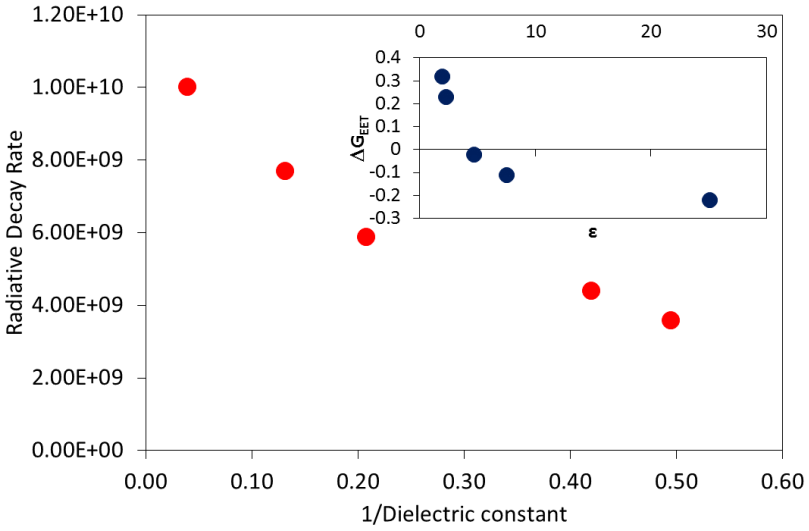

Figure 6.12. Singlet decay rate of BBP plotted against reciprocal dielectric constant. Inset the driving force for photoinduced electron transfer is plotted against solvent dielectric.

Since the rate constant for electron transfer depends exponentially on the driving force, it follows that electron transfer will be important only in polar solvents. It also follows that light-induced electron transfer cannot take place from the triplet-excited state because of the dramatic lowering of E_{00} in Equation 6.2. This positions the resultant charge-transfer state (iCTS) between the excitation energies for singlet and triplet states. As such, charge recombination will result in population of the triplet-excited state rather than the ground state, at least according to the Englman-Jortner energy-gap law.[16] This route cannot produce the excited-triplet state in a yield higher than 100% and it can lead only to T–G. Since the triplet yield decreases with increasing solvent polarity, it would appear that the energetic of the system are such that a potential CTS is positioned slightly below the singlet excited state.

There is no obvious indication for the formation of a radical ion pair in any of the transient differential absorption spectral records and the solvent effect on the triplet yield counts against rapid spin conversion within any such short-lived species. That the rate constant for iTTA and that for iSEF show similar escalations in polar solvents suggests a common mechanism or intermediate species. The latter would require some kind of charge-transfer character allowing for solvent stabilization. The report by Friend *et al*. indicates that the rate of iTTA decreases markedly with increasing viscosity of the host medium,[1] although this effect was not explained in the manuscript. We see a

similar effect with paraffin oil and with the thin film. It is possible that the solvent and viscosity effects are linked and point towards an optimum geometry for maximizing spin conversion involving through-bond interactions. Such effects are known for enhanced intersystem crossing occurring in geminate ion pairs evolving from excited-singlet states, where the importance of orthogonal geometries has been stressed.[17] Our results would require that the solvent plays a role in establishing the molecular geometry (by imposing partial charge-transfer character) and in restricting access to favourable geometries (by a viscosity-imposed barrier). There are two opposing situations: Increased charge-transfer interactions enhances the rate of deactivation of the excited state (either S–G or T–T) but the average conformation associated with such structures is not favourable for rapid intersystem crossing. A nonpolar environment, or a viscous medium, destabilizes the geometry required for rapid quenching but gives (distribution of) geometries more aligned to intersystem crossing.

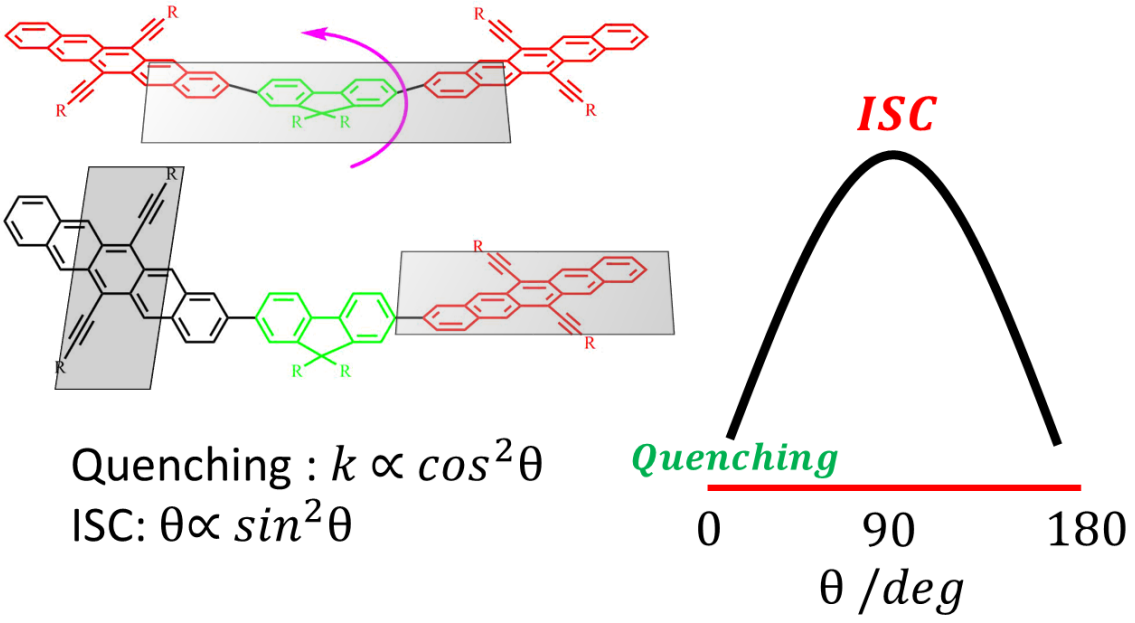

Figure 6.13. Scheme illustrating the effect of geometry on the rate of intersystem crossing in BBP.

Since even in cyclohexane the triplet yield falls short of the maximum value of 200%, it follows that the optimum geometry for intersystem crossing has not been attained. Most likely, super-exchange interactions play a role in promoting through-bond interactions in BBP and the small red-shifts found for absorption (and emission)

transitions confirm electronic interaction between pentacene and the fluorene spacer. A key feature in both iSEF and iTTA processes is the energy of the excited-triplet state. It seems that T–T and T–G might possess slightly different energies. The relationship between the electronic energies of S–G and T–T is critical for both processes but we have not succeeded in establishing a value for T–T (or indeed T–G). A further difficulty is that it is difficult to quantify the amount of delayed fluorescence with any real precision. Thus, we are still missing some important features that might help an improved understanding of the photophysics of BBP.

6.4 Conclusions

At this point it is clear that, in common with many other covalently-linked polyacenes[1-6], BBP populates the triplet manifold in yields higher than 100%. A few years ago, this would have been regarded as astonishing but, such has been progress in the field, this is no longer surprising. In this chapter, we have reached consensus on a triplet yield of 150% in toluene. The same value is found in benzene and cyclohexane. The fact that both SEF and TTA occur within thin films at high dilution confirms that these processes are based on intramolecular reactions. The effects of the surrounding medium are explained in terms of subtle geometry changes but more information is needed to fully explain the effects of polar solvent. We have found, but not discussed in detail here, that the rate of iTTA is weakly activated with an activation energy comparable to that of the solvent viscosity.

We are well aware that the energetics for BBP are critical and we have made every effort to establish a meaningful triplet excitation energy for this compound. Direct comparison between BBP and TIPS-P is not so meaningful because of significant shifts in electronic levels. We are attempting to establish if the longer-lived triplet state is able to sensitize formation of singlet molecular oxygen. Other on-going studies attempt to use photoacoustic calorimetry to measure the triplet energy. Neither study has advanced sufficiently to be included in this work. We have also examined iTTA for BBP in a thin film and expect to publish the results in a forthcoming article.

6.5 References

1. Lukman, S.; Musser, A.J.; Chen, K.; Athanasopoulos, S.; Yong, C.K.; Zeng, Z.; Ye, Q.; Chi, C.; Hodgkiss, J.M.; Wu, J.; Friend, R.H. *Adv. Funct. Mater.* **2015**, 25, 5452-5461.

2. Burdett, J.J; Bardeen, C.J., *J. Am. Chem. Soc.* **2012**, 134, 8597-8607.

3. Walker, B.J.; Musser, A.J.; Beljonne, D.; Friend, R.H. *Nat. Chem.* **2013**, 5, 1019-1024.

4. Sanders, S.N.; Kumarasamy, E.; Pun, A.B.; Trinh, M.T.; Choi, B.; Xia, J.; Taffet, E.J.; Low, J.Z.; Miller, J.R.; Roy, X.; Zhu, X.Y. Quantitative intramolecular singlet fission in bipentacenes. *J. Am. Chem Soc.* **2015**, 137, 8965-8972.

5. Zirzlmeier, J.; Lehnherr, D.; Coto, P.B.; Chernick, E.T.; Casillas, R.; Basel, B.S.; Thoss, M.; Tykwinski, R.R.; Guldi, D.M. *Proc. Natl. Acad. Sci. U.S.A*, **2015**, 112, 5325-5330.

6. Sakuma, T.; Sakai, H.; Araki, Y.; Mori, T.; Wada, T.; Tkachenko, N.V.; Hasobe, T. *J. Phys. Chem. A.* **2016**, 120, 1867-1875.

7. Bensasson, R.V.; Hill, T.; Lambert, C.; Land, E.J., Leach, S.; Truscott, T.G., Chem. Phys. Lett. **1993**, 201, 326-335.

8. Saltiel, J.; March, G.R.; Smothers, W.K.; Stout, S.A.; Charlton, J.L. *J. Am. Chem. Soc.*, **1981**, 103, 7159-7164.

9. Berera, R.; van Grondelle, R.; Kennis, J.T. Photosynth. Res. **2009**, 101, 105-118.

10. Margulies, E.A.; Miller, C.E.; Wu, Y.; Ma, L.; Schatz, G.C.; Young, R.M.; Wasielewski, M.R. *Nat. Chem.* **2016**, 8, 1120-1125.

11. Monahan, N.; Zhu, X.Y. *Annu. Rev. Phys. Chem.* **2015**, 66, 601-618.

12. Smith, M.B.; Michl, J. Recent advances in singlet fission. *Annu. Rev. Phys. Chem.* **2013**, 64, 361-386.

13. Liddell, P.A.; Kuciauskas, D.; Sumida, J.P.; Nash, B.; Nguyen, D.; Moore, A.L.; Moore, T.A.; Gust, D. J. Am. Chem. Soc. **1997**, 119, 1400-1405.

14. Rehm, D.; Weller, A. *Ber. Bunsenges. Phys. Chem.* **1969**, 73, 834-839.

15. Gaines III, G.L.; O'Neil, M.P.; Svec, W.A.; Niemczyk, M.P.; Wasielewski, M.R. *J. Am. Chem. Soc.* **1991**, 113, 719-721.51.

16. Englman, R.; Jortner, J. *Mol. Phys.* **1970**, 18, 145-164.

17. Osuka, A.; Maruyama, K.; Mataga, N.; Asahi, T.; Yamazaki, I.; Tamai, N. *J. Am. Chem. Soc.* **1990**, 112, 4958-4959.

Chapter 7: Cyanine Dyes as Ratiometric Fluorescence Standards for the Far-Red Spectral Window

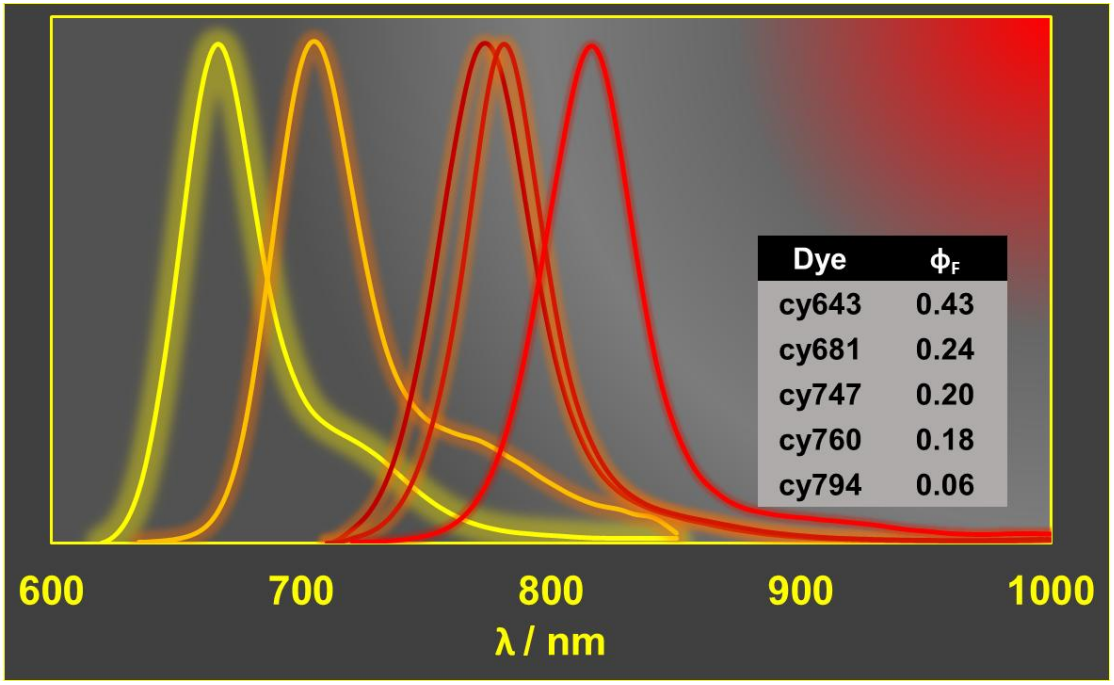

7.1 Introduction

The availability of fluorophores emitting in what might loosely be defined as the red-region (600-800 nm) of the visible and near-infrared (800-1000 nm) spectral ranges has increased precipitously in recent years.[1-3] Particularly for biomedical applications, this spectral window is important because light at wavelengths longer than 650 nm penetrates soft tissues and cells without causing damage.[4,5] Other advantages to targeting far-red fluorescence include lower levels of background signal and reduced scattering. For both fluorescence microscopy and photodynamic therapy, there are now a number of chromophores absorbing and emitting in this region.[6] Low band-gap polymers and NIR emitters are of interest in the context of organic semiconductors, solar concentrators and solar cells.[7,8,9]

In terms of quantitative analysis, there is a pressing need for reliable protocols which can be applied to determine fluorescence quantum yields for emitters in this spectral window. Few commercial instruments are well equipped to handle samples emitting in the far-red, at least without expensive attachments. There are few recommended ratiometric standards suitable for this spectral window and, where standards are available, these have not been subjected to the rigorous testing usually given to conventional standards. Specifically, there is not a simple series of readily available standard emitters to cover the region of interest and that could be used to construct calibration curves with which to correct existing instruments. An alternative to identifying ratiometric emitters is to use an integrating sphere but such instrumentation is not widely available to investigators.[10]

Given that the fluorescence quantum yield is a fundamental photophysical measurement, central to investigations in this thesis, this chapter sets out to address some of the problems with quantitative measurements of fluorescence in the 600 to 1000 nm spectral window. A new set of red-emitting fluorescence yield standards is proposed, using a series of commercially available cyanine dyes. In order to accurately measure the fluorescence yields, a previously reported technique, thermal blooming (aka. thermal lensing) spectroscopy[11,12], is reintroduced. Although the method was proposed in the 1970s by Magde and co-workers[13], the technique has been relatively

underexploited over the intervening decades. In this study, a bespoke thermal blooming spectrometer was constructed and we establish simple protocols for fluorescence yield measurements at a fraction of the cost of a commercial spectrophotometer.

The dyes employed for this work were studied in methanol solution at room temperature. The compounds were selected so as to span the emission wavelength region from 650 to 950 nm, with absolute emission quantum yields being determined by thermal blooming spectrometry. Where possible, fluorescence yields were also determined against previously established standards, using a conventional fluorescence spectrophotometer. These cyanine dyes were shown to be readily soluble in organic solvents, without sign of aggregation at appropriate concentrations, and to present a common structural platform. The latter is useful in attempting to rationalize the photophysical properties, as a check on the derived quantum yields. Calibration of the instrument is made by reference to aluminium(III) phthalocyanine tetrasulfonate and aza-BODIPY[14,15] in methanol.

7.2 Results and Discussion

A detailed description of the underlying theory and experimental setup for our thermal blooming instrument (Figure 7.1) is given in the Experimental Methods chapter. To précis the core concept, thermal blooming can be used to determine the absolute fluorescence quantum yield through an indirect measurement, namely recording the nonradiative component instead of fluorescence. A silicon photodiode detector is used to measure the change in refractive index of the solvent as excitation energy delivered from an incident laser beam is transferred from the absorbing fluorophore to the solvent.

Since commonly used solvents are transparent to lasers in the visible spectrum, it is safe to assume any heat deposited in the solvent arrives from nonradiative decay of the fluorophore. The lower the fluorescence yield, the more heat is transferred to the solvent through vibrational relaxation and vice versa. The total energy of the system can therefore be accounted for by assuming the excitation power must equal the sum of the transmitted power, fluorescence, and heat from nonradiative decay of the fluorophore.

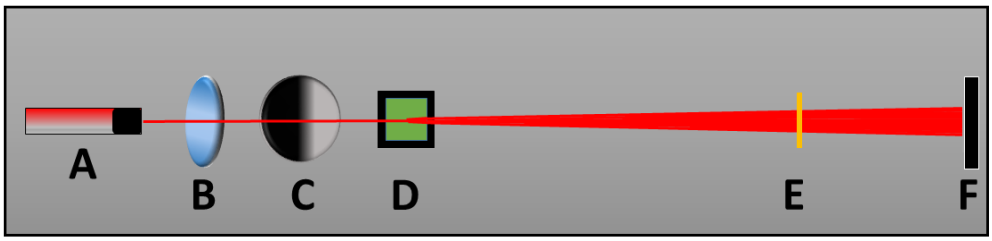

Figure 7.1. Scheme illustrating the thermal blooming spectrometer setup constructed for this study. A. laser; B. plano-convex lens; C. digital optical shutter; D. sample cuvette; E. filter; F. detector.

What the detector sees is the excitation beam, which has been focused onto the sample. As the solvent heats up after a brief exposure to the laser, light incident on the detector will defocus (i.e. expand or "bloom"), which will correspond to a transient decay of current, monitored with a digital oscilloscope. The recovered data are fitted to the model described by Equation 7.1.

7.2.1 Experimental Protocol

An important consideration for obtaining reliable thermal blooming measurements is to avoid depositing too much heat in the solvent reservoir, in which case the results become distorted due to aberration and convection currents. In methanol, the upper limit for incident laser power before these detrimental effects become noticeable is 0.6 mW.[16] For a given excitation source, the absorbed power must be kept below this threshold, either by adjusting the sample absorbance or by attenuating the laser beam. With the 3 mW 635 nm cw laser used here, liquid samples in a 1-cm quartz cuvette possessing an absorbance <0.1 (i.e. less than 20% of the incident laser power is absorbed by the sample) at the excitation wavelength fulfil this condition.

The sample must be placed in a region where the waist of the beam is uniform through the cell path length. This is referred to as the Rayleigh distance and can be optimized by adjusting the distance between lens and sample until the maximum thermal blooming signal is observed. The entire optical rail should be isolated from stray light during a measurement. The detector used here functions between 400 and 1100 nm, so any laser in that range could be used as an excitation source to obtain fluorescence yield measurements.

For fluorescence yield measurements, the following experimental procedure was established: solution samples containing the fluorophore of interest were measured in 1 cm quartz cuvettes against a non-fluorescent standard absorbing in the same region, Brilliant Green. Other standards tested include crystal violet and copper(II) sulfate. In the 635 nm region these were deemed usable alternatives. Brilliant Green is a particularly good choice because, as a member of the triarylmethine family, it has a well characterized, viscosity-dependent radiationless channel that serves to depopulate the excited-singlet state on a rapid timescale.[17] In a non-viscous solvent such as methanol, Brilliant Green (λ_{max}^{abs} = 625 nm in MeOH) shows no significant fluorescence at ambient temperature (fluorescence yield <0.001).

All samples were measured in air-equilibrated solution. Although one may consider purging solution samples of oxygen a more thorough approach, ensuring an absence of bimolecular quenching of fluorescence with molecular oxygen, this can be a superfluous exercise. It is impractical to try and establish a standard for the degree of deoxygenation of a solvent. Furthermore, any fluorophore with a singlet lifetime S_1 below 10 ns will have only a marginal possibility of quenching by diffusional contact with molecular oxygen[18], the fluorescence lifetime being effectively at the diffusion-controlled limit for common solvents.

The absorbance of each sample was carefully matched with the standard at 635 nm. This absorbance was maintained in the range 0.07 to 0.10. All measurements were made in the same cuvette held in the same orientation to avoid any error arising from manufacturing differences in the quartz surfaces. It was also important to isolate the instrument from vibrations.

Measurements involved opening a digital optical shutter for 0.5 s periods at 5 s intervals. Each measurement involves 16 repeats. An oscilloscope collects and averages the signal across a pre-determined number of recordings. Data sampling was at a rate of 10,000 counts per second. The photocurrent decay traces for both the standard and sample were analyzed according to Equation 7.1 in order to obtain the critical value θ. Finally, Equation 7.2 was used to determine the fluorescence yield. Each experiment was repeated at least 7 times. Absorption spectra were recorded with a Hitachi U-3310

spectrophotometer and fluorescence spectral measurements were made with a Horiba Fluorolog Tau-3 system, with a R928 detector being used for emission up to 830 nm, beyond that a R2658P detector was used (allowing spectra up to 1000 nm). A typical output from a thermal blooming measurement saw good agreement between the thermal blooming model and raw data.

$$\mathrm{I(t)} = \mathrm{I_0}\left[1 - \theta\left(1 + \frac{\mathrm{t_c}}{2\mathrm{t}}\right)^{-1} + \frac{1}{2}\theta^2\left(1 + \frac{\mathrm{t_c}}{2\mathrm{t}}\right)^{-2}\right]^{-1} \qquad (7.1)$$

$$\Phi_F = \left[1 - \frac{A_R}{A_S}\frac{\theta_S}{\theta_R}\right]\frac{v_{ex}}{v_F} \qquad (7.2)$$

Here $\mathrm{I_0}$ is initial laser intensity, t is time and $\mathrm{t_c}$ describes the thermal diffusivity of the solvent. The term θ is directly proportional to the radiant heat. In Equation 7.2, A refers to the absorbance of the sample S and non-fluorescent reference R. To account for energy lost to the Stokes' shift, the excitation energy (in wavenumber) v_{ex} is divided by the mean fluorescence maximum v_F to provide a correction factor. The preferred solvent for this work was methanol. Particularly in the case of the cyanine dyes, this solvent precludes influences from dimerization and aggregation apparent when an aqueous solvent is used. Beer-Lambert law plots of all samples showed no evidence of aggregation through a concentration range up to at least 1 x 10^5 M in CH_3OH. Due to its relatively large specific heat capacity, water is the "least sensitive" solvent for thermal blooming measurements. Each solvent has a characteristic diffusion time (in seconds), fitting raw data to Equation 7.1 typically resulted in a t_c value for CH_3OH of 0.055 s. This is in agreement with reports in the literature.[19]

7.2.2 Calibration with Control Compounds

To ensure the accuracy and reproducibility of the thermal blooming apparatus, the fluorescence quantum yield (Φ_F) of aluminium(III) phthalocyanine tetrasulfonate (AlPcS) in methanol was measured repeatedly over a four-month period by thermal blooming and by conventional measurements on a fluorometer (using a total of three different instruments). Results with thermal blooming spectroscopy were obtained with excitation at 635 nm and a series of concentrations was used. The non-fluorescent standard was Brilliant Green as for all other measurements. The mean Φ_F value was

found to be 0.55 ± 0.02 (Table 7.1). This can be compared with 0.51 as reported by Beeby *et al.*[20] Other literature values for the compound place the fluorescence yield for AlPcS in the range 0.51-0.55 in organic solvents.[21,22] In aqueous solution, dimerization will result in diminished fluorescence and at elevated concentration the inner filter effect has to be considered.[23] The absorption spectrum of AlPcS covers the wavelength range from 550 to 680 nm, with excellent absorption at the excitation wavelength. Fluorescence is readily observed in the red region (Figure 7.2). Using a conventional spectrophotometer (λ_{EX} = 610 nm), Φ_F was found to be 0.54 ± 0.05 in methanol by comparison to free-base *meso*-tetraphenylporphyrin in N,N-dimethylformamide solution (Φ_F = 0.12).[21] This set of results appears to be self-consistent and the validity of the thermal blooming set-up is therefore confirmed. Our sample of AlPcS gave a single-exponential decay profile, with an excited-state lifetime (τ_S) of 6.6 ± 0.2 ns, when excited at 635 nm under time-correlated, single photon counting conditions (Table 7.1). Overall, AlPcS is a promising fluorescence standard for excitation in the 580-640 nm for highly fluorescent dyes such as BODIPY, BOPHY and tetrapyrrolic pigments. Care should be taken to verify the authenticity of the standard sample here though.

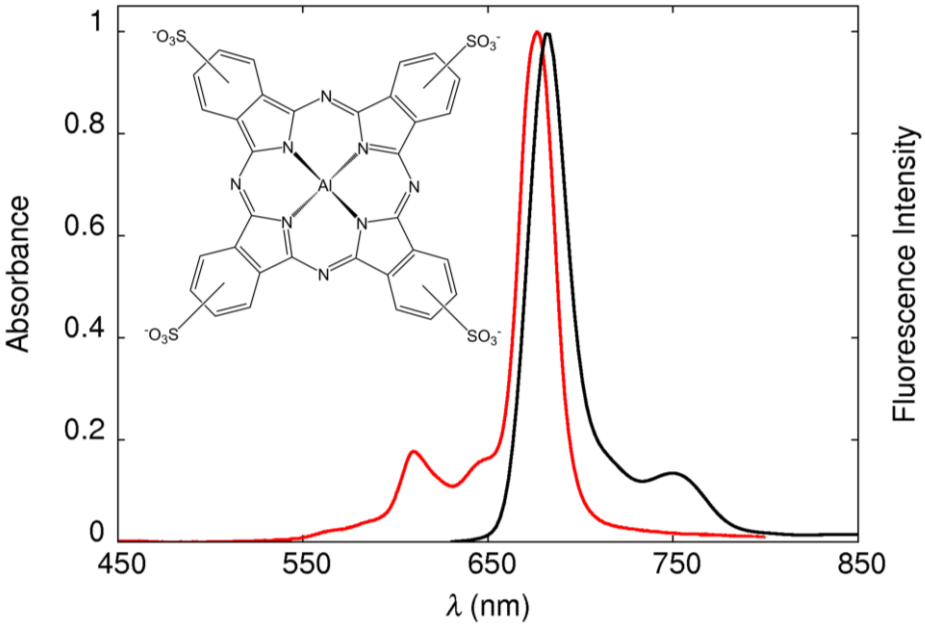

Figure 7.2. Room temperature steady-state absorption and fluorescence spectra of AlPcS in methanol. Molecular formula is given in the inset.

A further test of the experimental set-up was made using two aza-BODIPY derivatives aza-BOD-1 and aza-BOD-2 which differ only by substituents attached to the 3,5-aryl groups. The photophysical properties of aza-BOD-1 were discussed in Chapter 3 and are therefore well-established. For aza-BOD-1, Φ_F has a value of 0.56 and τ_S is 3.5 ns (Table 7.1). Thermal blooming studies in methanol gave rise to a Φ_F value of 0.58 ± 0.02 (Table 7.1). The same Φ_F was recovered for different concentrations within the micromolar range and under various experimental configurations. The value, at least in methanol solution, is consistent with hydrogen bonding to the *meso*-nitrogen on the BODIPY as already discussed in Chapter 3, and is a highly reproducible result.

Table 7.1. Summary of fluorescence quantum yields available for the compounds used to calibrate the thermal blooming set-up.[(a)]

Dye	Φ_F	Method	Error	τ_S / ns [(b)]
AlPcS	0.51	LIT [(c)]	±0.026	6.0
	0.54	SSF [(d)]	±0.050	6.6
	0.55	TBS [(e)]	±0.016	6.6
aza-BOD-1	0.60[(f)]	LIT	±0.030	-
	0.56	SSF	±0.028	3.5
	0.58	TBS	±0.017	3.5
aza-BOD-2	0.33	SSF	±0.017	2.3
	0.33	TBS	±0.017	2.3

(a) All measurements made in methanol at 20 ^{0}C. (b) Excited-singlet state lifetime measured by time-correlated, single photon counting. (c) Φ_F taken from the literature.[20] *(d) Φ_F measured in this work using conventional steady-state emission spectroscopy. (e) Φ_F measured in this work by thermal blooming spectrometry. (f) Lit. value in EtOH.*[14]

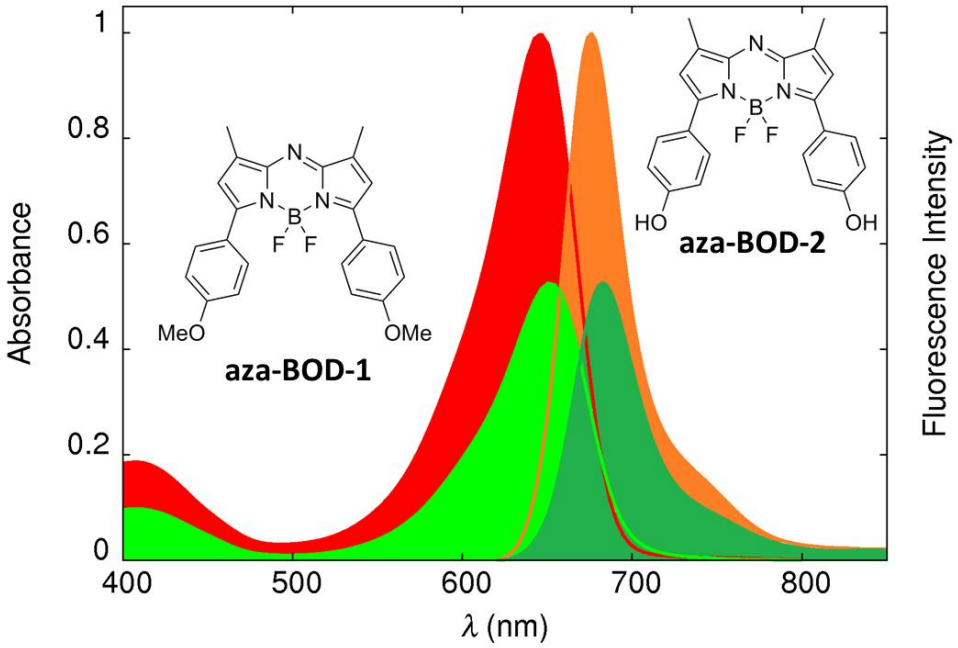

Figure 7.3. Steady-state absorption and emission spectra of aza-BOD-1 (red and orange) overlaid with aza-BOD-2 (green) at room temperature in methanol. The traces are normalized a ratio of 2:1 due to overlapping spectra.

The photophysical parameters for aza-BOD-2 have not previously been reported in the literature, but the absorption and emission maxima are very close to that of aza-BOD-1 (Figure 7.3, Table 7.2). Conventional determination of the fluorescence quantum yield using aza-BOD-1 as a reference gave a value of 0.33 (Table 7.1). The excited-state lifetime was found to be 2.3 ns, noticeably shorter than that found for aza-BOD-1 under identical conditions. Using the thermal blooming method, the fluorescence quantum yield for aza-BOD-2 was determined to be 0.33 ± 0.02. The modest differences in fluorescence yield and lifetime found for these two aza-BODIPY emitters is explained in terms of enhanced nonradiative deactivation promoted by the O-H bond present in aza-BOD-2. This finding is precisely in line with expectations based on the Englman-Jortner energy-gap law.[24] Overall, for both BODIPY dyes the level of agreement between conventional fluorescence measurements and thermal blooming is excellent across this particular (but narrow) wavelength range. Due to the apparent reliability of the technique, at least for moderately to highly fluorescent samples, we can now attempt to extend the range of fluorophores into the near-IR region, where most fluorometers are less reliable or cannot detect at all (see experimental chapter for a brief discussion).

Some consideration should be given to possible alternative fluorescent standards for the red region. Indocyanine Green and Cresyl Violet (λ_{max}^{abs} = 603 nm, λ_{max}^{fluor} = 622 nm in ethanol) have often been proposed. Indeed, Magde and co-workers proposed Cresyl Violet as a standard after measurements were made with thermal blooming.[25] As a practical proposition, however, fluorescence measurements obtained by other members of our research group have shown that the photophysical properties of Cresyl Violet are very sensitive to the nature of the solvent. Fluorescence yields and singlet decay lifetimes vary drastically with solvent polarity and concentration. A further alternative is the oxazine dye known as Nile Blue. This dye has reported fluorescence quantum yields ranging from 0.23 to 0.47.[26,27,28] Our measurements of Nile Blue in ethanol (λ_{max}^{abs} = 627 nm, λ_{max}^{fluor} = 664 nm) resulted in a value 0.23 by the thermal blooming and a value of 0.26 by conventional fluorescence measurements made against *meso*-tetraphenylporphyrin. Nile Blue clearly displayed scatter in its fluorescence spectrum. Furthermore, the dye exists as an equilibrium mixture of protonated and deprotonated forms unless a small amount of acid is added to the solution. In our hands, neither of these two alternatives is a viable emission standard, especially for use by non-specialist researchers.

By far the best fluorescent standard noted during work encompassed in this thesis is the free-base *meso*-tetraphylporphyrin (m-TPP). It has repeatedly been reported with a fluorescence yield between 0.11 and 0.13 in a range of solvents.[21,29,30] It also yields results very close to the thermal blooming measurements made here. The main disadvantage with m-TPP is that the fluorescence yield is relatively low, not ideal for comparison with strong fluorophores. An ideal fluorescence standard would have a fluorescence yield of 0.3 to fulfil this condition.[31] The porphyrin does have the advantage of providing a range of possible excitation wavelengths and, by way of direct excitation into the Soret band at 420 nm, of being usable at extremely low concentration.

7.2.3 Errors and Reproducibility

The sources of errors in conventional fluorescence yield measurements have been well documented, with the most obvious being self-absorption due to working with too concentrated solutions.[32-34] An equally important consideration is the presence of fluorescent impurities. With the thermal blooming technique, there are a number of potential sources of systematic error.[13] Chief amongst these is determining the exact amount of laser power being transmitted through the sample. The most practical way of achieving this result is by measuring the absorbance. A restriction specific to the thermal blooming technique comes about when the fluorescence yield is very small. In this case, the thermal blooming traces for the standard and sample become increasingly comparable. In this situation, the ratio $\frac{\theta_S}{\theta_R}$ (Equation 7.2) approaches unity and the emphasis on experimental error shifts to the recorded absorbance. For very low quantum yields, minor variations in absorbance translate into major uncertainties in the recovered parameters, leading to overall errors in excess of ±5%. As such this technique is not well suited to measuring fluorescence quantum yields less than ca. 0.05.

We emphasize the problem of fluorescent impurities present in the sample of interest; this is a real concern for some of the multi-component molecular systems studied across the field. For a fluorophore analyzed with a conventional fluorometer, any trace of highly fluorescent impurity will be detected in full, possibly even overlapping with the target fluorescence. Since the thermal blooming experiment operates by absorption and not by detecting fluorescence, the problem with small amounts of impurity can be minimized. For example, the presence of 1% of a totally fluorescent impurity could not make more than 1% difference to the thermal blooming yield. This is because thermal blooming does not measure emission and insignificant contributions to the overall absorbance made by trace impurities make little difference to the overall signal. Another important consideration is the inner-filter effect. Fundamentally, since one is not detecting fluorescence at the detector with thermal blooming, the effects of the inner-filter effect might be expected to be minimized with the technique.[35] Other pitfalls inherent to conventional fluorescence measurements, such as Raman and Rayleigh

scattering, and the non-linear response of detectors and diffraction gratings can also be marginalized.

As a representative example of the reproducibility of results obtained by the thermal blooming method, the fluorescence yield was measured for five samples of the cyanine dye cy643 (discussed later) at different absorbance values within the range 0.05 to 0.1. Under controlled conditions, the standard deviation of the recorded fluorescence yields was ±0.01 suggesting results are highly reproducible. Taking into account that the noise on a typical oscilloscope trace was found to be ±2% of the mean value, one can conclude that the accuracy of the measurement is well within ±5% for a reasonably emissive sample (> 20% fluorescence yield).

7.2.4 Cyanine Dyes

Cyanine dyes are some of the most important pigments used in the industrial age. Their photophysical properties are very well understood, as was discussed in the introductory chapter. With typically narrow fluorescence and emission maxima, high molar absorptivity, moderate to high fluorescence quantum yields and readily tunable spectral profiles across the UV-visible range into the near-IR, they are ideal candidates for fluorescence standards across a wide spectral window. For this study, a series of five commercially available cyanine dyes was selected on the basis of covering the 600-800 nm absorption range by varying the conjugation length (Figure 7.4). The target dyes are soluble in methanol and free from aggregation at the concentrations appropriate for this work (micromolar range). The purity of the samples was confirmed by NMR spectroscopy (coutesy of Dr C. Wills and Prof W. McFarlane). The molecular formulae are provided in Figure 7.4. For the two Cy5 dyes, cy643 and cy681, it was possible to determine Φ_F values by ratiometric measurements using AlPcS and free-base *meso*-tetraphenylporphyrin as reference. The values are collected in Table 7.2 and serve to indicate that the compounds are relatively strong emitters. Although the dyes selected for study here are commercially available, their photophysical properties have not previously been investigated in detail.

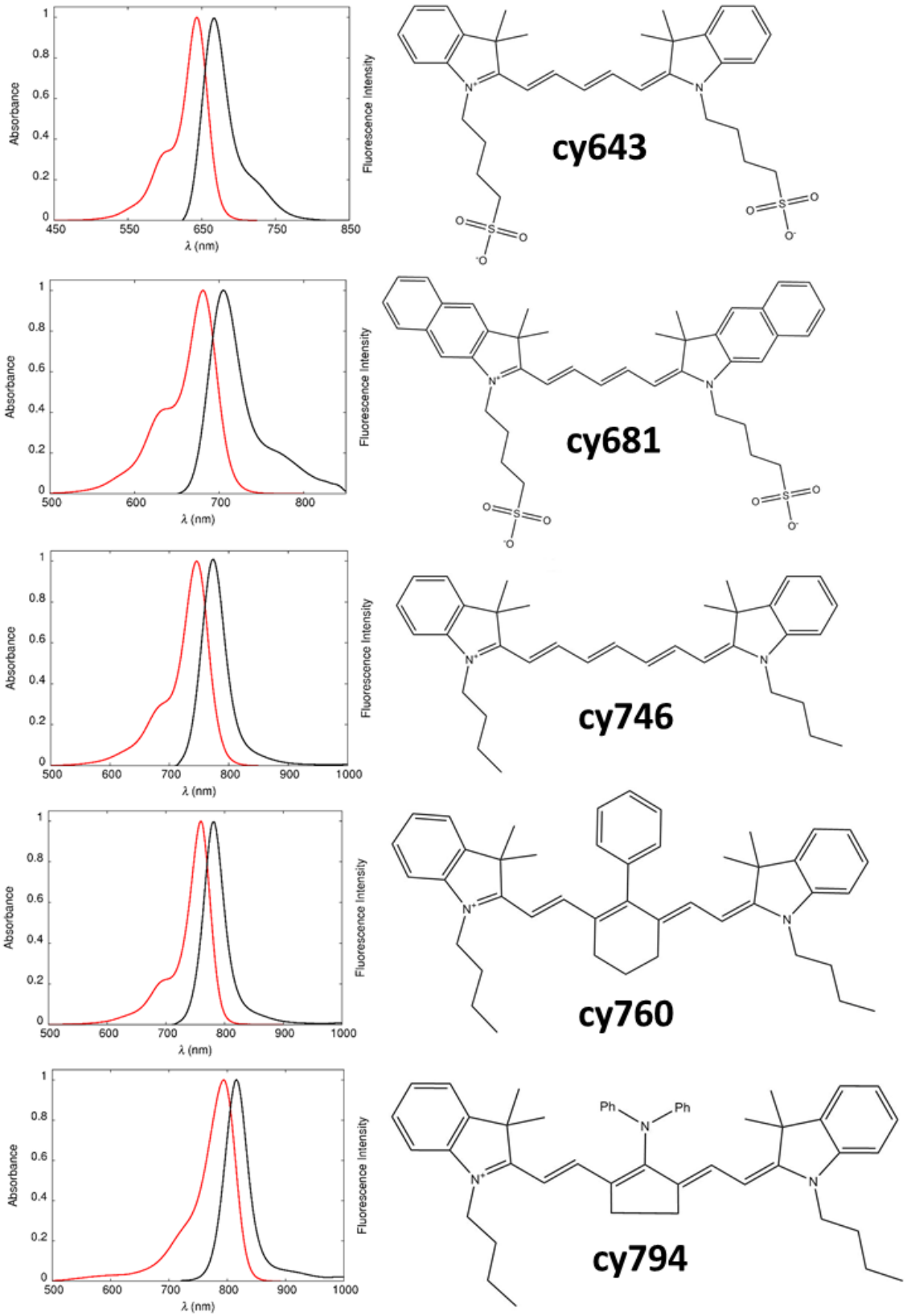

Figure 7.4. Chemical formulae for the cyanine dyes examined in this study alongside room temperature steady-state absorption and fluorescence spectra in CH_3OH.

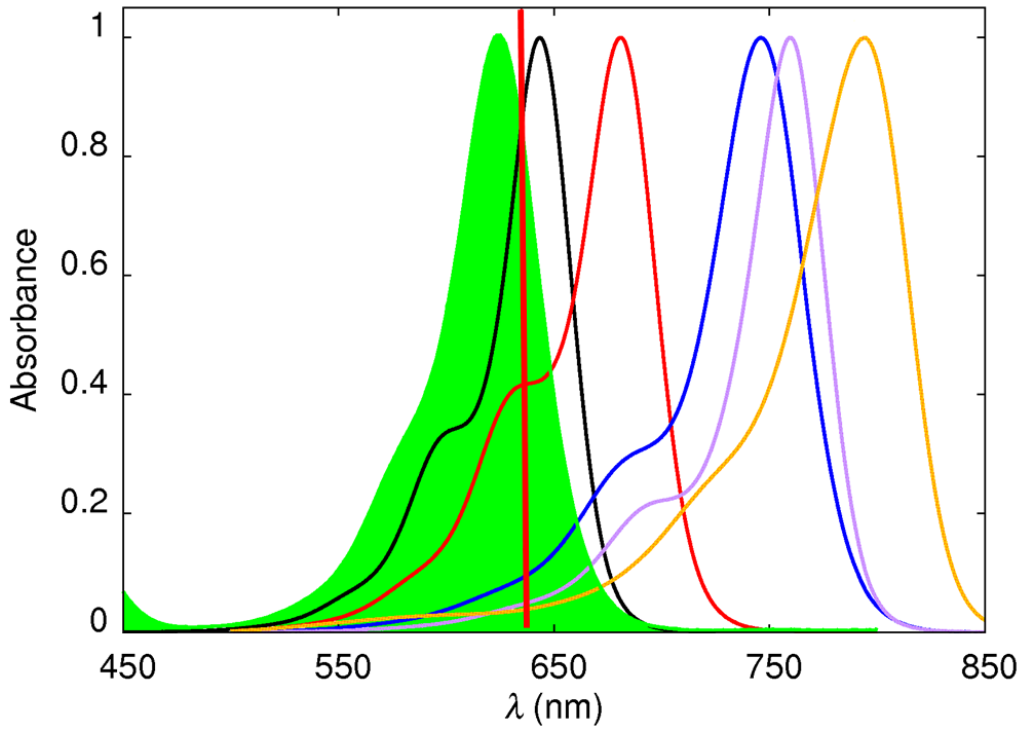

Figure 7.5. Normalized absorption spectra of the cyanine dye series in methanol. The colour of the trace corresponds to following compound: black: cy643, red: cy681, blue: cy746, purple: cy760, orange: cy794. The trace shaded green is that of the non-fluorescent standard, Brilliant Green. The vertical red line marks the excitation wavelength for thermal blooming measurements.

For the remaining cyanine dyes (cy746, cy760, cy794), it was not possible to generate meaningful Φ_F values by conventional steady-state emission spectroscopy due to the lack of appropriate control compounds. Instead, the thermal blooming technique was successfully applied to this problem. Comparison of Φ_F values measured by the two techniques for cy643 and cy681 in methanol showed agreement within 5% of each other (Table 7.2). Fluorescence yields for the cyanine dyes decrease steadily as the conjugation length increases, falling from 0.43 for cy643 to 0.056 for cy794 (Table 7.2). With a fluorescence yield of 0.056, cy794 is at the lower usable limit for thermal blooming measurements. Reproducibility of the results remained good throughout the series of dyes though. It is convenient that all the dyes investigated here can be excited with the single 635 nm source. Clearly there is an advantage to the absence of inner filter effects, otherwise accurate measurements of cy643 (for which the results agree very well with conventional fluorescence measurements) would not be possible.

For the dyes emitting in the near-IR, excitation is at a wavelength with low molar absorptivity (Figure 7.5), but results nonetheless remain highly reproducible. Table 7.3 summarizes the wavelength ranges covered by each of the cyanine dyes. This represents only a small selection of the dyes available from the manufacturer. Unsurprisingly, cyanine dyes being so well understood, many more derivatives with other excitation wavelengths and solubility characteristics are available. Overall, the current selection of dyes gives good coverage of the red to near-IR region with solubility in organic solvents for cy746, cy760 and cy794 and additionally water-solubilizing groups on cy643 and cy681 lend themselves towards being studied in aqueous environments, useful for biomedical applications.

Table 7.2. Compilation of the photophysical properties derived for the series of cyanine dyes in methanol solution at 20 ^{0}C.

Compound	**λ_{ABS} / nm**	**λ_{FLU} / nm**	**ε_{MAX} / M^{-1} cm^{-1}**	**τ_S / ns**	**Φ_F [(a)]**	**Φ_F [(b)]**	**τ_{SB} / ns [(c)]**	**k_{NR} / 10^7 s^{-1} [(d)]**
cy643	643	668	218,000	0.95	0.41	0.43	1.44	60.0 ± 9.0
cy681	681	706	166,000	0.87	0.24	0.24	1.10	87.6 ± 13.1
cy746	746	774	258,000	1.20	N/A	0.20	0.68	66.8 ± 10.0
cy760	760	782	312,000	1.00	N/A	0.18	0.72	81.5 ± 12.2
cy794	794	817	246,000	0.98	N/A	0.056	0.24	96.0 ± 14.4

(a) Fluorescence quantum yield measured by conventional steady-state fluorescence spectroscopy. (b) Measured by thermal blooming. (c) Radiative lifetime measured as the inverse of the radiative rate constant determined from the Strickler-Berg expression. (d) Rate constant for nonradiative deactivation of the emitting state.

Table 7.3. Summary of the most suitable excitation and emission spectral ranges for the cyanine dyes in methanol solution.[(a)]

Dye	Excitation Range / nm	Emission Range / nm
cy643	600-645	650-775
cy681	640-680	680-820
cy746	685-750	750-900
cy760	700-760	750-900
cy794	730-795	775-950

(a) These wavelength ranges should not be considered as being absolute but are representative a usable spectral window.

Cyanine dyes have been proposed as fluorescence standards before.[10,36,37] Indeed, they have featured prominently in fluorescence microscopy due to their being known for bright fluorescence over a wide range of energies. One of the better known IR-emitting cyanine dyes is Indocyanine Green, which is quite well characterized.[38] The fluorescence yield of Indocyanine Green is reported as 0.13 with an emission maximum at 835 nm (in dimethyl sulfoxide). Although the yield is low, many organic fluorophores have a fluorescence yield possessing a fraction of this because many dyes are modified to emit in the infrared by attaching several peripheral substituents, often with their own associated nonradiative relaxation pathways. This may make cy794 a desirable standard for those IR-emitters with very low fluorescence yields.

It will be noted that the reported Φ_F values decrease progressively as the emission maximum moves to lower energy (Figure 7.6). Indeed, Φ_F for the most red-shifted dye, cy794, is at the lower limit for accurate determination by thermal blooming. This finding suggests that cyanine dyes might not be appropriate standards for compounds that emit strongly at wavelengths longer than 800 nm. A fair conclusion based on the results obtained here is that cyanine dyes are very well suited as fluorescent reference compounds for excitation wavelengths stretching from 500 to 800 nm. A particular feature of these dyes concerns the sharp absorption profiles with pronounced shoulders on the high-energy side of the optical transition. This shoulder provides an ideal

excitation point, so that absorbance can be measured rather accurately. In methanol, no problems were encountered with the photostability of the cyanine dyes during prolonged and repeated measurements on the thermal blooming setup. For Brilliant Green, one must be aware that there is a gradual irreversible bleaching over longer periods, but this does not occur on the timescale of individual experiments.

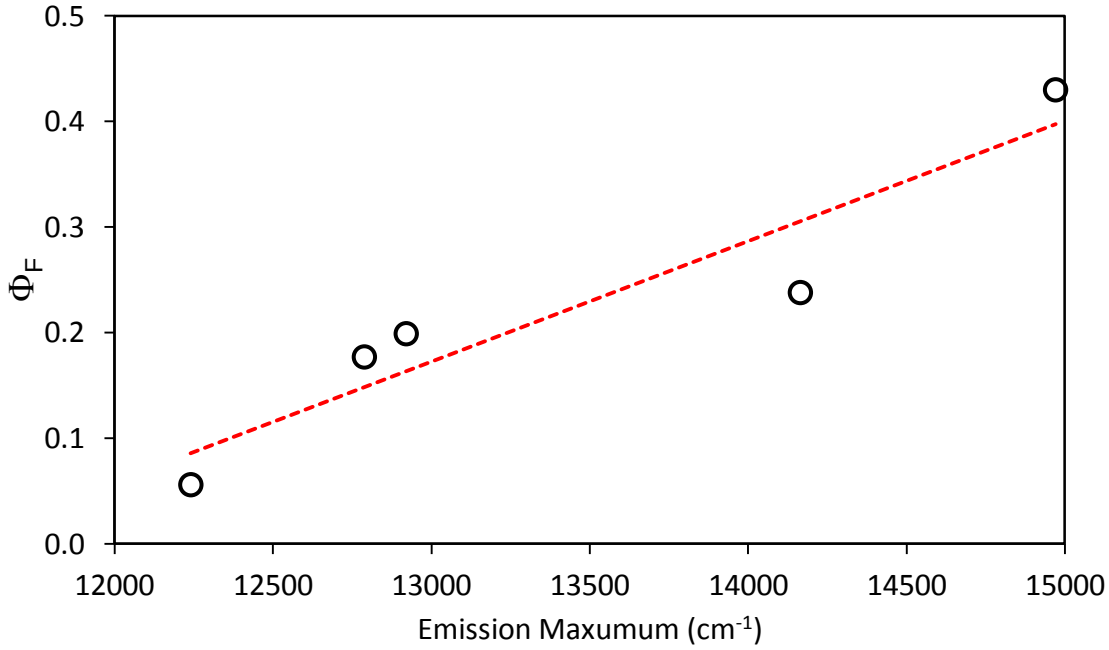

Figure 7.6. Correlation between the mean fluorescence spectral maximum and the fluorescence quantum yield measured for the cyanine dye by thermal blooming.

7.2.5 The Interplay of Radiative Decay and Isomerization

For the cyanine dyes reported here, the Stokes' shift falls within the range 350 to 580 cm^{-1}, indicating only minor structural changes between absorbing and emitting species. The molar absorption coefficients at the peak maximum (ε_{MAX}) are high and do not follow any clearly definable pattern. Notably, the radiative rate constants calculated from the Strickler-Berg expression[39] (k_{SB}) evolve smoothly across the series (Table 7.2), giving a clear correlation with the mean fluorescence maximum (ν_F) measured in terms of wavenumber. The singlet-exited state lifetimes however remain at approximately 1 ns throughout the cyanine dye series, which means the nonradiative rate constant changes very little under these circumstances. This is a somewhat surprising finding because the trend in nonradiative rate constant does not follow the observed trend in Φ_F (Table 7.2). This situation goes against a simplistic interpretation in terms of the energy-gap law, which would predict an increase in k_{NR} as the emission energy decreases.

To explain the crude correlation of emission energy versus fluorescence quantum yield seen in Figure 7.6, one must invoke contributions from an additional nonradiative pathway. Cyanine dyes are well-known to undergo photoinduced isomerization with cis-trans transformation along the polymethine chain.[40,41] This apparent trend is a result of the special circumstance where the rate constant (k_{NR}) for nonradiative deactivation of the excited state is essentially balanced by opposing changes in the radiative rate constant (k_{RAD}) across a series of emitters. The situation is quite rare but arises here because of competing processes on the relevant energy gap.[24,41] One would expect the rate of internal conversion to the ground state[24] to increase with decreasing ν_F but the rate of isomerization from the excited-singlet state will decrease with decreasing ν_F due to a loss of potential energy.[41] These two rate constants combine to give k_{NR} and the indications are that, across this series of cyanine dyes, the latter is purely by coincidence.

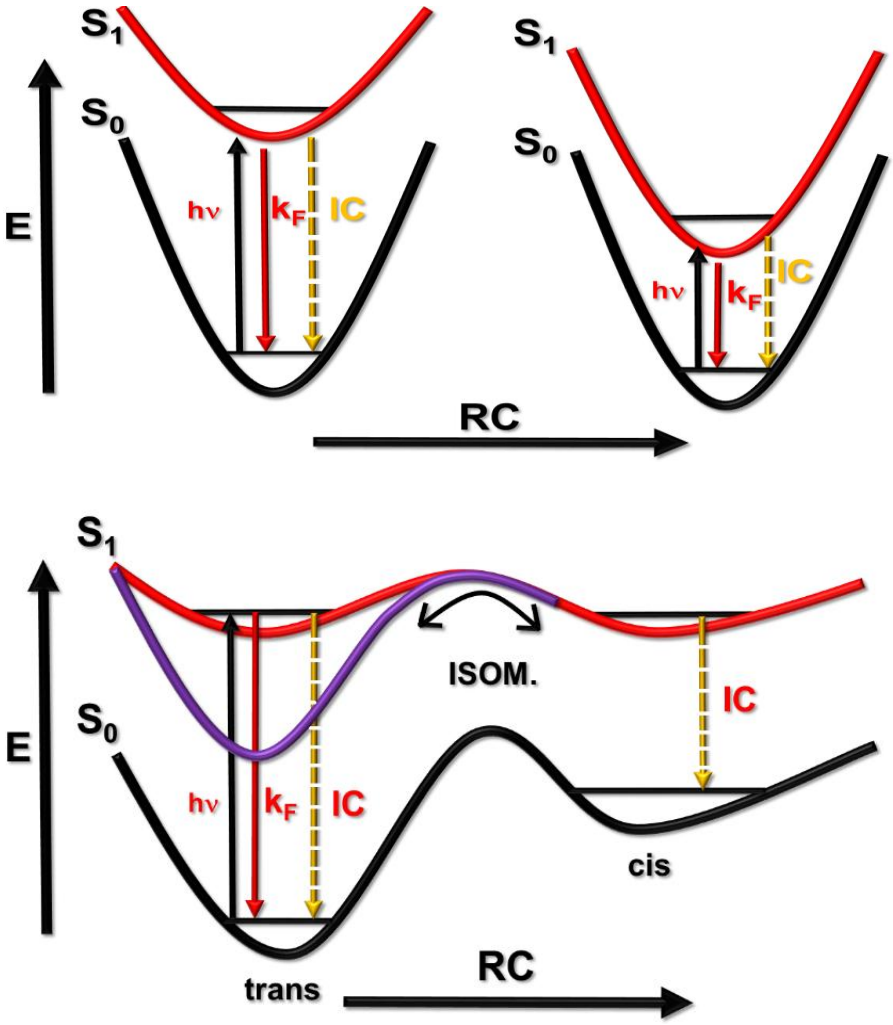

Figure 7.7. Illustration of how a change in the excitation energy affects the photophysical properties. The upper panel shows that the excitation energy is lowered by an increase in conjugation length of the cyanine dye. Reducing the energy gap between emitting state (S_1) and ground state (S_0) increases the rate of internal conversion (IC) but decreases the rate of radiative decay (k_F). The lower panel indicates the process of photoisomerization and shows that lowering the excitation energy (purple line) raises the energy barrier for isomerization.

To verify that isomerization was truly playing a part in the nonradiative decay processes, cy643 was examined with laser flash photolysis to determine the presence of the meta-stable isomer. Upon excitation with a nanosecond 610 nm pulse, in air-equilibrated de-ionized water, cy634 shows a transient absorption species with a lifetime of approximately 390 μs. The decay conforms to first-order kinetics. Spectral fitting allows one to determine the molar absorption coefficient of the isomer species as approximately 255 000 M^{-1} cm^{-1} The kinetics of the ground state bleach matched the positive signal centred at 690 nm. The sinusoidal character of the trace in Figure 7.8

corresponds to previous reports in the literature of cis-trans isomer, where the cis-isomer (it is generally accepted that the ground state is all-trans) has slightly red-shifted absorption relative to the ground state. Consequently, the isomer can still absorb a photon of the excitation light and rapidly revert to the all-trans structure.[42] Alternatively the isomer may absorb enough energy to cross over a second potential energy barrier and form a double isomer. Such considerations are somewhat beyond the scope of the study here, but are considered in Chapter 8. Suffice to say here with cy643 we see a long-lived transient species with an absorption spectrum characteristic of the ground-state, but slightly red shifted.

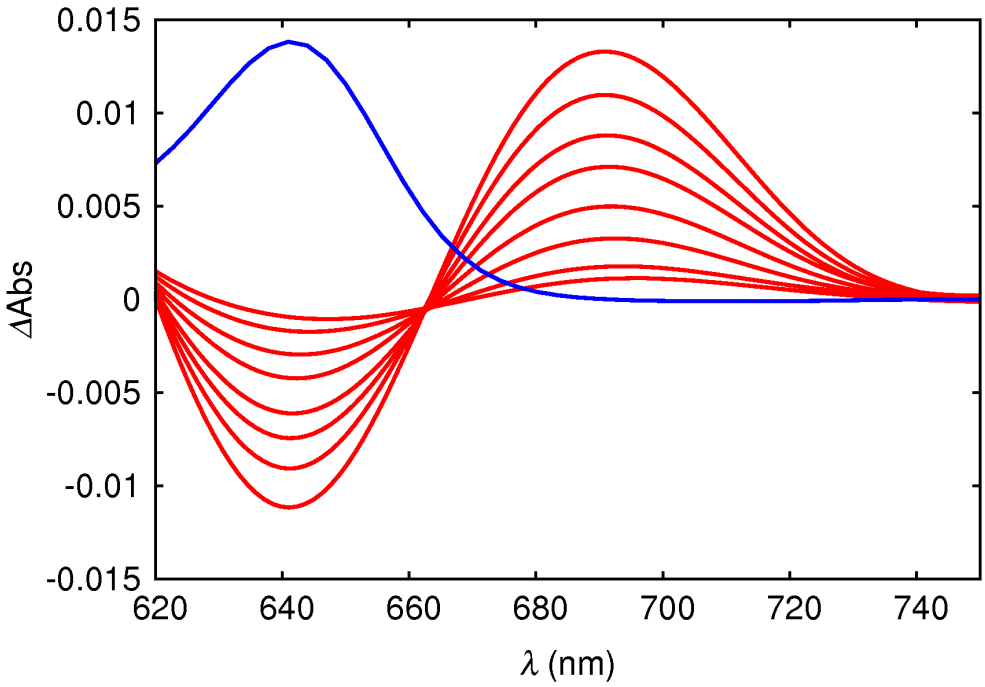

Figure 7.8. Transient absorption spectrum of cy643 in de-ionized water at a series of times between 10 us and 930 μs (red traces). The blue trace corresponds to the lowest energy transition of the ground state absorption spectrum.

Formation of the transient signal was insensitive to the presence of oxygen (unlike a triplet state species), but sensitive to solvent viscosity. There is little doubt therefore that the signal is due to the configurational isomer (Figure 7.8). We delay discussion of the transient spectroscopy associated with cis-trans isomerisation until Chapter 8. Here, we simply demonstrate that light-induced isomerisation competes with fluorescence and internal conversion for simple cyanine dyes.

As one moves to the lower-energy cyanine dyes, the S_0 to S_1 energy gap decreases, but the corresponding energy of the isomer remains relatively unchanged (Figure 7.7). This results in an increased energy barrier to formation of the isomer and consequently the rate constant for isomerization (k_{ISOM}) is decreased. As k_{ISOM} decreases, the observed fluorescence lifetime τ_{tot} must increase as shown by the relatinships in Equation 7.3 and 7.4. Here τ_n is the intrinsic fluorescence lifetime in the absence of nonradiative processes. The nonradiative rate is of course the sum of many possible processes such as intersystem crossing, electron transfer and internal conversion, but the emphasis is on k_{isom} in this system.

$$\tau_n = \frac{1}{k_{RAD}} \qquad (7.3)$$

$$\tau_{tot} = \frac{1}{k_{RAD} * k_{NR}} = \frac{1}{k_{ISC} * k_{ISOM} * k_{ET} * k_{IC} * k_f \ldots} \qquad (7.4)$$

7.3 Conclusions

Using thermal blooming spectroscopy, it has been possible to evaluate a set of commercially available fluorophores as potential ratiometric standards for the 650-850 nm region. The library of useful far-red emitters has been extended by providing absolute fluorescence quantum yields for soluble dyes using a readily reproducible technique and commercially available compounds. Cyanine dyes are particularly flexible in this application being widely available, easy to synthesize and possessing well-defined photophysical properties. They are also particularly relevant compounds in the context of fluorescence microscopy and as advanced probes, where their use is widespread.[43] Radiative rate constants tend to be high and poor spin-orbit coupling properties minimize intersystem crossing to the triplet manifold[41], although the role of isomerization as discussed adds a perhaps unwanted complication to the photophysical description. Usually, cyanine dyes dissolve easily in alcohol solvents but much less so in water, here we include two water-solubilized cyanine dyes to overcome this limitation. The cyanine dyes studied here are not amenable for facile attachment to biological materials but strategies exist for attaching anchoring groups to the backbone. It has in

fact been demonstrated that similar cyanine dyes, such as Alexa Fluor 647 NHS-ester, can be employed rather successfully is fluorescence microscopy.[44]

It is important to note the drop-off of fluorescence yield below 15 % as one moves the emission maximum past 800 nm. This is certainly a limitation of cyanine dyes and many other organic fluorophores. Diagnostic applications rely on good signal to noise ratios so there will be a call for strong NIR emitters. One may draw some inspiration from the past though as the ancient paint pigment Egyptian Blue is a strong NIR emitter. This brilliant blue mineral pigment has an emission maximum at 910 nm and a fluorescence quantum yield of 10.5 %.[45]

The strength of thermal blooming spectroscopy for the determination of fluorescence quantum yields revolves around the simplicity of the experiment, the high reproducibility of the results, the affordability and the facile circumvention of many of the problems encountered with fluorometer measurements. High quality laser diodes are readily available and open up the possibility of using other excitation sources to span a greater range of the UV-visible spectrum. All other components are readily available to researchers. To become popular, however, the technique needs diversifying to include solid samples, such as thin films, and operating devices, such as OLEDs. We are especially interested to see if the thermal blooming technique can be used to characterize emission from thin films. This is an important problem for industry and, in particular, for organic opto-electronic devices.

7.4 References

1. Lukinavičius, G.; Umezawa, K.; Olivier, N.; Honigmann, A.; Yang, G.; Plass, T.; Mueller, V.; Reymond, L.; Corrêa Jr, I.R.; Luo, Z.G.; Schultz, C. *Nat. Chem.* **2013**, *5*, 132-139.

2. Descalzo, A.B.; Xu, H.J.; Shen, Z.; Rurack, K. *Ann. N. Y. Acad. Sci.* **2008**, 1130, 164-171.

3. Yuan, L.; Lin, W.; Zheng, K.; He, L.; Huang, W. *Chem. Soc. Rev.* **2013**, 42, 622-661.

4. Hilderbrand, S.A.; Weissleder, R. *Curr. Opin. Chem. Biol.* **2010**, 14, 71-79.

5. Kolmakov, K.; Belov, V.N.; Bierwagen, J.; Ringemann, C.; Müller, V.; Eggeling, C.; Hell, S.W. *Chem. Eur. J.* **2010**, 16, 158-166.

6. Resch-Genger, U.; Grabolle, M.; Cavaliere-Jaricot, S.; Nitschke, R.; Nann, T. *Nat. Methods* **2008**, 5, 763-775.

7. Dou, L.; Liu, Y.; Hong, Z.; Li, G.; Yang, Y. *Chem. Rev.* **2015**, 115, 12633-12665.

8. Currie, M.J.; Mapel, J.K.; Heidel, T.D.; Goffri, S.; Baldo, M.A. *Science* **2008**, 321, 226-228.

9. Velusamy, M.; Justin Thomas, K.R.; Lin, J.T.; Hsu, Y.C.; Ho, K.C. *Org. Lett.* **2005**, 7, 1899-1902.

10. Rurack, K.; Spieles, M. *Anal. Chem.* **2011**, 83, 1232-1242.

11. Long, M.E.; Swofford, R.L.; Albrecht, A.C. *Science* **1976**, 191, 183-185.

12. Kliger, D.S. *Acc. Chem. Res.* **1980**, 13, 129-134.

13. Brannon, J.H.; Magde, D. *J. Phys. Chem.* **1978**, 82, 705-709.

14. Karlsson, J.K.; Harriman, A. *J. Phys. Chem. A.* **2016**, 120, 2537-2546.

15. Wu, D.; O'Shea, D.F. *Org. Lett.* **2013**, 15, 3392-3395.

16. Magde, D.; Brannon, J.H.; Cremers, T.L.; Olmsted, J. *J. Phys. Chem.* **1979**, 83, 696-699.

17. Nagasawa, Y.; Ando, Y.; Kataoka, D.; Matsuda, H.; Miyasaka, H.; Okada, T. *J. Phys. Chem. A.* **2002**, 106, 2024-2035.

18. Ware, W.R. *J. Phys Chem.* **1962**, 66, 455-458.

19. Bindhu, C. V.; Harilal, S. S.; Nampoori, V. P. N.; Vallabhan, C. P. G. *Opt. Eng*. **1998**, *37*, 2791-2794.

20. Ambroz, M.; Beeby, A.; MacRobert, A. J.; Svensen, R. K.; Phillips, D. *J. Photochem. Photobiol. B*. **1991**, 9, 87-95.

21. Owens, J. W.; Smith, R.; Robinson, R.; Robins, M. *Inorg. Chim. Acta* **1998**, 279, 226-231.

22. Owens, J. W.; Robins, M. *J. Porphyrins Phthalocyanines,* **2001**, 5, 460-464.

23. Dhami, S.; De Mello, A. J.; Rumbles, G.; Bishop, S. M.; Phillips, D.; Beeby, A. *Photochem. Photobiol*. 1995, 61, 341-346.

24. Englman, R.; Jortner, J. *Mol. Phys.* **1970**, 18, 145-172.

25. Magde, D.; Brannon, J.H.; Cremers, T.L.; Olmsted, J. *J. Phys. Chem.* **1979**, 83, 696-699.

26. Sens, R.; Drexhage, K.H. J. Lumin. **1981**, 24, 709-712.

27. V. A. Petukhov; M. B. Popov; A. I. Krymova. *Quantum Electron.* **1986**, 13, 777-786.

28. T. Wang; B. Q. Zhang; J. L. Pan; P. Gu; Q. Xu; Q. Sun, *Chin. Sci. Bull*. **1989**, *34*, 1756-1757.

29. Seybold, P.G.; Gouterman, M. *J. Mol. Spectrosc*. **1969**, 31, 1-13.

30. Bonnett, R.; McGarvey, D.J.; Harriman, A.; Land, E.J.; Truscott, T.G.; Winfield, U. *Photochem. Photobiol*, **1988**, 48, 271-276.

31. A. M. Brouwer, *Pure Appl. Chem*. **2011**, 83, 2213-2228.

32. Resch-Genger, U.; Rurack, K. *Pure Appl. Chem*. **2013**, 85, 2005-2013.

33. Würth, C.; Grabolle, M.; Pauli, J., Spieles, M.; Resch-Genger, U. *Nature Protocols* **2013**, 8, 1535-1550.

34. Fery-Forgues, S.; Lavabre, D. *J. Chem. Educ*. **1999**, 76, 1260-1264.

35. Fischer, M.; Georges, J. *Chem. Phys. Lett*. **1996**, 260, 115-118.

36. Olmsted, J. *J. Phys. Chem*. **1979**, *83*, 2581-2584.

37. Resch-Genger, U.; Grabolle, M.; Cavaliere-Jaricot, S.; Nitschke, R.; Nann, T. *Nature Methods,* **2008**, *5*, 763-775.

38. Benson, R. C.; Kues, H. A. *J. Chem. Eng. Data* **1977**, *22*, 379-383.

39. Strickler, S. J.; Berg, R. A. *J. Chem. Phys*. **1962**, *37*, 814−822.

40. Sundström, V.; Gillbro, T. *J. Phys. Chem.* **1982**, 86, 1788-1794.

41. Harriman, A. *J. Photochem. Photobiol. A Chem*. **1992**, *65*, 79-93.

42. Widengren, J.; Schwille, P. *J. Phys Chem. A.* **2000**, 104, 6416-6428.

43. Panchuk-Voloshina, N.; Haugland, R.P.; Bishop-Stewart, J.; Bhalgat, M.K.; Millard, P.J.; Mao, F.; Leung, W.Y.; Haugland, R.P. *J. Histochem. Cytochem.* **1999**, 47, 1179-1188.

44. Huang, B.; Bates, M.; Zhuang, X. *Annu. Rev. Biochem*. **2009**, 78, 993-1016.

45. Accorsi, G.; Verri, G.; Bolognesi, M.; Armaroli, N.; Clementi, C.; Miliani, C.; Romani, A. *Chem. Comm.* **2009**, 23, 3392-3394.

Chapter 8: Photoisomerization-Induced Fluorescence Blinking in a Far-Red Emitting Cyanine Dye under dSTORM Imaging Conditions

8.1 Introduction

Super-resolution fluorescence microscopy has developed rapidly over the past decade to the point where commercial instrumentation exists for nanometre resolution imaging of live biological samples. The field is dominated by techniques which rely on time-resolved activation of small subsets of spatially resolved fluorophores in order to achieve high image resolution. The development of these techniques complements advances in single molecule fluorescence detection during the 1980s and 1990s.[1-3] As has been mentioned in the introductory chapter, super-resolution fluorescence techniques such as PALM, STORM and STED[4-6] help overcome the optical diffraction barrier (setting a limit of ca. 200 nm lateral resolution for conventional optical microscopy) by some form of reversible on/off fluorescence modulation. Modern fluorescence microscopes use lasers to excite biological samples labeled with an appropriate fluorescent probe. With suitable software, this procedure allows for precise localization of single fluorophores, which would otherwise overlap in classical steady-state fluorescence microscopy (Figure 8.1), by building the image layer-by-layer from repeated snapshots.

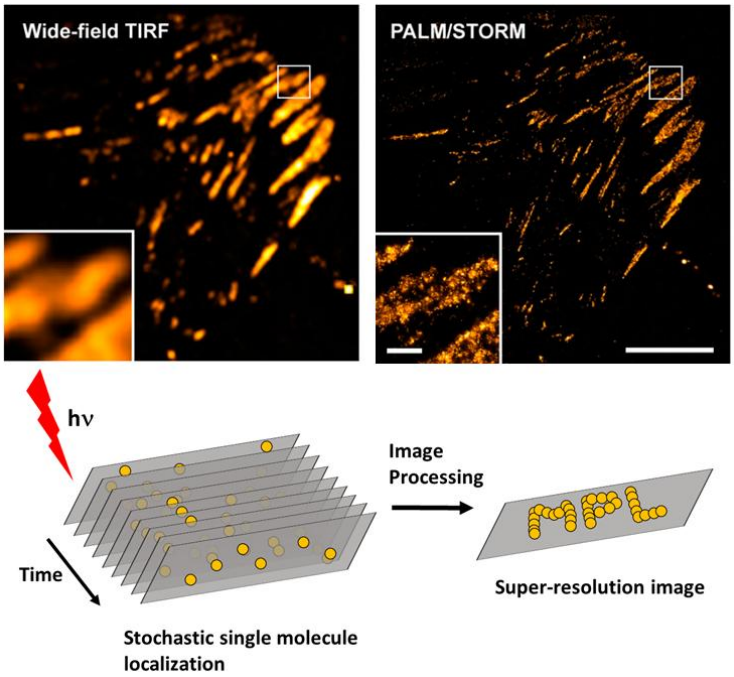

Figure 8.1. Simplified illustration of the single molecule localization method for obtaining super-resolution fluorescence images (bottom panel). The difference between a conventional total internal reflection fluorescence microscope image (TIRF) and super-resolution image is shown above.[7]

Despite rapid advances in fluorescence microscopy, less attention has been given to studying the underlying photophysical properties of prototypic fluorophore labels. Of particular concern is the need to understand how fluorophores in the stochastic super-resolution imaging techniques alternate between emissive and dark states. Here, we focus on one technique, Stochastic Optical Reconstruction Microscopy (STORM) in order to better appreciate the demands on the emitter during the microscope experiment. More specifically, we selected a class of dye ubiquitous to the technique, namely the red-emitting cyanine dyes (Cy5). This complements the previous knowledge accumulated on cyanine dyes in Chapter 7, which has already established them as highly fluorescent small emitters, this being an important prerequisite for fluorescence microscopy. A broader discussion of cyanine dyes is given in the introductory chapter.

Previous studies into the photo-switching mechanism of cyanine dyes and other organic fluorophores have focused on electron transfer and transitions to the dark triplet state.[8,9] This is because imaging is commonly done in a redox buffer solution. One study attributed the fluorescence blinking behaviour of Cy5 to formation of a thiol-adduct, the result of an encounter complex forming between a mild thiol reducing agent in a photo-switching buffer (which contains an oxygen scavenging enzyme) and the excited cyanine dye (Figure 8.2). Oxygen scavenging agents are used in these systems to avoid the build-up of reactive singlet oxygen, leading to cell damage and loss of fluorophore. It should be noted that this experiment was performed at a pH well above physiological conditions.[10] As the Cy5 thiol adduct accumulates in the system it can be excited with a UV-laser pulse to regenerate the starting material.

Other suggestions for the mechanism revolve around a similar idea, although applying a UV-pulse to switch between dark and bright states does not appear to be standard practice in imaging where there is a single dye. Instead, the UV-pulse is important in two-colour imaging where donor-acceptor systems, typically Cy3-Cy5 or Cy3-Cy7, are used[11] and excitation of the Cy3 dye reactivates Cy5 by electronic energy transfer. Nonetheless, mild reducing agents tend to be used in all imaging buffer solutions, and the understanding is that redox chemistry is performed via the triplet state.[12] Sulfonated

indocyanine dyes produce particularly good quality images and are widely used, members of the Alexa Fluor series being common examples.[13,14]

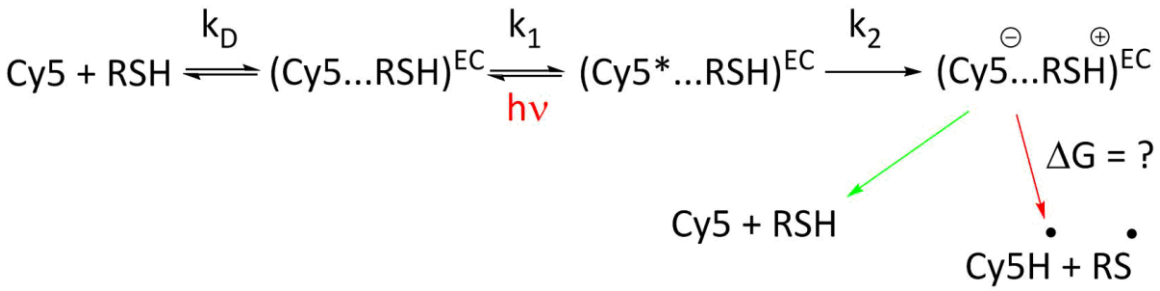

Figure 8.2. Generalized reaction scheme for producing a non-fluorescent radical anion of Cy5 by photochemical reduction with a mild thiol reducing agent. Here K_D is rate the constant for diffusion and EC an encounter complex.

Figure 8.2 shows a commonly proposed scheme for generating a long-lived, non-fluorescent form of a fluorophore, namely a radical anion. This scheme has been applied to Cy5[10] and could be used with many other organic chromophores. The critical considerations here are those of kinetics and thermodynamics. Formation of the encounter complex occurs by diffusion and will depend on relevant binding constants, which can be derived from the Stern-Volmer relationship. Taking the diffusional rate constant as ~6 x 10^9 M^{-1} s^{-1} in water[15] at room temperature, and realizing that most organic fluorophores have a fluorescence decay rate in the region of 10^9 s^{-1}, it becomes apparent that very high concentrations of quencher are required. Furthermore, the likelihood of charge-separation from the encounter complex depends strongly on thermodynamic factors (including the solution pH) and, because of spin considerations, rarely occurs for singlet-excited states.

One answer to the problem of the short-lived excited singlet state is, of course, to invoke the relatively long-lived triplet, which would allow time (typical triplet decay rates being 10^{-6} – 10^{-3} s^{-1}) to generated charge-separated species. However, many of the dyes commonly used in fluorescence microscopy are highly fluorescent and are not known for high yields of intersystem crossing. This is the case with cyanine dyes for example. It is possible that, at high excitation intensity, there are enough triplets being formed, albeit inefficiently, to generate super-resolution fluorescence microscope images. This has not been confirmed by experiment.

Alternative mechanisms should also be considered. Further studies have expanded the range of potential chromophores by careful consideration of the photophysical properties and redox conditions, using oxazine dyes.[16,9] This includes Rhodamine dyes, but these are excited with a ~500 nm laser, which is less desirable since biological samples are more permeable to light past 650 nm. Although STORM and PALM are stochastic methods, control of the redox chemistry could allow for a non-random modulation of fluorescence, where radical ion species are responsible for extinguishing fluorescence. This will no doubt be desirable in other sensing applications, although it is not necessarily a prerequisite as the microscopes work well with a variety of dyes.

The question of how fluorophores blink under the current paradigm still remains unclear. It is indeed possible that there are multiple pathways to generating the long-lived non-fluorescent states observed during super-resolution microscope experiments. For example, cyanine dyes are well-known to undergo photo-induced cis-trans isomerization[17], but this has not been investigated in great detail in the context of microscopy. Since cyanine dyes are otherwise well known for their fluorescence blinking behaviour, further investigation into the photo-switching mechanism seems justified. Drawing again on the results from Chapter 7, it is apparent that photo-induced isomerization in Cy5 occurs on a timescale similar to microscope imaging.

The present work has led to a detailed photophysics study of a popular commercial indocyanine (Cy5) dSTORM dye, Alexa Fluor® 647 (AF647). This is a highly fluorescent, red-emitting dye with good intrinsic stability against permanent photo-bleaching in aqueous media. Red-emitting dyes are preferable for biological samples due to cell structures being more permeable to light in this region (reducing scattering), avoid auto-fluorescence of cell structures[18], and are less susceptible to damage due to the lower excitation energies involved.[8] Careful examination of photo-isomerization, using laser flash photolysis, suggests it plays more of a role in mediating fluorescence blinking than previously thought. We show that isomerization can occur in competition with transitions to the triplet state and photo-induced electron transfer with imaging buffers. This has implications for future design of super-resolution fluorescence microscopy experiments.

It should be mentioned that all experiments involving the super-resolution microscope were performed in collaboration with Dr. Alex Laude of the Newcastle University Medical School. Dr. Laude also provided numerous samples of the (very expensive!) AF647.

8.2 Results and Discussion

8.2.1 Steady-State Spectroscopic Measurements

Key spectroscopic properties for AF647 are summarized in Table 8.1. In aqueous buffer solution, AF647 has a ground-state absorption maximum at 649 nm while emission is centred at 670 nm (Figure 8.3). The fluorescence quantum yield in water was determined to be 34% after several repeat measurements against *meso*-tetraphenylporphyrin on multiple instruments.[19] The fluorescence decay was found to conform with mono-exponential kinetics. Optical measurements were performed primarily in aqueous buffer (phosphate-buffered saline, PBS, pH 7.4) to better mimic the conditions of a STORM microscope experiment. However, there is no discernible difference between the fluorescence properties recorded in de-ionized water and in PBS. It was noted that in alcohol solvents the fluorescence quantum yield of AF647 dropped significantly, falling to 14% ethanol, and the singlet-excited state lifetime increased to 1.8 ns.

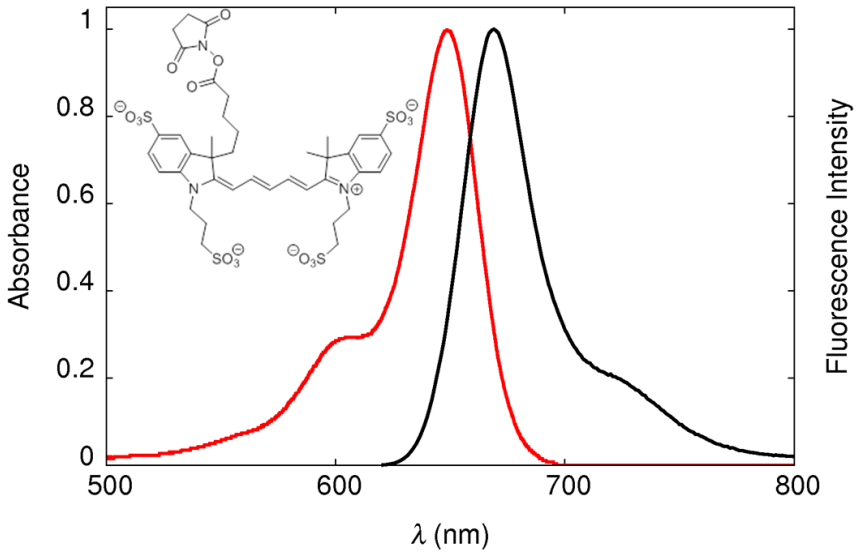

Figure 8.3. Normalized steady-state absorption and emission spectra recorded for AF647 in PBS room-temperature. Molecular formula shown as an inset.

λ_{abs}^{max} / nm	649 ± 1
λ_{fluor}^{max} / nm	670 ± 1
ϕ_F	0.34 ± 0.02
τ_{S1} / ns	1.2 ± 0.2
k_{RAD} / 10^8 s^{-1}	2.8 ± 0.3
k_{NR} / 10^8 s^{-1}	5.5 ± 0.6
ε / M^{-1} cm^{-1} (a)	270 000
f(b)	1.41 ± 0.14
S(c)	0.18 ± 0.02
Ess / cm^{-1} (d)	790 ± 40

Table 8.1. Compilation of spectroscopic properties for AF647 in PBS. (a) Molar absorption coefficient is a manufacturer specified value. (b) Calculated from lowest energy absorption transition (c) Huang-Rhys factor calculated from fitting the low-temperature emission spectrum to a series of four Gaussian components (d) Stokes' shift calculated after deconstruction of the absorption and emission spectra into Gaussian components.

Since a key component of the imaging buffer in dSTORM experiments is the redox agent, the effects of a mild thiol reducing agent commonly used in such buffers[20], 2-mercaptoethylamine-HCl (MEA-HCl, Sigma), were examined. Fluorescence quenching of AF647 with MEA-HCl was measured using the Stern-Volmer relationship.[21] This was achieved in PBS, maintaining the pH at 7.4 by adding small amounts of NaOH. The pH was monitored with a digital pH probe (Omega PHH222). It was apparent that, at physiological pH, MEA-HCl is an inefficient quencher of AF647 fluorescence.

Fluorescence quenching with the thiol was found to fit well to a 1:1 complexation model[22] (Equation 8.1) with a binding constant of 1 M^{-1} (Figure 8.4). No change in the singlet-excited state lifetime was observed upon adding the thiol. This finding is entirely consistent with static quenching, Adding base to the solution leads to a decrease in fluorescence as the thiol becomes more susceptible to deprotonation. This is also in agreement with prior quenching studies made at higher pH.[10] It is unlikely, however,

that microscope imaging studies would take place at pH 9 or above. The reported pH range for a suggested photo-switching buffer containing MEA-HCl is 6-8.5.[23]

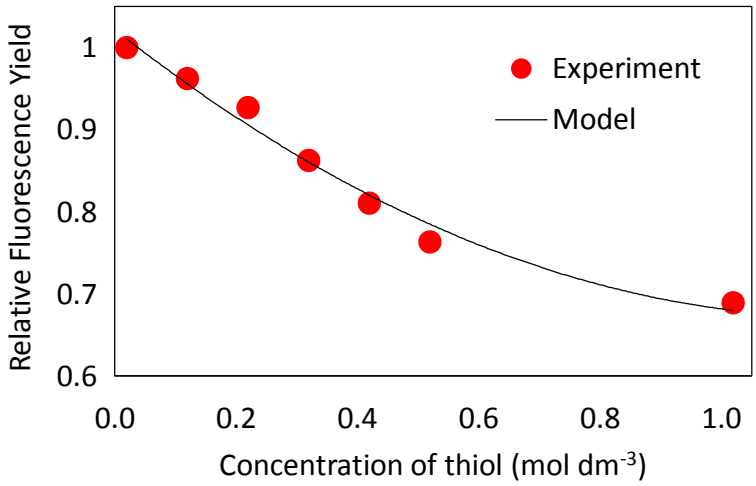

Figure 8.4. Steady-state fluorescence quenching of AF647 with MEA-HCl in PBS maintained at pH 7.4. Data corresponds to a 1:1 static fluorescence complexation model.

In Equation 8.1, I_0 is the integrated fluorescence area for the fluorophore before addition of quencher and I is the corresponding value at a certain concentration of added thiol. The term K refers to the binding constant, $[Q]$ is the molar concentration of quencher, and τ_0 corresponds to the fluorescence lifetime in the absence of quencher. For the purposes of postulating the likely source of fluorescence quenching under dSTORM microscope conditions in a biological buffer, electron transfer between the thiol and the cyanine dye is unlikely to be the dominant process. Furthermore, the relatively short fluorescence lifetime of 1.2 ns and the weak binding constant means that little of the excited state will form the encounter complex unless the quencher concentration is very high (Figure 8.2). Although electrochemical data for AF647 could not be obtained due to a scarcity of expensive sample, one can make an estimate of the thermodynamic driving force for photo-induced electron transfer using literature values. Thus, MEA-HCl has an oxidation potential of +0.9 V vs SCE[23] and the reduction potential for a typical Cy5 dye is -0.84 V vs SCE in water.[24] Given that the energy of the S_1 state is 1.84 eV, there is only a modest thermodynamic driving force for this process ($\Delta G \sim$ -0.1 V in the absence of electrostatic effects). The longer-lived triplet state will possess a lower electronic energy and the driving force will be non-existent.

$$\frac{I_0}{I} = (1 + K[Q])(1 + \tau_0[Q]) \qquad (8.1)$$

The photochemical stability of AF647 was tested under conditions similar to those used for aza-BODIPY in Chapter 3, which provides a useful point of comparison. Figure 8.5 shows the course of steady-state illumination of AF647 in de-aerated water with the same 400 W floodlight (>500 nm by the use of a cut-off filter) as used to irradiate aza-BOD. It is apparent that photo-bleaching of AF647 is far slower than found for aza-BOD with no observed build-up of a coloured product. As with aza-BOD, the loss of chromophore corresponds to first-order kinetics, but the decay rate is some two orders of magnitude slower under comparable levels of photon absorption. While the rate constant for photo-bleaching of aza-BOD is 6.0 x 10^{-7} M h^{-1}, it is just 3.0 x 10^{-9} M h^{-1} for AF647. The rate of degradation did not increase upon aerating the sample. Neither dye has an appreciable rate of intersystem crossing. Therefore, there must be some alternative non-radiative pathway responsible for photo-bleaching other than singlet oxygen formation.

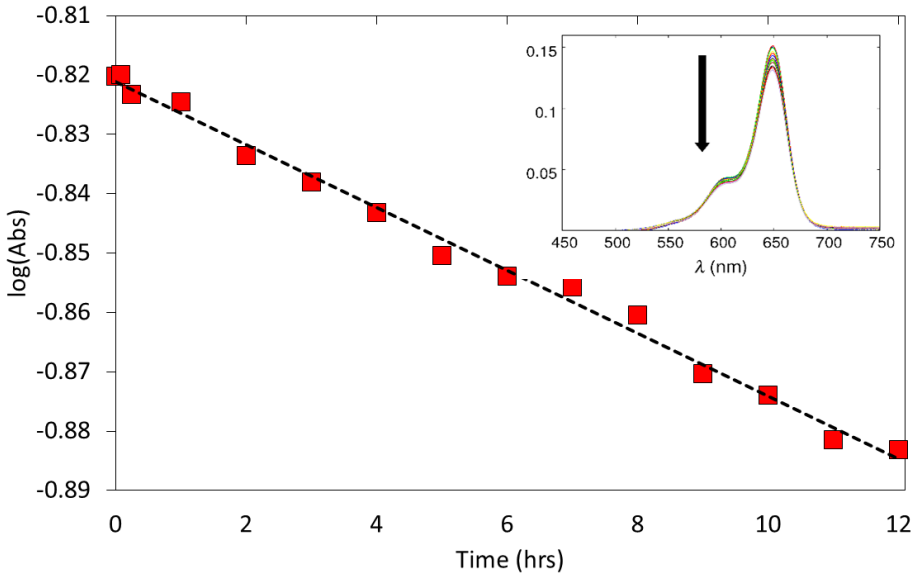

Figure 8.5. Steady-state photo-bleaching of AF647 in de-aerated, de-ionized water. Inset shows the evolution of the absorption spectrum for the dye over the course of the experiment. The loss of dye fits to a first-order decay (black line) with a rate constant of 3.0 x 10^{-9} M h^{-1} ± 10%.

Temperature dependence studies of AF647 fluorescence show that upon cooling to cryogenic temperatures, the fluorescence begins to decrease. This was observed across repeated experiments and is most readily explained by changes in solubility. It is possible that at lower temperatures the chromophore undergoes self-association, leading to a quenching of fluorescence.[25] In contrast, an Arrhenius plot across temperatures above room temperature gives rise to activation energy of at 4.9 kJ mol^{-1}.

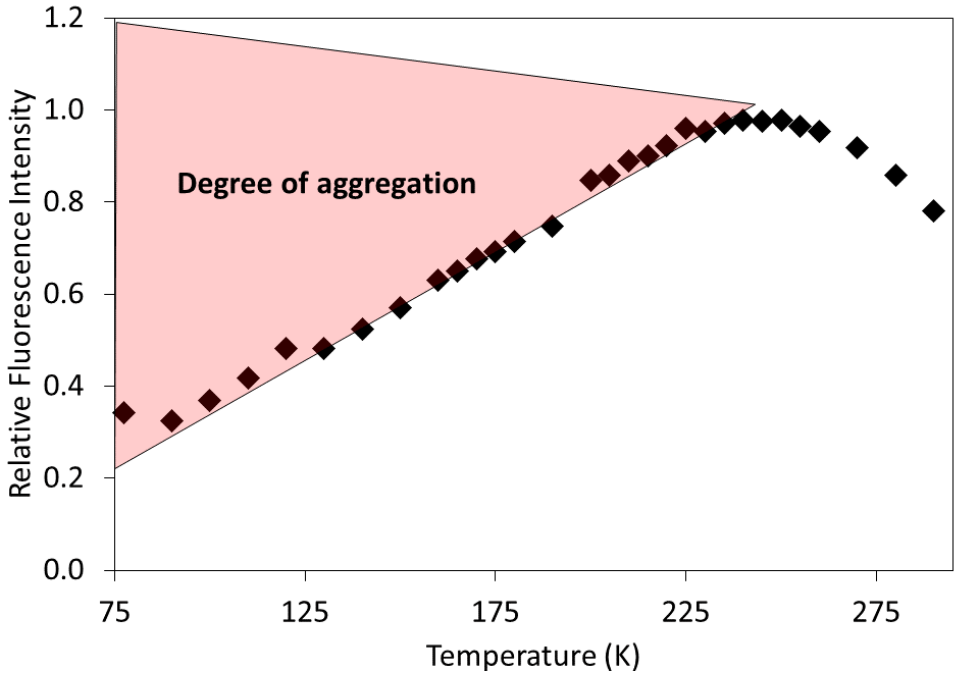

Figure 8.6. Temperature dependence of AF647 fluorescence between 77K and room temperature in dilute ethanol solution.

The estimate of the activation energy is reached by plotting the non-radiative rate constant against reciprocal temperature (Figure 8.7). It is assumed that the radiative rate constant remains independent of temperature. Therefore, the assumption that self-association is responsible for the loss of fluorescence at low temperature can be tested by projecting the Arrhenius plot back to 77K in order to determine the fluorescence yield in the absence of aggregation. This should be 100% and puts the emphasis on how accurately one has determined the radiative rate constant at room temperature. Using the data from Figure 8.7 and the fluorescence yield and lifetime for AF647 in ethanol, the derived fluorescence quantum yield is indeed 100% at 77K.

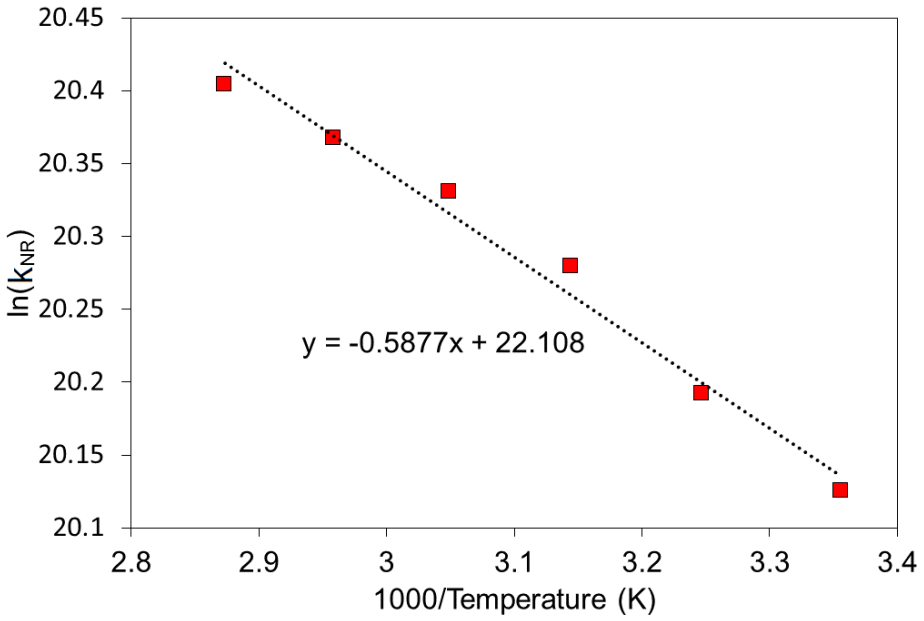

Figure 8.7. Arrhenius plot for AF647 fluorescence in dilute ethanol solution between 25 and 75 ^{o}C.

Self-association may play an important role in the context of microscopy. As has been discussed in the introductory chapter, dimerization and aggregation often lead to a loss of fluorescence. Also, according to Kasha's exciton splitting model,[26] formation of dimers can promote intersystem crossing. It was noted that when AF647 was dissolved in tetrahydrofuran (THF) the shape of the absorption spectrum changed drastically (Figure 8.8), showing symmetrical splitting of the lowest-energy π-π* transition. This is clear evidence for dimerization. Furthermore, the absorption spectrum in THF can be analyzed to give an estimate of the magnitude of exciton splitting, and this can then be compared with theory, when appropriate physical parameters are inserted. Deconstruction of the AF647 dimer spectrum into four Gaussian components of a common full-width gives a splitting of 1,300 cm^{-1}.

Calculation of the exciton splitting with Kasha's model requires knowledge of the transition dipole moment for the monomer as well as the relative orientation of the monomers and their transition dipole moments. Equation 8.2 yields the transition dipole moment μ_{ag}.[27] Here, the integral is taken for the lowest-energy transition of the molar absorptivity spectrum, h is Planck's constant, c the speed of light, ε_0 vacuum permittivity and N_A Avogadro's number. The derived transition dipole moment for the AF647 monomer is 14.1 D.

$$|\mu_{ag}|^2 = \frac{3hc\varepsilon_0 ln10}{2\pi^2 N_A}\int_{\upsilon_1}^{\upsilon_2}\frac{\varepsilon}{\upsilon}\,d\upsilon \qquad (8.2)$$

$$\mu_{ag}{}' = \mu_{ag}{}'' \qquad (8.3)$$

$$\sqrt{2\mu_{ag}cos\theta} = \sqrt{2\mu_{ag}sin\theta} \qquad (8.4)$$

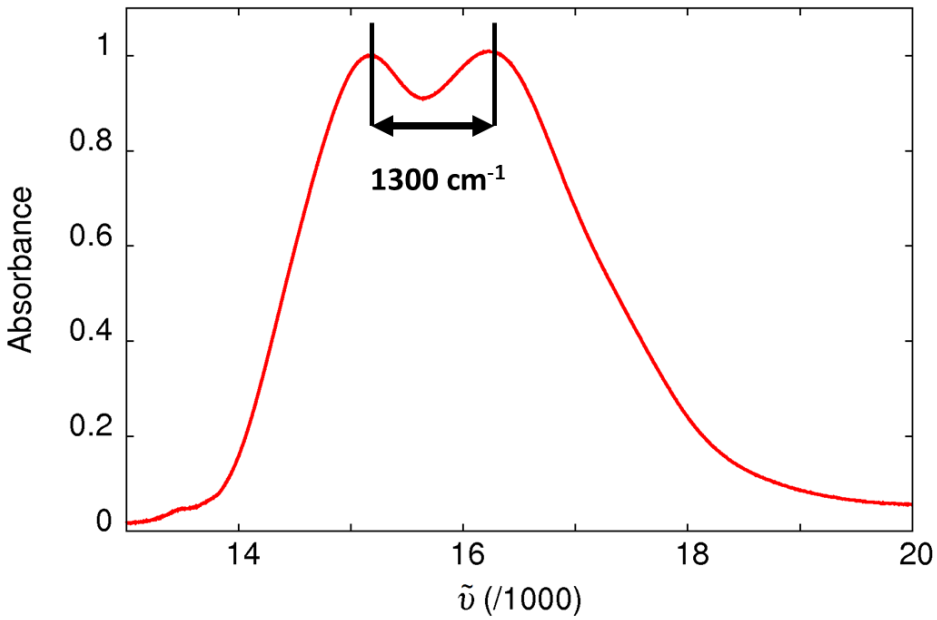

Figure 8.8. Absorption spectrum of μM concentration AF647 in THF. Energy is in wavenumber here to better show the exciton splitting.

Given that we know the exciton splitting from the absorption spectrum given in Figure 8.8, the angle between the two transition dipole moments can be estimated using equations 8.3 and 8.4. This is done by comparing the intensity of the exciton transitions in the dimer spectrum $\mu_{ag}{}'$ and $\mu_{ag}{}''$. Here, we appear to have a clear-cut case as the ratio is approx. 1:1. Simplifying equations 8.3 and 8.4 one will therefore one will obtain the result $\frac{sin}{cos} = 1$ (i.e. $tan\theta = 1$). The angle between the dipole moments must as a consequence be 45° in which case the angle between monomers is 90°. The remaining variable, the distance between monomer centre points was derived from semi-empirical molecular simulation of the ground-state optimized structures of two monomers at 90° to each other, giving a rough estimate of 13 Å.

$$\Delta\varepsilon = \frac{2|\mu_{ag}|}{r^3}(cos\alpha + 3cos^2\theta) \qquad (8.5)$$

The value for the exciton splitting energy $\Delta\varepsilon$ obtained for oblique transition dipole moments can now be obtained using Equation 8.5.[26] Here μ_{ag} is the transition dipole moment, r the centre-to-centre distance, α is the angle between two monomers and θ the angle between transition dipole moments. Using all the variables obtained above, we end up with a calculated exciton splitting value of 1360 cm^{-1}, which is in excellent agreement with the absorption spectrum in Figure 8.8. This gives us some information on how two AF647 monomers might interact as a dimer and may serve as an indication of aggregates formed during the microscope experiment.

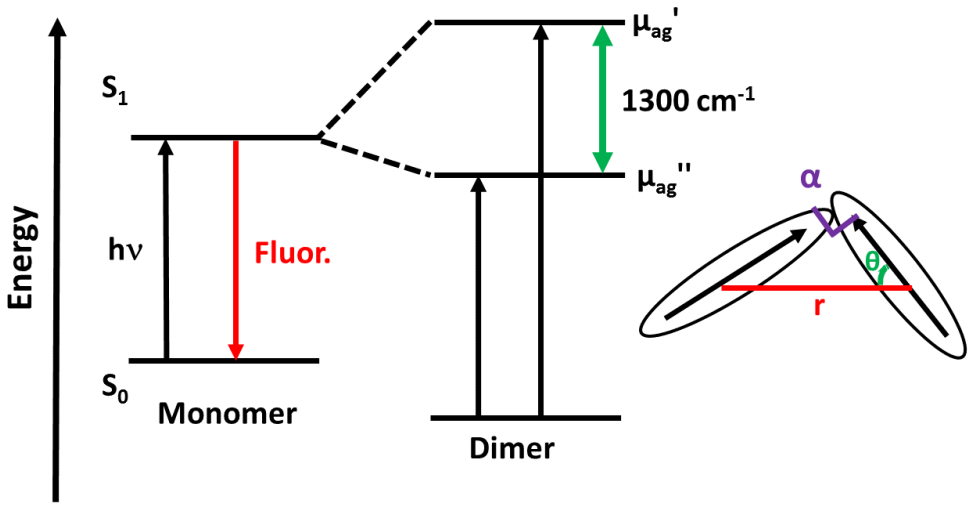

Figure 8.9. Scheme illustrating exciton splitting in a molecular dimer as derived using Kasha's model.

8.2.2 Characterizing the Triplet-Excited State

Attention now turns to the triplet-excited state where electron transfer between the thiol and the fluorophore becomes more feasible due to the long-lived nature of spin-forbidden triplet.[28] The enzymatic oxygen-scavenging environment employed in photo-switching buffers ensures quenching due to molecular oxygen is kept to a minimum.[29] Transient absorption spectroscopy and steady-state phosphorescence measurements were used to characterize the AF647 triplet-excited state. Although it was possible to detect a long-lived transient absorption signal upon adding an external heavy atom (e.g. by adding sodium iodide), it did not produce a clear spectrum. This suggests to us that intersystem crossing to the triplet manifold is ineffective, although there might be problems in that the iodine ion is not the best spin-orbit promotor.

Triplet-triplet energy transfer[30] was therefore used as an alternative to quantify the AF647 triplet state. Erythrosine was used as a triplet donor as it has a well-characterized and relatively long-lived triplet state generated with a high yield (~100% in water). The lowest energy triplet transition is centred at 580 nm and has a molar absorption coefficient (ε_T) of 11,000 M^{-1} cm^{-1}.[31, 32]

From the fit to a bi-exponential model, as seen in Figure 8.10, the relative absorbance signals of the donor and acceptor triplet states can be determined. Having measured the triplet lifetime of the donor alone (~150 μs), then observing the decrease in donor triplet lifetime across three different concentrations of AF647 acceptor, the efficiency of triplet transfer was determined. The derived bimolecular rate constant (k_{TT} = 2 x 10^9 M^{-1} s^{-1}) was found to somewhat less than the diffusion controlled limit. The differential molar absorption coefficient for the triplet state of AF647 in de-aerated water was determined by comparison with the donor to be 15,000 M^{-1} cm^{-1} at 650 nm. Comparison with another transient species, the cis-isomer (next section), gives an estimate of the triplet quantum yield at less than 1% for direct excitation of AF647. Figure 8.11 shows the derived differential transient absorption spectra from the sensitization experiment. The only prominent absorption feature for the triplet state occurs at approx. 720 nm.

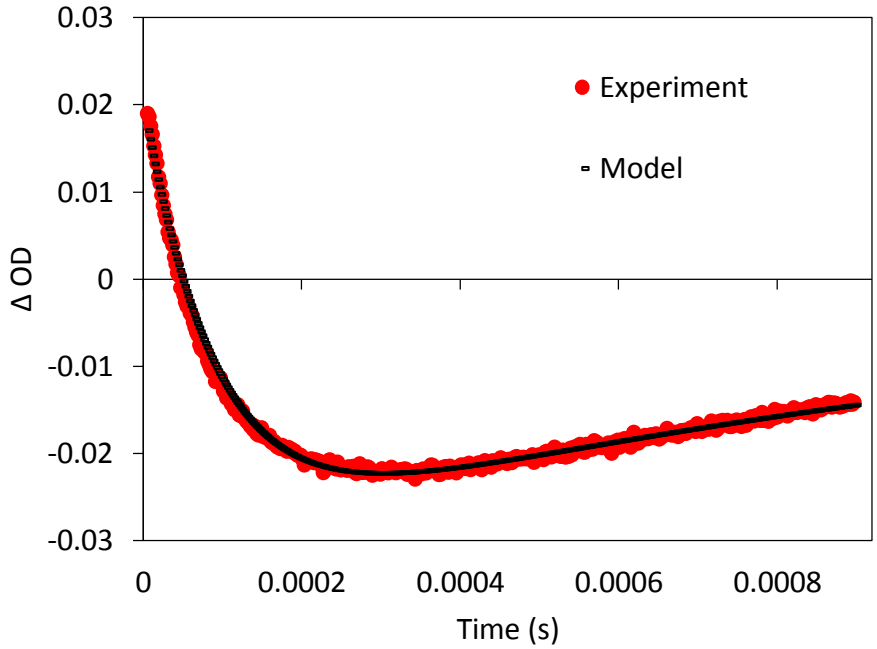

Figure 8.10. Fit to bi-exponential kinetics describing triplet-triplet energy transfer from Erythrosine to AF647. Excitation at 500 nm (5 mJ, 4 ns pulse), probe wavelength 650 nm.

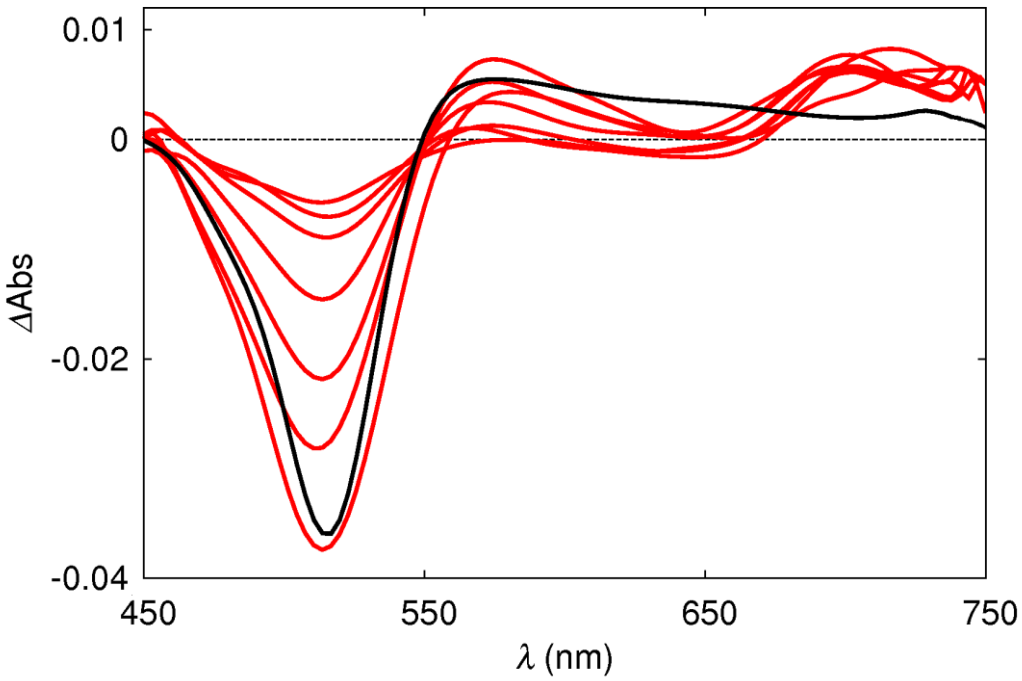

Figure 8.11. Sensitized AF647 triplet differential absorption -spectrum in de-ionized water between 5 and 200 μs. The black trace is the equivalent triplet spectrum for Erythrosine alone under matching conditions.

An estimate of the triplet lifetime was determined by plotting the decay rate at 650 nm in the presence of various concentrations of sodium iodide. This allows us to plot the change in lifetime and estimate the triplet decay rate in the absence of spin-orbit promoter. It was noted during this experiment that there was a second signal overlapping with the triplet, leading to a bi-exponential decay.

The second lifetime was unaffected by the presence of oxygen or iodide and was later found to be due to photo-induced isomerization. The triplet decay was nonetheless extracted by a simple bi-exponential fit and a limiting triplet lifetime of approx. 1.1 ± 0.1 ms obtained (Figure 8.12).

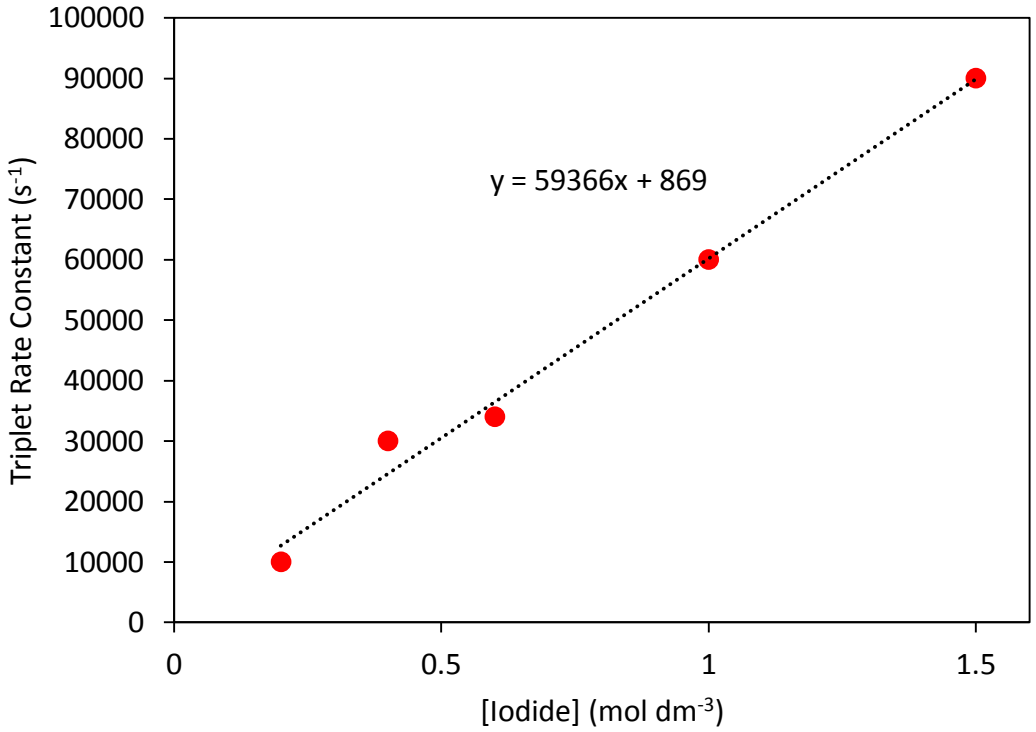

Figure 8.12. Plot of AF647 triplet decay rate constant versus concentration of sodium iodide in de-ionized water at room-temperature upon excitation at 610 nm (5 mJ, 4 ns pulse).

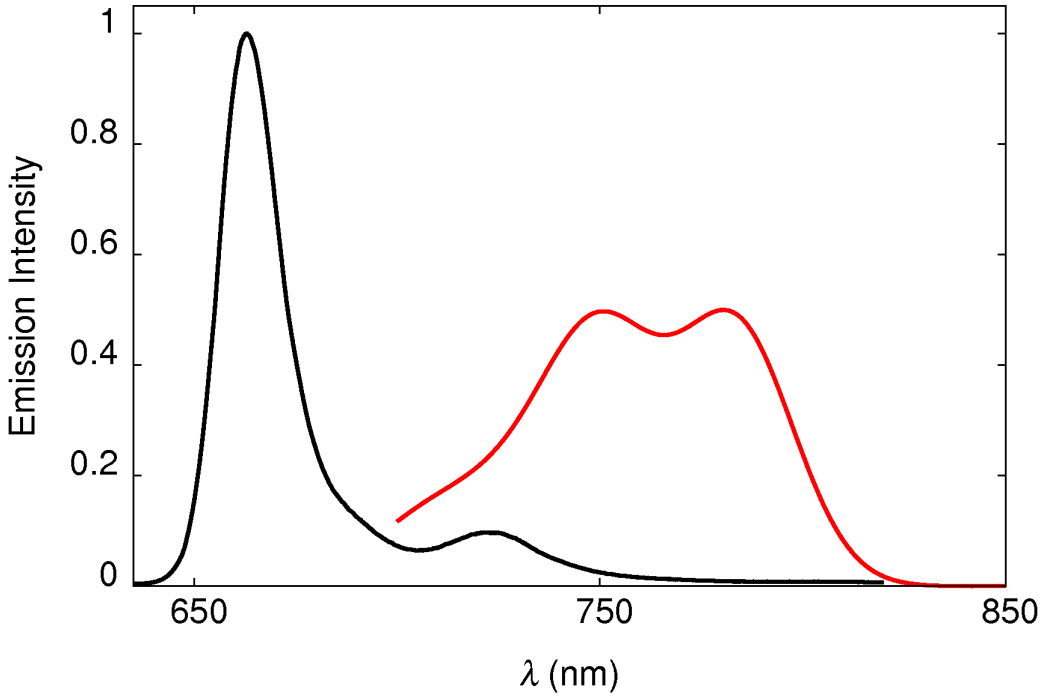

Figure 8.13. Black trace: fluorescence spectrum of AF647 in an ethanol optical glass at 77K. Red trace: AF647 phosphorescence recorded under the same conditions with 20% iodomethane. The phosphorescence spectrum is corrected for detector artefact and magnified. The true signal is extremely weak.

Phosphorescence measurements at 77K in an ethanol glass with added iodomethane (20% v/v) showed an extremely weak emission centred at 750 nm, consistent with previous reports.[33] We were unable to reach an estimate for the phosphorescence quantum yield because of the very weak signal. The triplet energy, however, could be estimated at 1.66 eV. This corresponds to a singlet-triplet energy gap of ca. 0.22 eV.

8.2.3 Photo-induced Isomerization

Cy5 is known to undergo photo-induced cis-trans isomerization, which can be observed using laser flash photolysis[34] or fluorescence correlation spectroscopy.[17] It is generally considered that the ground-state structure of most cyanine dyes is all-trans but there is little experimental support for this hypothesis. However, the ground-state structure for AF647 was identified as being (>98%) all-trans by two-dimensional ^{1}H NMR spectroscopy. Thus, NMR data for the ground state shows the characteristic coupling constants expected for an all-trans configuration. We thank Dr. Corinne Wills and Prof. William McFarlane for conducting the NMR analysis on our behalf. A few other indocyanine dyes

have been characterized by x-ray crystallography and again display an all-trans configuration along the polymethine backbone [35] Previous investigations into the photo-switching mechanism of cyanine dyes for super-resolution fluorescence imaging noted isomerization as a side-effect. Almost all studies propose the origin of the non-fluorescent state as being due to a triplet excited state reacting with components of the redox buffer.[36] Few investigators consider the realization that the triplet state is formed in very low quantum yield whereas isomerization is considerably more effective. This is certainly the case for AF647 in solution. Consequently, it was decided to characterize and quantify the cis-isomer(s) for AF647.

Laser flash photolysis was used to investigate formation of any isomers brought about by twisting the polymethine backbone. These species are expected to have a distinct absorption spectrum in some cases. This has in the past been done very successfully to characterize isomerization in a carbocyanine laser dye, which is not dissimilar to AF647.[37-41] A similar effect has been studied extensively in merocyanine dyes.[42-44] Probing on the hundreds of microseconds timescale in aerated solution (so as to exclude detection of a triplet) a transient signal centred at 686 nm was easily detected in de-ionized water. The corresponding lifetime of this light-induced absorption feature is ~500 μs, and is unaffected by the presence of oxygen. The characteristic sinusoidal pattern corresponding to the ground state bleach and the rise of the new absorption band suggests an isomer is formed, based on similar observations from previous reports.

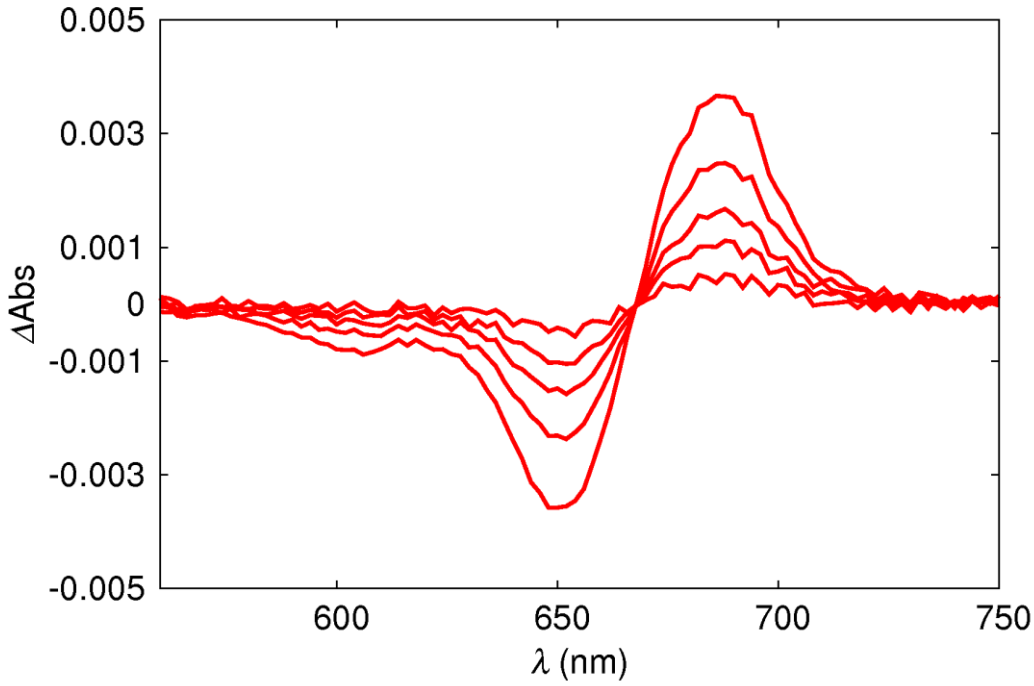

Figure 8.14. Transient absorption traces of a AF647 isomer at 20, 180, 340, 540 and 940 μs. The lifetime of the isomer is approximately 500 μs. Excitation 610 nm (5 mJ, 4 ns pulse).

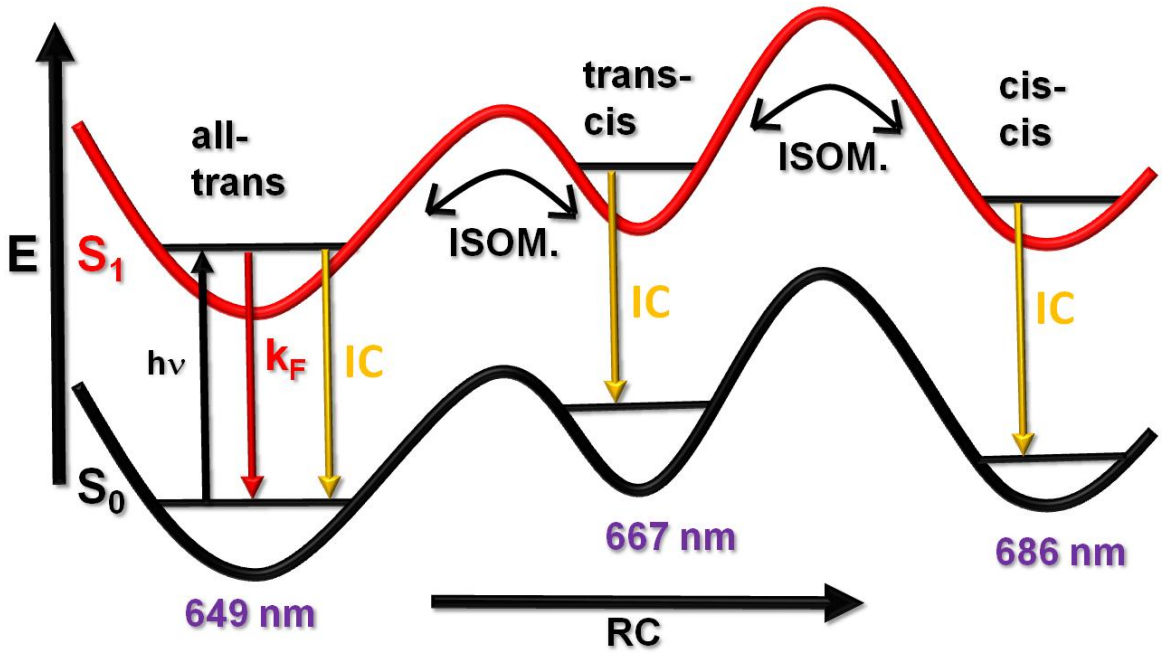

Figure 8.15. Schematic representation of isomerization in AF647. Note that back-isomerization is initiated by the same wavelength light as used for exciting the ground-state all-trans structure due to spectral overlap of the isomers.

Reconstruction of the isomer absorption spectrum is possible by adding successive amounts of ground state absorption back to the transient until the ground state bleach

has been completely recovered (Figure 8.18). The isomer spectrum derived from data seen in Figure 8.14 is some 37 nm red-shifted from the ground state. This is labelled "isomer 2", the reasoning for the ordering will become apparent shortly. Iterative spectral fitting using the methods described in Chapter 4 also allows one to estimate the molar absorption coefficient of this isomer, which was found to be 250 000 M^{-1} cm^{-1} at the absorption peak.

The forward reaction giving the cis-isomer is in competition with photo-induced back-isomerization, the potential energy barrier for the reverse process being small. Such a situation has previously been characterized for Cy5 dyes,[37] and has implications for determining the quantum yield of isomerization. The flash photolysis setup used for measurements here has a 150 W Xenon arc lamp as the probe light. The high intensity of the broadband probe light will quickly push a portion of the isomer back to the ground state. In order to determine the isomer yield of the forward reaction, a power dependence study must be included for the probe light to account for this.

By varying the percentage probe light transmitted with neutral density filters, it was possible to construct a probe light power dependence (Figure 8.16). From this the maximum absorbance of isomer was determined in the case where there is no broadband probe light present (i.e. as is the case in fluorescence microscopy). The absorbance of the isomer was then plotted at various laser energies at the selected probe light percentage. Finally, to estimate the isomer quantum yield for AF647, laser excitation power dependence studies for AF647 were compared against a standard (Figure 8.17). Comparison of the slope of the AF647 isomer power dependence with a well-characterized standard gives an approximation of the yield. Care was taken to maintain the temperature at 25 ^{o}C during these experiments, since the rate of isomerization will be sensitive to temperature.

The triplet of zinc tetraphenylporhyrin, Zn-TPP, (φ_T = 83%, ε_T = 73,000 M^{-1} cm^{-1} at 470 nm)[45] was used as a standard and both dyes were excited at 590 nm. The values obtained give an estimated 30% isomer yield, using Equation 8.6[46] The result repeated by experiment with fresh samples matched within 5%.

$$\frac{\varphi_X}{\varphi_S} = \frac{slope\ X}{slope\ S} * \frac{\varepsilon_S}{\varepsilon_X} \qquad (8.6)$$

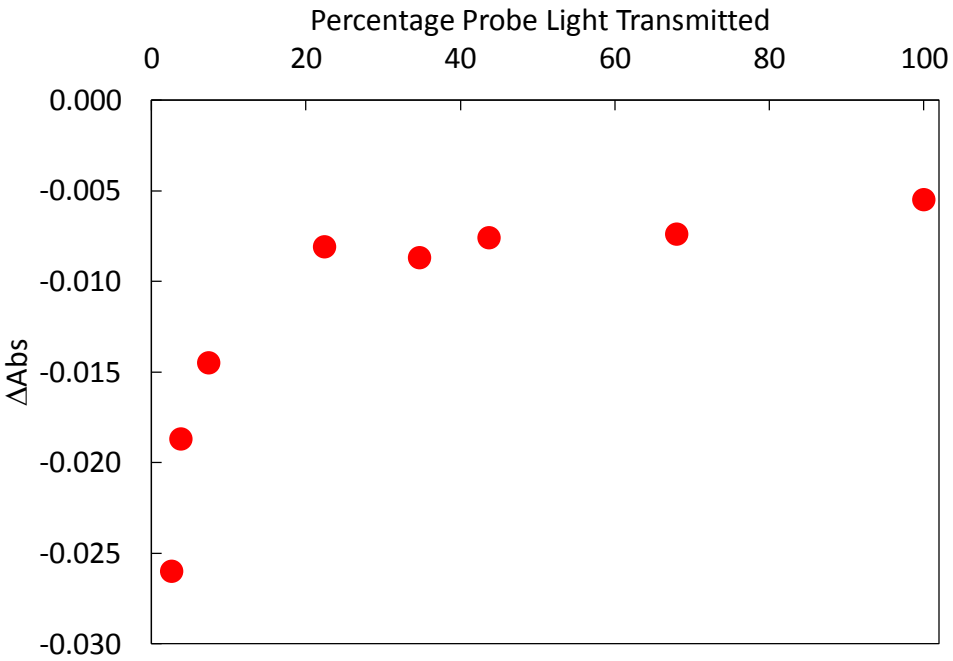

Figure 8.16. Relationship between absorbance and probe light power as monitored at the ground state bleach of AF647 in PBS (649 nm).

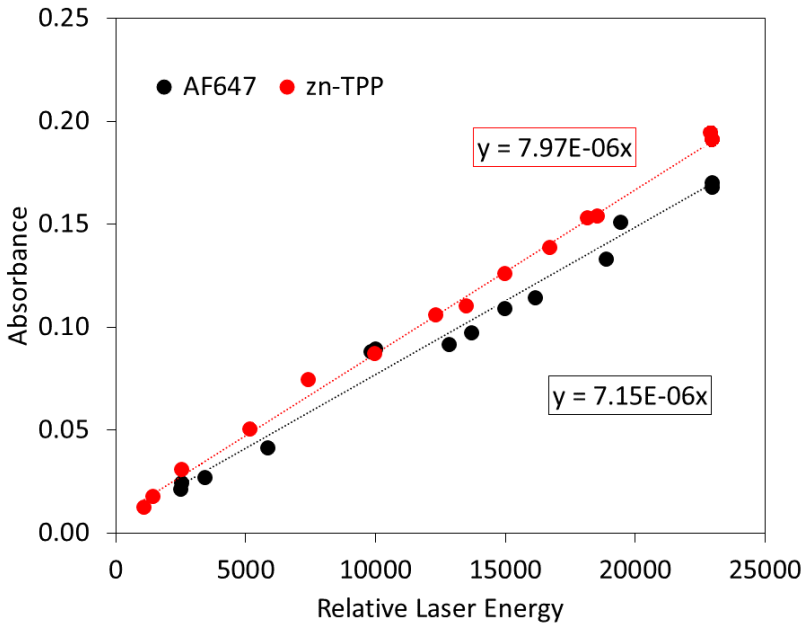

Figure 8.17. Laser power intensity studies of AF647 (in PBS) isomer at 686 nm vs Zn-TPP (in toluene) triplet at 470 nm. Pump wavelength 590 nm. Laser energy in arbitrary units.

It was noted from the flash photolysis probe light power dependence studies that the isomer lifetime was changing according to the amount of transmitted probe light. This

suggests there is more than one species involved in the isomerization step. Going back to the idea of reverse-isomerization, it follows that the first isomer could also undergo a second transformation to yield a double isomer. Indeed it was possible to obtain a distinct isomer spectrum in the case where the probe light intensity was 7.4 % that for the isomer seen in Figure 8.14. To clarify, isomer 1 is presumably the first formed isomer, *cis-trans* and is seen when the probe light is at its lowest, isomer 2 is most likely a double isomer (*cis-cis*) seen when the probe light is at its most intense. This gives two separate isomer spectra as seen in Figure 8.18. Such a situation has been observed in a diethylthiocarbocyanine dye which has the same backbone as Alexa Fluor 647.[47] It follows that there is sufficient energy in the probe light not only to push isomer 1 back to all-trans and also to rotate a second double bond on the methane bridge to give cis-cis. Therefore, the spectrum in Figure 8.14 is most likely predominantly the double isomer. The overall situation is summarized in Figure 8.15. Activation energies for the two isomers were obtained by temperature dependence studies (Figure 8.19). Predictably, the activation energy for the return of the isomer 2 to the ground state is higher (~50 kJ mol^{-1}) than the first isomer (~33 kJ mol^{-1}).

Table 8.2. Variation of isomer lifetime at 686 nm as a function of flash photolysis probe light intensity.

Probe Light Transmittance / %	**Isomer Lifetime / μs ± 5%**
100	500
72	440
51	400
43.7	373
22.4	332
7.4	300
1	200

$$\Phi_{t-c} = \frac{k_{t-c}}{k_{t-c} + k_{c-c}} \qquad (8.7)$$

Having determined the quantum yield for isomerization for the cis-trans (isomer 1), the yield can also be confirmed by employing the individual lifetimes in Equation 8.7. Using the values 500 μs for *trans-cis* and 200 μs for cis-cis, the derived quantum yield for

isomerization is 28.5%, very close to the experimentally observed value. This suggests we are primarily dealing with two isomers as illustrated by Figure 8.18.

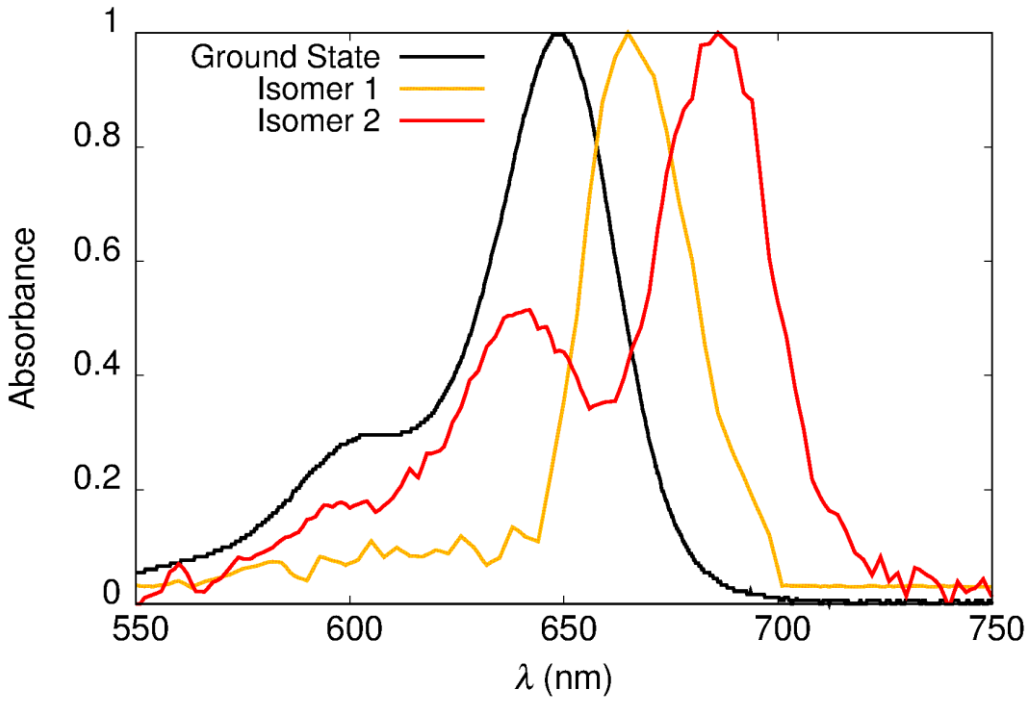

Figure 8.18. Normalized ground state absorption spectrum of AF647 in de-ionized water (black trace) and isomer absorption spectra (orange and red traces) reconstructed from transient absorption spectra.

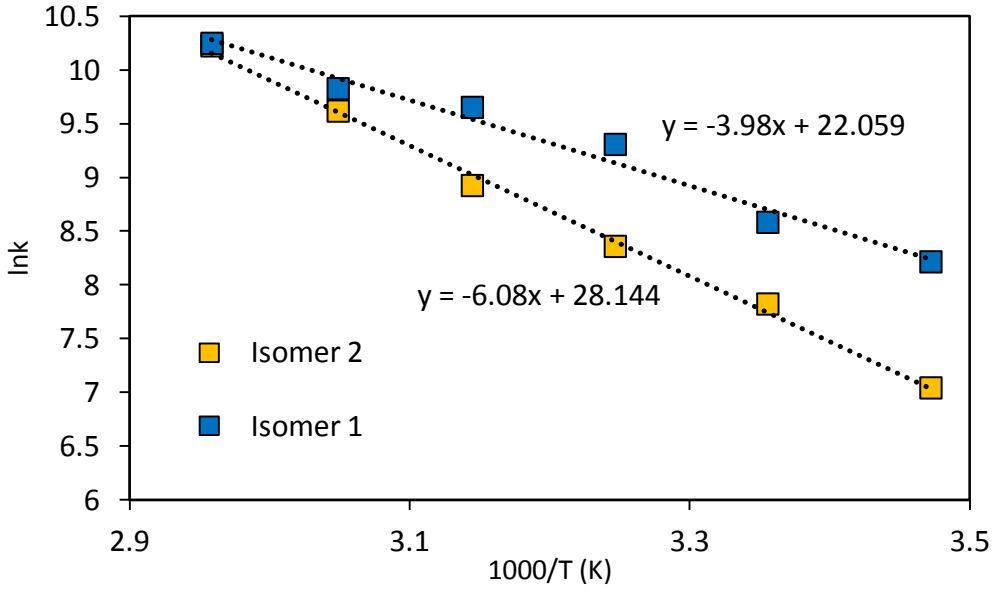

Figure 8.19. Temperature dependence of AF647 for the formation of the two resolved isomers in de-ionized water (15 – 65 ^{o}C). Transient decay rate constant monitored at ground state bleach to avoid artefacts arising from increasing unresolved fluorescence emission at the isomer absorbance wavelength.

Table 8.3. Photophysical properties of AF647 photo-induced isomers in aqueous buffer.

	λ_{max}^{abs} / nm	τ_{isomer} / μs ± 5%	ϕ_{isom} ±5%	E_a / kJmol^{-1} ±5%
Isomer 1 (*trans-cis*)	667	200	0.30	33
Isomer 2 (*cis-cis*)	686	500	0.05	50

Given the possibility that the free-dye NHS-ester might behave differently when bound to a protein, as would be the case in a microscope setup, similar studies were performed on a protein-labelled variant. Table 8.4 compares the photophysical properties of free-dye AF647 NHS-ester against goat anti-mouse secondary antibody AF647. Overall, the properties remain closely comparable except for the lifetime of isomer 2 (*cis-cis*), which has doubled on attachment to the protein. The increase of the isomer lifetime to the millisecond regime brings it into line with the reported fluorescence fluctuations associated with single-molecule fluorescence experiments involving Cy5.[31]

Table 8.4. Comparison of free dye and protein-bound AF647 photophysical properties.

	λ_{max}^{abs} / nm	λ_{max}^{fluor} / nm	ϕ_{fluor} ±0.01	τ_{s1} / ns	$\tau_{cis\text{-}cis}$ / μs
Free dye	649	670	0.34	1.2	500
Protein-bound	651	671	0.30	1.5	1,200

The data in the table show that the rate of isomerization is sensitive to the environment. Obviously the rate of isomerization is also very sensitive to temperature and viscosity. At higher viscosity, the rate of isomerization will decrease, favoring fluorescence. Conversely at higher temperature the yield of fluorescence diminishes and the isomerization yield increases.[48-50] The fluorescence temperature dependence seen in Figure 8.7 agrees with this trend.

The overarching conclusion drawn from this work is that the predominant non-radiative pathway in these dyes is that of light-induced isomerization, which itself is multifaceted. Control of the environment surrounding the dye will have a large impact on the magnitude of the non-radiative rate constant in this case, which is an important design consideration for fluorescence microscopy. There are conflicting reports in the scientific literature on the triplet state being accessible from one of the isomers, but our data do not support this hypothesis. Indeed, even in the presence of an external heavy-atom perturber that promotes direct population of the triplet, the isomer is still observed.[33,46,50-52]

8.2.4 STORM Microscope Data Analysis

It was deemed desirable to attempt to obtain quantitative information from a real STORM microscope imaging experiment, which records co-ordinates of single molecule localization events against time before deconvoluting an image. It should therefore be possible to track the on/off fluorescence times to single molecules in the experiment. This would prove useful for comparisons with the photophysical data obtained above. Analysis of a dSTORM data set was obtained from a software routine generated by Dr. Ata Amini of the Molecular Photonics Laboratory at Newcastle University. Here microscope imaging run were with 647 nm excitation at 100 mW and Alexa Fluor 647 as the dye. Details of the super-resolution microscope setup are provided in Chapter 2. Microscope imaging was conducted by Dr. Alex Laude of the Newcastle University Medical School Bio-Imaging Unit.

Analysis of the dSTORM data, where AF647 is used as the fluorophore, can be used to obtain quantitative information on the rate of on/off fluorescence switching. Statistical analysis of individual fluorophore spots as seen by the microscope show that 55% of blinking events involve a triangular pattern, going from dark to bright and dark again without ever re-appearing. This is possibly due to static quenching with the surrounding redox environment. The remaining 45% had a trackable pattern of on/off fluorescence blinking over a period of seconds before permanent photobleaching occurred. These fluorescence blinking patterns are complex, which is probably indicative of multiple processes.

The distribution of times taken to achieve permanent photo-bleaching of an individual fluorophore is centred at a value of approximately 1 s. On average, the fluorophore will fluctuate between bright and dark states 1-7 times, with a mean value of 4. The mean time occupied in the dark state is approximately 250 ms, based on analysis of several hundred datasets. A limitation of the imaging protocol here is temporal resolution. Exposure times are 16 ms, which may exclude some fast photo-switching events. Faster exposure times are understood to be possible, but were not routine at the time of the experiment.

8.2.5 Computational Modeling

Quantum chemical calculations are useful for determining the energies and rotational barriers to formation of the geometric isomers. Here, we decided to simplify the structure of AF647 down to the core, Cy5, dispensing with the solubilizing groups, which increased the speed for the calculations. Five possible isomers, brought about by twisting certain parts of the polymethine backbone, were considered (Figure 8.20). The likelihood is that some of these would be spectrally indistinguishable due to small differences in energies. Calculation of the isomer(s) excited-state energy was based on optimized geometries obtained using the *ab initio* MP3 method. Calculation of the excited-state geometry was performed with the ZINDO method using water as a solvent. The results confirm that cis-isomers have a somewhat red-shifted absorption spectrum in water relative to the all-trans species (Table 8.3).

Table 8.5. Simulated absorption maxima for AF647 configurational isomers.

Configuration	**Simulated Abs Maximum / nm**
all-trans	648
cis-indole	650
1,2-cis	662
3,4-cis	655
1,2-3,4 cis-cis	659

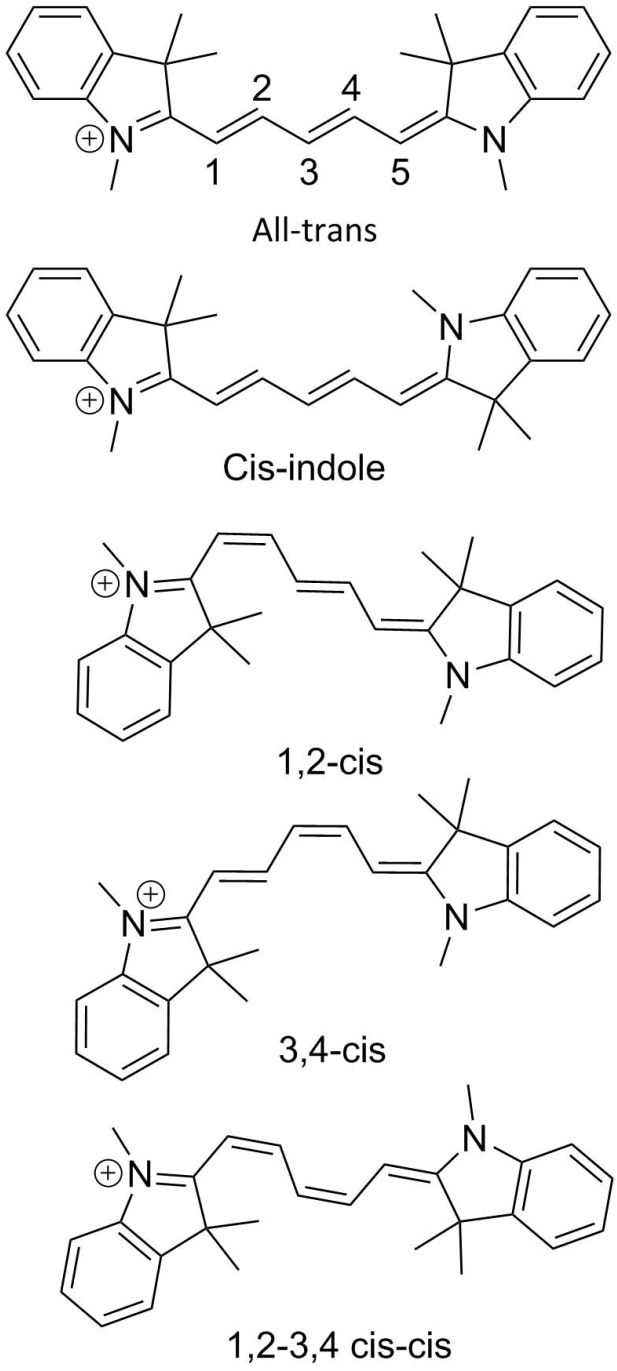

Figure 8.20. Configurational isomers of a simplified AF647 structure, whose energies were calculated by computational chemistry.

The computational studies indicate slight differences for the optical spectra of the most likely geometrical isomers expected for AF647 in fluid solution. The projected absorption maxima are close to that of the parent dye but show a slight red shift. This finding seems consistent with the experimental studies where illumination causes isomerization of the polymethine backbone. At this point, we know the starting structure and we have some

information on the likely optical properties of potential isomers. Pulsed laser photolysis of AF647 in fluid solution causes the formation of at least two geometrical isomers. It appears that there is not much of an obstacle to isomerization and, at the least, the inclusion of light-induced isomerization should be considered in the mechanism of fluorescence blinking under super-resolution microscopy. To our mind, isomerization is more likely than reactions of the triplet-excited state. To continue this hypothesis, we need to produce information about the rotational barriers and possible reaction pathways.

These rotational barrier calculations are time consuming, especially when conducted in a solvent reservoir. There are many possible pathways and, as a simplification step, we assume that the smallest molecular fragment will be the most likely rotor. With this in mind, the first light-induced step is transformation of the all-trans species to the cis-indole. This requires rotation around the first double bond. Of course, resonance structures along the polymethine backbone serve to reduce the bond order along the chain, thereby increasing the chances for isomerization. An energy profile computed for this first rotation is shown in Figure 8.21. Geometry optimizations across the range of dihedral angles were calculated using the PM6 semi-empirical method in a solvent reservoir (COSMO, ε_S = 20, refractive index 1.45) for the ground state.

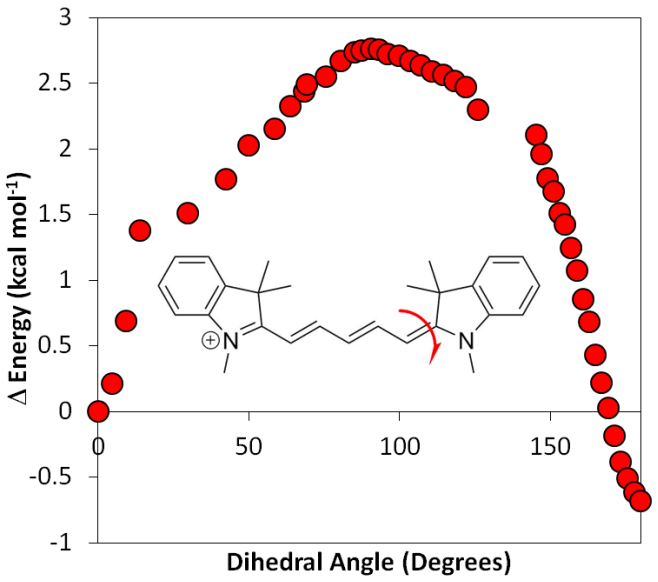

Figure 8.21. Calculated isomerization energy barriers for rotation of the Cy5 terminus as determined by quantum chemical calculations.

For the “cis-indole” rotation there is a modest energy barrier, somewhat lower than in a related study with more polar end groups, but this is to be expected.[37] The experimental values obtained for two isomers are considerably larger, although we cannot ascertain which structural changes these correspond to. Note however the computer simulations dispense with the bulky functional groups of on AF647, which will certainly have an effect on the absolute energies. Given the numerous permutations of cis-trans isomers, we are more interested in general trends. Following on from the simple rotation of the Cy5 end-group, Figure 8.22 extends the isomerization process by twisting the polymethine backbone. Perhaps unsurprisingly, we find that the energetic barrier to a double isomer (i.e., where the end-groups are trans and the 1,2 positions on the backbone are cis) is larger than obtained for the first step.

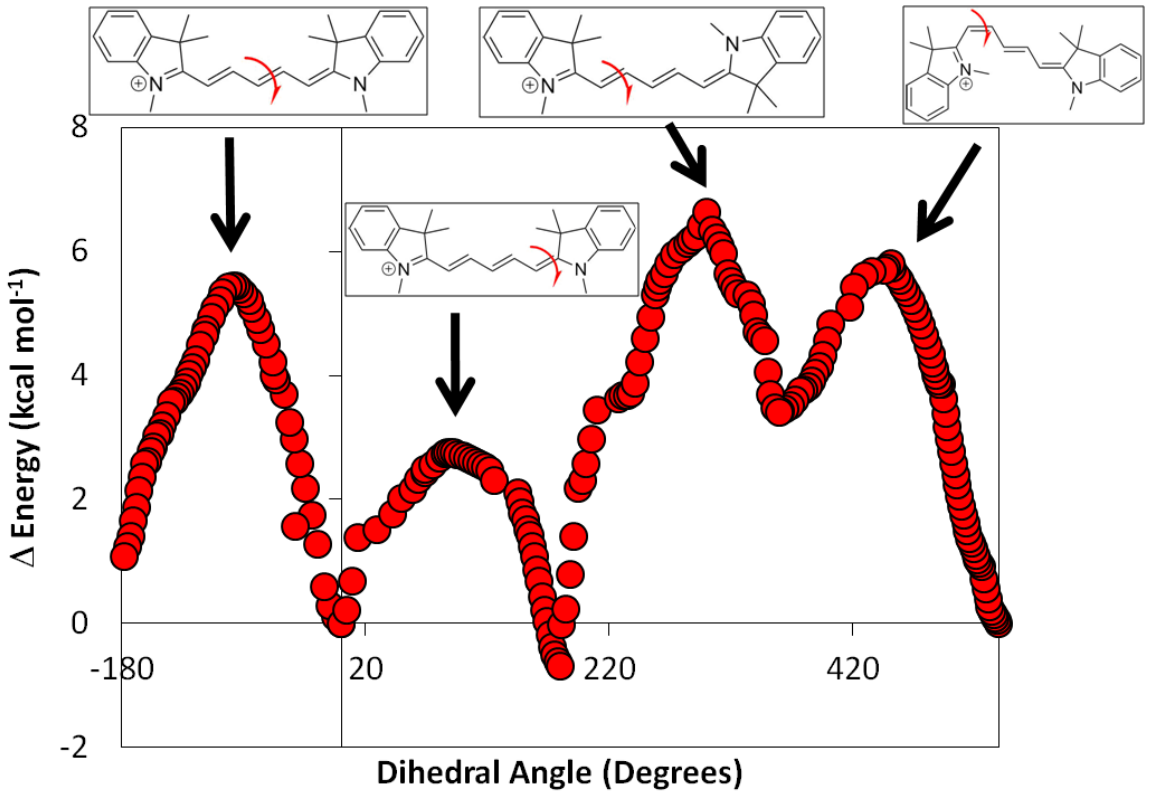

Figure 8.22. Isomerization surfaces for a sequence of isomerization processes about the Cy5 polymethine backbone. Dihedral angles are expressed as cumulative due to sequential rotations of the structure.

Animations of the various isomerization steps described above are provided in the electronic supporting information attached to this thesis.

Our preliminary findings suggest to us that light-induced isomerization might play an important role in the fluorescence blinking observed for certain types of super-resolution microscopy. It is easy to see that one of the many possible photo-isomers could revert to the original all-trans species under illumination, or via a slow thermal process, and begin the fluorescence on-off cycle once more. Indeed, it is difficult to argue against there being some involvement of photo-isomers, although most current practitioners prefer to cite a redox-active triplet state as being the key intermediate. Our computational studies did include calculation of the corresponding excited-state barrier crossing but we used only CI-singles method and this might not be adequate. We plan to continue this work and to repeat the computation work at a much higher level. Several earlier studies have looked at the potential surfaces for the excited-singlet state of cyanine dyes and concluded that these surfaces are flatter than for the ground state. This means light-induced isomerization will be fast. Our idea is that isomerization of all-trans to cis-indole might not be sufficient to account for the blinking. Further isomerization would give a species that reverts to the ground state on a relatively slow timescale and this could well be the responsible intermediate.

8.3 Conclusions

Reversible fluorescence on/off switching (or blinking) in the context of super-resolution fluorescence imaging has a number of viable origins. It might be that there is no single cause for the blinking and that different dyes will involve quite disparate blinking processes, although all the effective dyes seem to be based on the cyanine structure. Here, we have examined a well-known and widely used class of fluorophore, Cy5 (Alexa Fluor 647) in the context of STORM microscopy. The choice is in part due to the sheer versatility of this particular fluorophore, and also to reconcile the fact that fluorescence blinking has been seen to occur in numerous different environments.[53] In attempting to account for the origins of fluorescence blinking in AF647, our studies do not portray a role for light-induced electron transfer from the singlet- or triplet-excited states to produce a long-lived dark intermediate. Although this putative mechanism is the most often quoted cause of fluorescence blinking in the literature, conditions are against it.

The excited-singlet state is too short lived and the triplet state is formed in very low yield.

A standout feature of the Alexa Fluor 647 dye, as older literature would suggest, is the clear tendency to undergo light-induced isomerization. Cis-trans isomerization is a fundamental process in photobiology and is the origin of sight in the animal kingdom. Similar experiments with an analogous Cy5 dye show the phenomenon was not just restricted to one system and that the cis-isomers of Cy5 are indeed non-fluorescent.[17] Furthermore, work in Chapter 7 clearly demonstrates the tendency of Cy5 to undergo cis-trans isomerization. Therefore, these long-lived dark states may be a feature in the complex fluorescence blinking behaviour seen during a microscope experiment. Our work established that absorption spectra of the isomers overlap heavily with the all-trans ground state, which will enable rapid back-isomerization induced by the same 647 nm laser line commonly used with fluorescence microscopes. At the same time, a double isomer can form, whose larger activation barriers will see a longer decay time back to the ground state. Our experimental observations show that the yield for cis-trans isomerization is in excess of 30% with lifetimes of the double isomer being in excess of 1 ms, under conditions comparable to those used with the microscope. When immobilized a biological sample, the lifetime of the isomer is likely to increase due to restricted rotation.

Here, we have established physical parameters for cis-trans isomerization for a common fluorescent probe in fluorescence microscopy. Since this was not previously given much consideration in the context of microscopy, the information serves to highlight how a thorough understanding of the underlying photophysics is key to fully utilizing the instrumentation. This applies equally to conventional fluorescence microscopy as it does to super-resolution techniques. For the former, one wishes to eliminate fluorescence blinking, for the latter it is a requirement. Yet the same dye is used for both techniques! With suitable modifications to super-resolution fluorescence microscope techniques, this mode of fluorescence switching could be exploited without the need for complex redox buffer. If one wished to go in another direction then the target would be to eliminate cis-trans isomerization to force fluorescence blinking. Indeed this has been

touched upon where some reported that the Vitamin E derivative, Trolox, can stop fluorescence blinking in Cy5 and enhance photo-stability, but the mechanism is not understood.[54,55]

Our work here is rather preliminary and somewhat incomplete. Although we have tended to minimize the role of electron-transfer chemistry, it has to be stated that we have been unable to establish what level of chemical reactivity takes place in the actual fluorescence microscope. It is possible that even with a triplet quantum yield not much different from 1%, this could account for the observed blinking. There seems to be no reliable information on the actual details of these experiments. Although our working relationship with colleagues in the Medical School Bio-Imaging Unit has been excellent, it is clear that we do not share a common language when it comes to chemistry.

8.4 References

1. Moerner, W.E.; Kador, L. *Phys. Rev. Lett.* **1989**, 62, 2535-2538.

2. Nie, S.; Chiu, D.T.; Zare, R.N. *Science* **1994**, 266, 1018-1018.

3. Weiss, S. *Science* **1999**, 283, 1676-1683.

4. Betzig E.; Patterson G. H.; Sougrat R.; Lindwasser O. W.; Olenych S.; Bonifacino J. S.; Davidson M. W.; Lippincott-Schwartz J.; Hess H. F. *Science* **2006**, 313, 1642-1645.

5. Rust, M. J.; Bates, M.; Zhuang, X. *Nat. Methods* **2006**, 3, 793-796.

6. Huang, B.; Bates, M.; Zhuang, X. *Ann. Rev. Biochem.* **2009**, 78, 993-1016.

7. Schermelleh, L.; Heintzmann, R.; Leonhardt, H. J. Cell. Biol. **2010**, 190, 165-175.

8. Steinhauer, C.; Forthmann, C.; Vogelsang, J.; Tinnefeld, P. *J. Am. Chem. Soc.* **2008**, 130, 16840-16841.

9. van de Linde, S.; Krstić, I.; Prisner, T.; Doose, S.; Heilemann, M.; Sauer, M. *Photochem. Photobiol. Sci.* **2011**, 10, 499-506.

10. Dempsey, G. T.; Bates, M.; Kowtoniuk, W. E.; Liu, D. R.; Tsien, R. Y.; Zhuang, X. *J. Am. Chem. Soc.* **2009**, 131, 18192-18193.

11. Bates, M.; Huang, B.; Dempsey, G.T.; Zhuang, X. *Science* **2007**, 317, 1749-1753.

12. Aitken, C. E.; Marshall, R. A.; Puglisi, J. D. *Biophys. J.* **2008**, 94, 1826-1835.

13. Berlier, J.E.; Rothe, A.; Buller, G.; Bradford, J.; Gray, D.R.; Filanoski, B.J.; Telford, W.G.; Yue, S.; Liu, J.; Cheung, C.Y.; Chang, W. *J. Histochem. Cytochem*. **2003**, 51, 1699-1712.

14. Heilemann, M.; van de Linde, S.; Schüttpelz, M.; Kasper, R.; Seefeldt, B.; Mukherjee, A.; Tinnefeld, P.; Sauer, M. *Angew. Chem. Int. Ed*. **2008**, 120, 6266-6271.

15. Murov, S.L.; Carmichael, I.; Hug, G.L., 1993. Handbook of Photochemistry. CRC Press.

16. Vogelsang, J.; Cordes, T.; Forthmann, C.; Steinhauer, C.; Tinnefeld, P. *Proc. Natl. Acad. Sci. U.S.A*. **2009**, 106, 8107-8112.

17. Widengren, J.; Schwille, P. *J. Phys. Chem. A* **2000**, 104, 6416-6428.

18. Aubin, J.E. *J. Histochem. Cytochem.* **1979**, 27, 36-43.

19. Owens, J. W.; Smith, R.; Robinson, R.; Robins, M. *Inorg. Chim. Acta* **1998**, *279*, 226-231.

20. Metcalf, D. J.; Edwards, R.; Kumarswami, N.; Knight, A. E. *JoVE* **2013**, 79, e50579.

21. Lakowicz, J.R., 1983. Quenching of fluorescence. In Principles of fluorescence spectroscopy (pp. 257-301). Springer US.

22. Bowen, E.J.; Metcalf, W.S. *Proc. Roy. Soc. A* **1951**, 206, 437-447.

23. El-Hallag, I. S.; Al-Youbi, A. O.; Obaid, A. Y.; El-Mossalamy, E. H.; El-Daly, S. A.; Asiri, A. M. *J. Chilean Chem. Soc.* **2011**, 56, 837-841.

24. Vogelsang, J.; Kasper, R.; Steinhauer, C.; Person, B.; Heilemann, M.; Sauer, M.; Tinnefeld, P. *Angew. Chem. Int. Ed.* **2008**, 47, 5465-5469.

25. Ricchelli, F.; Gobbo, S.; Jori, G.; Salet, C.; Moreno, G. *Eur. J. Biochem.* **1995**, 233, 165-170.

26. Kasha, M.; Rawls, H.R.; Ashraf El-Bayoumi, M. *Pure Appl. Chem.* **1965**, 11, 371-392.

27. Thorley, K.J.; Würthner, F. *Org. Lett.* **2012**, 14, 6190-6193.

28. Lewis, G.N.; Kasha, M. *J. Am. Chem. Soc.* **1944**, 66, 2100-2116.

29. Olivier, N.; Keller, D.; Rajan, V.S.; Gönczy, P.; Manley, S. *Biomed. Opt. Express* **2013**, 4, 885-899.

30. Bensasson, R.V.; Land, E.J. *Trans. Faraday Soc.* **1971**, 67, 1904-1915.

31. Tomasini E. P.; Braslavsky SE; San Román E. *Photochem. Photobiol*. *Sci*. **2012**, 11, 1010-1117.

32. Tachikawa, T.; Kobori, Y.; Akiyama, K.; Katsuki, A.; Steiner, U.E.; Tero-Kubota, S. *Chem. Phys. Lett.*, **2002**, *360*, 13-21.

33. Huang, Z.; Ji, D.; Xia, A.; Koberling, F.; Patting, M.; Erdmann, R. *J. Am. Chem. Soc.* **2005**, *127*, 8064-8066.

34. Giuliano, C.; Hess, L.; Margerum, J. *J. Am. Chem. Soc.* **1968**, 90, 587-594.

35. Dai, Z.F.; Peng, B.X.; Chen, X.A. *Dyes Pigm.* **1999**, 40, 219-223.

36. Zheng, Q.; Jockusch, S.; Zhou, Z.; Altman, R. B.; Warren, J. D.; Turro, N. J.; Blanchard, S. C. *J. Phys. Chem. Lett.* **2012**, 3, 2200-2203.

37. Awad, M.M.; McCarthy, P.K.; Blanchard, G.J. *J. Phys Chem.* **1994**, 98, 1454-1458.

38. Rulliere, C. *Chem. Phys. Lett.* **1976**, 43, 303-308.

39. Dempster, D.N.; Morrow, T.; Rankin, R.; Thompson, G.F. *J. Chem. Soc. Faraday Trans. II*, **1972**, 68, 1479-1496.

40. Dempster, D.N.; Morrow, T.; Rankin, R.; Thompson, G.F. *Chem. Phys. Lett.* **1973**, 18, 488-492.

41. Benniston, A.C.; Harriman, A.; Gulliya, K.S. *J. Chem. Soc. Faraday Trans.* **1994**, 90, 953-961.

42. Benniston, A.C.; Harriman, A.; McAvoy, C. *J. Chem. Soc. Faraday Trans.* **1998**, *94*, 519-525.

43. Čunderlíková, B.; Šikurová, L. *Chem. Phys*. **2001**, 263, 415-422.

44. Harriman, A. *J. Photochem. Photobiol A*. **1992**, 65, 79-93.

45. Hurley, J.K.; Sinai, N.; Linschitz, H. *Photochem. Photobiol.* **1983**, *38*, 9-14.

46. Jia, K.; Wan, Y.; Xia, A.; Li, S.; Gong, F.; Yang, G. *J. Phys. Chem. A.* **2007**, 111, 1593-1597.

47. Vaveliuk, P.; Scaffardi, L.B.; Duchowicz, R. *J. Phys. Chem.* **1996**, 100, 11630-11635.

48. Sundstroem, V.; Gillbro, T. *J. Phys. Chem*. **1982**, 86, 1788-1794.

49. Aramendia, P.F.; Negri, R.M.; Roman, E.S. *J. Phys. Chem.* **1994**, 98, 3165-3173.

50. Hoebeke, M.; Pieite, J.; Van de Vorst, A. *J. Photochem. Photobiol. B*. **1990**, 4, 273-282.

51. Cooper, W.; Rome, K.A. *J. Phys. Chem.* **1974**, 78, 16-21.

52. Redmond, R.W.; Kochevar, I.E.; Krieg, M.; Smith, G.; McGimpsey, W.G. *J. Phys. Chem. A.* **1997**, 101, 2773-2777.

53. Chozinski, T.J.; Gagnon, L.A.; Vaughan, J.C. *FEBS Lett.* **2014**, 588, 3603-3612.

54. Rasnik, I.; McKinney, S.A.; Ha, T. *Nat. Methods,* **2006**, 3, 891-893.

55. Cordes, T., Vogelsang, J.; Tinnefeld, P. *J. Am. Chem. Soc.* **2009**, 131, 5018-5019.

*We thank Kimi Kurbanova, who drew the cover picture for this chapter.

Appendix

THE JOURNAL OF PHYSICAL CHEMISTRY A

Article

pubs.acs.org/JPCA

Origin of the Red-Shifted Optical Spectra Recorded for Aza-BODIPY Dyes

Joshua K. G. Karlsson and Anthony Harriman*

Molecular Photonics Laboratory, School of Chemistry, Bedson Building, Newcastle University, Newcastle upon Tyne, NE1 7RU, United Kingdom

Supporting Information

ABSTRACT: The optical properties are compared for two boron dipyrromethene (BODIPY) dyes that differ by virtue of the substituent at the *meso*-site, namely, aza-N versus C-methine atoms. Both compounds are equipped with aryl rings at the 3- and 5-positions of the dipyrrin backbone, which help to extend the degree of π-delocalization. The aza-BODIPY dye absorbs and fluoresces at much lower energy than does the conventional BODIPY dye, with red shifts of about 100 nm being observed in fluid solution, but with comparable fluorescence yield and lifetime. Hydrogen bonding donors, such as alcohols, attach to the aza-N atom and promote nonradiative decay without affecting the properties of the conventional dye. Triplet formation is ineffective in the absence of a spin-orbit coupler. Quantum chemical calculations indicate that the electronegative aza-N atom lowers the energy of the LUMO while having little effect on the corresponding HOMO energy. The resultant decrease in the HOMO−LUMO energy gap is primarily responsible for the red shift. The HOMO−LUMO energy gap is also affected by the dihedral angle subtended by the aryl rings, but this is insensitive to the geometry around the central 6-membered ring. The aza-N atom, by virtue of restricting spatial overlap between the HOMO and LUMO, decreases the energy gap between excited-singlet and -triplet states.

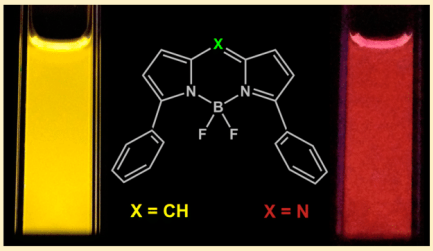

INTRODUCTION

Fluorescent dyes have numerous and highly varied applications, ranging from environmental sensors to selective labels, markers, screens, and analytical reagents.[1−5] Such materials, while retaining considerable fundamental interest,[6−8] have found prominent use in biological systems[9] and are making important contributions to medical imaging.[10,11] Of particular note are fluorescent dyes possessing exceptional photochemical stability together with strong emission in the far-red region of the spectrum, where absorption and/or scattering from background materials can be minimized. Within the vast array of known fluorescent dyes, the boron dipyrromethene (BODIPY) family[12−14] has gained ascendency during recent years, partly because of their facile synthetic modification, exceptional versatility, robustness, and ready availability. These dyes require structural modification, however, in order to push their absorption and emission transitions to longer wavelengths, but the so-called extended-BODIPY dyes[15,16] tend to be somewhat more susceptible to degradation on prolonged exposure to sunlight.[17,18] It has been noted by several research groups that replacing the *meso*-methine group in the conventional BODIPY core with an aza-N atom serves the purpose of lowering the energy of both absorption and emission transitions.[19−22] Indeed, the resultant aza-BODIPY (i.e., aza-difluoroboradiaza-*s*-indacene) dyes[12] are known to absorb and emit within the spectral window stretching from 600 to 750 nm. The cause of this pronounced red shift remains obscure since most derivatives are also equipped with peripheral aryl groups, notably benzene rings, which add to the overall π-conjugation pathway. As a consequence, the role of the aza-N atom becomes somewhat hidden. One of the main objectives of this investigation is to delineate the effects of extended conjugation from the electronic and/or steric effects of aza substitution.

An interesting application of the aza-BODIPY dyes concerns their potential use as sensitizers for photodynamic therapy (PDT),[23] which stems in part from their improved optical properties. It is well-known that conventional BODIPY dyes are not amenable to intersystem crossing to the triplet manifold,[24] although the triplet state can be populated by indirect means,[25] even in the presence of spin−orbit couplers. The successful utilization of aza-BODIPY dyes in PDT might be considered suggestive of increased spin−orbit coupling promoted by the aza-N atom, but little is known about the triplet states of these compounds. As part of our investigations, we have explored the possibility of triplet state formation in aza-BODIPY dyes with a view to establishing the triplet-state energy.

Received: February 5, 2016
Revised: March 28, 2016
Published: April 5, 2016

DOI: 10.1021/acs.jpca.6b01278
J. Phys. Chem. A 2016, 120, 2537−2546

To realize these aims, we compare two BODIPY dyes which differ mainly in terms of the nature of the *meso*-site (Scheme 1).

Scheme 1. Molecular Formulae of the Aza-BODIPY (Aza-BOD) and Its Conventional Analogue (BOD) Compared with the Basic BODIPY Core Illustrating the Numbering System[a]

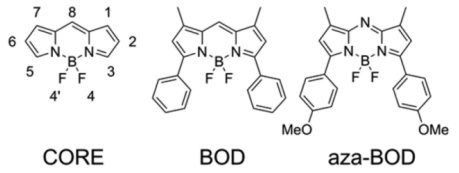

[a]See Supporting Information for computed energy-minimized geometries.

Compound BOD, which is already known in the scientific literature,[26] is a member of the conventional family of BODIPY dyes[12] but bears aryl appendages at the 3,5-positions. Since there is no aryl substituent at the *meso*-carbon (i.e., the 8-position) atom, this dye does not function as a molecular-scale rotor[27] and, as a consequence, is strongly fluorescent in fluid solution. The corresponding aza-BODIPY derivative, aza-BOD, is equipped with the 3,5-aryl substituents such that the extent of π-delocalization should be comparable in both compounds; aryl substituents attached to the dipyrrin nucleus are known[28] to push the absorption and fluorescence maxima to lower energies. Although no similar comparison of conventional and aza-BODIPY dyes has been reported in the literature, some preliminary photophysical data have been described[22] for aza-BOD in chloroform solution. Specifically, these measurements indicate that the dye absorbs in the region of 650 nm, while fluorescence is found at around 680 nm with a quantum yield of 0.44 in $CHCl_3$ at room temperature. The same study reported that the 4-methoxy group on the aryl substituents of aza-BOD contributed an additional bathochromic shift of ca. 30 nm. This information forms the starting point for the present investigation.

RESULTS AND DISCUSSION

The optical absorption spectra recorded for BOD and aza-BOD in 2-methyltetrahydrofuran (MTHF) solution at room temperature are compared by way of Figure 1. The most striking feature relates to the significant red shift noted for the aza-derivative. Thus, the lowest-energy absorption transition observed for BOD shows a prominent maximum (λ_{MAX}) at 549 nm, with a series of vibronic satellites stretching toward higher energies. The molar absorption coefficient (ε_{MAX}) measured at the band maximum is 62,100 M^{-1} cm^{-1} under these conditions. For aza-BOD, λ_{MAX} is shifted to 651 nm (i.e., an apparent red shift of 2,855 cm^{-1}), again with a prominent series of vibronic satellites at higher energy. After deconstruction of the absorption transitions into a series of five Gaussian-shaped components of common half-width (Figures S5, S6), this being the minimum number of bands needed to reconstruct the entire transition, we can refine the extent of the red shift as being 2,760 cm^{-1}. Furthermore, it is clear that the Gaussian components derived for BOD (fwhm = 965 cm^{-1}) are somewhat broader than found for aza-BOD (fwhm = 770 cm^{-1}). The value of ε_{MAX} found for aza-BOD is 81,000

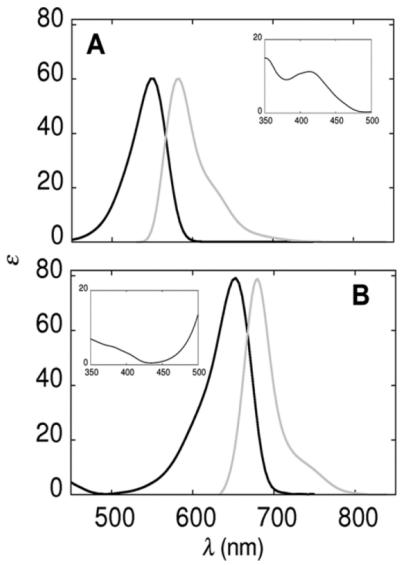

Figure 1. Normalized absorption (black curve) and emission (gray curve) spectra recorded for (A) BOD and (B) aza-BOD in MTHF at room temperature. Molar absorptivity, ε, is given in units of M^{-1} cm^{-1}/1000. The insets show the near-UV regions of absorption spectra for BOD (upper panel) and aza-BOD (lower panel).

M^{-1} cm^{-1} such that the calculated oscillator strengths (f) for the two compounds are closely comparable (0.50 for BOD and 0.58 for aza-BOD). These derived parameters are collected in Table 1. For both compounds, the onset of the second absorption transition can be recognized in the near-UV region (Figure 1). This transition is significantly weaker than the

Table 1. Compilation of the Spectroscopic Properties Recorded for the Target Dyes in MTHF at Ambient Temperature

property	BOD	aza-BOD
λ_{MAX}/nm	549 ± 1	651 ± 1
ε_{MAX}/M^{-1} cm^{-1}	62,100 ± 5,000	81,000 ± 7,000
f^a	0.50 ± 0.04	0.58 ± 0.06
λ_{FLU}/nm	585 ± 3	680 ± 3
Φ_F	0.92 ± 0.05	0.95 ± 0.05
τ_S/ns	6.6 ± 0.2	4.3 ± 0.2
E_{SS}/cm^{-1}[b]	585 ± 25	395 ± 15
k_{RAD}/10^7 s^{-1}[c]	13 ± 2	7.0 ± 1
S^d	0.20	0.12
ν_M/cm^{-1}	1,050 ± 200	1,375 ± 150
ν_L/cm^{-1}	530 ± 100	570 ± 100
k_{NR}/10^7 s^{-1}	1.2 ± 0.2	1.2 ± 0.2

[a]Oscillator strength calculated for the lowest-energy absorption transition. [b]The Stokes shift calculated after deconstruction of the absorption and emission spectra into Gaussian components. [c]Radiative rate constant calculated from the Strickler–Berg expression. [d]Huang–Rhys factor calculated from fitting the low-temperature emission spectrum to a series of five Gaussian components.

DOI: 10.1021/acs.jpca.6b01278
J. Phys. Chem. A 2016, 120, 2537–2546

corresponding $S_0 \rightarrow S_1$ transition and overlaps with a higher-energy transition. There is an obvious red shift for the $S_0 \rightarrow S_2$ transition for aza-BOD relative to BOD, which amounts to ca. 4,315 cm^{-1}.

Fluorescence is readily observed for both dyes in MTHF at room temperature (Figure 1), and again there is a clear red shift for aza-BOD. Thus, the emission maxima (λ_{FLU}) are located at 585 and 680 nm, respectively, for BOD and aza-BOD at room temperature. At 77 K in a MTHF optical glass, the emission spectra sharpen and appear at 580 and 690 nm, respectively, for BOD and aza-BOD. The slight blue shift noted for BOD is commonplace for BODIPY-based dyes and reflects the change in solvent polarizability on freezing,[29] but the red shift observed for aza-BOD is unusual. The magnitude of this shift exceeds 10 nm if due allowance is made for the anticipated effect of polarizability and most likely arises from improved alignment of the peripheral aryl rings with the dipyrrin unit. The two spectral patterns can be deconstructed into a series of five Gaussian-shaped components, thereby allowing derivation of the Huang−Rhys factor[30] (S), which provides a measure of the strength of electron−phonon interactions, and the size of the accompanying vibronic modes that accompany nonradiative deactivation of the excited state[31] (Table 1). In both cases, spectral reconstruction requires the introduction of low- (ν_L) and medium-frequency (ν_M) modes; the former modes are attributed to structural distortions of the dipyrrin backbone while the latter modes reflect small changes in the C═C and C═N bond lengths and/or angles during de-excitation. The energy difference between the 0,0 transitions derived by this type of spectral fitting allows estimation of the Stokes' shift (E_{SS}) for each compound. The derived values are small, although that found for BOD is the higher of the two, and indicate that the global geometry changes during excitation are rather small.

It is notable that the S-factor derived for aza-BOD at 77 K (Table 1) is somewhat reduced relative to that for BOD, although both values are small and are indicative of π,π^* transitions.[32] A higher S-factor implies more displacement between potential energy surfaces for ground and excited states,[33] and hence a larger Stokes shift. A smaller S-factor is also consistent with more extended π-conjugation,[34] and this particular feature could help toward explaining the red-shifted absorption and emission spectra observed for aza-BOD. On warming to room temperature, the S-factor for aza-BOD increases to 0.26, which is consistent with a somewhat reduced degree of planarity of the aryl rings on melting the glass.

Fluorescence quantum yields (Φ_F) and excited singlet state lifetimes (τ_S) were measured for each compound in MTHF at room temperature (Table 1). Under these conditions, both compounds are highly fluorescent and there is only a minor contribution from nonradiative decay. Time-resolved fluorescence decay curves are monoexponential in each case, and there is very good agreement between absorption and excitation spectra. The derived radiative rate constants (k_{RAD}) are in reasonable agreement with those calculated on the basis of the Strickler−Berg expression[35] (Table 1). In particular, k_{RAD} found experimentally for aza-BOD is relatively high for a BODIPY dye, especially when taking into consideration the low energy of the fluorescence transition. Nonradiative decay, as characterized by the corresponding rate constant ($k_{NR} = (1 - \Phi_F)/\tau_S$), is unimportant under these conditions (Table 1).

However, the presence of a hydrogen-bonding substrate, introduced in the form of a cosolvent such as ethanol, switches on nonradiative decay for aza-BOD without affecting the properties of BOD. This effect is exemplified by the following observation: Upon preparing solutions of aza-BOD with varying mole fractions of chloroform and ethanol, a clear drop in fluorescence was observed with increasing alcohol content. An initial quantum yield of 0.94 in pure chloroform falls to 0.60 in neat ethanol with a progressive quenching of fluorescence for intermediate cases (Figure 2). The clear

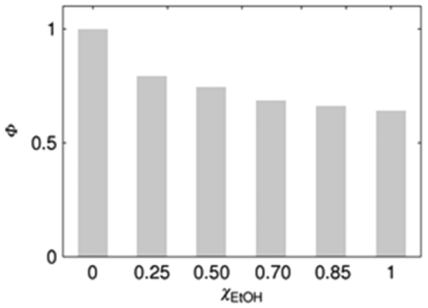

Figure 2. Relative fluorescence quantum yields φ found for aza-BOD in chloroform at room temperature as a function of the mole fraction χ of added ethanol.

inference is that the hydrogen-bond donor attaches to the aza-N atom and promotes nonradiative decay by providing a high-energy vibronic mode.[36] The same effect is found for related aza-BODIPY dyes and with other hydrogen-bond donors, including water, and counts against using aza-BODIPY dyes as sensitizers in aqueous media. It might be noted that a similar effect was reported earlier for aza-porphyrins,[37] where it was observed that isobutanol shortened the excited singlet state lifetime to 1.5 ns compared to a value of 3.4 ns found in toluene, and was explained in a similar manner. Interestingly, ethanol has only a marginal effect[38] on the excited singlet state lifetime of a highly constrained analogue of aza-BODIPY, where attachment to the *meso*-aza N atom is partially blocked by aryl substituents at the 1,7-positions.

Steady-state fluorescence anisotropy measurements of both BOD and aza-BOD were carried out between 25 and 60 °C in glycerol.[39] Although these dyes are structurally similar and possess near identical molar volumes, aza-BOD was found to possess a consistently higher anisotropy than BOD. At room temperature, for example, BOD had a measured anisotropy of 0.24 whereas that for aza-BOD was 0.29. Higher anisotropy values are associated with slower fluorescence depolarization (i.e., a retardation of the molecular reorientation time).[40] The result strengthens the notion of specific solvent−solute interactions occurring with aza-BOD, since hydrogen bonding with glycerol would result in a larger effective volume of the rotor.

As might be expected in light of the high fluorescence yields, it was not possible to detect phosphorescence from these BODIPY-based dyes in MTHF at 77 K. On addition of 20% v/v iodomethane, weak phosphorescence could be observed for aza-BOD at 77 K after decay of the fluorescence. The peak maximum appears at 775 nm (Figure 3), corresponding to an approximate triplet energy of 1.6 eV (i.e., 12,900 cm^{-1}) and an S_1-T_1 energy gap of 1,800 cm^{-1}. Phosphorescence from

DOI: 10.1021/acs.jpca.6b01278
J. Phys. Chem. A 2016, 120, 2537−2546

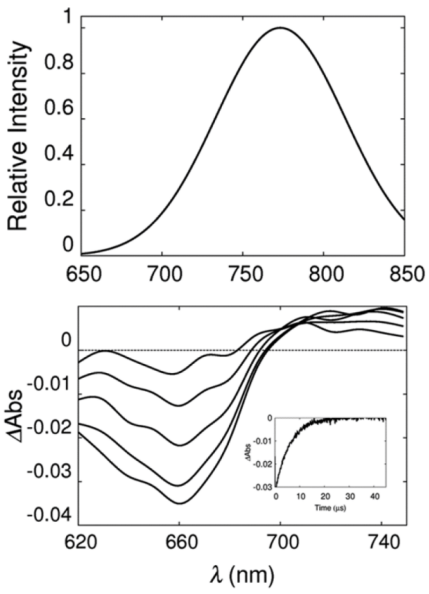

Figure 3. Upper panel: Phosphorescence spectrum recorded for aza-BOD at 77 K in an ethanol glass containing 20% v/v iodomethane. Lower panel: Transient absorption spectra recorded for aza-BOD in MTHF containing 20% v/v iodomethane with laser excitation at 610 nm. The time-resolved spectra were recorded at delay times of 1, 2, 5, 10, and 20 μs. The inset shows a typical kinetic trace recorded at 650 nm.

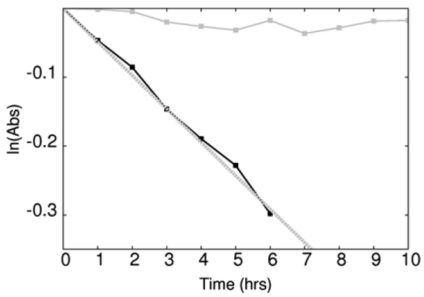

Figure 4. Plot showing steady-state photobleaching of BOD (gray curve) and aza-BOD (black curve) monitored with absorption spectroscopy. The dashed line represents a fit assuming first order kinetics for aza-BOD predicting a rate constant for photobleaching of 6.0×10^{-7} M h^{-1} ± 10%.

conventional BODIPY-based dyes is notoriously difficult to detect but has been reported[24] to occur at ca. 750 nm. On this basis, the S_1-T_1 energy gap is significantly smaller for aza-BOD. Confirmation of triplet formation for aza-BOD was obtained by ns-laser flash photolysis with illumination at 610 nm. Here, excitation of aza-BOD in deoxygenated dimethyl sulfoxide gave no detectable yield of the triplet state, or indeed any other long-lived transient species. On addition of 20% iodomethane, however, the triplet state could be detected. The dominant signal corresponds to transient bleaching of the S_0-S_1 transition centered at around 660 nm with weak absorption on either side of the bleached signal (Figure 3). The triplet lifetime was found to be 6.0 ± 1.2 μs under these conditions but was shortened to 1.2 ± 0.06 μs on aeration of the solution. In deaerated MTHF containing 50% v/v iodomethane, the triplet lifetime was found to be 1.2 ± 0.2 μs. Thus, intersystem crossing is negligible in the absence of a spin−orbit promoter but is effectively switched on by an external heavy-atom effect.[41]

Both dyes were found to be relatively stable under steady-state illumination with light of wavelength longer than 495 nm for BOD or 550 nm for aza-BOD. Thus, continuous illumination for 6 h caused approximately 30% loss of the aza-BOD chromophore in deaerated *N*,*N*-dimethylformamide solution. Aeration of the solution did not lead to a significant increase in the rate of photochemical bleaching. The bleaching process follows first-order kinetics (Figure 4) but does not lead to the appearance of any specific product absorbing in the visible region. There is no recovery of a partially bleached sample upon standing in the dark. Somewhat related aza-BODIPY dyes were found to exhibit similar levels of photoactivity in deaerated solution, and it is clear that these compounds possess reasonably good levels of photostability; bleaching is too inefficient for quantum yield measurements. Under comparable conditions, illumination of BOD for more than 12 h caused no significant (i.e., <5%) bleaching of the sample. Thus, the aza-N atom appears to (weakly) promote instability under continuous illumination with visible light.

We now return to the apparent red shift noted for absorption and fluorescence maxima, but not for the phosphorescence spectral maximum, and quantified as above. Quantum chemical calculations (see Experimental Details) carried out for the two dyes in a solvent reservoir with dielectric constant equal to 10 predict optical properties in fair agreement with the experimental data. Thus, the computed lowest-energy absorption transitions (λ_{MAX}) and oscillator strengths (f) are reasonably close to the actual values while the transition dipole moments (μ_{TD}) are in line with literature values[42] for related BODIPY dyes (Table 2). The molecular geometries were computed at different levels of theory, but the only marked variations relate to the dihedral angles for the 3,5-aryl rings. Even here, there was reasonable consensus between the different methods as outlined in the Supporting Information.

The energy-minimized structure calculated for BOD (see Supporting Information) indicates that the dipyrrin unit is essentially planar. The 3,5-aryl rings adopt a dihedral angle of 59° relative to the dipyrrin nucleus (Table 2), although these groups can gyrate over a modest variance (Figure 5). The rotational barrier (E_0) for reaching the planar structure, which amounts to 15.9 kcal/mol, arises from repulsion between the *ortho*-H atom on the rotor and a fluorine atom. In fact, to accommodate the planar geometry it is necessary for the dipyrrin backbone to buckle slightly. This introduces a small degree of asymmetry as judged by the F−H bond distances of 1.683 and 1.824 Å. Loss of π-electron delocalization at 90° introduces a more subtle barrier (E_{90} = 1.3 kcal/mol) for forming the perpendicular geometry (Figure 5).

It seems reasonable to suppose that the dipyrrin−aryl dihedral angle will impart an important influence on the absorption maximum.[43] In fact, aza-BODIPY dyes with constrained aryl groups at the 3,5-positions, where the dihedral

DOI: 10.1021/acs.jpca.6b01278
J. Phys. Chem. A 2016, 120, 2537−2546

Table 2. Summary of the Structural Data Derived from Computer Modeling of the Target Compounds in a Solvent Reservoir Having a Dielectric Constant of 10[a]

property	BOD	aza-BOD
λ_{MAX}/nm	533	619
f	0.51	0.47
μ_{TD}/D	2.6	2.29
$S_0 \rightarrow T_1$/nm	790	855
E_{HOMO}/eV	−5.46	−5.31
E_{LUMO}/eV	−3.19	−3.45
C−X−C/°[b]	121.6	120.1
N−B−N/°[c]	110.1	108.5
F−B−F/°[d]	104.8	105.1
N−C-aryl/°[e]	59	54
C−X/Å	1.389	1.332
N−B/Å	1.564	1.570
X−B/Å[f]	3.031	3.029
B−F/Å	1.380	1.377
C_1-C_7/Å[g]	5.921	5.696

[a]See Supporting Information for clarification of the structural features. [b]Angle around the meso-site. [c]Angle around the boron atom. [d]Angle around the F−B−F unit. [e]Dihedral angle between the dipyrrin unit and the appended aryl ring. [f]Distance between the *meso*-atom (C or N) and the boron atom. [g]Distance between the methyl C atoms appended at the 1,7-positions.

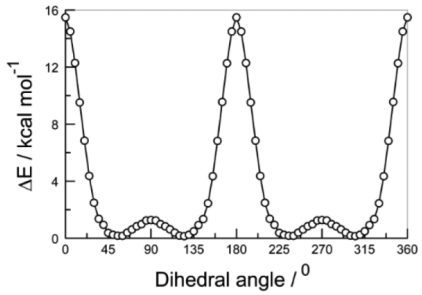

Figure 5. Effect of dihedral angle on the total energy calculated for ground-state BOD in a solvent reservoir with dielectric constant equal to 10.

angles are close to zero, are known[44] to absorb and emit at correspondingly lower energies. Also, it is well documented[45−47] that the HOMO−LUMO energy gap is sensitive to the dihedral angle for related dyes, and this situation was found to hold true for BOD (Figure 6). For the energy-minimized geometry, the computed HOMO−LUMO energy gap is 2.27 eV, corresponding to an optical transition of 546 nm. This is remarkably close to the observed value. It was noted that varying the dihedral angle had somewhat more effect on the HOMO energy than on the LUMO energy (Figure 6), again a feature that has been recognized for other dyes with rotatable aryl appendages.[48,49]

The energy-minimized structure calculated for aza-BOD (see Supporting Information) also indicates a planar dipyrrin unit but with a smaller bite angle around the aza-N atom. Insertion of the aza-N leads to a reduction in the overall length of the dipyrrin upper rim. This latter effect can be seen by comparing the distances between the carbon atoms (as methyl groups)

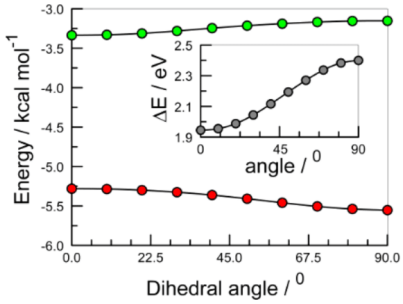

Figure 6. Effect of dihedral angle on the calculated energies of the LUMO (green points) and HOMO (red points) for BOD. The inset shows the calculated HOMO−LUMO energy gap (in units of eV) as a function of the same dihedral angle range.

attached to the C1 and C7 atoms, the distance being reduced from 5.92 Å for BOD to only 5.70 Å for aza-BOD (Table 2). The geometry around the boron atom is similar in both cases but with an increased N−B−N angle for BOD. With aza-BOD, the mean dihedral angle for the 3,5-aryl rings is marginally smaller than found for BOD, but significantly reduced barriers for ring rotation (E_0 = 11.2 kcal/mol; E_{90} = 0.70 kcal/mol) are apparent (Figure 7). This latter effect is a consequence of the

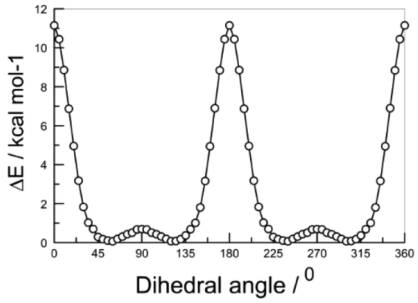

Figure 7. Effect of the dihedral angle on the total energy calculated for aza-BOD in a solvent reservoir with dielectric constant equal to 10.

slight but important geometry changes imposed on the 6-membered ring by replacing CH with N. The larger C−X−C and N−B−N angles seen for BOD serve to stretch the long molecular axis, and this, in turn, affects the dihedral angle and the ease of rotation of the aryl rings. For the planar structure, the F−H distances are elongated relative to BOD, with values of 1.787 and 1.897 Å, but again the dipyrrin unit has to distort to accommodate this geometry.

It is instructive to note that the 4-methoxy substituent makes a minor contribution to the disparity in rotational barriers noted between BOD and aza-BOD. Thus, the corresponding aza-BODIPY lacking this substituent exhibits E_0 and E_{90} values, respectively, of 12.6 and 0.90 kcal/mol. There is a similar, although minor, effect on the mean dihedral angle since that for the unsubstituted aza-BODIPY is slightly higher, at a value of 56°, than found for aza-BOD (Table 2). There is no obvious single structural feature that accounts for the effect of the 4-

DOI: 10.1021/acs.jpca.6b01278
J. Phys. Chem. A 2016, 120, 2537−2546

methoxy substituent, perhaps indicating the importance of an electronic effect.[50,51] At the energy-minimized geometry, the aza-N atom has a significant effect on the energies of both the LUMO and the HOMO (Table 2). The HOMO−LUMO energy gap is reduced dramatically to 1.86 eV, which corresponds to an optical transition of 665 nm. Again, this is remarkably close to the experimental value. Furthermore, it becomes clear that the red-shifted absorption and fluorescence maxima are well explained in terms of the effect of the aza-N atom on the HOMO and LUMO energies. A small contribution toward this generic effect can be attributed to the fact that the aza-N atom reduces the dihedral angle for the aryl rings from 59 to 54°. Thus, the relationship between dihedral angle and the energies of the HOMO and LUMO is illustrated by way of Figure 8. Here, it can be deduced that the effect of increased planarity noted for aza-BOD corresponds to a red shift of ca. 10 nm.

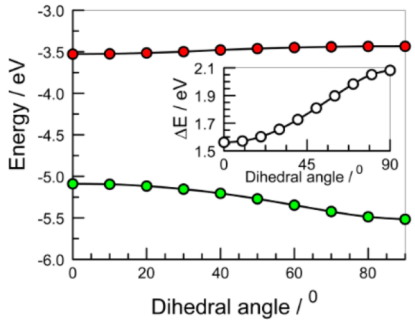

Figure 8. Effect of dihedral angle on the calculated energies of the LUMO (green points) and HOMO (red points) for aza-BOD. The inset shows the calculated HOMO−LUMO energy gap (in units of eV) as a function of the same dihedral angle range.

It is also apparent that the angular effect on the HOMO energy is greatly enhanced for aza-BOD compared to BOD while the LUMO energy varies with dihedral angle in a similar fashion for both compounds. It is important to establish that this effect is not a direct consequence of the 4-methoxy substituent. To this aim, identical calculations were performed for the aza-BODIPY lacking these substituents. Here, the energies of the LUMO and HOMO at the energy-minimized geometry were found to be −3.52 and −5.45 eV, respectively. The HOMO−LUMO energy gap (ΔE = 1.93 eV) corresponds to an optical transition of 643 nm. Thus, the 4-methoxy groups contribute a red shift of around 22 nm, which is quite significant. The effect of the dihedral angle (Figure 8) on the HOMO and LUMO energies follows the pattern established for BOD, with the effect on the HOMO energy being almost twice that on the LUMO energy over a 90° variation.

The quantum chemical calculations indicate that the HOMO and LUMO electronic distributions, illustrated conveniently in the form of Kohn−Sham contour plots,[52] for BOD are centered mainly on the BODIPY nucleus. A fraction of the overall distribution is off-loaded to the appended aryl rings for the energy-minimized configuration (Figure 9). It is useful to note that the bridgehead methine-C site attracts considerable electron density at the LUMO but not at the HOMO.

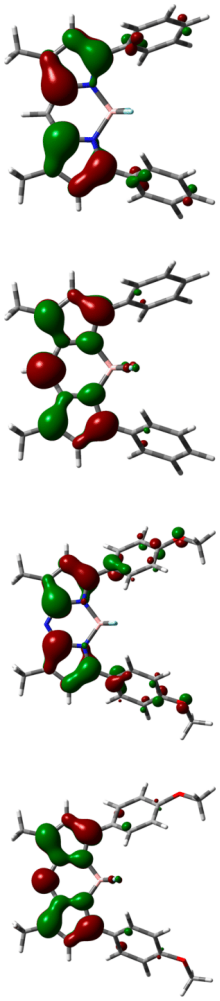

Figure 9. Kohn−Sham distributions for (running down the page from top to bottom) BOD-HOMO, BOD-LUMO, aza-BOD-HOMO and aza-BOD-LUMO as an isodensity of 0.02.

Comparable Kohn−Sham plots are found for aza-BOD, again there is off-loading of electronic distribution onto the appended aryl rings but most of the relevant electron density lies on the dipyrrin unit at both LUMO and HOMO (Figure 9). The aza-N atom is heavily involved in the composition of the LUMO but not the HOMO. As such, the nature of the *meso*-site has less influence on the energy of the HOMO (E_{HOMO}) than on that of the LUMO (Table 2). In contrast, the 4-methoxy substituents lower E_{HOMO} but have little effect on E_{LUMO}; recall that the dihedral angle primarily affects E_{HOMO}. For example, at a fixed dihedral angle of 70°, the presence of two 4-methoxy

DOI: 10.1021/acs.jpca.6b01278
J. Phys. Chem. A 2016, 120, 2537−2546

groups raises the LUMO energy by 30 meV while lowering the HOMO energy by 105 meV. This finding indicates that fine-tuning of the orbital energies might be accomplished by consideration of different substituents.

It would be useful to be able to confirm the trends in the computed HOMO and LUMO energies by a direct experimental study, such as cyclic voltammetry. Unfortunately, this was not possible because some of the electrochemical processes are irreversible. Thus, BOD undergoes a reversible, one-electron oxidation step with a half-wave potential of 1.11 V vs SCE. The corresponding one-electron reduction step is electrochemically irreversible in CH_2Cl_2 and shows a peak potential of −0.98 V vs SCE. For aza-BOD under identical conditions, one-electron reduction is electrochemically reversible, occurring with a half-wave potential of −1.00 V vs SCE, but oxidation shows an irreversible, two-electron step.

On the basis of TD-DFT calculations, we conclude that the torsional potential energy surfaces for the triplet excited state are similar to those derived for the corresponding ground states. For the S_1 surface, the aryl rings are more planar with the dipyrrin unit by ca. 5° and there are slight changes in geometry around the *meso*-site (see Supporting Information). The net result is that, at room temperature (k_BT = 208 cm^{-1}), an exciton at the S_1 level can sample a wide variance in dihedral angle for aza-BOD, with a high fraction being able to traverse the barrier (E_{90} = 245 cm^{-1}) for reaching the perpendicular geometry. Because of the higher barrier (E_{90} = 455 cm^{-1}), the S_1 exciton for BOD is less likely to deviate from the lowest-energy minimum. When allied to simple harmonic motion principles, this realization could explain the observation that, whereas aza-BOD undergoes a red shift at 77 K, BOD exhibits a small blue shift at this temperature.

Finally, we draw attention to the observation that the aza-N atom serves to decrease the S_1−T_1 energy gap, an important feature in terms of designing new sensitizers for PDT, thermally activated delayed fluorescence, and singlet fission. There is, in fact, some precedence for a similar effect with other compounds. For example, phosphorescence from *N*,*N*′-diazapyrenium dication occurs some 15 nm to the blue compared[53] to pyrene while the S_0−T_1 absorption transition computed[54] zinc(II) tetraazaporphyrin lies 0.07 eV to the blue of that calculated for zinc(II) porphyrin. The S_1−T_1 energy gap corresponds to twice the electron exchange energy,[55] which itself is set[56] by the extent of HOMO−LUMO spatial separation and the mutual overlap. Indeed, a higher overlap of HOMO and LUMO and a smaller spatial separation lead to an increase in the S_1−T_1 energy gap. By directing a substantial fraction of the HOMO, but not the LUMO, onto the peripheral aryl rings, the aza-N atom provides for lower overlap and increased spatial separation of the HOMO and LUMO. In our case, this is a qualitative observation, essentially made by comparing the LUMO and HOMO orbital distributions for the ground state, and there are few means by which to quantify the HOMO−LUMO overlap and degree of separation. In fact, the lack of effective tools for this task is considered to be a key obstacle in terms of developing computational approaches to the design of organic compounds exhibiting optimal yields of thermally activated delayed fluorescence. A few attempts,[57] notably using transition density cube methodology, are being considered but have not yet reached maturity. Although we lack quantitative information on the HOMO−LUMO separation (Figure 9), it seems highly likely that this effect is an important contributor for the decrease in the S_1−T_1 energy gap reported for aza-BOD.

■ CONCLUDING REMARKS

This work has provided a logical explanation for the photophysical properties derived for aza-BOD with respect to BOD. Unfortunately, there are minor but significant perturbations associated with the 4-methoxy substituents present in aza-BOD but not BOD. These groups extend the red-shifted absorption and fluorescence maxima and exert a small influence on the dihedral angle extended between dipyrrin and aryl groups. Our results indicate that the red shift arises from a combination of an electronic effect imposed by the electronegative aza-N atom on the energy of the LUMO and greater involvement of the aryl rings in determining the magnitude of the HOMO−LUMO energy gap. It seems reasonable to suppose that this energy gap could be increased further by optimizing the electronic nature of any substituent on the aryl ring.

One notable result is that the aza-N atom affects the S_1−T_1 energy gap without promoting triplet formation. Indeed, aza-BOD is highly fluorescent but more susceptible to photochemical degradation than is the conventional BODIPY chromophore. A further concern raised with aza-BOD is the propensity to attach hydrogen-bond donors at the *meso*-N atom. The resultant N−H bond catalyzes nonradiative deactivation of the S_1 state, in accordance with the Englman−Jortner energy-gap law.[58] This particular problem might be overcome by positioning bulky groups at the 1,7-positions, but this strategy adds further complications for the synthesis of new derivatives. Nonetheless, aza-BODIPY dyes look to be attractive candidates where a small dye is required to emit in the red region. This realization has led to the discovery[59] that water-soluble analogues of aza-BODIPY possess useful applications in the field of fluorescence microscopy.

■ EXPERIMENTAL DETAILS

Synthetic details for the two target compounds have been reported previously.[22,26] Samples of these compounds were supplied by Dr. M. J. Hall (Newcastle University) and Dr. R. Ziessel (ECPM-Strasbourg). Solvents were spectroscopic grade (Sigma-Aldrich Ltd.) and were checked for fluorescent impurities before use. Absorption spectra were recorded with a Hitachi U3310 spectrophotometer, and fluorescence spectra were recorded with a Horiba Fluorolog Tau-3 spectrometer. It was confirmed that aza-BOD follows Beer's law over a wide concentration range (see Supporting Information), most notably over the full range of concentrations used for the various spectroscopic studies. Excited singlet state lifetimes were recorded with a PTI EasyLife single-photon counting instrument equipped with short-duration laser diodes as excitation source. Fluorescence quantum yields were measured relative to free-base *meso*-tetraphenylporphyrin (φ_F = 0.12 in *N*,*N*-dimethylformamide)[60] using optically dilute solutions (absorbance set to be less than 0.1 at excitation wavelength) at room temperature. Instrument performance was verified by way of checking the lamp excitation spectrum scan and a diagnostic water Raman spectrum.

Phosphorescence was recorded with a Hitachi F-4500 spectrophotometer equipped with an optical Dewar operated at 77 K. Transient differential absorption spectra were recorded with an Applied Photophysics Ltd. LKS-70 using laser

DOI: 10.1021/acs.jpca.6b01278
J. Phys. Chem. A 2016, 120, 2537−2546

excitation (fwhm = 5 ns) at 610 nm. The solution of aza-BOD was deaerated by purging with dry N_2. Triplet lifetimes were determined at fixed wavelength by averaging at least 10 individual decay records. Anisotropy measurements were made with the fluorophore dissolved in glycerol at a series of temperatures using the Fluorolog Tau-3 instrument equipped with high-grade autopolarizers. See ref 39 for further details on the method.

Photochemical bleaching studies were made using a JCC Lighting Products IP66 floodlight operating at 400 W at a distance of 85 cm to the sample. The solute was dissolved in spectroscopic grade *N*,*N*-dimethylformamide and deaerated by purging with dry N_2. The sample was contained in a quartz cuvette and positioned in front of the lamp. A glass cutoff filter was inserted before the sample cell to eliminate heat and to prevent illumination by near-UV light. Absorption spectra were recorded at frequent intervals in order to monitor the course of reaction. The experiment was repeated several times, including samples that had not been deaerated.

Quantum chemical calculations were made using commercial software. Preliminary studies were made with AMPAC 10[61] using the PM6 semiempirical method[62] with the COSMO solvation model.[63] This method was used to generate input structures for subsequent DFT calculations, carried out with TURBOMOLE V7.0.[64] Geometry optimizations on ground-state structures were achieved using density functional theory with the CAM-B3LYP functional[65] and the cc-pVTZ basis set.[66] To model the effects of solvent on the minimized geometries, which were rather small, reoptimization was performed using the polarizable continuum model (IEF-PCM)[67] and universal force field atomic radii with parameters set for a dielectric constant of 10. Results were in reasonable agreement with the comprehensive studies reported[68] by Momeni and Brown on a series of aryl substituted aza-BODIPY dyes. Rotational barriers for the 3,5-aryl groups were computed with the 6-311++G(3df,2pd) basis set.[69] Benchmark studies were made using 1,1′-bi-2-naphthol as a model compound[70] in order to ensure comparability with the literature. Eigenvalues for the HOMO and LUMO, and the subsequent HOMO−LUMO energy gap, were computed at the B3LYP level with the 6-31G(d) basis set.

Excitation energies were calculated by time-dependent density functional theory (TD-DFT), as has been applied to several BODIPY dyes by other authors.[68,71,72] Again, the CAM-B3LYP functional was used. Tight convergence critera (e.g., maximum displacement of 6×10^{-7} and RMS displacement of 6×10^{-5}) were applied to both ground and excited state calculations. Additional calculations for the excited-state geometries were made with configuration interaction determined using single excitations,[73] including perturbative corrections for double excitations.[74]

■ ASSOCIATED CONTENT

Supporting Information

The Supporting Information is available free of charge on the ACS Publications website at DOI: 10.1021/acs.jpca.6b01278.

Molecular modeling details, steady-state photobleaching plots, temperature-dependent fluorescence anisotropy measurements, plots showing emission spectra reconstruction using fitted Gaussian peaks, and a Beers law plot for aza-BOD (PDF)

■ AUTHOR INFORMATION

Corresponding Author

*E-mail: Anthony.harriman@ncl.ac.uk. Tel: +44191 2088660.

Notes

The authors declare no competing financial interest.

■ ACKNOWLEDGMENTS

We thank Newcastle University for financial support, including a research scholarship for J.K.G.K. We also gratefully acknowledge the gifts of samples of BOD and aza-BOD from Dr. Raymond Ziessel and Dr. Michael J. Hall, respectively.

■ REFERENCES

(1) Yoon, S.; Miller, E. W.; He, Q.; Do, P. H.; Chang, C. J. A Bright and Specific Fluorescent Sensor for Mercury in Water, Cells, and Tissue. *Angew. Chem., Int. Ed.* **2007**, *46*, 6658−6661.

(2) Waggoner, A. Fluorescent Labels for Proteomics and Genomics. *Curr. Opin. Chem. Biol.* **2006**, *10*, 62−66.

(3) Schmued, L. C.; Hopkins, K. J.; Fluoro-Jade, B. A High Affinity Fluorescent Marker for the Localization of Neuronal Degeneration. *Brain Res.* **2000**, *874*, 123−130.

(4) Skehan, P.; Storeng, R.; Scudiero, D.; Monks, A.; McMahon, J.; Vistica, D.; Warren, J. T.; Bokesch, H.; Kenney, S.; Boyd, M. R. New Colorimetric Cytotoxicity Assay for Anticancer-Drug Screening. *J. Natl. Cancer Inst.* **1990**, *82*, 1107−1112.

(5) Singer, V. L.; Jones, L. J.; Yue, S. T.; Haugland, R. P. Characterization of PicoGreen Reagent and Development of a Fluorescence-based Solution Assay for Double-Stranded DNA Quantitation. *Anal. Biochem.* **1997**, *249*, 228−238.

(6) Ricchelli, F. Photophysical Properties of Porphyrins in Biological Membranes. *J. Photochem. Photobiol., B* **1995**, *29*, 109−118.

(7) Levitus, M.; Ranjit, S. Cyanine Dyes in Biophysical Research: The Photophysics of Polymethine Fluorescent Dyes in Biomolecular Environments. *Q. Rev. Biophys.* **2011**, *44*, 123−151.

(8) Würthner, F.; Kaiser, T. E.; Saha-Möller, C. R. J-Aggregates: From Serendipitous Discovery to Supramolecular Engineering of Functional Dye Materials. *Angew. Chem., Int. Ed.* **2011**, *50*, 3376−3410.

(9) Giepmans, B. N.; Adams, S. R.; Ellisman, M. H.; Tsien, R. Y. The Fluorescent Toolbox for Assessing Protein Location and Function. *Science* **2006**, *312*, 217−224.

(10) Escobedo, J. O.; Rusin, O.; Lim, S.; Strongin, R. M. NIR Dyes for Bioimaging Applications. *Curr. Opin. Chem. Biol.* **2010**, *14*, 64−70.

(11) Huang, B.; Bates, M.; Zhuang, X. Super Resolution Fluorescence Microscopy. *Annu. Rev. Biochem.* **2009**, *78*, 993.

(12) Ulrich, G.; Ziessel, R.; Harriman, A. The Chemistry of Fluorescent BODIPY Dyes: Versatility Unsurpassed. *Angew. Chem., Int. Ed.* **2008**, *47*, 1184−1201.

(13) Loudet, A.; Burgess, K. BODIPY Dyes and Their Derivatives: Syntheses and Spectroscopic Properties. *Chem. Rev.* **2007**, *107*, 4891−4932.

(14) Boens, N.; Leen, V.; Dehaen, W. Fluorescent Indicators Based on BODIPY. *Chem. Soc. Rev.* **2012**, *41*, 1130−1172.

(15) Chen, J.; Burghart, A.; Derecskei-Kovacs, A.; Burgess, K. 4, 4-Difluoro-4-bora-3a, 4a-diaza-s-indacene (BODIPY) Dyes Modified for Extended Conjugation and Restricted Bond Rotations. *J. Org. Chem.* **2000**, *65*, 2900−2906.

(16) Bura, T.; Hablot, D.; Ziessel, R. Fluorescent Boron Dipyrromethene (BODIPY) Dyes Having Two and Four Vinyl Residues. *Tetrahedron Lett.* **2011**, *52*, 2370−2374.

(17) Hinkeldey, B.; Schmitt, A.; Jung, G. Comparative Photostability Studies of BODIPY and Fluorescein Dyes by Using Fluorescence Correlation Spectroscopy. *ChemPhysChem* **2008**, *9*, 2019−2027.

(18) Harriman, A.; Stachelek, P.; Sutter, A.; Ziessel, R. Stepwise Photoconversion of an Artificial Light-Harvesting Array Built from Extended BODIPY Units. *Photochem. Photobiol. Sci.* **2015**, *14*, 1100−1109.

DOI: 10.1021/acs.jpca.6b01278
J. Phys. Chem. A 2016, 120, 2537−2546

(19) Allik, T. H.; Hermes, R. E.; Sathyamoorthi, G.; Boyer, J. H. Spectroscopy and Laser Performance of New BF2-Complex Dyes in Solution. *Proc. SPIE* **1994**, *2115*, 240−248.
(20) Gresser, R.; Hummert, M.; Hartmann, H.; Leo, K.; Riede, M. Synthesis and Characterization of Near-Infrared Absorbing Benzannulated Aza-BODIPY Dyes. *Chem. - Eur. J.* **2011**, *17*, 2939−2947.
(21) Zhang, X.; Yu, H.; Xiao, Y. Replacing Phenyl Ring with Thiophene: an Approach to Longer Wavelength Aza-Dipyrromethene Boron Difluoride (Aza-BODIPY) Dyes. *J. Org. Chem.* **2012**, *77*, 669−673.
(22) Wu, D.; O'Shea, D. F. Synthesis and Properties of BF2−3,3′-Dimethyldiarylazadipyrromethene Near-Infrared Fluorophores. *Org. Lett.* **2013**, *15*, 3392−3395.
(23) Kamkaew, A.; Lim, S. H.; Lee, H. B.; Kiew, L. V.; Chung, L. Y.; Burgess, K. BODIPY dyes in photodynamic therapy. *Chem. Soc. Rev.* **2013**, *42*, 77−88.
(24) Singh-Rachford, T. N.; Haefele, A.; Ziessel, R.; Castellano, F. N. Boron Dipyrromethene Chromophores: Next Generation Triplet Acceptors/Annihilators for Low Power Upconversion Schemes. *J. Am. Chem. Soc.* **2008**, *130*, 16164−16165.
(25) Sauerwein, B.; Schuster, G. B. External Iodine Atoms Influence Over the Intersystem Crossing Rate of Cyanine Iodide Ion Pair in Benzene Solution. *J. Phys. Chem.* **1991**, *95*, 1903−1906.
(26) Bahaidarah, E.; Harriman, A.; Stachelek, P.; Rihn, S.; Heyer, E.; Ziessel, R. Fluorescent Molecular Rotors Based on the BODIPY Motif: Effect of Remote Substituents. *Photochem. Photobiol. Sci.* **2014**, *13*, 1397−1401.
(27) Kuimova, M. K.; Yahioglu, G.; Levitt, J. A.; Suhling, K. Molecular Rotor Measures Viscosity of Live Cells via Fluorescence Lifetime Imaging. *J. Am. Chem. Soc.* **2008**, *130*, 6672−6673.
(28) Burghart, A.; Kim, H.; Welch, M. B.; Thoresen, L. H.; Reibenspies, J.; Burgess, K.; Bergström, F.; Johansson, L. B. Å. 3, 5-Diaryl-4,4-difluoro-4-bora-3a, 4a-diaza-s-indacene (BODIPY) Dyes: Synthesis, Spectroscopic, Electrochemical and Structural Properties. *J. Org. Chem.* **1999**, *64*, 7813−7819.
(29) Valeur, B.; Berberan-Santos, M. N. *Molecular Fluorescence: Principles and Applications*; John Wiley & Sons: Paris, 2012.
(30) Asada, K.; Kobayashi, T.; Naito, H. Temperature Dependence of Photoluminescence in Polyfluorene Thin Films—Huang−Rhys Factors of as-Coated, Annealed and Crystallized Thin Films. *Thin Solid Films* **2006**, *499*, 192−195.
(31) Lavrentiev, M. Y.; Barford, W. Electron−Phonon Interactions in Poly (para-phenylene) Oligomers. *J. Chem. Phys.* **1999**, *111*, 11177−11182.
(32) Bässler, H.; Schweitzer, B. Site-Selective Fluorescence Spectroscopy of Conjugated Polymers and Oligomers. *Acc. Chem. Res.* **1999**, *32*, 173−182.
(33) Karabunarliev, S.; Baumgarten, M.; Bittner, E. R.; Müllen, K. Rigorous Franck−Condon Absorption and Emission Spectra of Conjugated Oligomers from Quantum Chemistry. *J. Chem. Phys.* **2000**, *113*, 11372−11381.
(34) Strouse, G. F.; Schoonover, J. R.; Duesing, R.; Boyde, S.; Jones, W. E. J.; Meyer, T. J. Influence of Electronic Delocalization in Metal-to-Ligand Charge Transfer Excited States. *Inorg. Chem.* **1995**, *34*, 473−487.
(35) Strickler, S. J.; Berg, R. A. Relationship between Absorption Intensity and Fluorescence Lifetime of Molecules. *J. Chem. Phys.* **1962**, *37*, 814−822.
(36) Zhao, G. J.; Han, K. L. Hydrogen bonding in the electronic excited state. *Acc. Chem. Res.* **2012**, *45*, 404−413.
(37) Shushkevich, I. K.; Pershukevich, P. P.; Stupak, A. P.; Solov'ev, K. N. Influence of a Solvent on the Quantum Yield and Duration of the Fluorescence of Tetraazaporphin. *J. Appl. Spectrosc.* **2005**, *72*, 767−770.
(38) Zhao, W.; Carreira, E. M. Conformationally Restricted Aza-BODIPY: A Highly Fluorescent, Stable, Near-Infrared-Absorbing Dye. *Angew. Chem., Int. Ed.* **2005**, *44*, 1677−1679.
(39) Dutt, G. B.; Krishna, G. R. Temperature-Dependent Rotational Relaxation of Nonpolar Probes in Mono and Diols: Size Effects versus Hydrogen Bonding. *J. Chem. Phys.* **2000**, *112*, 4676−4682.
(40) Lakowicz, J. R. *Principles of Fluorescence Spectroscopy*; Springer Science & Business Media: New York, 2006.
(41) Koziar, J. C.; Cowan, D. O. Photochemical Heavy-Atom Effects. *Acc. Chem. Res.* **1978**, *11*, 334−341.
(42) Ziessel, R.; Ulrich, G.; Haefele, A.; Harriman, A. An Artificial Light-Harvesting Array Constructed from Multiple Bodipy Dyes. *J. Am. Chem. Soc.* **2013**, *135*, 11330−11344.
(43) Kim, H.; Burghart, A.; Welch, M. B.; Reibenspies, J.; Burgess, K. Synthesis and Spectroscopic Properties of a New 4-Bora-3a, 4a-diaza-s-indacene (BODIPY) Dye. *Chem. Commun.* **1999**, 1889−1890.
(44) Loudet, A.; Bandichhor, R.; Burgess, K.; Palma, A.; McDonnell, S. O.; Hall, M. J.; O'Shea, D. F. B, O-Chelated Azadipyrromethenes as Near-IR Probes. *Org. Lett.* **2008**, *10*, 4771−4774.
(45) Brownell, L. V.; Robins, K. A.; Jeong, Y.; Lee, Y.; Lee, D. C. Highly Systematic and Efficient HOMO-LUMO Energy Gap Control of Thiophene-Pyrazine Acenes. *J. Phys. Chem. C* **2013**, *117*, 25236−25247.
(46) Omomo, S.; Furukawa, K.; Nakano, H.; Matano, Y. Comparison of Electronic Effects of Beta-Aryl Substituents on Optical and Electrochemical Properties of 5,15-Diazaporphyrin pi-systems. *J. Porphyrins Phthalocyanines* **2015**, *19*, 775−785.
(47) Bura, T.; Retailleau, P.; Ulrich, G.; Ziessel, R. Highly Substituted BODIPY Dyes with Spectroscopic Features Sensitive to the Environment. *J. Org. Chem.* **2011**, *76*, 1109−1117.
(48) Schmidt, E. Y.; Zorina, N. V.; Dvorko, M. Y.; Protsuk, N. I.; Belyaeva, K. V.; Clavier, G.; Méallet-Renault, R.; Vu, T. T.; Mikhaleva, A. I.; Trofimov, B. A. A General Synthetic Strategy for the Design of New BODIPY Fluorophores Based on Pyrroles with Polycondensed Aromatic and Metallocene Substituents. *Chem. - Eur. J.* **2011**, *17*, 3069−3073.
(49) Brownell, L. V.; Robins, K. A.; Jeong, Y.; Lee, Y.; Lee, D. C. Highly Systematic and Efficient HOMO−LUMO Energy Gap Control of Thiophene-Pyrazine-Acenes. *J. Phys. Chem. C* **2013**, *117*, 25236−25247.
(50) Dumas-Verdes, C.; Miomandre, F.; Lépicier, E.; Galangau, O.; Vu, T. T.; Clavier, G.; Méallet-Renault, R.; Audebert, P. BODIPY-Tetraazine Multichromophoric Derivatives. *Eur. J. Org. Chem.* **2010**, *2010* (13), 2525−2535.
(51) Zatsikha, Y. V.; Yakubovskyi, V. P.; Shandura, M. P.; Dubey, I. Y.; Kovtun, Y. P. An Efficient Method of Chemical Modification of BODIPY Core. *Tetrahedron* **2013**, *69*, 2233−2238.
(52) Baerends, E. J.; Ricciardi, G.; Rosa, A.; van Gisbergen, S. J. A. A DFT/TDDFT Interpretation of the Ground and Excited States of Porphyrin and Porphyrazine. *Coord. Chem. Rev.* **2002**, *230*, 5−27.
(53) Brun, A. M.; Harriman, A. Photochemistry of Intercalated Quaternary Diazaaromatic Salts. *J. Am. Chem. Soc.* **1991**, *113*, 8153−8159.
(54) Nguyen, K. A.; Pachter, R. Jahn-Teller Triplet Excited State Structures and Spectra of Zinc Complexes of Porphyrin and Phthalocyanine: A Density Functional Theory Study. *J. Chem. Phys.* **2003**, *118*, 5802−5810.
(55) Karsten, B. P.; Viani, L.; Gierschner, J.; Cornil, J.; Janssen, R. A. J. An Oligomer Study on Small Band Gap Polymers. *J. Phys. Chem. A* **2008**, *112*, 10764−10773.
(56) Wasserberg, D.; Marsal, P.; Meskers, S. C. J.; Janssen, R. A. J.; Beljonne, D. Phosphorescence and Triplet State Energies of Oligothiophenes. *J. Phys. Chem. B* **2005**, *109*, 4410−4415.
(57) Chen, T.; Zheng, L.; Yuan, J.; An, Z.; Chen, R.; Tao, Y.; Li, H.; Xie, X.; Huang, W. Understanding the Control of Singlet-Triplet Splitting for Organic Exciton Manipulating: A Combined Theoretical and Experimental Approach. *Sci. Rep.* **2015**, *5*, 10923.
(58) Englman, R.; Jortner, J. The Energy Gap Law for Radiationless Transitions in Large Molecules. *Mol. Phys.* **1970**, *18*, 145−164.
(59) Collado, D.; Vida, Y.; Najera, F.; Perez-Inestrosa, E. PEGylated aza-BODIPY Derivatives as NIR Probes for Cellular Imaging. *RSC Adv.* **2014**, *4*, 2306−2309.

DOI: 10.1021/acs.jpca.6b01278
J. Phys. Chem. A 2016, 120, 2537−2546

(60) Owens, J. W.; Smith, R.; Robinson, R.; Robins, M. Photophysical Properties of Porphyrins, Phthalocyanines and Benzochlorins. *Inorg. Chim. Acta* **1998**, *279*, 226−231.
(61) *AMPAC 10*, 1992−2013; Semichem, Inc.: 12456 W 62nd Terrace - Suite D, Shawnee, KS 66216.
(62) Stewart, J. J. P. Optimization of Parameters for Semi-empirical Methods V: Modification of NDDO Approximations and Application to 70 Elements. *J. Mol. Model.* **2007**, *13*, 1173−1213.
(63) Klamt, A. Calculation of UV/VIS Spectra in Solution. *J. Phys. Chem.* **1996**, *100*, 3349−3353.
(64) TURBOMOLE V7.0 2015, A development of University of Karlsruhe and Forschungszentrum Karlsruhe GmbH, 1989−2007, TURBOMOLE GmbH, since 2007; available from http://www.turbomole.com.
(65) Yanai, T.; Tew, D. P.; Handy, N. C. A New Hybrid Exchange-Correlation Functional Using the Coulomb-Attenuating Method (CAM-B3LYP). *Chem. Phys. Lett.* **2004**, *393*, 51−57.
(66) Woon, D. E.; Dunning, T. H., Jr. Gaussian-basis Sets for Use in Correlated Molecular Calculations. III. The Atoms Aluminum Through Argon. *J. Chem. Phys.* **1993**, *98*, 1358−1371.
(67) Cossi, M.; Scalmani, G.; Rega, N.; Barone, V. New Developments in the Polarizable Continuum Model for Quantum Mechanical and Classical Calculations on Molecules in Solution. *J. Chem. Phys.* **2002**, *117*, 43−54.
(68) Momeni, M. R.; Brown, A. Why Do TD-DFT Excitation Energies of BODIPY/aza-BODIPY Families Largely Deviate from Experiment? Answers from Electron Correlated and Multireference Methods. *J. Chem. Theory Comput.* **2015**, *11*, 2619−2632.
(69) Kieninger, M.; Cachau, R. E.; Oberhammer, H.; Ventura, O. N. Comparison of Large Basis Set DFT and MP2 Calculations in the Study of the Barrier for Internal Rotation of 2,3,5,6-Tetrafluoroanisole. *Int. J. Quantum Chem.* **2007**, *107*, 403−417.
(70) Sahnoun, R.; Koseki, S.; Fujimura, Y. Theoretical Investigation of 1,1'-Bi-2-naphthol Isomerization. *J. Mol. Struct.* **2005**, *735*, 315−324.
(71) Chibani, S.; Laurent, A. D.; Le Guennic, B.; Jacquemin, D. Improving the Accuracy of Excited-State Simulations of BODIPY and aza-BODIPY Dyes with a Joint SOS-CIS(D) and TD-DFT Approach. *J. Chem. Theory Comput.* **2014**, *10*, 4574−4582.
(72) Petrushenko, I.; Petrushenko, K. Effect of meso-Substituents on the Electronic Transitions of BODIPY Dyes. *Spectrochim. Acta, Part A* **2015**, *138*, 623−627.
(73) Foresman, J. B.; Head-Gordon, M.; Pople, J. A.; Frisch, M. J. Toward a Systematic Molecular-Orbital Theory for Excited States. *J. Phys. Chem.* **1992**, *96*, 135−149.
(74) Head-Gordon, M.; Rico, R. J.; Oumi, M.; Lee, T. J. A Doubles Correction to Electronic Excited States from Configuration-Interaction in the Space of Single Substitutions. *Chem. Phys. Lett.* **1994**, *219*, 21−29.

DOI: 10.1021/acs.jpca.6b01278
J. Phys. Chem. A 2016, 120, 2537−2546

Photochemical & Photobiological Sciences

PAPER

View Article Online
View Journal

Cite this: DOI: 10.1039/c7pp00333a

Cyanine dyes as ratiometric fluorescence standards for the far-red spectral region†

Joshua K. G. Karlsson, [a] Owen J. Woodford,[a] Heinz Mustroph[b] and Anthony Harriman *[a]

Received 5th September 2017,
Accepted 4th December 2017
DOI: 10.1039/c7pp00333a
rsc.li/pps

Most quantitative fluorescence measurements report emission quantum yields by referring the integrated fluorescence profile to that of a well-known standard compound measured under carefully controlled conditions. This simple protocol works well provided an appropriate standard fluorophore is available and that the experimental conditions used for reference and unknown are closely comparable. Commercial fluorescence spectrophotometers tend to perform very well at wavelengths between 250 and 650 nm but are less responsive at longer wavelengths. There are no recognized emission standards for the far-red region. We now report fluorescence quantum yields for a series of commercially available cyanine dyes in methanol solution at room temperature. The compounds are selected to span the wavelength region from 600 to 850 nm, with absolute emission quantum yields being determined by thermal blooming spectrometry. Calibration of the instrument is made by reference to aluminium(III) phthalocyanine tetrasulfonate and aza-BODIPY in methanol.

Introduction

There appears to be an almost insatiable appetite for new fluorescent dyes. Indeed, a bewildering variety of applications has been found for such materials, sometimes by serendipity but more often by design. In characterizing new fluorescent dyes, the minimum information that must be provided is the fluorescence quantum yield under carefully specified conditions. This value, together with absorption and emission spectral profiles, can be used by other researchers seeking components for yet more applications. Of course, the excited-state lifetime and the extent of any environmental effects on this parameter and on the fluorescence yield add to the value of the basic information.[1] As applications become more diverse, so does the awareness that compounds absorbing and emitting in the far-red region are of prime importance. This is especially so for bio-labels[2] and fluorescent probes[3] intended for biochemical or medicinal purposes, as soft tissues are best permeated by light of wavelength greater than 650 nm. In turn, this realization means that there is a growing need to measure emission quantum yields at relatively long wavelength where many commercial fluorescence spectrophotometers display limited sensitivity. There are few standard compounds[4] with well documented emission properties, perhaps Indocyanine Green is the best known example,[5] which is a further limitation for the determination of fluorescence yields *via* the comparative method. Other approaches, notably the use of an integrating sphere,[6] are possible but the necessary equipment is not always at hand.

In searching for likely emitters that could function as fluorescence standards, it has to be recognized that no single compound will suffice for the far-red region: we take the latter to cover the range from 650 to 900 nm. This translates to the need for a family of dyes of comparable chemical structures and physiological properties but differing conjugation lengths. Any standard compound must be commercially available in a pure form and soluble in common organic solvents. Ideally, the fluorescence quantum yield should be around 0.25 so that comparison can be made with strong and weak fluorophores.[4] Secondary requisites include good stability and resistance to aggregation. With these limitations in mind, we have identified the family of cyanine dyes as strong contenders. This particular family includes fluorophores currently used in super-resolution microscopy.[7]

We now report the absolute fluorescence quantum yields, measured under highly comparable conditions, for a small set of cyanine dyes. These dyes cover the appropriate spectral range and show moderate emission yields in methanol solution at ambient temperature. To measure the quantum yields, we have used the photo-initiated thermal blooming protocol

[a]Molecular Photonics Laboratory, School of Chemistry, Bedson Building, Newcastle University, Newcastle upon Tyne, NE1 7RU, UK. E-mail: anthony.harriman@ncl.ac.uk
[b]FEW Chemicals GmbH, Ortsteil Wolfen, Technikumstr. 1, 06766 Bitterfeld-Wolfen, Germany

† Electronic supplementary information (ESI) available: Individual molecular formulae, absorption/fluorescence spectra and Beer–Lambert plots, analytical data and additional details. See DOI: 10.1039/c7pp00333a

introduced many years ago by Magde and co-workers,[8] but largely overlooked in the meantime. For the series of methanol-soluble cyanine dyes, it has been possible to use a single excitation wavelength of 635 nm. This greatly simplifies the experiments. The choice of a non-emissive standard is more problematic than one might think, but eventually was solved using Brilliant Green. This dye, which is a member of the triarylmethine family, has a well characterized viscosity-dependent, radiationless channel that serves to depopulate the excited-singlet state on a rapid timescale. In a non-viscous solvent such as methanol, Brilliant Green shows no significant fluorescence at ambient temperature.[9]

Experimental section

Background

The hardware requirements for a thermal blooming (also referred to as thermal lensing) apparatus, as well as the underlying theory for determining the absolute fluorescence quantum yield, have been outlined by Magde and co-workers.[8,10,11] No commercial thermal blooming spectrometers exist, but the technique requires relatively few components, all of which are commercially available. A thermal blooming instrument must, as a minimum, have a cw laser with Gaussian mode TEM_{00} output at a wavelength appropriate for excitation of the chromophore, a suitable lens to expand the laser beam onto the detector, a digital optical shutter, a silicon photodiode detector and a digital oscilloscope for data collection. The set-up needs to be vibration-free and the laser excitation source needs to be properly screened.

For a laser beam incident on a liquid sample, the output power, P_L, will be the sum of three components according to eqn (1). Here, P_T is the transmitted laser power, P_F the emitted fluorescence, and P_{TH} describes the amount of heat released into the system by way of nonradiative decay of the excited state. The thermal blooming experiment does not record fluorescence directly, but detects the radiationless processes described by P_{TH}. The heat dissipated into the liquid solvent can be determined by accurately measuring the absorbance of the sample at the excitation wavelength and knowing the power of the excitation laser.

$$P_L = P_T + P_F + P_{TH} \quad (1)$$

In the thermal blooming experiment, fluorescence quantum yields are determined indirectly by recording the change in refractive index of the solvent as a result of brief exposure of the sample to laser excitation. It is essential that the solvent is transparent at the excitation wavelength. It is also important that, under illumination, the fluorophore does not react with the solvent, a valid assumption in the majority of cases. During excited-state decay, the combined non-radiative channels will equilibrate with the surrounding solvent by transferring excess heat. According to the nature of the solvent, heating will be manifest by a change in refractive index, which is seen as a "blooming" of the laser beam on a photodiode detector. The signal is recorded with a digital oscilloscope, and the output is analyzed in terms of eqn (2). The key variable is θ, which is a parameter directly proportional to the radiant thermal power. In eqn (2), I_0 is the initial laser beam intensity and t is time. The value t_c is a property of the solvent which characterizes thermal diffusion (related to thermal diffusivity) from the initial injection of heat to a steady-state level. Our experimental results, where methanol was the solvent of choice, tended to yield t_c values of *ca.* 55 ms, largely consistent with reports in the literature.[12]

$$I(t) = I_0\left[1 - \theta\left(1 + \frac{t_c}{2t}\right)^{-1} + \frac{1}{2}\theta^2\left(1 + \frac{t_c}{2t}\right)^{-2}\right]^{-1} \quad (2)$$

By comparing the thermal blooming data collected for a non-fluorescent standard and for the compound of interest under identical conditions, it is reasonable to associate any change in optical properties to the solvent reservoir. Experimental traces can be analyzed in terms of eqn (2) to give a value for θ. Signal averaging is applied and numerous traces are used to construct a suitable database for averaging. With values recorded for both sample S and reference R, the fluorescence quantum yield, Φ_F, can be obtained on the basis of eqn (3). Here, A is the relative number of photons absorbed at the excitation wavelength, ν_F is the mean wavenumber corresponding to the fluorescence maximum, and ν_{ex} is the excitation energy in wavenumbers.

$$\Phi_F = \left[1 - \frac{A_R}{A_S}\frac{\theta_S}{\theta_R}\right]\frac{\nu_{ex}}{\nu_F} \quad (3)$$

Methodology

The experimental set-up for the thermal blooming measurements reported here (Fig. 1) comprises an aluminum optical table, 130 cm long, with slots and mounting points for all the main components. A laser diode (Coherent 3.0 mW; 635 nm; VHK Circular Beam Visible Laser Diode) provides the excitation source. A digital beam shutter (Thorlabs SC10) controls exposure of the sample to the incident laser beam. The signal

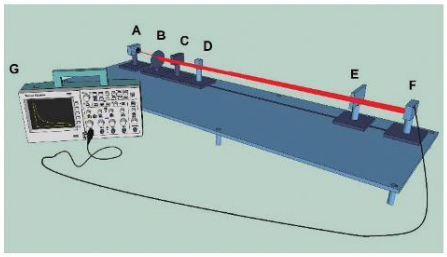

Fig. 1 Illustration of the thermal blooming apparatus used for determining fluorescence quantum yields. A. Laser, B. lens, C. optical shutter, D. sample cell, E. filter, F. detector, G. digital oscilloscope.

is monitored with a silicon photodiode detector (Thorlabs PDA100A-EC). The detector was positioned sufficiently remote from the focussing lens to ensure that the expanding beam spot was larger than the surface area of the detector. Output was recorded with a Tektronix DPO71254 digital oscilloscope. The entire instrument is housed in a light-tight chamber.

A plano-convex glass lens with a focal length of 10 cm was used to expand the laser beam. The shutter is placed between the lens and the sample. Liquid samples were measured in quartz cuvettes. The sample must be in a region where the waist of the beam is uniform through the path length. This is referred to as the Rayleigh distance and can be optimized by adjusting the distance between lens and sample until the maximum thermal blooming signal is observed.

Too much heat deposited in the solvent perturbs the thermal blooming signal due to aberrations and convection currents. In methanol, the upper limit for incident laser power before these detrimental effects become noticeable is 0.6 mW.[10] For a given excitation source, the absorbed power must be kept below this threshold, either by adjusting the sample absorbance or attenuating the laser beam. As a benchmark, our set-up used liquid samples possessing an absorbance <0.1 (*i.e.* less than 20% of the incident laser power is absorbed by the sample) in a 1 cm pathlength cuvette.

Fig. 2 shows a typical output from a thermal blooming measurement and the general agreement of eqn (2) with the raw data. The protocol for fluorescence quantum yield measurements is as follows: a non-fluorescent standard, consisting of Brilliant Green in methanol, was measured against the fluorophore of interest after carefully matching the absorbance values at 635 nm. This absorbance was maintained in the range 0.07 to 0.10. The sample was contained in the same quartz cuvette (path length 1 cm) and kept in the same orientation to avoid any error arising from manufacturing differences in the quartz surfaces. The entire optical rail was isolated from stray light. Measurements were performed by opening the optical shutter for 0.5 s periods at regular intervals once a stable baseline had been attained. The oscilloscope collected the average signal across a pre-determined number of recordings. Data sampling was at a rate of 10 000 counts per second. The photocurrent decay traces for both the standard and sample were analyzed according to eqn (2) to obtain the critical value θ. Finally, eqn (3) was used to determine the fluorescence yield. Each experiment was repeated at least 7 times. Absorption spectra were recorded with a Hitachi U-3310 spectrophotometer and fluorescence spectral measurements were made with a Horiba Fluorolog Tau-3 system.

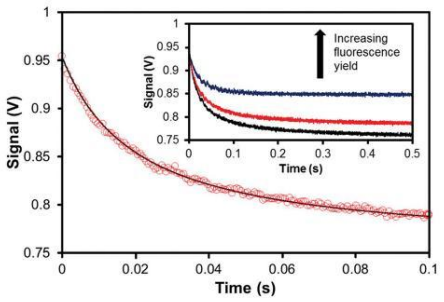

Fig. 2 Typical oscilloscope output at early times for a thermal blooming measurement with a chromophore in liquid solution. Red circles: raw data. Black line: experimental fit according to eqn (2). Inset, thermal blooming measurement followed until a steady-state equilibration has been achieved.

Errors and reproducibility

It must be emphasized that determining an absolute fluorescence quantum yield is a nontrivial task, despite advances in the underlying technology. The sources of errors in conventional fluorescence yield measurements have been well documented.[13–15] With the thermal blooming technique, there are a number of potential sources of systematic error.[8] Chief amongst these is the exact amount of laser power being transmitted through the sample. This requires an accurate measurement of the absorbance. As the fluorescence yield approaches zero, thermal blooming traces become increasingly similar to that of the non-fluorescent standard. In this situation the ratio θ_S/θ_R (eqn (3)) approaches unity and the main experimental error shifts to the measured absorbance. As such this technique is not well suited to measuring fluorescence quantum yields less than *ca.* 0.05. For very low quantum yields, minor variations in absorbance translate to major uncertainties in the recovered parameters, leading to overall errors in excess of ±5%.

Conversely, thermal blooming can largely eliminate one of the key sources of error in a typical fluorescence measurement, namely minor contamination by highly emissive impurities. This is because thermal blooming does not measure emission and insignificant contributions to the overall absorbance made by trace impurities make no difference to the overall signal. Likewise, this technique is not affected by the inner-filter effect.[16] Other pitfalls inherent to conventional fluorescence measurements, such as Raman and Rayleigh scattering, and the non-linear response of detectors and diffraction gratings can also be marginalized.

A key factor in the usefulness of the thermal blooming technique comes down to reproducibility of results. As a representative example, the fluorescence yield was measured for five samples of cy643 at different absorbance values within the range 0.05 to 0.1. Under carefully controlled conditions, the standard deviation of the recorded fluorescence yields was ±0.01 suggesting results are highly reproducible. Taking into account that the noise on a typical oscilloscope trace was found to be ±2% of the mean value, one can conclude that the accuracy of the measurement is well within ±5% for a reasonably emissive sample.

Materials

Methanol (Sigma-Aldrich) was spectroscopic grade and was used as received after confirming the absence of fluorescent

impurities. Samples of the aza-BODIPY dyes were available from a previous study.[17] Aluminium(III) phthalocyanine tetrasulfonate was a gift from Dr F. Hardy of The Procter & Gamble Co. According to elemental analyses, the sample is the tetrasulfonate derivative, although the positions of the sulfonate groups could not be determined. Samples of the cyanine dyes were obtained from FEW Chemicals GmbH and were used as received. Note NMR spectra are provided as part of the ESI.† A sample of Brilliant Green was obtained from Acros Organics and used without further purification after analysis by NMR spectroscopy. The sample displayed no significant fluorescence in methanol solution at room temperature. All other materials were obtained from Sigma-Aldrich. The molecular formulas for all compounds are provided in the ESI (Fig. S1 to S8†).

Results

Calibration

To ensure the reliability of our thermal blooming apparatus, the fluorescence quantum yield (Φ_F) of aluminium(III) phthalocyanine tetrasulfonate (AlPcS) in methanol was measured repeatedly over a four-month period. Excitation was made at 635 nm and a series of concentrations was used. The mean Φ_F value was found to be 0.55 ± 0.02 (Table 1). This can be compared with 0.51 as reported by Beeby *et al.*[18] A survey of the literature shows a general consensus for the AlPcS fluorescence yield falling between 0.51 and 0.55 in organic solvents,[19,20] but dimerization in aqueous solution or at high concentration should be considered.[21] The absorption spectrum of AlPcS (Fig. S1†) covers the wavelength range from 550 to 680 nm, with excellent absorption at the excitation wavelength. Fluorescence is readily observed in the red region (Fig. S1†). Using a conventional spectrophotometer (λ_{EX} = 610 nm), Φ_F was found to be 0.54 ± 0.05 in methanol by comparison to free-base *meso*-tetraphenylporphyrin (TPP) in *N*,*N*-dimethylformamide (Φ_F = 0.12).[19] This set of results appears to be self-consistent and thereby confirm the validity of the thermal blooming set-up. Our sample of AlPcS gave a single-exponential decay profile, with an excited-state lifetime (τ_S) of 6.6 ± 0.2 ns, when excited at 635 nm under time-correlated, single photon counting conditions (Table 1). Overall, AlPcS is a promising fluorescence standard for excitation in the 580–640 nm spectral window.

A further test of the experimental set-up was made using aza-BODIPY (aza-BOD-1) in methanol. The photophysical properties of this compound in methanol were established recently,[17] where Φ_F has a value of 0.56 and τ_S is 3.5 ns (Table 1). Thermal blooming studies in methanol gave rise to a Φ_F value of 0.58 ± 0.02 (Table 1). This level of agreement is considered to be excellent. The same Φ_F was recovered for different concentrations of aza-BODIPY and under various experimental configurations. The value, at least in methanol where the aza-nitrogen atom enters into hydrogen bonding with the solvent, is highly reproducible. Thus, aza-BODIPY seems to be a good secondary fluorescence standard for emission in the 650–730 nm window but it is not available commercially.

A second aza-BODIPY derivative was available, this differing only in terms of the peripheral substituents, but has not been reported in the literature. For this compound (aza-BOD-2) in methanol, the absorption and emission spectra closely resemble those recorded for aza-BOD-1. Conventional determination of the fluorescence yield using aza-BOD-1 as a reference gave a value of 0.33 (Table 1). The excited-state lifetime was found to be 2.3 ns, somewhat lower than that found for aza-BOD-1 under the same conditions. Thermal blooming studies allowed determination of the absolute fluorescence quantum yield for aza-BOD-2 as being 0.33 ± 0.02. This measurement is in excellent agreement with that made by ratiometric methods. It serves to emphasize the reliability of the thermal blooming technique and to extend the database of known emitters for the red region. The modest differences in fluorescence yield and lifetime found for these two aza-BODIPY emitters is explained in terms of enhanced nonradiative deactivation promoted by the O–H bond present in aza-BOD-2. This finding is precisely in line with expectations based on the Englman–Jortner energy-gap law.[22]

Table 1 Summary of fluorescence quantum yields available for the compounds used to calibrate the thermal blooming set-up[a]

Dye	Φ_F	Method	Error	τ_S[b]/ns
AlPcS	0.51	Ref. 19[c]	±0.026	6.0
	0.54	SSF[d]	±0.050	6.6
	0.55	TBS[e]	±0.016	6.6
aza-BOD-1	0.60[f]	Ref. 17	±0.030	—
	0.56	SSF	±0.028	3.5
	0.58	TBS	±0.017	3.5
aza-BOD-2	0.33	SSF	±0.017	2.3
	0.33	TBS	±0.017	2.3

[a] All measurements made in methanol at 20 °C. [b] Excited-singlet state lifetime measured by time-correlated, single photon counting. [c] Φ_F taken from the literature. [d] Φ_F measured in this work using conventional steady-state emission spectroscopy. [e] Φ_F measured in this work by thermal blooming spectrometry. [f] Literature value in ethanol.

Cyanine dyes

Cyanine dyes, which were first synthesized over a century ago and used to sensitize photographic plates, comprise an inordinately diverse family of fluorophores. With their narrow absorption and fluorescence spectral profiles, together with high oscillator strengths for the lowest-energy absorption transition, these dyes are ideal candidates for fluorescence standards for the far-red region. To this effect, a series of five cyanine dyes was selected on the basis of covering the 600–800 nm absorption range by varying the conjugation length (Fig. 3). The target dyes are soluble in methanol and free from aggregation at the concentrations appropriate for this work.

Their molecular formulas are provided in the ESI,† together with some basic spectroscopic information. For the two

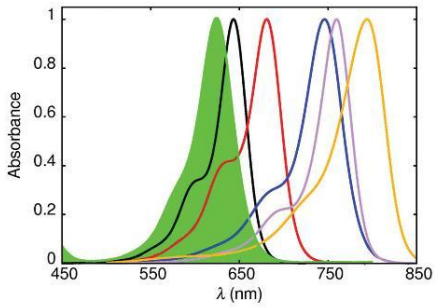

Fig. 3 Normalized absorption spectra of the cyanine dye series in methanol. The colour of the trace corresponds to the following compounds: black: cy643, red: cy681, blue: cy746, purple: cy761, orange: cy794. The trace shaded green is that of the non-fluorescent standard, Brilliant Green.

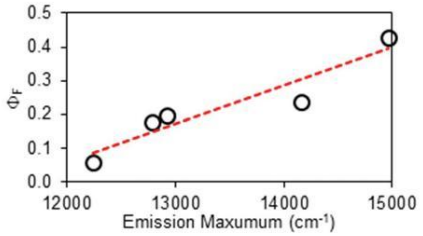

Fig. 4 Correlation between the mean fluorescence spectral maximum and the fluorescence quantum yield measured for the cyanine dyes by thermal blooming.

shorter conjugation lengths, cy643 and cy681, it was possible to determine Φ_F values by ratiometric measurements using AlPcS and free-base *meso*-tetraphenylporphyrin as a reference. The values are collected in Table 2 and serve to indicate that these compounds are relatively strong emitters.

For the remaining cyanine dyes, it was not possible to generate meaningful Φ_F values by conventional steady-state emission spectroscopy due to the lack of appropriate control compounds. Instead, the thermal blooming technique was successfully applied to this problem. Firstly, it was noted that Φ_F values measured by the two techniques for cy643 and cy681 in methanol were within 5% of each other (Table 2). Fluorescence is not so pronounced for the other cyanine dyes but reliable quantum yields could be established by the thermal blooming technique under standardised conditions.

The measured Φ_F values decrease steadily with increasing conjugation length (or decreasing emission energy) of the dye (Fig. 4), and fall from 0.43 for cy643 to 0.056 for cy794 (Table 2). Reproducibility remained high over multiple repeats and absolute errors were kept to within ±0.02, even for cy794 where Φ_F is approaching the lower limit for this technique. It will be noted from Fig. 3 that the more red-shifted cyanine dyes are at the edge for excitation at 635 nm but nonetheless highly reproducible and reliable estimates of Φ_F were forthcoming. A major benefit of the thermal blooming set-up relates to the absence of inner-filter effects, which would prevent the use of 635 nm excitation for conventional fluorescence measurements. The net result is that we now possess a useful set of fluorescence standards covering the far-red spectral range. Table 3 summarizes the wavelength ranges covered by each of the cyanine dyes and it should be noted that many more such dyes are available if needed to improve coverage of the spectral window.

Common alternatives

Cyanine dyes are not the only compounds available as standards for the far-red spectral range but they have the advantage of forming a closely knit family where incremental changes in the optical properties can be achieved. Cresyl Violet[23] is a popular fluorophore for the 630–700 nm window

Table 3 Summary of the most suitable excitation and emission spectral ranges for the cyanine dyes in methanol solution[a]

Dye	Excitation range/nm	Emission range/nm
cy643	600–645	650–775
cy681	640–680	680–820
cy746	685–750	750–900
cy761	700–760	750–900
cy794	730–795	775–950

[a] These wavelength ranges should not be considered as being absolute but are intended to be representative of the spectral regions where particular dyes are most useful.

Table 2 Compilation of the photophysical properties derived for the series of cyanine dyes in methanol solution at 20 °C

Compound	λ_{ABS}/nm	λ_{FLU}/nm	ϵ_{MAX}/M^{-1} cm^{-1}	τ_S/ns	Φ_F[a]	Φ_F[b]	τ_{SB}[c]/ns	k_{NR}[d]/10^7 s^{-1}
cy643	643	668	218 000	0.95	0.41	0.43	1.44	60.0 ± 9.0
cy681	681	706	166 000	0.87	0.24	0.24	1.10	87.6 ± 13.1
cy746	746	774	258 000	1.20	N/A	0.20	0.68	66.8 ± 10.0
cy761	760	782	312 000	1.00	N/A	0.18	0.72	81.5 ± 12.2
cy794	794	817	246 000	0.98	N/A	0.056	0.24	96.0 ± 14.4

[a] Fluorescence quantum yield measured by conventional steady-state fluorescence spectroscopy. [b] Measured by thermal blooming. [c] Radiative lifetime measured as the inverse of the radiative rate constant determined from the Strickler–Berg expression. [d] Rate constant for nonradiative deactivation of the emitting state.

with excitation at *ca.* 560 nm but concerns have been raised about self-association,[24] inner-filter effects[25] and Φ_F values that range from 0.54 to 0.70 in ethanol or methanol.[10,11,26–29] Methylene Blue (Φ_F = 0.02) is a well-known reference compound[30] but the quantum yield is very low and the compound should be used only in water. A more suitable option might be Nile Blue.[31] This dye, for which the purity of our commercial sample was <90% with notable contamination by coloured material, has λ_{ABS} at 627 nm and λ_{FLU} at 665 nm. It is pH sensitive and has limited solubility in methanol but is workable over 550–650 nm for excitation and 650–750 nm for emission. After purification, we recorded Φ_F values of 0.26 by steady-state fluorescence spectroscopy using TPP as reference and Φ_F = 0.23 by thermal blooming. Literature data include Φ_F values in ethanol of 0.23,[26] by thermal phase grating, and 0.47,[27] by thermal lensing. In our hands, fully reliable results were obtained only after addition of a trace amount of acid.

Moving to lower energies, there is little real choice other than cyanine-based dyes. For example, Indocyanine Green has been used[32] for many years in ophthalmology for imaging retinal blood vessels. This compound, which is a cyanine dye that aggregates extensively in solution,[33] can be excited in the region around 750 nm to give fluorescence at wavelengths longer than 800 nm. It is widely used as a fluorescent label for tissue,[34] during for example colorectal surgery where knowledge of quantum yields are not necessary. In methanol, the fluorescence quantum yield (Φ_F = 0.043)[35] is too low for many purposes.

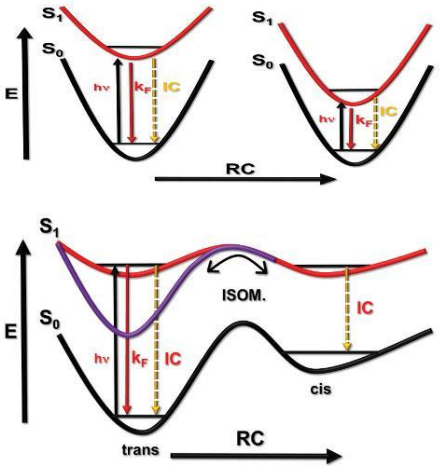

Fig. 5 Illustration of how a change in the excitation energy affects the photophysical properties. The upper panel shows that the excitation energy is lowered by an increase in conjugation length of the cyanine dye. Reducing the energy gap between emitting state (S_1) and ground state (S_0) increases the rate of internal conversion (IC) but decreases the rate of radiative decay (k_F). The lower panel indicates the process of photoisomerisation and shows that lowering the excitation energy raises the energy barrier for isomerization.

Discussion

The concept of proposing cyanine dyes as fluorescence standards is not new[5,28,35,36] and many such compounds are used in contemporary fluorescence microscopy as advanced probes.[37] In this report, we have extended the library of useful far-red emitters by providing absolute fluorescence quantum yields for soluble dyes that emit within a spectral window covering the wavelength range 650–950 nm. It will be noted that the reported Φ_F values decrease progressively as the emission maximum moves to lower energy (Fig. 4). Indeed, Φ_F for the most red-shifted dye, cy794, is at the lower limit for accurate determination by thermal blooming. This finding suggests that cyanine dyes might not be appropriate standards for compounds that absorb at wavelengths longer than 800 nm. In our opinion, cyanine dyes are highly attractive reference compounds for excitation wavelengths stretching from 500 to 800 nm. A particular feature of these dyes concerns the sharp absorption profiles with pronounced shoulders on the high-energy side of the optical transition. This shoulder provides an ideal excitation point. We have not encountered any undue problems of poor stability or dye fatigue during prolonged spectroscopic studies.

For the cyanine dyes described in this report, the Stokes' shift falls within the range 350 to 580 cm^{-1}, indicating only minor structural changes between absorbing and emitting species. The molar absorption coefficients at the peak maximum (ε_{MAX}) are high and possibly sensitive to the nature of the compound (Table 2). Nonetheless, the radiative rate constants calculated from the Strickler–Berg expression[38] (k_{SB}) evolve smoothly across the series, giving a clear correlation with the mean fluorescence maximum (ν_F) measured in terms of wavenumber. Somewhat surprisingly, the singlet-excited state lifetimes (τ_S) tend to remain at around 1 ns and do not follow the observed trend in Φ_F (Table 2). There appears to be a crude relationship between the mean emission maximum and Φ_F, as is illustrated by Fig. 4. This apparent trend is a result of the special circumstance where the rate constant (k_{NR}) for nonradiative deactivation of the excited state is essentially balanced by opposing changes in the radiative rate constant (k_{RAD}) across a series of emitters (Fig. 5). This situation is quite rare but arises here because of conflicting dependences on the relevant energy gap.[22,39] Thus, the rate of internal conversion to the ground state is expected[22] to increase with decreasing ν_F but the rate of isomerization from the excited-singlet state will decrease with decreasing ν_F due to a loss of potential energy.[40] These two rate constants combine to give k_{NR} and the indications are that, across this series of cyanine dyes, the latter is accidently fixed.

Conclusions

Combining thermal blooming with a series of structurally-related cyanine dyes, it has been possible to evaluate a set of

commercially-available fluorophores as potential ratiometric standards for the 650–900 nm region. Cyanine dyes possess certain advantages as reference compounds, including ease of synthesis, ready availability, well-defined absorption and emission profiles that retain their spectral patterns in different environments, and strong fluorescence. Radiative rate constants tend to be high and poor spin–orbit coupling properties minimize intersystem crossing to the triplet manifold.[40] Usually, cyanine dyes dissolve easily in alcohol solvents but much less so in water. Limited light fastness and competing light-induced isomerization are obvious drawbacks for the proposed application. The cyanine dyes studied here are not amenable for facile attachment to biological materials but strategies exist for appending appropriate anchoring groups to the backbone. In fact, cyanine dyes such as Alexa Fluor 647 are used extensively in super-resolution microscopy.[41]

To establish absolute fluorescence quantum yields, we have re-introduced the technique known as photo-initiated thermal blooming.[8] The ready availability of suitable laser diode modules means that it is feasible to construct a working prototype from relatively inexpensive components. Advantages of this approach include ease of operation, rapid screening of samples, and minimisation of inner-filter effects. To become popular, however, the technique needs diversifying to include solid samples, such as thin films, and operating devices, such as OLEDs. Preliminary work suggests such applications are possible with minor modifications to the basic set-up.

Conflicts of interest

There are no conflicts to declare.

Acknowledgements

We thank Newcastle University and EPSRC (Industrial CASE Award) for financial support of this work. We also thank Dr N. R. Walker (Newcastle University) for the loan of the Tektronix DPO71254 oscilloscope, Dr M. J. Hall (Newcastle University) for donating samples of aza-BODIPY dyes and Dr Corinne Wills and Prof. William McFarlane for recording the NMR spectra. Finally, we thank John Corner and Gary Day of the School of Chemistry Mechanical Workshop for help constructing the thermal blooming instrument.

Notes and references

1 J. R. Lakowicz, Radiative decay engineering: Biophysical and biomedical applications, *Anal. Biochem.*, 2001, **298**, 1–24.
2 K. Kolmakov, V. N. Belov, J. Bierwagen, C. Ringemann, V. Müller, C. Eggeling and S. W. Hell, Red emitting rhodamine dyes for fluorescence microscopy and nanoscopy, *Chem. – Eur. J.*, 2010, **16**, 158–166.
3 L. Yuan, W. Lin, K. Zheng, L. He and W. Huang, Far-red to near infrared analyte-responsive fluorescent probes based on organic fluorophore platforms for fluorescence imaging, *Chem. Soc. Rev.*, 2013, **42**, 622–661.
4 A. M. Brouwer, Standards for photoluminescence quantum yield measurements in solution, *Pure Appl. Chem.*, 2011, **83**, 2213–2228.
5 R. C. Benson and H. A. Kues, Absorption and fluorescence properties of cyanine dyes, *J. Chem. Eng. Data*, 1977, **22**, 379–383.
6 L. Porres, A. Holland, L. O. Pålsson, A. P. Monkman, C. Kemp and A. Beeby, Absolute measurements of photoluminescence quantum yields of solutions using an integrating sphere, *J. Fluoresc.*, 2006, **16**, 267–273.
7 A. Lampe, V. Haucke, S. J. Sigrist, M. Heilemann and J. Schmoranzer, Multicolour direct STORM with red emitting carbocyanines, *Biol. Cell*, 2012, **104**, 229–237.
8 J. H. Brannon and D. Magde, Absolute quantum yield determination by thermal blooming, *J. Phys. Chem.*, 1978, **82**, 705–709.
9 Y. Nagasawa, Y. Ando, D. Kataoka, H. Matsuda, H. Miyasaka and T. Okada, Ultrafast excited state deactivation of triphenylmethane dyes, *J. Phys. Chem. A*, 2002, **106**, 2024–2035.
10 D. Magde, R. Wong and P. G. Seybold, Fluorescent quantum yields and their relation to lifetimes of rhodamine 6G and fluorescein in nine solvents: Improved absolute standards for quantum yields, *Photochem. Photobiol.*, 2002, **75**, 327–334.
11 D. Magde, J. H. Brannon, T. L. Cremers and J. Olmsted, Absolute luminescence yield of cresyl violet, a standard for the red, *J. Phys. Chem.*, 1979, **83**, 696–699.
12 C. V. Bindhu, S. S. Harilal, V. P. N. Nampoori and C. P. G. Vallabhan, Thermal diffusivity measurments in organic liquids using transient lens calorimetry, *Opt. Eng.*, 1998, **37**, 2791–2794.
13 J. N. Demas and G. A. Crosby, Measurement of photoluminescent quantum yields. A review, *J. Phys. Chem.*, 1971, **75**, 991–1024; T. Karstens and K. Koba, Rhodamine B and rhodamine 101 as reference substances for fluorescent quantum yield measurements, *J. Phys. Chem.*, 1980, **84**, 1871–1872.
14 D. F. Eaton, Reference materials for fluorescence measurement, *Pure Appl. Chem.*, 1988, **60**, 1107–1114; C. Würth, M. Grabolle, J. Pauli, M. Spieles and U. Resch-Genger, Relative and absolute determination of fluorescence quantum yields of transparent samples, *Nat. Protoc.*, 2013, **8**, 1535–1550.
15 S. Fery-Forgues and D. Lavabre, Are fluorescence quantum yields so tricky to measure? A demonstration using familiar stationery products, *J. Chem. Educ.*, 1999, **76**, 1260–1264.
16 M. Fischer and J. Georges, Fluorescence quantum yield of rhodamine 6G in ethanol as a function of concentration using thermal lens spectroscopy, *Chem. Phys. Lett.*, 1996, **260**, 115–118.
17 J. K. Karlsson and A. Harriman, Origin of the red shifted optical spectra recorded for aza-BODIPY Dyes, *J. Phys. Chem. A*, 2016, **120**, 2537–2546.

18 M. Ambroz, A. Beeby, A. J. MacRobert, R. K. Svensen and D. Phillips, Preparative, analytical and fluorescence spectroscopic studies of sulphonated aluminium phthalocyanine photosensitisers, *J. Photochem. Photobiol., B*, 1991, **9**, 87–95.
19 J. W. Owens, R. Smith, R. Robinson and M. Robins, Photophysical properties of porphyrins, phthalocyanines and benzochlorins, *Inorg. Chim. Acta*, 1998, **279**, 226–231.
20 J. W. Owens and M. Robins, Phthalocyanine photophysics and photosensitizer efficiency on human embryonic lung fibroplasts, *J. Porphyrins Phthalocyanines*, 2001, **5**, 460–464.
21 S. Dhami, A. J. De Mello, G. Rumbles, S. M. Bishop, D. Phillips and A. Beeby, Phthalocyanine fluorescence at high concentration: Dimers or reabsorption effect?, *Photochem. Photobiol.*, 1995, **61**, 341–346.
22 R. Englman and J. Jortner, The energy gap law for radiationless transitions in large molecules, *Mol. Phys.*, 1970, **18**, 145–172.
23 A. Alvarez-Buylla, C.-Y. Ling and J. R. Kirn, Cresyl violet: A red fluorescent nissl stain, *J. Neurosci. Methods*, 1990, **33**, 129–133.
24 Y. Sakai, M. Kawahigashi, T. Minami, T. Inoue and S. Hirayama, Deconvolution of non-exponential decays arising from reabsorption of emitted Light, *J. Lumin.*, 1989, **42**, 317–324; G. Zhang and W. Chen, Fluorescence spectroscopic studies on intermolecular energy transfer of RH6G-cresyl violet mixture solution, *Acta Phys.-Chim. Sin.*, 1990, **6**, 163–168.
25 S. J. Isak and E. M. Eyring, Fluorescence quantum yield of cresyl violet in methanol and water as a function of concentration, *J. Phys. Chem.*, 1992, **96**, 1738–1742.
26 V. A. Petukhov, M. B. Popov and A. I. Krymova, Determination of the quantum efficiency of the fluorescence of the solutions of organic dyes by diffraction on a thermal phase grating induced by laser radiation, *Kvantovaya Elektron.*, 1986, **13**, 777–786.
27 T. Wang, B. Q. Zhang, J. L. Pan, P. Gu, Q. Xu and Q. Sun, Determination of absolute fluorescence quantum yield of laser dyes by thermal lens calorimetry, *Chin. Sci. Bull.*, 1989, **34**, 1756–1757.
28 J. Olmsted, Calorimetric Determinations of absolute fluorescence quantum yields, *J. Phys. Chem.*, 1979, **83**, 2581–2584.
29 K. H. Drexhage, What's ahead in laser dyes, *Laser Focus*, 1973, 35–39; K. H. Drexhage, Fluorescence efficiency of laser dyes, *J. Res. NBS A Phys. Chem.*, 1976, **80**, 421–428.
30 S. J. Atherton and A. Harriman, Photochemistry of intercalated methylene blue: Photoinduced hydrogen atom abstraction from guanine and adenine, *J. Am. Chem. Soc.*, 1993, **115**, 1816–1822.
31 A. Douhal, Photophysics of nile blue in proton-accepting and electron-donating solvents, *J. Phys. Chem.*, 1994, **98**, 13131–13137.
32 J. T. Alander, I. Kaartinen, A. Laakso, T. Pätilä, T. Spillmann, V. V. Turchin, M. Venermo and P. Välisuo, A review of indocyanine green fluorescence imaging in surgery, *Int. J. Biomed. Imaging*, 2012, 940585.
33 M. L. Landsman, G. Kwant, G. A. Mook and W. G. Zijlstra, Light-absorbing properties, stability and spectral stabilization of indocyanine green, *J. Appl. Physiol.*, 1976, **40**, 575–583; B. Yuan, N.-G. Chen and Q. Zhu, Emission and absorption properties of indocyanine green in intralipid solution, *J. Biomed. Opt.*, 2004, **9**, 497–503.
34 T. Desmettre, J. M. Devoisselle and S. Mordon, Fluorescent properties and metabolic features of indocyanine green (ICG) as related to angiography, *Surv. Ophthalmol.*, 2000, **45**, 15–27.
35 R. Philip, A. Penzkofer, W. Bäumler, R. M. Szeimies and C. Abels, Absorption and fluorescent spectroscopic investigation of indocyanine green, *J. Photochem. Photobiol., A*, 1996, **96**, 137–148.
36 K. Rurack and M. Spieles, Fluorescence quantum yields of a series of red and near infrared dyes emitting at 600–1000 nm, *Anal. Chem.*, 2011, **83**, 1232–1242.
37 J. C. Vaughan, G. T. Dempsey, E. Sun and X. Zhuang, Phosphine quenching of cyanine dyes as a versatile tool for fluorescence microscopy, *J. Am. Chem. Soc.*, 2013, **125**, 1197–1200.
38 N. Panchuk-Voloshina, R. P. Haugland, J. Bishop-Stewart, M. K. Bhalgat, P. J. Millard, F. Mao, W. Y. Leung and R. P. Haugland, Alexa dyes, a series of new fluorescent dyes that yield exceptionally bright, photostable conjugates, *J. Histochem. Cytochem.*, 1999, **47**, 1179–1188.
39 S. J. Strickler and R. A. Berg, Relationship between absorption intensity and fluorescence lifetime of molecules, *J. Chem. Phys.*, 1962, **37**, 814–822.
40 A. Harriman, (Photo)isomerization dynamics of merocyanine dyes in solution, *J. Photochem. Photobiol., A*, 1992, **65**, 79–93.
41 M. Bates, B. Huang, G. T. Dempsey and X. Zhuang, Multicolour super resolution imaging with photoswitchable fluorescent probes, *Science*, 2007, **317**, 1749–1753.

Pulse Radiolysis of TIPS-Pentacene and a Fluorene-bridged Bis-Pentacene: Proof of Intramolecular Singlet-Exciton Fission

Joshua K. G. Karlsson,[a] Alparslan Atahan,[a] Anthony Harriman,[a,] Sachiko Tojo,[b] Mamoru Fujitsuka[b] and Tetsuro Majima[b]*

(a) Molecular Photonics Laboratory, School of Natural and Environmental Science (Chemistry), Bedson Building, Newcastle University, Newcastle upon Tyne, NE1 7RU, United Kingdom and (b) The Institute of Scientific and Industrial Research (SANKEN), Osaka University, Ibaraki, Osaka 567-0047, Japan

Corresponding Author

anthony.harriman@ncl.ac.uk

ABSTRACT: Exposing TIPS-pentacene in de-aerated benzene to pulses of ionizing radiation generates a mixture of singlet- and triplet-excited states. The singlet-excited state undergoes radiative decay without spin conversion whereas the triplet-excited state decays exponentially to restore the ground state. The corresponding bis-pentacene forms two excited-triplet states but the excited-singlet state is not observed on the ns-timescale. The two triplets can be resolved both spectroscopically and kinetically, a situation unique to this system. The species having only a single pentacene promoted to the triplet state decays relatively slowly by exponential kinetics. The corresponding species with both pentacenes at the triplet level, which arises exclusively from intramolecular singlet-exciton fission, undergoes intramolecular triplet-triplet annihilation. On the basis of dosimetry measurements, it is concluded that intramolecular singlet-exciton fission forms the triplet-excited states in a combined yield of 150% in non-polar solvent.

TOC GRAPHICS

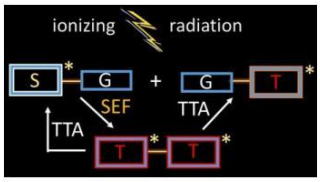

KEYWORDS: Photophysics : Radiation Chemistry : Excited States : Kinetics : Pentacene

The concept of singlet-exciton fission[1] (SEF) has gained immense popularity over the past decade and numerous chromophores, notably poly(acenes) such as tetracene[2] and pentacene,[3] are known to generate triplet states with quantum efficiencies close to 200%. The SEF process requires two or more chromophores to reside in close proximity and to satisfy certain energy restrictions. Early studies made use of condensed phases, including crystals[4] and thin-solid films,[5] but later work extended the field to covalently-linked bichromophores, such as bis-pentacene derivatives.[6,7] The main thermodynamic limitation[1] is that the energy of the triplet-excited state must be close to or less than one-half that of the excited-singlet state. The most notable features of SEF are a much reduced fluorescence quantum yield and lifetime, relative to the isolated single chromophore, and a quantum efficiency for formation of the excited-triplet state that exceeds 100%. This latter feature is considered the primary signature of SEF. Details of the SEF mechanism,[7] especially involving bichromophores in dilute solution,[8] remain elusive but the notion that SEF takes place in appropriate molecular systems is beyond dispute.

The conventional approach to examination of SEF involves monitoring evolution of the triplet state from the singlet precursor using ultrafast transient absorption spectroscopy.[9] Now, we use a different protocol and report on the events that follow from exposure of a dilute benzene solution of a bis-pentacene to a pulse of ionizing radiation. Such conditions favor formation of excited-states of benzene by way of charge recombination of the primary radical ions. These highly energetic excited states[10] transfer excitation energy to the poly(acene), although they are short-lived species (Scheme 1). The pulse radiolysis technique allows the properties of triplet-excited states to be characterized and, in this case, provides a proof for intramolecular SEF. An advantage of this approach is that the partitioning of the excited-singlet state during SEF can be monitored by dosimetry.

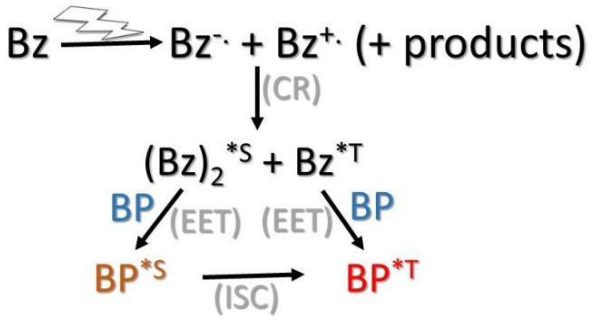

Scheme 1. The use of ionizing radiation to sensitize formation of the benzophenone (BP) triplet-excited state via intermediary formation of the benzene (Bz) singlet- and triplet-excited states.

The target bis-pentacene, BBP, and the corresponding isolated chromophore, TIPS-P, were synthesized in-house. The ethyne-silyl groups are added to increase solubility in organic solvents. The molecular formulae are given as Figure 1 and brief details of the synthesis and characterization are provided in the Supporting Information. It might be noted that TIPS-P has been used as a reference compound for many prior reports of SEF. Also noteworthy is the realization that the geometry of BBP, having a rigid fluorene spacer group between the TIPS-P terminals, is expected to promote through-bond electronic interactions.[11] Pulse radiolysis experiments were carried out with the Osaka linac, delivering 8-ns pulses of 27 MeV (0.87 kGy per pulse) ionizing radiation. Measurements were made in de-aerated benzene at room temperature, with confirmatory studies being made in toluene. Benzophenone[12] was used to calibrate the radiation dose.

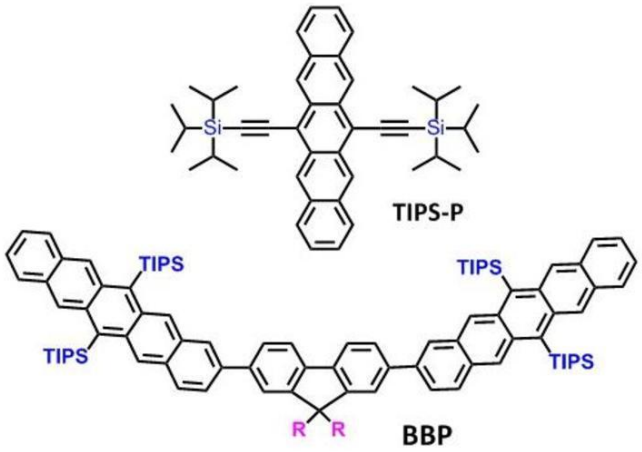

Figure 1. Molecular formulae for the control, TIPS-P, and target bis-pentacene, BBP; R = n-hexyl.

Pulse radiolysis of benzophenone (BP) in de-aerated benzene produces the well-known triplet-excited state of the solute (Figure S2).[12] This species, which has a lifetime of ca. 1 μs under these conditions, displays a sharp absorption maximum centered at 532 nm for which the molar absorption coefficient has been reported[13] to be 7,630 M^{-1} cm^{-1}. The singlet-excited state of BP is known[14] to undergo rapid intersystem crossing to the triplet manifold with a quantum efficiency of 100%. Thus, the BP excited-triplet state is the sole species present soon after the end of the ionizing pulse. The concentration of BP was varied to ensure complete trapping of the excited-state benzene molecules; the appropriate concentration was <5 mM. Now, the concentration of triplet BP, determined from the initial absorbance at 532 nm, equals the total concentration of benzene excited (singlet and triplet) states formed during the ionizing pulse. This concentration, which was in the region of 30-50 μM, was recorded for each subsequent experiment.

Charge recombination to form the initial excited states of benzene is expected to deliver three triplet states for each singlet state. The excited-singlet state of benzene, which forms an excimer

in pure benzene,[15] is relatively long lived, having a typical lifetime of 20 ns. In contrast, the lifetime of the benzene excited-triplet state, which extends to about 240 ns in dilute cyclohexane solution,[16] is effectively quenched by ground-state benzene. In fact, the triplet lifetime falls to less than 10 ns in pure benzene. There is an additional issue for poly(acenes) caused by the low triplet energy. Thus, the bimolecular rate constant for triplet-triplet energy transfer will fall within the Marcus inverted region[17] and is likely to be significantly less than that for singlet-singlet electronic energy transfer. The result is that the amount of excited-singlet state species that can be formed will exceed the predicted 25% limit and needs to be established experimentally.

Experiments were performed with TIPS-P in de-aerated benzene; the optimum concentration for complete trapping was found to 1.2 mM. The differential absorption spectrum recorded under these conditions is shown as Figure 2a. On long timescales (i.e., >200 ns), the triplet-excited state of TIPS-P can be recognized by its characteristic triplet-triplet absorption spectrum.[18] The peak of the differential absorption spectrum is at 505 nm. This species decays via first-order kinetics with a lifetime of 20 ± 3 μs under these conditions. There is no indication for bimolecular triplet-triplet annihilation occurring on the ns-μs timescale (Figure 2b). The derived triplet absorption spectrum recorded at 500 ns matches well with that produced by laser excitation of TIPS-P in toluene containing iodoethane (20% v/v) as spin-orbit promoter (Figures S3 and S4). (N.B. The TIPS-P triplet-excited state is not formed in measurable amount by laser excitation in the absence of the heavy-atom.) Under these latter conditions, the triplet lifetime is 9.0 ± 0.5 μs while aeration of the solution lowers this to 5.5 ± 0.3 μs.

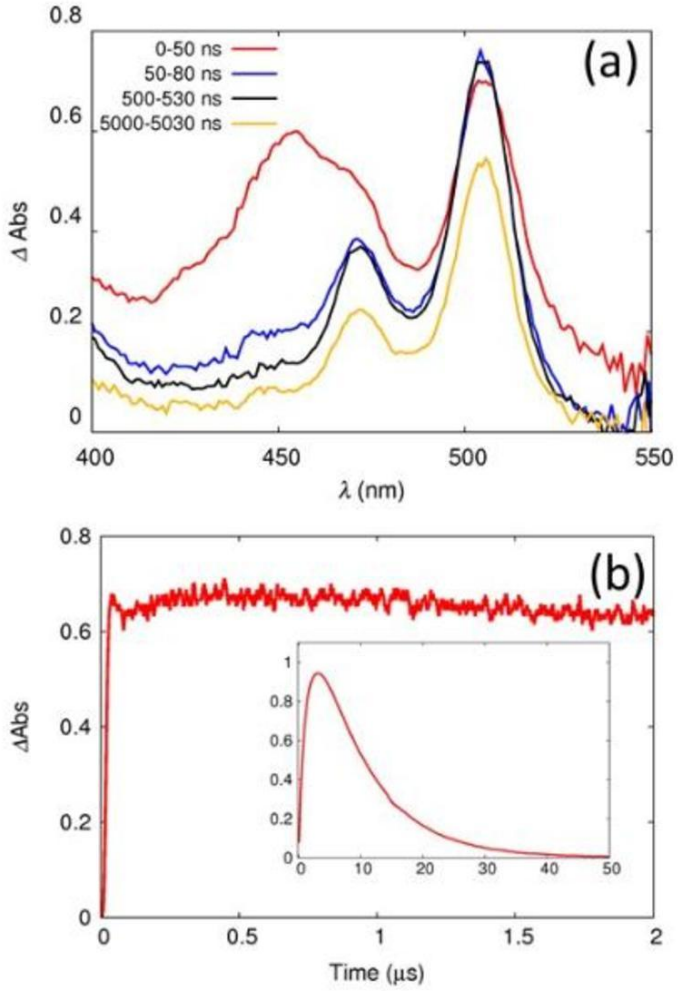

Figure 2. (a) Transient absorption spectra obtained for TIPS-P in deoxygenated benzene following pulse radiolysis, with the time delays indicated in the panel. (b) Transient decay traces at early (0-2 μs) and late (0-50 μs) times are shown.

On shorter timescales, an additional absorption band centered at ca. 455 nm is seen in the pulse radiolysis records (Figure 2a). This feature decays quickly, having a lifetime of some tens of ns, without further population of the excited-triplet state. From transient absorption spectroscopic studies (Figure S8), this short-lived species can be identified as the excited-singlet state of TIPS-P. Time-correlated, single photon counting studies indicate that the fluorescence lifetime is 22.3 ± 0.1 ns in de-aerated toluene. The fluorescence quantum yield measured at sub-μM concentration in air-equilibrated toluene is 0.75, but in de-aerated toluene fluorescence is essentially quantitative. From the measured molar absorption coefficient ($\varepsilon_S = 36{,}000\ M^{-1}\ cm^{-1}$) for the excited-singlet state at 455 nm, we can establish the relative ratio of the concentrations of the excited-states. Using the calibration provided from radiolysis of BP ($[BT]_T = 31.5\ \mu M$), we find initial concentrations of 16.7 and 14.8 μM, respectively, for excited-singlet and -triplet states of TIPS-P. These results indicate that, under our conditions, formation of the singlet-excited state of TIPS-P is slightly favored (i.e., 55%) over the triplet-excited state. It should be stressed that there is no significant interconversion between these excited states and no recycling of the ground state on the relevant timescale. Closely comparable results were obtained for TIPS-P in de-aerated toluene.

The above experiment leads to an estimate for the molar absorption coefficient (ε_T) of 67,600 $M^{-1}\ cm^{-1}$ at 505 nm for the excited-triplet state of TIPS-P in benzene. This value can be compared to that determined by laser flash photolysis in de-aerated toluene containing various concentrations of iodoethane (see Supporting Information). The laser photolysis studies gave a value for ε_T of 72,000 $M^{-1}\ cm^{-1}$ at a TIPS-P concentration of ca. 5 μM. These two estimates are in excellent agreement. It is also important to stress that intermolecular triplet-triplet annihilation[19] could not be observed for TIPS-P under our experimental conditions.

Attention now turns to the corresponding bis-pentacene, BBP. Pulse radiolysis of BBP (0.7 mM) in de-aerated benzene gives rise to a differential absorption spectrum which resembles that observed for the triplet-excited state of TIPS-P but without indication of the corresponding excited-singlet state (Figure 3). Time-correlated, single photon counting indicates that the fluorescence lifetime of BBP is only 200 ± 25 ps, while the fluorescence quantum yield falls to 0.03 ± 0.005 in toluene. The BBP triplet differential absorption spectrum has a maximum at 525 nm (Figure 3) and is noticeably broader than that of TIPS-P under the same conditions. Indeed, the spectral profile evolves over a few hundred ns and the maximum shifts to 515 nm (Figure 3). The differential absorption spectrum recorded after laser (FWHM = 4 ns) flash photolysis at 532 nm closely resembles that observed following radiolysis of BBP in benzene. Again, the relatively broad absorption band with a maximum at 525 nm seen immediately after excitation undergoes modest narrowing and a 10-nm blue shift on a sub-μs timescale. It is important to note that a spin-orbit promoter is not required to ensure efficient population of the excited-triplet state of BBP.

There are also important changes in the decay kinetics recorded at 525 nm when comparing BBP with TIPS-P in de-aerated benzene. Most notably, decay of the triplet-excited state of BBP shows a biphasic profile with a short-lived component superimposed over a slow, first-order step (Figure 3 inset). The lifetime of the latter decay is ca. 6.5 μs, although measurements made on longer timescales show this to be an underestimate. The overall decay profile is not explained in terms of a fast bimolecular process and a slower first-order step, as would be applicable[20] for bimolecular triplet-triplet annihilation at high triplet concentration. This situation is common for long-lived triplet-excited states[21] but does not hold for BBP. Instead, the entire decay profile fits well to consecutive first-order processes. According to this analysis, the lifetime for the faster process is

100 ± 10 ns in de-aerated benzene. The same behavior is observed in de-aerated toluene, with lifetimes of 90 ns and 5.3 μs.

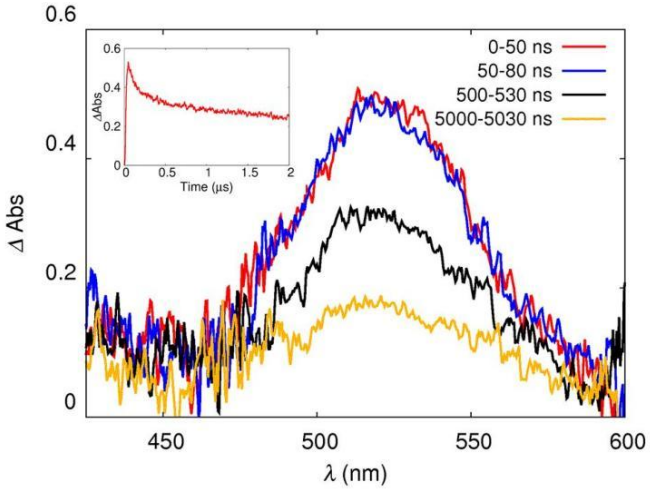

Figure 3. Transient absorption spectra obtained for BBP in deoxygenated benzene by pulse radiolysis. The initial transient decay as monitored at 525 nm is shown as an inset.

We can interpret the pulse radiolysis results in terms of two triplet-excited states that are not in equilibrium. The longer-lived species is attributed to a BBP moiety with a single pentacene unit promoted to the triplet state (Scheme 2, T_G). This species arises primarily by way of energy transfer from the benzene excited-triplet state. The shorter-lived species can be assigned to those BBP molecules having both pentacene units promoted to the triplet-excited state (T_T). This species is formed uniquely by way of SEF from the BBP singlet-excited state,[1,6,7] which in turn evolves from electronic energy transfer from the benzene excited-singlet state. The fast decay is because of intramolecular triplet-triplet annihilation,[21] which in part reforms the S_1 state but also generates a crop of the singly-excited triplet species. To allow for the full product balance, we

include the possibility that SEF also forms the ground state, G_G, and the mono-triplet species, T_G. The overall reaction sequence is illustrated in Scheme 2 and allows for some level of recycling of the excited states. According to this analysis, the singly-excited triplet species is responsible for the absorption peak at 510 nm while the dual-excited triplet shows maximum absorption centered at 530 nm (Figures S11-S13).

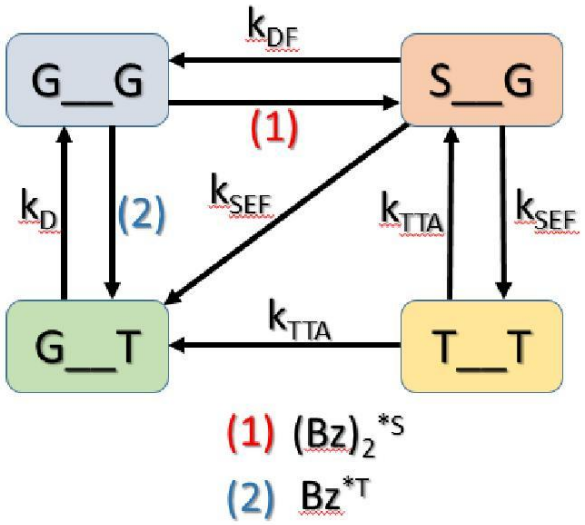

Scheme 2. Illustration of the processes that follow from exposure of the bis-pentacene in de-aerated benzene to pulses of ionizing radiation; EET = electronic energy transfer, SEF = intramolecular singlet-exciton fission, D = nonradiative decay, TTA = intramolecular triplet-triplet annihilation, DF = delayed fluorescence.

Intramolecular triplet-triplet annihilation (TTA) should lead to the appearance of delayed fluorescence.[22] This was indeed observed following laser excitation of BBP in de-aerated toluene. The lifetime of this delayed emission was ca. 50 ± 10 ns, which is in excellent agreement with the

expected value of one-half the corresponding triplet lifetime. A further requisite for this situation to arise is that the triplet energy must be close to one-half that of the excited-singlet state. We have not been able to verify this latter point and, in particular, we could not detect phosphorescence from either TIPS-P or BBP in a methylcyclohexane glass at 77K.

Extrapolation of the dual-exponential kinetic fits obtained for BBP in de-aerated benzene to zero time indicates that the contribution of dual-excited to total amount of triplet states is 40%. A similar contribution was found in toluene. Now, using TIPS-P as a standard, the expected contribution in benzene is 55%, if SEF from the S_1 state is quantitative. The simplest conclusion is that intramolecular SEF in benzene does not give the dual triplet as the only product. Comparison with the BP dosimeter shows the initial BBP triplet concentration amounts to ca. 50 μM, compared to a BP triplet concentration of 40 μM. Assuming the dual triplet T_T accounts for the fast decay, its concentration must be 10 μM (i.e., 20 μM in terms of excited-triplet state). The initial concentration of mono-triplet, T_G, obtained by difference is 30 μM, of which only 18 μM arises via energy transfer from triplet benzene. The residual 12 μM must be generated from S_G during the singlet-exciton fission step. Since electronic energy transfer from singlet benzene forms S_G at an initial concentration of 22 μM, we can establish the precise partitioning of SEF. The result is that for BBP in benzene the initially-formed S_G species splits (almost) evenly to give T_T and T_G in roughly equal yields, without direct formation of the ground-state species, G_G. The total triplet yield arising from SEF, therefore, is 150%. The entire cycle could be modelled successfully using slightly adapted kinetic parameters (Figures S14-S16).

In conclusion, the pulse radiolysis technique provides convenient access to the triplet-excited state of the bis-pentacene under conditions where the number of triplet species associated with each molecule can be readily assigned. This situation has not been reported for any other

symmetrical bis-chromophore. Intramolecular triplet-triplet annihilation[20,21] confirms identity of the species having both pentacenes promoted to the triplet-excited state and leads to delayed fluorescence.[22] The pulse radiolysis technique, together with the capacity to distinguish between mono- and dual-triplet species, allows the partitioning of the SEF process to be analyzed precisely. For BBP, decay of the excited-singlet state shows roughly equal probability for forming the mono- and dual-triplet species in nonpolar solvent, where charge-transfer interactions are unlikely. This system presents a rare opportunity to examine the outcome of SEF without arguments based on elaborate magnetic measurements. The onset of intramolecular triplet-triplet annihilation, and concomitant delayed fluorescence, adds a further restraint on the energy of the excited-triplet state. Obtaining an accurate triplet energy will be a final test of the system.

EXPERIMENTAL METHODS

Full experimental details are provided as part of the ESI.

Supporting Information. Includes experimental details, pulse radiolysis of BP dosimeter, absorption, fluorescence and transient absorption spectroscopy for target compounds, deconstruction of triplet spectra for BBP and modelling of photophysics cycle.

Notes

AA permanent address: Department of Polymer Engineering, Faculty of Technology, Duzce University, 81620, Duzce, Turkey.

The authors declare no competing financial interests.

ACKNOWLEDGMENT

We thank Newcastle University for financial support. AA thanks TUBITAK (The Scientific and Technological Research Council of Turkey) for the award of a research fellowship and JGKK

acknowledges the award of a travel scholarship from the RSC. TM thanks the Ministry of Education, Culture, Sports, Science and Technology of the Japanese Government for partly support by Grant-in-Aid for Scientific Research (Projects 25220806 and others).

REFERENCES

(1) Smith, M. B.; Michl, J. Singlet Fission. *Chem. Rev.* **2010**, *110*, 6891-6936.

(2) Wilson, M. W. B.; Rao, A.; Johnson, K.; Gélinas, S.; di Pietro, R.; Clark, J.; Friend, R. H. Temperature-Independent Singlet Exciton Fission in Tetracene. *J. Am. Chem. Soc.* **2013**, *135*, 16680-16688.

(3) Walker, B. J.; Musser, A. J.; Beljonne, D.; Friend, R. H. Singlet Exciton Fission in Solution. *Nature Chem.* **2013**, *5*, 1019-1024.

(4) Zimmerman, P. M.; Bell, F.; Casanova, D.; Head-Gordon, M. Mechanism for Singlet Fission in Pentacene and Tetracene: From Single Exciton to Two Triplets. *J. Am. Chem. Soc.* **2011**, *133*, 19944-19952.

(5) Wilson, M. W. B.; Rao, A.; Clark, J.; Kumar, R. S. S.; Brida, D.; Cerullo, G.; Friend, R. H. Ultrafast Dynamics of Exciton Fission in Polycrystalline Pentacene. *J. Am. Chem. Soc.* **2011**, *133*, 11830-11833.

(6) Zirzlmeier, J.; Lehnherr, D.; Coto, P. B.; Chernick, E. T.; Casillas, R.; Basel, B. S.; Thoss, M.; Tykwinski, R. R.; Guldi, D. M. Singlet Fission in Pentacene Dimers. *Proc. Natl. Acad. Sci.* **2015**, *112*, 5325-5330.

(7) Sakuma, T.; Sakai, H.; Araki, Y.; Mori, T.; Wada, T.; Tkachenko, N. V.; Hasobe, T. Long-Lived Triplet Excited States of Bent-Shaped Pentacene Dimers by Intramolecular Singlet Fission. *J. Phys. Chem. A* **2016**, *120*, 1867-1875.

(8) Sanders, S. N.; Kumarasamy, E.; Pun, A. B.; Trinh, M. T.; Choi, B.; Xia, J.; Taffet, E. J.; Low, J. Z.; Miller, J. R.; Roy, X.; Zhu, X.-Y.; Steigerwald, M. L.; Sfeir, M. Y.; Campos, L. M. Quantitative Intramolecular Singlet Fission in Bipentacenes. *J. Am. Chem. Soc.* **2015**, *137*, 8965-8972.

(9) Basel, B. S.; Zirzlmeier, J.; Hetzer, C.; Phelan, B. T.; Krzyaniak, M. D.; Reddy, S. R.; Coto, P. B.; Horwitz, N. E.; Young, R. M.; White, F. J.; Hampel, F.; Clark, T.; Thoss, M.; Tykwinski, R. R.; Wasielewski, M. R.; Guldi, D. M. Unified Model for Singlet Fission Within a Non-Conjugated Covalent Pentacene Dimer. *Nature Commun.* **2017**, *8*, 15171.

(10) Okamoto, K.; Saeki, A.; Kozawa, T.; Yoshida, Y. Tagawa, S. Sub-picosecond Pulse Radiolysis Study of Geminate Ion Recombination in Liquid Benzene. *Chem. Lett.* **2003**, *32*, 834-835.

(11) Naleway, C. A.; Curtiss, L. A.; Miller, J. R. Superexchange-Pathway Model for Long-Distance Electronic Couplings. *J. Phys. Chem.* **1991**, *95*, 8434-8437.

(12) Tamai, N.; Asahi, T.; Maushara, H. Intersystem Crossing of Benzophenone by Femtosecond Transient Grating Spectroscopy. *Chem. Phys. Lett.* **1992**, *198*, 413-418.

(13) Hurley, J. K.; Sinai, N.; Linschitz, H. Actinometry in Monochromatic Flash Photolysis: The Extinction Coefficient of Triplet Benzophenone and Quantum Yield of Triplet Zinc Tetraphenylporphyrin. *Photochem. Photobiol.* **1983**, *38*, 9-14.

(14) Aloïse, S.; Ruckebusch, C.; Blanchet, L.; Réhault, J.; Buntinx, G.; Huvenne, J.-P. The Benzophenone $S_1(n,\pi^*) \rightarrow T_1(n,\pi^*)$ States Intersystem Crossing Reinvestigated by Ultrafast Absorption Spectroscopy and Multivariate Curve Resolution. *J. Phys. Chem. A* **2008**, *112*, 224-231.

(15) Bensasson, R. V.; Thomas, J. K.; Gangwer, T.; Richards, J. T. Spectra of Transitory Species in Pulse Radiolysis of Alkyl Benzenes. *Chem. Phys. Lett.* **1972**, *14*, 430-438.

(16) Bensasson, R. V.; Richards, J. T.; Thomas, J. K. The Pulsed Laser Photolysis of Benzene in Cyclohexane. *Chem. Phys. Lett.* **1971**, *9*, 13-16.

(17) Closs, G. L.; Piotrowiak, P.; MacInnis, J. M.; Fleming, G. R. Determination of Long-Distance Intramolecular Triplet Energy Transfer Rates – A Quantitative Comparison with Electron-Transfer. *J. Am. Chem. Soc.* **1988**, *110*, 2652-2653.

(18) Wu, Y.; Liu, K.; Liu, H.; Zhang, Y.; Zhang, H.; Yao, J.; Fu, H. Impact of Intermolecular Distance on Singlet Fission in a Series of TIPS Pentacene Compounds. *J. Phys. Chem. Lett.* **2014**, *5*, 3451-3455.

(19) Cheng, Y. Y.; Khoury, T.; Clady, R. G. C. R.; Tayebjee, M. J. Y.; Ekins-Daukes, N. J.; Crossley, M. J.; Schmidt, T. W. On the Efficiency Limit of Triplet-Triplet Annihilation for Photochemical Upconversion. *Phys. Chem. Chem. Phys.* **2010**, *12*, 66-71.

(20) Birks, J. B. Photophysics of Aromatic Molecules. Wiley-Interscience, London, 1970.

(21) Singh-Rachford, T. N.; Castellano, F. N. Photon Upconversion Based on Sensitized Triplet-Triplet Annihilation. *Coord. Chem. Rev.* **2010**, *254*, 2560-2573.

(22) Benniston, A. C.; Harriman, A.; Howell, S. L.; Sams, C. A.; Zhi, Y. G. Intramolecular Excimer Formation and Delayed Fluorescence in Sterically-Constrained Pyrene Dimers. *Chem. Eur. J.* **2007**, *13*, 4665-4674.

THE JOURNAL OF PHYSICAL CHEMISTRY A
Cite This: J. Phys. Chem. A 2017, 121, 8569-8576
Article
pubs.acs.org/JPCA

Effects of Temperature and Concentration on the Rate of Photobleaching of Erythrosine in Water

Joshua K. G. Karlsson, Owen J. Woodford, Roza Al-Aqar, and Anthony Harriman*

Molecular Photonics Laboratory, School of Chemistry, Newcastle University, Bedson Building, Newcastle upon Tyne NE1 7RU, United Kingdom

Supporting Information

ABSTRACT: Erythrosine, a popular food dye, undergoes fast O_2-sensitive bleaching in water when subjected to visible light illumination. In dilute solution, erythrosine undergoes photobleaching via first-order kinetics, where the rate of bleaching depends critically on the rate of photon absorption and on the concentration of dissolved oxygen. Kinetic studies indicate that this inherent bleaching is augmented by self-catalysis at higher concentrations of erythrosine and on long exposure times. Under the conditions used, bleaching occurs by way of geminate attack of singlet molecular oxygen on the chromophore. Despite the complexity of the overall photobleaching process, the rate constants associated with both inherent and self-catalytic bleaching reactions follow Arrhenius-type behavior, allowing the activation parameters to be resolved. Bleaching remains reasonably efficient in the solid state, especially if the sample is damp, and provides a convenient means by which to construct a simple chemical actinometer.

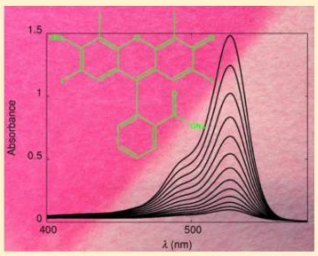

INTRODUCTION

Organic dyes[1,2] are useful colorants for a variety of applications, ranging from cosmetics to printing inks and to anticounterfeit devices. Historically, such dyes were selected for the strength and range of their colors, and many, for example indigo, have played an important role in shaping our lifestyle.[3] More recently there has been a move toward identifying nontoxic dyes that dissolve readily in water.[4,5] These latter compounds are highly attractive to the food industry[6] and are popular with artists, while being valuable agents for bioconjugation.[7,8] A major concern for all organic dyes relates to their likely instability under prolonged exposure to visible light. Indeed, photodegradation can be a serious limitation for certain classes of dye,[9] although engineering (e.g., the omission of molecular oxygen and introduction of screens or filters) can provide important levels of relief.[10] Despite the practical inconvenience of dye photofading, there have been relatively few detailed studies describing the kinetics of light-induced degradation under controlled conditions.[11−16] Such studies might be complicated by self-catalysis[17] and invariably require multiple numbers of photons for complete bleaching of an individual molecule. Mechanistic studies are especially difficult in those cases where the quantum yields are very low. It might be mentioned that the photofading process is used routinely for measuring diffusion coefficients via fluorescence recovery after photobleaching (FRAP).[18]

Here, we report on the photochemical degradation of erythrosine in aqueous solution with particular reference to its temperature dependence. Erythrosine is a water-soluble, cherry-pink dye with a long tradition as a food colorant.[19] It is commonly used in fruit cocktails but has additional applications in printing ink, as a sensitizer for orthochromic photographic plates, and as a biological stain.[20] Our interest in this compound stems from its known ability to function as a triplet state photosensitizer in water. Indeed, xanthene dyes[21,22] in general are promising sensitizers for antimicrobial studies[23,24] because of their relatively low toxicity, high triplet energies, near-quantitative triplet state quantum yields, and relatively long triplet lifetimes. The interest in killing bacteria by way of photodynamic therapy[25] has led to further development of new sensitizers. Some of these reagents look promising but would be subject to lengthy clinical and legislative regulation. More immediate benefits might arise from the use of compounds already employed in the food industry.

One aspect of these photosensitizers, often overlooked in the search for optimum performance, is the need to eliminate the compound from the system at the conclusion of the process. This can be done most conveniently by photochemical means since the system is already under illumination (Figures S1 and S2). In turn, this situation demands a detailed understanding of the photofading kinetics such that destruction of the sensitizer occurs only on completion of the desired photochemistry. Optimization of the sensitizer concentration is a key requisite in the challenge to achieve optimal performance in terms of product yield and dye depletion. When sunlight is used to drive the reactions, this being the only sustainable way to promote large-scale photochemistry, the temperature of the aqueous reservoir

Received: June 30, 2017
Revised: October 18, 2017
Published: October 19, 2017

DOI: 10.1021/acs.jpca.7b06440
J. Phys. Chem. A 2017, 121, 8569−8576

will increase markedly during the reaction—hence the need to measure activation parameters for the photofading processes. Such studies are rare.

RESULTS AND DISCUSSION

Background. In water, erythrosine exhibits an absorption maximum at 530 nm, with a molar absorption coefficient at the peak of 75 000 M^{-1} cm^{-1}, and shows weak fluorescence centered at 550 nm (Figure S3). The compound in water follows Beer's law over a wide concentration range, covering that relevant to this work (Figure S4). The fluorescence quantum yield in dilute aqueous solution is 3% while the excited-singlet state lifetime is 0.25 ns. The corresponding triplet-excited state can be detected readily by transient absorption spectroscopy following laser excitation at around 520 nm (Figure S5). At low laser intensity, the triplet state decays via first-order kinetics with a lifetime of ca. 150 μs in the absence of molecular oxygen. This latter species shortens the triplet lifetime, the corresponding bimolecular rate constant being 1.4×10^9 M^{-1} s^{-1} for aqueous solution at 20 °C. The product of this interaction is singlet molecular oxygen ($O_2(^1\Delta_g)$), formed via electronic energy transfer, although superoxide ions might also be formed in low yield under certain conditions.

The quantum yield[26] for formation of $O_2(^1\Delta_g)$ in air-saturated D_2O is 0.68 at 20 °C under conditions where the triplet quantum yield (Φ_T = 0.97) is close to unity. Singlet molecular oxygen, which has a lifetime of ca. 4 μs in H_2O,[27] can attack erythrosine to initiate the bleaching process.[28] Here, we address the kinetics of the photofading reaction and, in particular, consider the effects of temperature and chromophore concentration on the rate of dye degradation. To the best of our knowledge, there are no reports in the scientific literature describing the activation parameters associated with photobleaching of an organic dye.

There have been several prior records[29−32] of the photobleaching of xanthene dyes in water, but few quantitative details are available. Consequently, preliminary studies were made to assess the significance of photobleaching by exposing an air-equilibrated, aqueous solution of erythrosine to white light. Under such conditions, the main absorption transition centered at 530 nm bleaches. There are no colored products, but absorption spectroscopy indicates the buildup of one or more species absorbing in the near-UV region (Figure 1). These latter products, which are either formed in low yield or possess a weak molar absorption coefficient, are relatively stable toward further illumination. After saturating the solution with N_2, the photobleaching process is much less evident but still proceeds at a measurable rate (Figure 1). Laser flash photolysis studies carried out in deaerated aqueous solution have shown[33] that the rate of decay of the triplet excited state increases with increasing concentration of erythrosine. The bimolecular rate constant for this reaction, which is a kind of self-quenching process, is 4×10^8 M^{-1} s^{-1}. This situation is far from uncommon[34] and could be the reason why photofading occurs in the absence of molecular oxygen. In air-equilibrated solution at the highest substrate concentration used here, self-quenching will account for less than 3% of the total triplet-state deactivation.

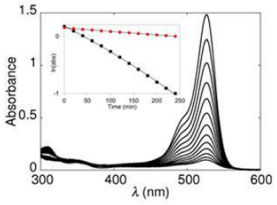

Figure 1. Stepwise bleaching of erythrosine in air-equilibrated water under broadband illumination. The inset shows kinetic plots in the absence (red circles) and presence (black circles) of molecular oxygen.

At 20 °C, monochromatic (λ = 523 nm) illumination of erythrosine in air-equilibrated water leads to loss of color. No change occurs in the dark, and as mentioned above, the rate of photobleaching is decreased significantly on removal of dissolved oxygen. The course of reaction is insensitive to changes in pH at pH greater than 4. The initial rate of photobleaching increases linearly with increasing light intensity (see later), as might be expected for a photoinduced reaction. At fixed incident light intensity, the rate shows a linear dependence on the fraction of light absorbed by the chromophore. Thus, the rate of photobleaching depends critically on the rate of photon uptake.

The usual consequence of attack by $O_2(^1\Delta_g)$ on an aryl heterocycle in solution is an endoperoxide.[35] In water, this latter species will rearrange to form stable products derived from substitution at the hydroperoxide group.[36,37] For erythrosine, it was found that a partially bleached solution formed an instantaneous precipitate on treatment with $AgNO_3$ solution. It was observed, however, that the addition of KI (ca. 1 mM) to a solution of erythrosine in aerated H_2O has essentially no effect on the rate of photobleaching, although iodide is known to quench singlet molecular oxygen.[38,39] Examination of partially bleached solutions of erythrosine in D_2O by ^1H and ^{13}C NMR spectroscopy was inconclusive as to the nature of the final products (Figures S6−S8).

Concentration Dependence. The absence of colored products allows kinetic measurements to be made by following absorbance changes at wavelengths around the peak maximum (Figures S9−S15). This can be done most conveniently by illuminating an aqueous solution of erythrosine with a light-emitting diode (LED) emitting at 523 nm and detecting the amount of transmitted light with an appropriate photocell (Figure S1). At modest concentrations (i.e., 3 μM, where the dye absorbs ca. 40% of the incident light intensity at the onset of the experiment), the rate of photobleaching appears first-order with respect to erythrosine (Figure 2); a similar conclusion was reached[40] earlier for photobleaching of phloxine B in water. First-order kinetics with respect to erythrosine are likewise observed at all concentrations less than ca. 7 μM (Figure 2). However, the apparent first-order rate constant, k_F, derived from eq 1 depends on the initial concentration of erythrosine (Table 1). Here, [ER] and $[ER]_0$ refer respectively to erythrosine concentrations at time t and before starting illumination. This situation might reflect differences in penetration depth and nonhomogeneous illumination issues or, more likely, point to a complex mechanism.

$$\ln[ER] = \ln[ER]_0 - k_F t \quad (1)$$

At 20 °C under monochromatic illumination, the approximate quantum yield for photobleaching, measured from the absorbance change at 530 nm, is around 1×10^{-3}. This value is very much lower than the quantum yield[26] for formation of singlet molecular oxygen (Φ_Δ = 0.68) under comparable conditions. This indicates that the rate-limiting factors are set essentially by the rate of formation of $O_2(^1\Delta_g)$ rather than the

DOI: 10.1021/acs.jpca.7b06440
J. Phys. Chem. A 2017, 121, 8569−8576

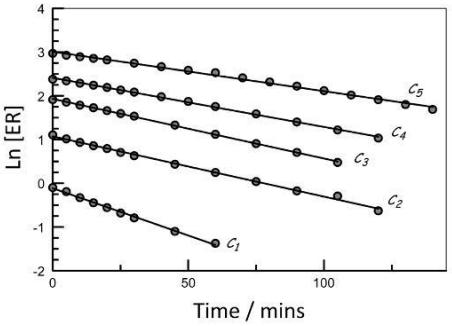

Figure 2. Examples of semilogarithmic fits to eq 1 for the photobleaching of erythrosine in air-equilibrated water at 20 °C. Initial concentrations of erythrosine are C_1 = 0.91 μM, C_2 = 3.03 μM, C_3 = 6.77 μM, C_4 = 10.8 μM, and C_5 = 19.5 μM. Standard deviations for fits to eq 1 are 0.0180, 0.0210, 0.0117, 0.025, and 0.033, respectively.

Table 1. Kinetic Parameters Derived for the Photobleaching of Erythrosine in Air-Equilibrated Water at 20 °C

$[ER]_0$ (μM)	I_{ABS} (%)[a]	ω_0 (μM min^{-1})[b]	k_F (min^{-1})[c]	COR[d]
0.91	14.5	0.0192	0.0216	0.9998
3.03	40.7	0.0515	0.0138	0.9997
6.77	69.0	0.0838	0.0136	0.9992
10.8	84.5	0.100	0.0112	0.9984
19.5	96.6	0.127	0.0090	0.9971

[a]Percent light absorbed by the sensitizer according to eq 2. [b]Initial rate of photobleaching. [c]Apparent first-order rate constant for bleaching derived according to eq 1. [d]Goodness-of-fit correlation.

subsequent chemical modifications,[35−37] leading to formation of the final product.

$$I_{ABS} = 1 - 10^{-A} \quad (2)$$

$$P_O = \frac{k_B[O_2]}{k_B[O_2] + k_D} \quad (3)$$

$$P_\Delta = \frac{\Phi_\Delta}{P_T} \quad (4)$$

$$k_F = (I_\lambda I_{ABS}\gamma)P_T P_O \kappa \quad (5)$$

$$P_Q = \frac{k_Q[ER]}{k_Q[ER] + k_\Delta} \quad (6)$$

At an erythrosine concentration of 3 μM, it was observed that both the apparent first-order rate constant, k_F, and the initial rate of photobleaching, ω_0, decreased linearly with decreasing light intensity, I_λ (Figure S16). Apart from changing the incident light intensity, the rate of photon uptake also varies according to the fraction of light absorbed, I_{ABS}, by erythrosine according to eq 2. Here, A refers to the absorbance in a 1 cm cuvette at 523 nm. In fact, it was observed that the product of k_F, I_λ, and I_{ABS} remained constant across several sets of conditions. The initial rate of photobleaching depends also on the concentration of dissolved oxygen. To be more precise, ω_0 depends on the probability, P_O, with which O_2 quenches the triplet state of erythrosine under the experimental conditions. This particular term can be expressed by way of eq 3, where k_B (= 1.4 × 10^9 M^{-1} s^{-1}) refers to the bimolecular rate constant for quenching triplet erythrosine by O_2 and k_D (= 6.7 × 10^3 s^{-1}) refers to the corresponding rate constant for decay of the triplet state in the absence of O_2. Under our conditions, P_O is essentially unity. We can define the probability P_Δ, with which interaction between the triplet state and O_2 leads to formation of singlet molecular oxygen in terms of eq 4. Here, P_T (= 0.97) is the probability for formation of the triplet excited state and Φ_Δ (= 0.68) is the quantum yield for formation of singlet molecular oxygen.

It was observed that at constant incident light intensity the rate of photobleaching of erythrosine could be well described in terms of eq 5, where γ is simply a factor for converting the incident light intensity into photons per minute. This expression, with the partition coefficient κ reflecting the likelihood that triplet quenching will lead to product formation, was found to hold under all conditions except for long exposure times at high erythrosine concentrations. It will be noted that eq 5 does not include the concentration of erythrosine in any form other than its role as an absorber (i.e., a sensitizer for formation of singlet molecular oxygen). This might seem unusual since part of the overall reaction scheme should include a term for trapping singlet oxygen via chemical modification of the substrate; in this case the substrate is also the sensitizer. This leads to eq 6 where k_Q is the bimolecular rate constant for chemical trapping of $O_2(^1\Delta_g)$ by erythrosine and k_Δ (= 2.5 × 10^5 s^{-1}) is the rate constant[41] for nonradiative decay of $O_2(^1\Delta_g)$ in water. We do not have a direct measure of k_Q, but from literature information,[35] this term is unlikely to exceed a value of ca. 10^7 M^{-1} s^{-1}. As such, P_Q will be essentially zero, even at the highest concentration of erythrosine used in this work.

This situation can be rationalized in terms of a certain fraction of $O_2(^1\Delta_g)$ reacting with the sensitizer immediately after excitation energy transfer. Assuming activation of O_2 occurs via the electron exchange[42] (i.e., Dexter-type electronic energy transfer) mechanism, there must be orbital contact between erythrosine and O_2. The geminate bleaching proposed here would involve a fraction of $O_2(^1\Delta_g)$ reacting with the sensitizer before dissociation of the contact pair. This geminate pair can dissociate by way of diffusive separation (k_{SP}), followed by nonradiative deactivation of $O_2(^1\Delta_g)$, or undergo chemical modification (k_P) to yield a product, EROO, as summarized by way of Scheme 1. Comparing Φ_Δ with the quantum yield for photobleaching, the probability of reaction within the geminate pair is around 0.1%.

Self-Catalysis at Higher Concentrations. At erythrosine concentrations above ca. 7 μM there is a marked positive deviation from first-order kinetics, even over short illumination periods (Figure 3). This suggests that a product formed during

Scheme 1. Summary of the Key Steps Leading to Photobleaching of Erythrosine in Aerated Water, with P1 and P2 Representing Products from Inherent and Self-Catalyzed Reactions

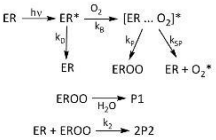

DOI: 10.1021/acs.jpca.7b06440
J. Phys. Chem. A 2017, 121, 8569−8576

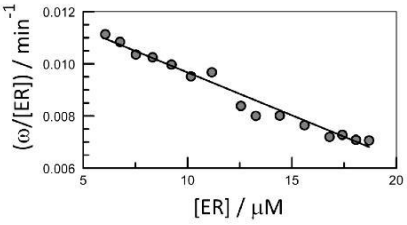

Figure 3. Example of kinetic analysis in terms of inherent and selfcatalytic bleaching reactions, with the solid line drawn through the data points representing a fit to eq 7. The initial concentration of erythrosine was 20 μM.

the inherent photobleaching reaction enters into the chemistry and augments the quenching of triplet erythrosine. According to this model (Scheme 1), the kinetic data can be analyzed in terms of eq 7, which allows for self-catalysis.[43] Here, ω refers to the observed rate of reaction, k_1 is the first-order rate constant for primary (i.e., inherent) photobleaching, and k_2 is the corresponding bimolecular rate constant for self-catalysis.[44]

$$\frac{\omega}{[\mathrm{ER}]} = (k_1 + k_2[\mathrm{ER}]_0) - k_2[\mathrm{ER}] \quad (7)$$

Analysis of the photobleaching data in terms of eq 7 allows determination of the two rate constants (Figure 3). The apparent first-order rate constant, $k_1 = 0.0069$ min^{-1}, can be equated with k_F considered at lower concentrations, although different incident light intensities were used for the different experiments. The derived values are collected in Table 2. The rate constant for

Table 2. Summary of Kinetic Parameters Extracted from Fitting the Bleaching Data to Eq 7

$[ER]_0$ (μM)	T (°C)	$[O_2]$ (μM)	k_1 (min^{-1})	k_2 (nM^{-1} min^{-1})
8.1	20	0.232	0.0093	0.39
19.5	10	0.285	0.0049	0.31
19.5	20	0.232	0.0069	0.46
19.5	30	0.196	0.0082	0.63
19.5	40	0.172	0.0091	0.82
19.5	50	0.156	0.0122	0.92
19.5	60	0.145	0.0137	1.01
19.5	70	0.138	0.0172	1.34

self-catalysis, k_2, at 20 °C was found to be 0.46 nM^{-1} min^{-1} at an initial erythrosine concentration of 20 μM. Similar values were recovered at lower (i.e., 8 μM) concentration (Table 2) and at different incident light intensities.

Confirmation that self-catalysis is likely for this reaction was obtained by illumination of eruthrosine in the presence 0.05 M furfuryl alcohol. This compound is used as a trap for singlet molecular oxygen,[45] where reaction leads to the formation of labile peroxides and hydroperoxides. The rate of photobleaching of erythrosine is accelerated by the presence of the substrate (Figure S17). We interpret this result in terms of furfuryl alcohol intercepting singlet molecular oxygen generated from the triplet-excited state of erythrosine to form highly reactive peroxyl species.[46−48] Subsequent dark reactions with erythrosine lead to further bleaching of the dye. In self-catalysis,[49−52] the primary breakdown products replace the peroxyl species formed from furfuryl alcohol. There is no recovery of coloration on leaving a bleached sample in the dark.

The overall bleaching process is "collectively autocatalytic" since one or more products form and promote further bleaching of the chromophore. The best known examples of autocatalytic reactions are the Belousov−Zhabotinsky clock reactions, although certain hydrolysis reactions are also believed to exhibit self-catalysis. Other well-known examples include the spontaneous degradation of aspirin to salicylic acid and DNA replication. Photochemical examples are less common, but the bleaching of a dye in the presence of a reactive substrate such as furfuryl alcohol seems a likely candidate. The normal signature of self-catalysis is a sigmoidal variation in product concentration with reaction time. It is also a basic requirement that the reaction order is nonlinear since at least one step involves the square of concentration. A complication particular to the bleaching studied here is that the number of absorbed photons changes as the reaction proceeds. This effect can disturb the shape of the product evolution profile.

It is also clear that self-catalysis serves to augment the overall bleaching but by itself provides only a modest acceleration in rate. The primary bleaching process involves attack on erythrosine by $O_2(^1\Delta_g)$. The fact that self-catalysis occurs only at relatively high concentration of erythrosine is taken as being indicative of a dark reaction. The most likely scenario is that erythrosine intercepts a peroxyl species formed during primary attack by $O_2(^1\Delta_g)$ before it can undergo chemical modification to form an unreactive permanent product (Scheme 1).

In the absence of molecular oxygen, the rate of photobleaching is relatively slow and shows no indication for self-catalysis. In fact, the rate decreases with increasing illumination time (see Figure S20) even when the level of light absorption remains essentially constant. This situation might indicate that low concentrations of oxygen are present at the onset but decrease as reaction proceeds.

Temperature Dependence. At a fixed erythrosine concentration of 3 μM, the apparent first-order rate constant k_F derived from eq 1 shows a modest dependence on temperature and increases more than 2-fold on raising the temperature from 20 to 60 °C. The adherence to eq 1 can be used to argue that the mechanism remains the same over this temperature variation. Indeed, most of the terms associated with eq 5 are essentially insensitive to temperature, but this is not so for the concentration of dissolved molecular oxygen (Table 2). The probability for quenching the triplet-excited state by O_2, however, remains in excess of 0.95 at all accessible temperatures because of the long inherent triplet lifetime. It can be seen that k_F varies smoothly with temperature over the available range (Figure 4). The rate constants follow Arrhenius behavior and give rise to an effective activation energy of 17.1 ± 1.0 kJ/mol and a pre-exponential factor of 15.6 min^{-1} (Figure 3). The latter value provides strong confirmation that our standardized experimental conditions are well short of being optimal for bleaching because of the low concentration of erythrosine.

The derived activation energy is modest,[53] but we could not find any meaningful comparator in the literature. In fact, it seems reasonable to suppose that this parameter is associated with addition of molecular oxygen across one of the double bonds present in erythrosine within the geminate pair. The resultant product (i.e., EROO in Scheme 1) is liable to hydrolyze in water, and there are crude indications for the release of halide ions. Gorman et al.[36] have shown that the diffusional addition of singlet molecular oxygen across double bonds provided by simple alkenes involves an activation energy close to zero. Such

DOI: 10.1021/acs.jpca.7b06440
J. Phys. Chem. A 2017, 121, 8569−8576

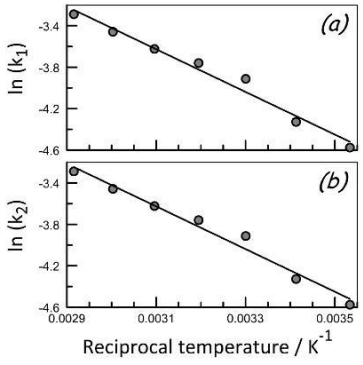

Figure 4. Arrhenius-type plots for the (a) inherent first-order rate constant and (b) the selfcatalytic reaction determined for photofading of erythrosine in air-equilibrated water. The solid lines correspond to least-squares nonlinear fits to the Arrhenius expression.

reactions are driven by entropic changes. It has also been reported[54] that the lifetime of $O_2(^1\Delta_g)$ in water is insensitive to changes in temperature. The measured activation energy must be related to partitioning of the encounter complex, as expressed in eq 5 in the form of κ. In the simplest case, this represents competition between k_{SP} and k_P (Scheme 1). The former is not expected to show a significant temperature dependence since the density of water does not change much over the temperature range of interest. That suggests to us that the activation energy is mostly associated with k_P.

At higher concentration of erythrosine, it was found that k_2 increased progressively with increasing temperature (Table 2). Indeed, k_2 follows Arrhenius-type behavior over the accessible temperature range, giving an activation energy of 18.5 kJ/mol while the extrapolated maximum k_2 value is 0.9 μM^{-1} min^{-1}. It is less surprising that k_2 might follow an activated route since the key reaction must involve diffusional contact between erythrosine and a product from its chemical breakdown. Indeed, other autocatalytic reactions have been reported[55−57] to proceed via an activated process. The activation energy derived here for erythrosine photobleaching is closely comparable to that for the inherent bleaching step, indicating perhaps a similarity between the two processes. Using furfuryl alcohol as a model, we can speculate that self-catalysis involves reactions of peroxyl species with erythrosine (Scheme 1). Such chemical processes, which are often chain reactions involving free radicals, are known to involve small activation barriers.[58]

Our understanding of this self-catalysis is based on a dark reaction between erythrosine and one of its intermediary breakdown products. It is easy to imagine that the latter (stable) intermediate (i.e., EROO in Scheme 1) will degrade faster at higher temperatures. This makes it more challenging for erythrosine to intercept the intermediate before its conversion to a benign product (i.e., P2 in Scheme 1). Temperature, therefore, plays a key role in the overall bleaching chemistry, and it becomes essential that we extend our knowledge of such processes if we are to control the photofading steps.

Bleaching in the Solid State. Erythrosine is a readily available food dye with a characteristic color and, as such, could make a convenient universal standard by which to compare and contrast the photostability of other dyes. This situation is made possible by the realization that bleaching occurs on a relatively fast time scale, at least in aerated aqueous solution. For a viable standard photosystem, the most convenient protocol would utilize controlled bleaching of erythrosine in the form of solid-state samples. This, of course, has implications for the photobleaching of dye adsorbed on textiles, printed on paper, or painted on canvas. As a demonstration of this principle, we note that filter paper soaked in aqueous erythrosine solution and dried makes an ideal medium for recording the beam characteristics of the LED used for illumination of the samples (Figure S2). For adsorbent paper (300 g/m^2) soaked in erythrosine solution, the pink coloration disappears gradually on exposure to sunlight, leaving a progressively bleached panel. The difference is obvious to the naked eye even on short irradiations (see Table of Contents graphic). This makes for an excellent actinometer since the residual color is a marker for the integrated number of absorbed photons.

Photochemical bleaching of erythrosine adsorbed onto different substrates (e.g., silica, KBr, titania, cotton, or translucent rubber) occurs on exposure to room light. With paper as the support, the rate of photobleaching increases markedly if the paper is kept damp. Notably, the rate of bleaching of erythrosine on dried paper shows no sign of increasing with increasing illumination time. This suggests that autocatalysis is not so important under these conditions, where contact with molecular oxygen cannot be guaranteed within the triplet lifetime. This realization, together with the apparently uniform bleaching kinetics observed, offers promise for the design of a viable actinometer for sunlight.

■ CONCLUSION

This work has advanced our general understanding of the photochemical bleaching of organic dyes by reporting activation parameters for both the inherent first-order step and the accompanying autocatalytic process. Such information is essential, especially for exterior applications where exposure to sunlight will lead to an inevitable increase in temperature for the system. Indeed, evermore applications are being proposed for organic chromophores, but little attention is being given to their stability under operating conditions. Of particular importance is the observation that at high concentrations of chromophore self-catalysis becomes significant. For improved design of advanced reagents it is necessary to move away from serendipitous discovery of unusually stable dyes and to construct databases containing critical entries useful for the recognition of optimum experimental conditions. It should be noted that the onset of self-catalysis means that the rate of bleaching takes on a significant time dependence. It should be emphasized that there are other examples of photochemical self-catalyzed reactions in the literature.[59−64] These reactions cover a variety of systems where light promotes unusual chemistry but nonetheless the range of photochemical self-catalyzed processes remains relatively small.

The bleaching reaction under consideration here is one of the simplest cases; involvement of singlet molecular oxygen was confirmed by the realization that the rate doubles in D_2O relative to H_2O (Figure S18). This latter effect arises because the lifetime of $O_2(^1\Delta_g)$ is increased markedly in D_2O. Under such conditions, product formation is enhanced because of diffusional attack by singlet oxygen—a process denied in H_2O. Even so, the probable involvement of peroxyl species makes it difficult to control the rate. In the absence of an activation barrier and under our

DOI: 10.1021/acs.jpca.7b06440
J. Phys. Chem. A 2017, 121, 8569−8576

experimental conditions, the inherent rate constant for bleaching of erythrosine in aerated water is 16 min^{-1}. Converting this rate to a formal quantum yield for photobleaching leads to a value of 0.001 at 20 °C under conditions where all incident light is absorbed at the onset. At 50 °C, a temperature easily reached under direct sunlight, the quantum yield is doubled. The many parameters derived during this study could be applied to simulate the rate of photochemical bleaching of erythrosine at low initial concentration—the only adjustable parameter being the rate of photon injection, γ, needed to standardize the units. The final result (Figure 5) gives a good representation of the experimental behavior recorded with a starting concentration of 3 μM.

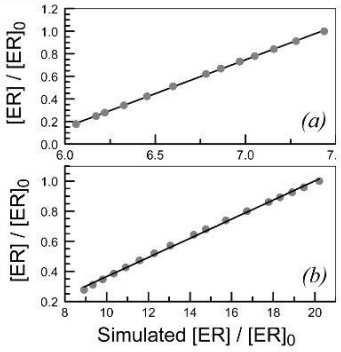

Figure 5. Comparison of observed and simulated concentration ratios for starting concentrations of (a) 3.0 μM and (b) 19.5 μM. The simulation was made on the basis of eqs 2–6 without consideration of the photon flux. The lines drawn through the data points refer to nonlinear least-squares fits to eq 1. Note that the fit for the higher concentration is poor, and this is the justification for including self-catalysis in this case.

Self-catalysis increases both the rate and quantum yield. A net result is that erythrosine is too susceptible to photodegradation to be proposed as a viable sensitizer for sustainable photochemical processes. It is ideal, however, for use as a sensitizer for any process where the final product distribution needs to be colorless. It is also apparent that a simple chemical actinometer can be formulated by impregnation of the dye onto adsorbent paper.

■ ASSOCIATED CONTENT

Supporting Information

The Supporting Information is available free of charge on the ACS Publications website at DOI: 10.1021/acs.jpca.7b06440.

Full experimental details, tables of statistical fits, absorption/emission spectra, triplet-state differential absorption spectra, examples of kinetic profiles, light-intensity dependences, effects of furfuryl alcohol on bleaching kinetics (PDF)

■ AUTHOR INFORMATION

Corresponding Author

*(A.H.) E-mail Anthony.harriman@ncl.ac.uk; Tel +44 1912088660.

ORCID

Anthony Harriman: 0000-0003-0679-2232

Notes

The authors declare no competing financial interest.

■ ACKNOWLEDGMENTS

We thank Newcastle University and EPSRC (Industrial Case Award) for financial support of this work. The sample of erythrosine was kindly donated by The Procter & Gamble Company. Ms. R. Al-Aqar acknowledges The Higher Committee for Education Development in Iraq (HCED) for the award of a research scholarship. We are especially grateful to Dr. Corinne Wills and Prof. William McFarlane for recording the NMR spectra reported in this manuscript.

■ REFERENCES

(1) Zollinger, H. *Color Chemistry. Syntheses, Properties and Applications of Organic Dyes and Pigments*, 3rd ed.; Wiley-VCH: Weinheim, 2003.
(2) Kim, S.-H. *Functional Dyes*; Elsevier: Amsterdam, 2006.
(3) Gurr, E. *Synthetic Dyes in Biology, Medicine and Chemistry*; Academic Press: London, 1971.
(4) Imran, M.; Yousaf, A. B.; Zhou, X.; Liang, K.; Jiang, Y. F.; Xu, A. W. Oxygen-Deficient TiO(2-x)-Methylene Blue Colloids: Highly Efficient Photoreversible Intelligent Inks. *Langmuir* **2016**, *32*, 8980–8987.
(5) Narwal, S.; Kumar, S.; Verma, P. K. Synthesis and Therapeutic Potential of Quinoline Derivatives. *Res. Chem. Intermed.* **2017**, *43*, 2765–2798.
(6) *Colour Additives for Food and Beverages*; Scotter, M. J., Ed.; Woodhead Publishing Series in Food Science, Technology and Nutrition; Elsevier: Amsterdam, 2015.
(7) Johnson, I. Fluorescent Probes for Living Cells. *Histochem. J.* **1998**, *30*, 123–140.
(8) Greenspan, P.; Mayer, E. P.; Fowler, S. D. Nile Red – A Selective Fluorescent Stain for Intracellular Lipid Droplets. *J. Cell Biol.* **1985**, *100*, 965–973.
(9) Van Beek, H. C. A.; Heertjes, P. M. Fading by Light of Organic Dyes on Textiles and Other Materials. *Stud. Conserv.* **1966**, *11*, 123–132.
(10) Padfield, T.; Landi, S. The Light Fastness of Natural Dyes. *Stud. Conserv.* **1966**, *11*, 181–196.
(11) Alamiry, M. A. H.; Harriman, A.; Haefele, A.; Ziessel, R. Photochemical Bleaching of an Elaborate Artificial Light-Harvesting Antenna. *ChemPhysChem* **2015**, *16*, 1867–1872.
(12) Harriman, A.; Stachelek, P.; Sutter, A.; Ziessel, R. Stepwise Photoconversion of an Artificial Light-Harvesting Array Built from Extended BODIPY Units. *Photochem. Photobiol. Sci.* **2015**, *14*, 1100–1109.
(13) Georgakoudi, I.; Nichols, M. G.; Foster, T. H. The Mechanism of Photofrin® Photobleaching and its Consequences for Photodynamic Therapy. *Photochem. Photobiol.* **1997**, *65*, 135–144.
(14) Carretero, L.; Blaya, S.; Mallavia, R.; Madrigal, R. F.; Belendez, A.; Fimia, A. Theoretical and Experimental Study of the Bleaching of a Dye in a Film-Polymerization Process. *Appl. Opt.* **1998**, *37*, 4496–4499.
(15) Huston, A. L.; Reimann, C. T. Photochemical Bleaching of Adsorbed Rhodamine 6G as a Probe of Binding Geometries on a Fused-Silica Surface. *Chem. Phys.* **1991**, *149*, 401–407.
(16) Batchelor, S. N.; Carr, D.; Coleman, C. E.; Fairclough, L.; Jarvis, A. The Photofading Mechanism of Commercial Reactive Dyes on Cotton. *Dyes Pigm.* **2003**, *59*, 269–275.
(17) Fazekas, T.; Nagy, A.; Treindl, L. Analysis of Asymmetric Sigmoid Kinetic Curves of Autocatalytic Reactions. *Collect. Czech. Chem. Commun.* **1993**, *58*, 775–782.
(18) Axelrod, D.; Koppel, D. E.; Schlessinger, J.; Elson, E.; Webb, W. W. Mobility Measurement by Analysis of Fluorescence Photobleaching Recovery Kinetics. *Biophys. J.* **1976**, *16*, 1055–1069.
(19) Chequer, F. M. D.; Venancio, V. P.; Bianchi, M. L. P.; Antunes, L. M. G. Genotoxic and Mutagenic Effects of Erythrosine B, a Xanthene Food Dye, on HepG2 Cells. *Food Chem. Toxicol.* **2012**, *50*, 3447–3451.

(20) Krause, A. W.; Carley, W. W.; Webb, W. W. Fluorescent Erythrosine B is Preferable to Trypan Blue as a Vital Exclusion Dye for Mammalian-Cells in Monolayer-Culture. *J. Histochem. Cytochem.* **1984**, *32*, 1084−1090.
(21) Sibrian-Vazquez, M.; Escobedo, J. O.; Lowry, M.; Fronczek, F. R.; Strongin, R. M. Field Effects Induce Bathochromic Shifts in Xanthene Dyes. *J. Am. Chem. Soc.* **2012**, *134*, 10502−10508.
(22) Maryakhina, V. S. Nature of Phosphorescence Kinetics of Xanthene Dyes in Biological Media. *Laser Phys.* **2016**, *26*, 105603.
(23) Pellosi, D. S.; Batistela, V. R.; De Souza, V. R.; Scarminio, I.; Caetano, W.; Hioka, N. Evaluation of Photodynamic Activity of Xanthene Dyes on Artemia Salina Described by Chemometric Approaches. *An. Acad. Bras. Cienc.* **2013**, *85*, 1267−1274.
(24) Wood, S.; Metcalf, D.; Devine, D.; Robinson, C. Erythrosine is a Potential Photosensitizer for the Photodynamic Therapy of Oral Plaque Biofilms. *Antimicrob. Chemother.* **2006**, *57*, 680−684.
(25) Wainwright, M. Photodynamic Antimicrobial Chemotherapy (PACT). *Antimicrob. Chemother* **1998**, *42*, 13−58.
(26) Arakane, K.; Ryu, A.; Takarada, K.; Masunaga, T.; Shinmoto, K.; Kobayashi, R.; Mashito, S.; Hirobe, M. Measurement of 1268 nm Emission for Comparison of Singlet Oxygen ((1)Delta(g)) Production Efficiency of Various Dyes. *Chem. Pharm. Bull.* **1996**, *44*, 1−4.
(27) Lindig, B. A.; Rodgers, M. A. J. Laser Photolysis Studies of Singlet Molecular Oxygen in Aqueous Micellar Dispersions. *J. Phys. Chem.* **1979**, *83*, 1683−1688.
(28) Kanofsky, J. R.; Sima, P. D. Structural and Environmental Requirements for Quenching of Singlet Oxygen by Cyanine Dyes. *Photochem. Photobiol.* **2000**, *71*, 361−368.
(29) Herculano, L. S.; Malacarne, L. C.; Zanuto, V. S.; Lukasievicz, G. V. B.; Capeloto, O. A.; Astrath, N. C. G. Investigation of the Photobleaching Process of Eosin Y in Aqueous Solution by Thermal Lens Spectroscopy. *J. Phys. Chem. B* **2013**, *117*, 1932−1937.
(30) Gerola, A. P.; Semensato, J.; Pellosi, D. S.; Batistela, V. R.; Rabello, B. R.; Hioka, N.; Caetano, W. Chemical Determination of Singlet Oxygen from Photosensitizers Illuminated with LED: New Calculation Methodology Considering the Influence of Photobleaching. *J. Photochem. Photobiol., A* **2012**, *232*, 14−21.
(31) Talhavini, M.; Corradini, W.; Atvars, T. D. Z. The Role of the Triplet State on the Photobleaching Process of Xanthene Dyes in Poly(vinyl alcohol) Matrix. *J. Photochem. Photobiol., A* **2001**, *139*, 187−197.
(32) Dibbern-Brubelli, D.; De Oliveira, M. G. Temperature Dependence of the Photobleaching Process of Fluorescein in Poly(vinyl alcohol). *J. Photochem. Photobiol., A* **1995**, *85*, 285−289.
(33) Brennetot, R.; Georges, J. Transient Absorption of the Probe Beam by the Erythrosine Triplet in Pulsed-Laser Thermal Lens Spectrometry: The Influence of the Solvent, Oxygen and Dye concentration. *Chem. Phys. Lett.* **1998**, *289*, 19−24.
(34) Harriman, A.; Porter, G.; Searle, N. Reversible Photo-oxidation of Zinc Tetraphenylporphine by Benzo-1,4-quinone. *J. Chem. Soc., Faraday Trans. 2* **1979**, *75*, 1515−1521.
(35) Gorman, A. A.; Rodgers, M. A. J. Singlet Molecular Oxygen. *Chem. Soc. Rev.* **1981**, *10*, 205−231.
(36) Gorman, A. A.; Lovering, G.; Rodgers, M. A. J. Entropy-Controlled Reactivity of Singlet Oxygen ((1)Delta(g)) Toward Furans and Indoles in Toluene − Variable Temperature Study by Pulse Radiolysis. *J. Am. Chem. Soc.* **1979**, *101*, 3050−3055.
(37) Usui, Y.; Kamogawa, K. Standard System to Determine Quantum Yield of Singlet Oxygen Formation in Aqueous Solution. *Photochem. Photobiol.* **1974**, *19*, 245−247.
(38) Li, F. H.; Kong, Q. Q.; Chen, P.; Chen, M.; Liu, G. G.; Lv, W. Y.; Yao, K. Effect of Halide Ions on the Photodegradation of Ibuprofen in Aqueous Environments. *Chemosphere* **2017**, *166*, 412−417.
(39) Goda, Y.; Sato, K.; Hori, N.; Takeda, M.; Maitani, T. Liberation of Halide Ions from Xanthene Colours by Photoirradiation. *Chem. Pharm. Bull.* **1994**, *42*, 1510−1513.
(40) Keum, Y. S.; Kim, J. H.; Li, Q. X. Relationship Between Singlet Oxygen Formation and Photolysis of Phloxine B in Aqueous Solution. *J. Photosci.* **2003**, *10*, 219−223.
(41) Rodgers, M. A. J.; Snowden, P. T. Lifetime of O2((1)Delta(g)) in Liquid Water as Determined by Time-Resolved Infrared Luminescence Measurements. *J. Am. Chem. Soc.* **1982**, *104*, 5541−5543.
(42) Brun, A. M.; Harriman, A. Energy-Transfer and Electron-Transfer Processes Involving Palladium Porphyrins Bound to DNA. *J. Am. Chem. Soc.* **1994**, *116*, 10383−10393.
(43) King, G. A. M. Self-catalysis. *Chem. Soc. Rev.* **1978**, *7*, 297−316.
(44) Mata-Perez, F.; Perez-Benito, J. F. The Kinetic Rate Law for Autocatalytic Reactions. *J. Chem. Educ.* **1987**, *64*, 925−927.
(45) Haag, W. R.; Hoigne, J.; Gassman, E.; Braun, A. M. Singlet Oxygen in Surface Waters. 1. Furfuryl Alcohol as a Trapping Agent. *Chemosphere* **1984**, *13*, 631−640.
(46) Tanaka, K.; Miura, T.; Urano, Y.; Kikuchi, K.; Higuchi, T.; Nagano, T. Rational Design of Fluorescein-Based Fluorescence Probes, Mechanism-Based Design of a Maximum Fluorescence Probe for Singlet Oxygen. *J. Am. Chem. Soc.* **2001**, *123*, 2530−2536.
(47) Levitus, M.; Ranjit, S. Cyanine Dyes in Biophysical Research; The Photophysics of Polymethine Fluorescent Dyes in Biomolecular Environments. *Q. Rev. Biophys.* **2011**, *44*, 123−151.
(48) Ishiyama, K.; Nakamura, K.; Ikai, H.; Kanno, T.; Kohno, M.; Sasaki, K.; Niwano, Y. Bactericidal Action of Photogenerated Singlet Oxygen from Photosensitizers Used in Plaque Disclosing Agents. *PLoS One* **2012**, *7*, e37871.
(49) Perez-Benito, J. F. Autocatalytic Reaction Pathway on Manganese Dioxide Colloidal Particles in the Permanganate Oxidation of Glycine. *J. Phys. Chem. C* **2009**, *113*, 15982−15991.
(50) Perez-Benito, J. F.; Arias, C.; Amat, E. A Kinetic Study of the Reduction of Colloidal Manganese Dioxide by Oxalic Acid. *J. Colloid Interface Sci.* **1996**, *177*, 288−297.
(51) d'Arlas, B. F.; Rueda, L.; Stefani, P. M.; de la Caba, K.; Mondragon, I.; Eceiza, A. Kinetic and Thermodynamic Studies of the Formation of a Polyurethane Based on 1,6-Hexamethylene Diisocyanate and Poly(carbonate-co-ester) Diol. *Thermochim. Acta* **2007**, *459*, 94−103.
(52) Siani, G.; Angelini, G.; De Maria, P.; Fontana, A.; Pierini, M. Solvent Effects on the Rate of the Keto-Enol Interconversion of 2-Nitrocyclohexanone. *Org. Biomol. Chem.* **2008**, *6*, 4236−4241.
(53) Gottfried, V.; Kimel, S. Temperature Effects on Photosensitized Processes. *J. Photochem. Photobiol., B* **1991**, *8*, 419−430.
(54) Bregnhoj, M.; Westberg, M.; Jensen, F.; Ogilby, P. R. Solvent-Dependent Singlet Oxygen Lifetimes: Temperature Effects Implicate Tunneling and Charge-Transfer Interactions. *Phys. Chem. Chem. Phys.* **2016**, *18*, 22946−22961.
(55) Wang, J.; Gu, J. D.; Nguyen, M. T.; Springsteen, G.; Leszczynski, J. From Formamide to Purine: A Self-Catalyzed Reaction Pathway Provides a Feasible Mechanism for the Entire Process. *J. Phys. Chem. B* **2013**, *117*, 9333−9342.
(56) Mihaylov, T. T.; Parac-Vogt, T. N.; Pierloot, K. A Mechanistic Study of the Spontaneous Hydrolysis of Glycylserine as the Simplest Model for Protein Self-Cleavage. *Chem. - Eur. J.* **2014**, *20*, 456−466.
(57) Rodriguez, R.; Arroyo, R.; Salinas, P. Dynamic Light-Scattering Studies of the Stability and Growth of Silica Particles. *J. Non-Cryst. Solids* **1993**, *159*, 73−79.
(58) Neta, P.; Huie, R. E.; Ross, A. B. Rate Constants for Reactions of Peroxyl Radicals in Fluid Solution. *J. Phys. Chem. Ref. Data* **1990**, *19*, 413−505.
(59) Horvath, A. K.; Nagypal, I.; Epstein, I. R. Oscillatory Photochemical Decomposition of Tetrathionite Ion. *J. Am. Chem. Soc.* **2002**, *124*, 10956−10957.
(60) Filary, A.; Horvath, A. K. Photochemically Induced Catalysis of Iodide Ion and Iodine in the Tetrathionite-Periodate Reaction. *Phys. Chem. Chem. Phys.* **2010**, *12*, 6742−6749.
(61) Nakanishi, H.; Satoh, M.; Norisuye, T.; Tran-Cong-Miyata, Q. Phase Separation of Interpenetrating Polymer Networks Synthesized by Using an Autocatalytic Reaction. *Macromolecules* **2006**, *39*, 9456−9466.
(62) Thapaliya, E. R.; Swaminathan, S.; Captain, B.; Raymo, F. M. Autocatalytic Fluorescence Photoactivation. *J. Am. Chem. Soc.* **2014**, *136*, 13798−13804.

DOI: 10.1021/acs.jpca.7b06440
J. Phys. Chem. A 2017, 121, 8569−8576

(63) Woodford, O.; Harriman, A.; McFarlane, W.; Wills, C. Dramatic Effect of Solvent on the Rate of Photobleaching of Organic Pyrrole-BF2 (BOPHY) Dyes. *ChemPhotoChem.* **2017**, *1*, 317−325.
(64) Thapaliya, E. R.; Captain, B.; Raymo, F. M. Plasmonic Acceleration of a Photochemical Replicator. *Asian J. Org. Chem.* **2015**, *4*, 233−238.

DOI: 10.1021/acs.jpca.7b06440
J. Phys. Chem. A 2017, 121, 8569−8576